

EXPERIMENTAL AND COMPUTATIONAL
INVESTIGATION OF JAHN-TELLER ACTIVE
AND OTHER MOLECULES

DISSERTATION

Presented in Partial Fulfillment of the Requirements for
the Degree Doctor of Philosophy in the Graduate
School of The Ohio State University

By

Ilias Sioutis, B.Sc.

* * * * *

The Ohio State University

2006

Dissertation Committee:

Terry A. Miller, Adviser

Russell M. Pitzer

John W. Wilkins

Approved by

Adviser

Chemical Physics Program

ABSTRACT

The electronic-structure characteristics and vibrational properties of Jahn-Teller active and other molecules are investigated using experimental and computational methods. The molecules that are studied are representative examples of a wide area of Chemical Physics. These are alkoxy radicals (1-propoxy, 1-butoxy, 2-propoxy, and 2-butoxy), Jahn-Teller-active molecules (the silver trimer and the tropyl radical), and larger molecular systems bound by weak dispersion forces or charge-dipole electrostatic forces (the complex systems formed between the xenon atom or the iodide ion and decaborane).

The vibrational structures of 1-propoxy, 1-butoxy, 2-propoxy, and 2-butoxy radicals in their ground \tilde{X} and low-lying \tilde{A} electronic states are investigated using the laser excited, dispersed fluorescence spectroscopic technique. Analysis of the spectra yields the energy separations of the vibrationless levels of the ground \tilde{X} and low-lying \tilde{A} electronic state as well as their vibrational frequencies.

Extensive *ab initio* calculations were performed for the \tilde{X}^2E' and \tilde{A}^2E'' states of the silver trimer Ag_3 . An important goal of these calculations is to guide the analysis of the experimentally observed $\tilde{A}^2E''-\tilde{X}^2E'$ electronic spectrum. Vibrational frequencies of Ag_3 for both the \tilde{X} and \tilde{A} state are reported. Spectroscopically obtainable parameters describing the Jahn-Teller effect are calculated for the \tilde{X} and

\tilde{A} states. Using all this information, the $\tilde{X} - \tilde{A}$ electronic spectrum is predicted for Ag_3 . Following extensive parameter fitting, the absorption and emission spectra are simulated and the bands are assigned.

Theoretical calculations are performed for the \tilde{X}^2E_2'' and \tilde{A}^2E_3'' states of the tropyl radical C_7H_7 , and are used as an aid to the analysis of the experimentally observed $\tilde{A}^2E_3'' - \tilde{X}^2E_2''$ electronic spectrum. Spectroscopically obtainable parameters describing the Jahn-Teller effect are calculated for the \tilde{X} and \tilde{A} states. The $\tilde{X} - \tilde{A}$ electronic spectrum is predicted for C_7H_7 . The experimental molecular parameters characterizing the Jahn-Teller interaction in the \tilde{X} and \tilde{A} states of C_7H_7 are compared to theoretical results.

The interaction of decaborane ($\text{B}_{10}\text{H}_{14}$) with the I^- ion and the (isoelectronic) Xe atom is studied using a number of theoretical methods: MP2, CCSD(T), CCSD, spin-orbit CISD, and DFT using the B3LYP, B3PW91, PW91PW91, and PBE0 methods. All non-DFT and some DFT methods agree that $\text{B}_{10}\text{H}_{14}\text{I}^-$ is bound by charge-dipole electrostatic forces, charge- and dipole-induced-dipole forces, and dispersion forces while $\text{B}_{10}\text{H}_{14}\text{Xe}$ is bound by dipole-induced-dipole forces and dispersion forces.

To My Parents Eleni & Pavlos Sioutis,
In Memory Of My Grandparents
Giannoula Siouti & Ilias Tsotsis,
And An Old Friend
Vladimir A. Lozovsky

ACKNOWLEDGMENTS

I would like to thank my advisor, Terry A. Miller, for his guidance and training in science. I would like to thank Russell M. Pitzer and Anne B. McCoy as they have always played an instrumental and encouraging role throughout my years at The Ohio State University. Our discussions were always constructive and enjoyable, and will always be remembered.

I would like to thank the past and present members of the Miller group. Many thanks to Vadim L. Stakhursky for his support and contribution on various scientific discussions. I would like to thank my fellow graduate students: Jinjun Liu and Erin Sharp. Special thanks to Shenghai Wu who was the one that introduced me in the laboratory and taught me a great deal of things in the experimental work. I enjoyed the times that I spent with Patrick Rupper. I had the best time ever with my officemates Lichang Wang, Tomas Hirsch, Lily Zu and John Yi. I will always carry the memories of the good times that I had with all these people.

I will miss the most Becky Gregory. She has been a good friend and has always supported me from the beginning. She has always been an optimistic person and always shared this optimism with me. She has always shown patience and had the capability to brighten my dark days in the office.

I would like to offer my deepest thanks to Vanda Glezakou, Manos Mavrakis, Gabriel Just, Georgos Tserdanelis, Tania Psathas, Antonis Tsakotellis, Rajni Tyagi, and Ali Hassanali. I will always be indebted to them for their constant support, help, encouragement and friendship. These all know what they mean to me.

I thank my parents for their encouragement, understanding and love. Oftentimes the moments were very stressful and difficult and without their support it is unlikely that I would have kept going.

VITA

1977	Born, Moschato, Attikis, Greece
1999	B.Sc., Department of Chemistry, National and Capodistrian University of Athens, Athens, Greece
2000-2002	Graduate Teaching Assistant, Department of Chemistry, The Ohio State University
2003-present	Graduate Research Assistant, Chemical Physics Program, The Ohio State University

PUBLICATIONS

Jin Jin, Ilias Sioutis, György Tarczay, Sandhya Gopalakrishnan, Andrew Bezant, and T. A. Miller. Dispersed Fluorescence Spectroscopy of Primary and Secondary Alkoxy Radicals. *J. Chem. Phys.* **121**, p. 11780, 2004.

Ilias Sioutis and Russell M. Pitzer. Theoretical Investigation of the Binding Energies of the Iodide Ion and Xenon Atom with Decaborane. *J. Phys. Chem. A* **110**, p. 12528, 2006.

FIELDS OF STUDY

Major Field: Chemical Physics

TABLE OF CONTENTS

ABSTRACT	ii
DEDICATION	iv
ACKNOWLEDGMENTS	v
VITA	vii
LIST OF FIGURES	xii
LIST OF TABLES	xix
CHAPTER	
1 Introduction	1
2 Theoretical Investigation of the Binding Energies of the Iodide Ion and Xenon Atom with Decaborane	11
2.1 Introduction	11
2.2 Theoretical and Computational Methods	13
2.2.1 Evaluation of the Interaction Energy	13
2.2.2 Core Potentials	15
2.2.3 Basis Sets	16
2.2.4 Computational Methods	19
2.3 Results	21
2.3.1 SCF Results for $B_{10}H_{14}I^-$	21
2.3.2 Single-Reference S0-CISD Results for $B_{10}H_{14}I^-$	24
2.3.3 MP2, CCSD, CCSD(T) and DFT Results for $B_{10}H_{14}I^-$	26
2.3.4 SCF Results for $B_{10}H_{14}Xe$	28

2.3.5	Single-Reference S0-CISD Results for $B_{10}H_{14}Xe$	29
2.3.6	MP2, CCSD, CCSD(T) and DFT Results for $B_{10}H_{14}Xe$	30
2.4	Discussion	31
2.5	Conclusions	34
3	Dispersed Fluorescence Spectroscopy of Primary and Secondary Alkoxy Radicals	36
3.1	Introduction	36
3.2	Experimental Details	37
3.3	Results	39
3.3.1	Quantum Chemistry Calculations	41
3.3.2	LEDF Observations	55
3.3.3	1-Propoxy	58
3.3.4	1-Butoxy	68
3.3.5	2-Propoxy	76
3.3.6	2-Butoxy	81
3.4	Discussion	88
3.5	Conclusions	93
4	The <i>Ab Initio</i> Calculation of Spectroscopically Observable Parameters for the \tilde{X}^2E' and \tilde{A}^2E'' Electronic States of the Silver Trimer	95
4.1	Introduction	95
4.2	The Silver Trimer Potential Energy Surface and Jahn-Teller Effects	99
4.2.1	General Features	99
4.2.2	Nuclear Displacement Coordinates	101
4.2.3	The Spectroscopic Model of the Jahn-Teller PES	102
4.2.4	Spin-Orbit Interaction	112
4.3	Calculational Details	114
4.3.1	Electronic Structure Calculations	114
4.3.2	Basis-Set Construction	124
4.4	Results	128
4.4.1	The \tilde{X} State	129
4.4.2	The \tilde{A} State	144
4.5	Discussion	149
4.6	Conclusions	157

5	Vibrational Analysis of the $\tilde{A}^2E''-\tilde{X}^2E'$ Electronic Transition of the Silver Trimer	159
5.1	Introduction	159
5.2	Theoretical	161
5.2.1	Vibronic Eigenvalues and Eigenfunctions	161
5.2.2	Line Intensities and Selection Rules	163
5.2.3	Theoretical Simulations	169
5.3	Results	171
5.3.1	Assignment of the \tilde{A}^2E'' State	171
5.3.2	Assignment of the \tilde{X}^2E' State	180
5.3.3	Emission from Band 1 of the \tilde{A} State of Ag_3	180
5.3.4	Emission from Band 3 of the \tilde{A} State of Ag_3	187
5.3.5	Emission from Band 4 of the \tilde{A} State of Ag_3	189
5.3.6	Emission from Bands 2 and 5 of the \tilde{A} State of Ag_3	194
5.4	Discussion	199
5.5	Conclusions	204
6	Computational and Experimental Investigation of the Jahn-Teller Effect in the Ground and Excited States of the Tropyl Radical: Vibrational Analysis of the $\tilde{A}^2E''_3-\tilde{X}^2E''_2$ Electronic Transition	205
6.1	Introduction	205
6.2	The Tropyl Potential Energy Surface	206
6.2.1	General Features	206
6.2.2	The Spectroscopic Model of the Jahn-Teller PES	210
6.3	Theoretical	221
6.3.1	Vibronic Eigenvalues and Eigenfunctions	221
6.3.2	Selection Rules	227
6.4	Experimental Details	228
6.5	Results	231
6.5.1	Assignment of the $\tilde{A}^2E''_3$ State	231
6.5.2	Assignment of the $\tilde{X}^2E''_2$ State	246
6.5.3	Emission from Bands A and B of the \tilde{A} State of C_7H_7	247
6.5.4	Emission from Band C of the \tilde{A} State of C_7H_7	261
6.6	Discussion	262
6.7	Conclusions	265

7	Conclusions	266
	BIBLIOGRAPHY	272

LIST OF FIGURES

FIGURE	PAGE
2.1 The molecular configuration and numbering scheme of $B_{10}H_{14}I^-$ and $B_{10}H_{14}Xe$. The bridging hydrogens ($\mu - H$) are between B(2), B(4,5) and B(1), B(6,3). There is no bond between B(4), B(5) and B(6), B(3) but between B(4), B(5) and B(10), and B(6), B(3) and B(9)	12
3.1 Newman projections of three unique conformational structures of 2-butoxy at their local minima. The designation of the conformers is based on the value of the dihedral angle ϕ which is formed by C_2-C_1-O and $C_1-C_2-C_3$ planes; rotation about the C_1-C_2 bond changes ϕ from 60° (<i>gauche clockwise G+</i>), to 180° (<i>trans T</i>) and -60° (<i>gauche counterclockwise G-</i>).	42
3.2 Survey scans of the LIF spectra of the primary radicals. The line labeled B in 1-propoxy extends off-scale so as to show more clearly the weaker transitions.	56
3.3 Survey scans of the LIF spectra of the secondary alkoxies. Note the difference in frequency scales.	57
3.4 LEDF spectra of the <i>T</i> and <i>G</i> conformations of 1-propoxy radical. The top trace was obtained by pumping band B (Fig. 3.2), the origin of the <i>T</i> conformer, at 29218 cm^{-1} while the bottom trace was obtained by pumping band A (Fig. 3.2), the origin of the <i>G</i> conformer, at 28634 cm^{-1} . The x axis indicates (red) shift from the pump frequency. The intensities are not corrected for the grating efficiency and the camera sensitivity curves. The experimental resolution was 15 cm^{-1}	59

3.5 An expanded view of the LEDF spectra of the <i>T</i> and <i>G</i> conformations of 1-propoxy radical. The top trace was obtained by pumping band B (Fig. 3.2), the origin of the <i>T</i> conformer, at 29218 cm ⁻¹ while the bottom trace was obtained by pumping band A (Fig. 3.2), the origin of the <i>G</i> conformer, at 28634 cm ⁻¹ . The x axis indicates (red) shift from the pump frequency. The intensities are not corrected for the grating efficiency and the camera sensitivity curves. The experimental resolution was 15 cm ⁻¹ .	60
3.6 LEDF spectra of the <i>T</i> ₁ <i>G</i> ₂ , <i>T</i> ₁ <i>T</i> ₂ , and <i>G</i> ₁ <i>T</i> ₂ conformations of 1-butoxy radical. The top trace was obtained by pumping band C (Fig. 3.2), the origin of the <i>T</i> ₁ <i>G</i> ₂ conformer, at 29164 cm ⁻¹ , the middle trace was obtained by pumping band B (Fig. 3.2), the origin of the <i>T</i> ₁ <i>T</i> ₂ conformer, at 29095 cm ⁻¹ while the bottom trace by pumping band A (Fig. 3.2), the origin of the <i>G</i> ₁ <i>T</i> ₂ conformer, at 28649 cm ⁻¹ . The x axis indicates (red) shift from the pump frequency. The intensities are not corrected for the grating efficiency and the camera sensitivity curves. The experimental resolution was 15 cm ⁻¹ .	69
3.7 An expanded view of the LEDF spectra of the <i>T</i> ₁ <i>G</i> ₂ , <i>T</i> ₁ <i>T</i> ₂ , and <i>G</i> ₁ <i>T</i> ₂ conformations of 1-butoxy radical. The top trace was obtained by pumping band C (Fig. 3.2), the origin of the <i>T</i> ₁ <i>G</i> ₂ conformer, at 29164 cm ⁻¹ , the middle trace was obtained by pumping band B (Fig. 3.2), the origin of the <i>T</i> ₁ <i>T</i> ₂ conformer, at 29095 cm ⁻¹ while the bottom trace by pumping band A (Fig. 3.2), the origin of the <i>G</i> ₁ <i>T</i> ₂ conformer, at 28649 cm ⁻¹ . The x axis indicates (red) shift from the pump frequency. The intensities are not corrected for the grating efficiency and the camera sensitivity curves. The experimental resolution was 15 cm ⁻¹ .	70
3.8 LEDF spectra of 2-propoxy radical. The top trace was obtained by pumping band B (Fig. 3.3), the frequency of the first member of the CO stretch progression, at 27734 cm ⁻¹ . The bottom trace corresponds to an expanded view of the LEDF data shown in the top trace. The x axis indicates (red) shift from the pump frequency. The intensities are not corrected for the grating efficiency and the camera sensitivity curves. The experimental resolution was 30-35 cm ⁻¹ .	78

3.9 LEDF spectra of the A and B conformations of 2-butoxy radical. The lowest trace was obtained by pumping band A (Fig. 3.3), the origin of the A conformer at 26760 cm^{-1} while the next to the lowest trace was obtained by pumping band B (Fig. 3.3), the origin of the B conformer, at 27068 cm^{-1} . The trace obtained by pumping band C, at 27321 cm^{-1} , corresponds to the transition which includes one quantum of the CO stretch vibration of the A conformer in the \tilde{B} state, while the trace through D, at 27682 cm^{-1} , to the same type of excitation but for the B conformer. The x axis indicates (red) shift from the pump frequency. The intensities are not corrected for the grating efficiency and the camera sensitivity curves. The experimental resolution was $30\text{-}35\text{ cm}^{-1}$.	82
3.10 An expanded view of the LEDF spectra of the A and B conformations of 2-butoxy radical. The lowest trace was obtained by pumping band A (Fig. 3.3), the origin of the A conformer at 26760 cm^{-1} while the next to the lowest trace was obtained by pumping band B (Fig. 3.3), the origin of the B conformer, at 27068 cm^{-1} . The trace obtained by pumping band C, at 27321 cm^{-1} , corresponds to the transition which includes one quantum of the CO stretch vibration of the A conformer in the \tilde{B} state, while the trace through D, at 27682 cm^{-1} , to the same type of excitation but for the B conformer. The x axis indicates (red) shift from the pump frequency. The intensities are not corrected for the grating efficiency and the camera sensitivity curves. The experimental resolution was $30\text{-}35\text{ cm}^{-1}$.	83
4.1 The symmetry displacements of a planar triatomic equilateral nuclear conformation. The displacements Q_{e_y} and Q_{e_x} are, respectively, the real and imaginary parts of the complex coordinate $Q_{e',\pm}$.	100

4.2 Downward-looking view of the linear and quadratic Jahn-Teller distorted lower PES appropriate for Ag_3 . The coordinates Q_{e_x} and Q_{e_y} denote the two unique dimensions along which motion resolves the degeneracy of the conical intersection corresponding to the $^2\text{E}'$ or $^2\text{E}''$ state. Around the perimeter of the figure are pictures of the distorted Ag_3 geometries for the corresponding value of the pseudo-rotation phase angle ϕ . The quadratic Jahn-Teller effect introduces a ϕ dependence in the energy. The radius of the pseudo-rotation circle is given by the magnitude of the distortion parameter ρ . The pictures are schematic only and do not attempt to represent all details of the distortion, e.g., the exact positions of the Ag atoms.	109
4.3 Ag_3 potential energy curves for the $^2\text{A}_1$ and $^2\text{B}_2$ components of the \tilde{X} $^2\text{E}'$ state along the C_{2v} coordinate Q_{e_y} of the single Jahn-Teller active \tilde{X} -state e' vibrational mode.	116
4.4 Ag_3 potential energy curves at the SCF and CISD levels of theory for the $^2\text{A}_1$ and $^2\text{B}_2$ components of the \tilde{X} $^2\text{E}'$ state along the C_{2v} coordinate Q_{e_y} of the single Jahn-Teller active \tilde{X} -state e' vibrational mode.	117
4.5 Ag_3 potential energy curves at the SOCISD level of theory for the $^2\text{A}_1$ and $^2\text{B}_2$ Jahn-Teller components of the \tilde{X} $^2\text{E}'$ state along the C_{2v} coordinate Q_{e_y} of the single Jahn-Teller active \tilde{X} -state e' vibrational mode.	118
4.6 Ag_3 potential energy curves at the SCF and CISD levels of theory for the $^2\text{A}_2$ and $^2\text{B}_1$ components of the \tilde{A} $^2\text{E}''$ state along the C_{2v} coordinate Q_{e_y} of the single Jahn-Teller-active \tilde{A} -state e' vibrational mode.	119
4.7 Ag_3 potential energy curves at the SOCISD level of theory for the $^2\text{A}_2$ and $^2\text{B}_1$ Jahn-Teller components of the \tilde{A} $^2\text{E}''$ state along the C_{2v} coordinate Q_{e_y} of the single Jahn-Teller-active \tilde{A} -state e' vibrational mode.	120

4.8	Ag_3 potential energy curves for the $^2\text{A}_1$ and $^2\text{B}_2$ components of $\tilde{X} \ ^2\text{E}'$ along the coordinate Q_{e_y} of the e' vibrational mode. The curves Type II and Type I correspond, in respect, to CISD energy calculations that explicitly include or omit in the list of correlating MOs those that give rise to $^2\text{A}'_1$, $^2\text{E}'$, $^2\text{E}'$, $^2\text{A}'_2$ and $^2\text{A}'_1$	122
5.1	Qualitative energy level scheme of the vibronic energy levels of a $^2\text{E}'$ state under D_{3h} symmetry, with a single Jahn-Teller active mode of e' symmetry, for the following Hamiltonians.	164
5.2	Qualitative energy level scheme of the vibronic energy levels of a $^2\text{E}''$ state under D_{3h} symmetry, with a single Jahn-Teller active mode of e' symmetry, for the following Hamiltonians.	165
5.3	Energy level diagram of the lowest three spin-vibronic levels of the \tilde{X} state and those that characterize bands 1-5 of the \tilde{A} state. The ordering of the energy levels is not in scale. Their labels based on the $ j, n_j\rangle \Sigma\rangle$ and the spin-double group notations are given at the left side of the Figure. Their energies (relative to the lowest level of the \tilde{X} and \tilde{A} states) were computed using the best-fit spectral parameters of the \tilde{X} and \tilde{A} states, and are shown at the right side of the Figure, in cm^{-1} . The dashed line at the left corresponds to the simulation's origin transition of the excitation spectrum depicted by 0 cm^{-1} in the fifth column of Table 5.3, and the star on top of it means that the spin-double group symmetry of the terminating level in the excitation is $e_{3/2}$. The transition with excitation frequency -2 cm^{-1} refers to $ \frac{1}{2}, 1\rangle - \frac{1}{2}\rangle$ of $\tilde{X} \rightarrow \frac{1}{2}, 1\rangle - \frac{1}{2}\rangle$ of \tilde{A} . The terminating level in this transition has $e_{1/2}$ symmetry. The dashed line at the right corresponds, for the simulation of the emission spectrum laser excited to the origin of \tilde{A} , to the transition with the emission frequency of 0 cm^{-1} depicted in the fourth column of Table 5.4, and the star on top of it means that the terminating level in the emission has $e_{5/2}$ symmetry. The transition $ \frac{1}{2}, 1\rangle - \frac{1}{2}\rangle$ of $\tilde{A} \rightarrow \frac{1}{2}, 1\rangle - \frac{1}{2}\rangle$ of \tilde{X} has an emission frequency of 2 cm^{-1} and terminates to a level of the \tilde{X} state with $e_{3/2}$ symmetry. . .	172
5.4	Excitation spectrum of Ag_3 , from $ \frac{1}{2}, 1\rangle \pm \frac{1}{2}\rangle$ of the $\tilde{X} \ ^2\text{E}'$ state. . . .	175

5.5	Emission spectrum of Ag_3 , laser excited to the vibrationless level of the $\tilde{A}^2\text{E}''$ state.	182
5.6	Emission spectrum of Ag_3 , laser excited to band 3 of the $\tilde{A}^2\text{E}''$ state.	188
5.7	Emission spectrum of Ag_3 , laser excited to band 4 of the $\tilde{A}^2\text{E}''$ state.	190
5.8	Emission spectrum of Ag_3 , laser excited to band 2 of the $\tilde{A}^2\text{E}''$ state.	195
5.9	Emission spectrum of Ag_3 , laser excited to band 5 of the $\tilde{A}^2\text{E}''$ state.	200
6.1	Plot of the \tilde{X} -state (or \tilde{A} -state) PES of the tropyl radical, where E is energy and Q_a and Q_b are the unique directions that lift the degeneracy present at the D_{7h} geometry.	207
6.2	Slice through the \tilde{X} -state potential (or the \tilde{A} -state potential) at an arbitrary angle around the moat (shown in Fig. 6.1). The point X_0 defines the geometry of the symmetric D_{7h} (conical intersection) point on the \tilde{X} -state PES (or the \tilde{A} -state PES), and X_{min} is the geometry of the global minimum on the \tilde{X} -state PES (or \tilde{A} -state PES). The vector \vec{d} is the distortion vector. The parameter ε_T is the total linear Jahn-Teller stabilization energy, while ρ_{JT}^{min} is the distance from X_0 to X_{min}	208
6.3	Schematic diagram of the experimental apparatus for obtaining the LIF spectrum. The apparatus for the LEDF experiments was similar except the fluorescence was dispersed.	229
6.4	REMPI (top) and LIF (bottom) spectra of C_7H_7 . The REMPI spectrum was taken from Ref. 1 and the LIF spectrum comes from the present work. The stars in the excitation spectrum designate the bands of the \tilde{A} state that we have dispersed emission from. Of central importance for the analysis of the vibronic structure of the $\tilde{X}^2\text{E}_2''$ state is the LEDF emission collected by pumping bands A-C of the $\tilde{A}^2\text{E}_3''$ state. The x axis indicates the excitation frequency. The intensities observed in the LIF spectrum were not corrected for the dye-laser power deviations. The experimental resolution was 4 cm^{-1}	233

6.5 Dispersed fluorescence spectra of the C ₇ H ₇ radical collected by pumping bands A (bottom), B (middle), and C (top) of the $\tilde{A}^2E''_3$ state. The entrance slit width before the monochromator was 125 μm . The x axis indicates (red) shift from the pump frequency. The intensities were not corrected for the grating efficiency and the camera sensitivity curves. The experimental resolution was 20 cm^{-1} . Note also that the structure observed approximately < 700 cm^{-1} in the emission from bands A and B are due to artifacts of the discharge source.	237
6.6 Dispersed fluorescence spectra of the C ₇ H ₇ radical collected by pumping bands A (bottom) and B (top) of the $\tilde{A}^2E''_3$ state. The entrance slit width before the monochromator was 125 μm . For the emission through band A, the x axis indicates (red) shift from the pump frequency. The emission through band B in this figure corresponds to the subtraction of the emission frequencies of Fig. 6.5B by 415 cm^{-1} . The intensities were not corrected for the grating efficiency and the camera sensitivity curves. The experimental resolution was 20 cm^{-1}	238
6.7 Excitation spectrum of C ₇ H ₇ , laser excited from the vibrationless level of the $\tilde{X}^2E''_2$ state.	244
6.8 Emission spectrum of C ₇ H ₇ , laser excited to the vibrationless level of the $\tilde{A}^2E''_3$ state, band A.	249
6.9 Emission spectrum of C ₇ H ₇ , laser excited to the 1/2, 2> Jahn-Teller level of the $\tilde{A}^2E''_3$ state, band C.	263

LIST OF TABLES

TABLE	PAGE
2.1 I cc-pVTZ Basis Set: (5s5p5d1f)/[4s3p3d1f]	17
2.2 SCF and SO-CISD energies relative to -144 E _h for B ₁₀ H ₁₄ I ⁻ at its equilibrium geometry using various basis-set contraction schemes on the I atom. The ΔE values are correlation energies (in E _h).	18
2.3 Xe cc-pVDZ Basis Set: (3s3p5d1f)/[3s2p3d1f]	19
2.4 B cc-pVDZ Basis Set : (4s4p1d)/[3s2p1d]	20
2.5 SCF and spin-orbit CI (singles and doubles) energies (in E _h) for B ₁₀ H ₁₄ I ⁻ at R _e and at R=100 (both in b). ΔE is the dissociation energy (in kcal/mol).	21
2.6 Ground-state B ₁₀ H ₁₄ SCF Mulliken Population Analysis. Boron has three valence electrons and the labels refer to the symmetry-distinct atoms. The labels of the hydrogens are the same as those of the borons that they are bonded to and μ - H is for the bridging hydrogens. . .	23
2.7 Ground-state B ₁₀ H ₁₄ I ⁻ SCF Mulliken Population Analysis. The number of valence electrons is three for boron and eighteen for iodide. The labels refer to the symmetry-distinct atoms. The labels of the hydrogens are the same as those of the borons that they are bonded to and μ - H is for the bridging hydrogens.	23
2.8 Wave-function-based results for B ₁₀ H ₁₄ I ⁻ . The binding energy (BE) is in kcal/mol and CP denotes counterpoise procedure.	27

2.9 DFT and SO-DFT results for $\text{B}_{10}\text{H}_{14}\text{I}^-$. The binding energy (BE) is in kcal/mol and CP denotes counterpoise procedure.	27
2.10 Ground-state $\text{B}_{10}\text{H}_{14}\text{Xe}$ SCF Mulliken Population Analysis at $R_e=8.73293$ and at $R=100$ b. The number of valence electrons is three for boron and eighteen for xenon. The labels refer to the symmetry-distinct atoms. The labels of the hydrogens are the same as those of the borons that they are bonded to and $\mu - H$ is for the bridging hydrogens.	29
2.11 SCF and spin-orbit CI (singles and doubles) energies (in E_h) for $\text{B}_{10}\text{H}_{14}\text{Xe}$ at $R_e=8.73293$ b. and at $R=100$ b. ΔE denotes the dissociation energy (in kcal/mol).	30
2.12 Wave-function-based results for $\text{B}_{10}\text{H}_{14}\text{Xe}$. The binding energy (BE) is in kcal/mol and CP denotes counterpoise procedure.	31
2.13 DFT and SO-DFT results for $\text{B}_{10}\text{H}_{14}\text{Xe}$. The binding energy (BE) is in kcal/mol and CP denotes counterpoise procedure.	31
3.1 Summary of the conditions used for the experiments with the primary and secondary alkoxies.	38
3.2 Energy differences (in cm^{-1}) relative to the energy of the lowest energy conformation of the primary and secondary radicals in their ground electronic state as obtained at the B3LYP/6-31+G* level of theory.	43
3.3 Experimental and calculated $\tilde{A}-\tilde{X}$ energy separation (in cm^{-1}) of a number of open-chain alkoxy radicals.	44
3.4 The calculated lowest 15 vibrational frequencies (in cm^{-1}) of the T conformer of 1-propoxy radical in its ground electronic state as obtained at the B3LYP/6-31+G* level of theory.	46
3.5 The calculated lowest 17 vibrational frequencies (in cm^{-1}) of the G conformer of 1-propoxy radical in its ground electronic state as obtained at the B3LYP/6-31+G* level of theory.	47

3.6 The calculated lowest 15 vibrational frequencies (in cm^{-1}) of the T_1T_2 conformer of 1-butoxy radical in its ground electronic state as obtained at the B3LYP/6-31+G* level of theory.	48
3.7 The calculated lowest 16 vibrational frequencies (in cm^{-1}) of the T_1G_2 conformer of 1-butoxy radical in its ground electronic state as obtained at the B3LYP/6-31+G* level of theory.	49
3.8 The calculated lowest 16 vibrational frequencies (in cm^{-1}) of the G_1T_2 conformer of 1-butoxy radical in its ground electronic state as obtained at the B3LYP/6-31+G* level of theory.	50
3.9 The calculated lowest 15 vibrational frequencies (in cm^{-1}) of 2-propoxy radical in its ground electronic state as obtained at the B3LYP/6-31+G* level of theory.	51
3.10 The calculated lowest 17 vibrational frequencies (in cm^{-1}) of the G^+ conformer of 2-butoxy radical in its ground electronic state as obtained at the B3LYP/6-31+G* level of theory.	52
3.11 The calculated lowest 17 vibrational frequencies (in cm^{-1}) of the T conformer of 2-butoxy radical in its ground electronic state as obtained at the B3LYP/6-31+G* level of theory.	53
3.12 The calculated lowest 17 vibrational frequencies (in cm^{-1}) of the G^- conformer of 2-butoxy radical in its ground electronic state as obtained at the B3LYP/6-31+G* level of theory.	54
3.13 Assignment of the LEDF spectrum of the T conformer of 1-propoxy radical. The vibrational assignment is made for the emission pumping bands shown in Fig. 3.5.	62
3.14 Assignment of the LEDF spectrum of the G conformer of 1-propoxy radical. The vibrational assignment is made for the emission pumping bands shown in Fig. 3.5.	65

3.15 Assignment of the LEDF spectrum of the $T_1 T_2$ conformer of 1-butoxy radical. The vibrational assignment is made for the emission pumping bands shown in Fig. 3.7.	72
3.16 Assignment of the LEDF spectrum of the $T_1 G_2$ conformer of 1-butoxy radical. The vibrational assignment is made for the emission pumping bands shown in Fig. 3.7.	74
3.17 Assignment of the LEDF spectrum of the $G_1 T_2$ conformer of 1-butoxy radical. The vibrational assignment is made for the emission pumping bands shown in Fig. 3.7.	77
3.18 Assignment of the LEDF spectrum pumped via the first member of the CO stretch progression of the excitation spectrum of 2-propoxy radical. The vibrational assignment is made for the emission pumping bands shown in Fig. 3.8.	80
3.19 Assignment of the LEDF spectrum of the “B” conformer of 2-butoxy radical. The vibrational assignment is made for the emission pumping bands shown in Fig. 3.10.	85
3.20 Assignment of the LEDF spectrum of the “A” conformer of 2-butoxy radical. The vibrational assignment is made for the emission pumping bands shown in Fig. 3.10.	86
3.21 Summary (in cm^{-1}) of experimentally determined \tilde{X} and \tilde{A} state vibrational fundamental frequencies of the CO stretch mode of the primary and secondary alkoxy radicals. The table summarizes the results of this work unless noted otherwise. The reported standard deviation of $\omega_e x_e$ is determined by the fit and it does not include the uncertainties of ω_0	92
4.1 The Jahn-Teller coupling coefficients that parameterize the effective spectroscopic Hamiltonian and their relationships to the terms of the Taylor series expansion of the potential.	105
4.2 Ag core cc-pVDZ Basis Set:(5s5p5d1f)/[5s4p3d1f]	125

4.3	Theoretically calculated lowest three energy states of Ag based on our newly constructed cc-pVDZ basis set and comparison with corresponding experimental values.	127
4.4	Geometries and energy separation of the \tilde{X}^2E' - and \tilde{A}^2E'' -Jahn-Teller-split states of Ag_3	130
4.5	Summary of geometries and symmetric stretch frequencies for the \tilde{X}^2E' state and a number of low-lying excited electronic state of Ag_3	131
4.6	Molecular parameters of the \tilde{X}^2E' electronic state of Ag_3	142
4.7	Mulliken population analysis for Ag_3 . ^a	143
4.8	Molecular parameters of the \tilde{A}^2E'' electronic state of Ag_3	148
4.9	Geometries of Ag_3 at the global minima and saddle points as well as at the conical intersection of the Jahn-Teller distorted PES of the \tilde{X}^2E' electronic state. Comparison of the present work's results with past theoretical studies in reverse chronicle order.	154
5.1	Jahn-Teller and Spin-Orbit interaction parameters of the \tilde{X}^2E' and \tilde{A}^2E'' electronic states of Ag_3	160
5.2	Fitted and calculated spectral parameters, FC_{ki} , relevant to the determination of the Franck-Condon factors along the totally symmetric mode for Ag_3	168
5.3	Frequencies and \tilde{A}^2E'' - \tilde{X}^2E' transition assignments of Ag_3	173
5.4	Calculated and experimentally observed spectral transitions to the \tilde{X}^2E' state originating in bands 1 and 3 of the \tilde{A}^2E'' state of Ag_3	186
5.5	Calculated and experimentally observed spectral transitions to the \tilde{X}^2E' state originating in band 4 of the \tilde{A}^2E'' state of Ag_3	193
5.6	Calculated and experimentally observed spectral transitions to the \tilde{X}^2E' state originating in band 2 of the \tilde{A}^2E'' state of Ag_3	197

5.7	Calculated and experimental stabilization energies and barriers to pseudorotation of the \tilde{X}^2E' - and \tilde{A}^2E'' -state potential energy surfaces of Ag_3	203
6.1	The Jahn-Teller coupling coefficients that parameterize the effective spectroscopic Hamiltonian and their relationships to the terms of the Taylor series expansion of the potential.	212
6.2	Allowed values of s_e , s_v and s_k for $n \leq 7$ and $k = 1$ or 2	214
6.3	The vibrational frequencies (cm^{-1}) of the geometrically optimized $C_7H_7^+$ in its $\tilde{X}^1A'_1$ state calculated at the B3LYP/6-31G** level of theory compared to experimental values of the $\tilde{X}^2E''_2$ and $\tilde{A}^2E''_3$ states of C_7H_7	222
6.4	Jahn-Teller Parameters of the $\tilde{X}^2E''_2$ and $\tilde{A}^2E''_3$ electronic states of C_7H_7	224
6.5	Summary of the conditions used for the LIF and LEDF experiments with the tropyl radical.	230
6.6	Frequencies and $\tilde{A}^2E''_3 \leftarrow \tilde{X}^2E''_2$ transition assignments of C_7H_7	234
6.7	Calculated and experimentally observed Jahn-Teller transitions to the $\tilde{A}^2E''_3$ state of $C_7H_7^a$	245
6.8	Experimentally observed spectral transitions to the $\tilde{X}^2E''_2$ state originating in bands A-C of the $\tilde{A}^2E''_3$ state of C_7H_7	248
6.9	Calculated and experimentally observed Jahn-Teller transitions to the $\tilde{X}^2E''_2$ state of $C_7H_7^a$	252

CHAPTER 1

Introduction

The research presented in this dissertation involves the investigation of the electronic and vibrational properties of a number of interesting molecules. The common theme of these studies lies in the development and description of suitable computational methodologies and experimental approaches to tackle the individual problems accompanying each of the molecules and topics studied. It is the synergic relationship between theory and experiment in combination with the advanced computational resources that make it possible today to successfully determine and understand the characteristics and peculiarities of a wide array of molecules. The work described in this dissertation involves alkoxy radicals, specifically, 1-propoxy, 1-butoxy, 2-propoxy, and 2-butoxy, Jahn-Teller-active molecules, i.e., the silver trimer and the tropyl radical, and large molecules bound by weak dispersion forces or charge-dipole electrostatic forces, i.e., the complex system between the xenon atom or the iodide ion and decaborane.

Members of the family of the alkoxy radicals are subject to unique physico-chemical interactions (Jahn-Teller or pseudo-Jahn-Teller) which further complicate their analyses. For example, the simplest molecule with Jahn-Teller effects is methoxy

CH_3O in its ground electronic state \tilde{X}^2E . As the Jahn-Teller effect causes coupling between the electronic and vibrational degrees of freedom, a very complicated pattern of vibronic levels is expected for Jahn-Teller active molecules.

In this dissertation the Jahn-Teller effects of silver trimer and the tropyl radical are also studied. These studies may be used as benchmark examples of Jahn-Teller analyses. Aside from being prototypical systems to study the Jahn-Teller effect, they are also interesting molecules to investigate due to various characteristics that they exhibit and also due to the fact that their previous analyses, where available, have been ambiguous.

Aside from basic scientific interest, these molecules are studied due to their important role in chemical processes or their wider applications in industrial processes. For example, the alkoxy radicals are key components in the oxidation chemistry of the atmosphere. The oxidation of hydrocarbons is among the most important of chemical processes, with combustion and the degradation of volatile organic compounds injected in our atmosphere being the prime examples. The reactions of the simplest oxygen-containing organic radicals, e.g., alkoxy, RO , and peroxy, RO_2 radicals, affect the yield of ozone, air toxics, and organic aerosols in the atmosphere.² Combustion of hydrocarbon fuels at temperatures ≤ 1000 K share many mechanistic details with their atmospheric oxidation. The existence of multiple reaction pathways for these radicals complicates efforts for the understanding of the potential oxidation scheme of hydrocarbons, as it is the competition among the various radical reaction pathways

that determines the end products of the oxidation.³ Hence elucidation of their chemistry is paramount for obtaining a better understanding of combustion processes and the impact of hydrocarbons in the atmosphere.

There have been extensive spectroscopic investigations, via the $\tilde{B}-\tilde{X}$ electronic transition, of the smaller alkoxy radicals⁴ as well as some study of larger ones.⁵ Laser-induced fluorescence (LIF) excitation spectroscopy of jet-cooled radicals has provided a good deal of information about the excited states. Very recently, high-resolution rotationally resolved spectroscopy of a number of bands of jet-cooled primary alkoxy radicals^{6,7} yielded detailed information about the structure and geometries of both the \tilde{B} and \tilde{X} states. It was found that various bands of the LIF spectra uniquely correlated with different conformers of a given structural isomer.

However, information about the excitation energy of the low-lying \tilde{A} state as well as the ground \tilde{X} state's vibrational structure and dynamics has been relatively sparse. A suitable technique for investigating this area is laser excited, dispersed fluorescence (LEDF) spectroscopy. It has been used to probe the vibronic levels in the ground state of CH_3O ⁸ and $\text{C}_2\text{H}_5\text{O}$.⁹ However, LEDF studies have not been extended to larger alkoxy radicals thus far.

In the work described in this thesis, LIF spectroscopy was combined with supersonic free-jet expansion techniques to record the LEDF spectra from a number of \tilde{B} state levels of the 1- and 2- isomers of the propoxy and butoxy radicals. These spectra can yield the direct measurements of the $\tilde{A} - \tilde{X}$ electronic state separation.

Silver clusters have received considerable attention¹⁰ from both theoreticians and experimentalists for (*i*) their catalytic properties; (*ii*) their role in the formation of latent photographic images; and (*iii*) their role as a bridge between the molecular sciences and surface and solid-state sciences.

Among the simplest silver clusters is the silver trimer, Ag_3 , which is the middle member of the coinage (Cu, Ag, Au) metal trimers. It has been used as a typical system to investigate the contrast in the bonding between the second and third row transition metal clusters.¹¹⁻¹³ The \tilde{X} -state is ${}^2E'$ in the nominal D_{3h} symmetry with an allowed transition to the \tilde{A}^2E'' excited electronic state. The degeneracy of both the \tilde{A}^2E'' and \tilde{X}^2E' states is lifted due to the Jahn-Teller distortion along the e' bending coordinate. It is a single-mode system with linear and quadratic Jahn-Teller activity subject to spin-orbit coupling. This system offers an opportunity, both theoretically and experimentally, to investigate a single mode Jahn-Teller system with potentially large spin-orbit coupling, a situation where data is largely lacking.

Experimental data on the \tilde{X}^2E' Ag_3 state is relatively sparse. The dispersed fluorescence spectroscopic study by Ellis *et al*¹⁴ gave some information about the \tilde{X} -state vibronic structure. The theoretical work by Walch *et al*¹⁵ predicted for the linear¹⁶ Jahn-Teller coupling constant ($D_{e'}$) a value of 7.33 and for the quadratic Jahn-Teller coupling constant ($K_{e'}$) a value of 0.107. Note that the Jahn-Teller parameters were extracted from the topology of the Jahn-Teller-distorted potential energy surface (PES). Wedum *et al*¹⁷ refined the \tilde{X} -state *ab initio*¹⁵ Jahn-Teller parameters by fitting the experimental intensities of the transitions to the \tilde{A} state. They concluded that

a better fit to positions in the Ag_3 origin emission spectrum is obtained from the experimental Jahn-Teller parameters than the *ab initio*¹⁵ ones. The work by Wedum *et al.*¹⁷ concluded that $D_{e'}=1.86$ and $K_{e'}=0.25$. The analysis by these authors assumed no spin-orbit interaction in the \tilde{X} state. In a different analysis by Riley *et al.*¹⁸ $D_{e'}$ was found to be 3.20 and $K_{e'}=0.12$. These were recalculated from *ab initio*¹⁵ results after readjustment of the theoretical bending mode frequency. No spin-orbit coupling was considered. None of these works successfully interpreted the existing dispersed fluorescence spectra.¹⁴ Therefore, no consensus concerning the vibronic structure of \tilde{X}^2E' has been achieved thus far.

The \tilde{A}^2E'' state has been experimentally described comparably better than the \tilde{X}^2E' , but the interpretation of the data is still less than satisfactory. LIF¹⁴ and resonance enhanced multiphoton ionization (REMPI) experiments^{17–20} were previously used to measure the $\tilde{A}^2E'' \leftarrow \tilde{X}^2E'$ spectrum. There are three distinct analyses that appear to fit the data relatively well. The first two are summarized in the work by Wedum *et al.*¹⁷ These authors empirically fitted the lower vibronic levels of the excited state to a theoretical spectrum generated from an $E \otimes e$ vibronic coupling scheme using two different methods. These included either spin-orbit coupling (190 cm^{-1}) and linear-only Jahn-Teller coupling ($D_{e'}=0.04$) or linear and quadratic Jahn-Teller coupling and no spin-orbit coupling. ($D_{e'}=0.02$ and $K_{e'}=0.02$.) The third analysis by Riley *et al.*¹⁸ included both linear and quadratic coupling terms, simultaneously with the spin-orbit coupling. Their best fit gave $D_{e'}=5.03$, $K_{e'}=0.354$ and for the spin-orbit coupling 1500 cm^{-1} .

The cycloheptatrienyl (tropylium) cation $c\text{-C}_7\text{H}_7^+$ is a prototypical member of the family of the aromatic systems; it exhibits its aromaticity because it meets the requirements of the $(4n+2)$ Hückel rule as a monocyclic and planar polyene containing 6π electrons (isovalent with benzene). The gas-phase isomerization reaction between the cationic forms of tropyl and benzyl ($\text{C}_6\text{H}_5\text{CH}_2$) has been studied extensively in the past.^{1,21,22} Similar reaction routes have been proposed for the neutral radicals of these moieties but not in a definitive way; the tropyl radical has been suggested to be a possible intermediate in the ring-opening sequence reactions of the benzyl radical.^{1,23} Further spectroscopic investigation on C_7H_7 is necessary for a better understanding of these reactions. In contrast to the tropylium ion, information on the vibrational properties of the tropyl radical is lacking.

Whereas the tropyl cation is more stable than the benzyl cation by ca. 0.24 eV,²⁴ the benzyl radical is more stable than the tropyl radical by ca. 0.73 eV.²¹ The total resonance energy for the tropyl radical comes from contributions by the resonance energy of the cycloheptatriene system and the energy due to the delocalization of the unpaired electron present in a degenerate antibonding e_2'' molecular orbital. While the barrier for the isomerization from the tropyl cation to the benzyl cation has been calculated (3 eV²⁵), the corresponding one for the neutral species is unknown. However, the tropyl radical is believed to convert rapidly to the benzyl radical.^{1,23}

Tropyl has a $\tilde{X} \ ^2E_2''$ ground electronic state in D_{7h} symmetry with a dominant electronic configuration of

$$\dots(a_2'')^2(e_1'')^4(e_2'')^1(e_3'')^0, \quad (1.1)$$

considering only the π molecular orbitals explicitly. The removal of one electron to form the excited electronic state in question $\tilde{A} \ ^2E_3''$ yields the electronic configuration,

$$\dots(a_2'')^2(e_1'')^4(e_2'')^0(e_3'')^1. \quad (1.2)$$

Tropyl is the only species known with D_{7h} symmetry,¹ and is subject to a Jahn-Teller distortion away from the D_{7h} nuclear geometry in its ground and first excited electronic states, due to their double electronic degeneracy. The double electronic degeneracy of the $\tilde{X} \ ^2E_2''$ and $\tilde{A} \ ^2E_3''$ states of *c*-C₇H₇ (in D_{7h} symmetry) is resolved into two planar Jahn-Teller electronic components with 2A_2 and 2B_1 symmetries (in the C_{2v} point group). Consequently the molecule has a very complicated vibrational structure in its \tilde{X} and \tilde{A} states which has largely eluded characterization by either experimental or *ab initio* methods.

The $\tilde{X} \ ^2E_2''$ state of tropyl was previously studied both experimentally and theoretically. The ESR spectroscopy²⁶ was applied in the early 1960s and based on the observations of seven equivalent ESR proton hyperfine couplings and a uniform spin distribution, the effective structure of tropyl may likely correspond to a dynamic D_{7h} symmetry. The photoelectron spectroscopy²⁷ presented tropyl as a highly fluxional molecule in its ground electronic state, in agreement with the ESR results. The gas-phase IR absorption spectra of C₇H₇ were recorded in the 400-1800 cm⁻¹ spectral

energy region.²¹ As there was no Jahn-Teller analysis of the observed vibronic structure, no conclusive results about the Jahn-Teller interactions in the \tilde{X}^2E_2'' state could be produced. *Ab initio* molecular orbital and density functional theory calculations were also performed on the tropyl radical.²² Harmonic vibrational frequencies were calculated as well as the first adiabatic and vertical ionization energies. The results indicated that the molecule has a C_{2v} equilibrium geometry.

Other spectroscopic techniques applied were [2+1]²³- and [1+1]¹-REMPI spectroscopy and were performed in the visible and near-UV energy region, respectively. Pioneering was the effort of Thrush and Zwolenik²⁸ who reported the electronic spectrum of C₇H₇ by direct absorption in the visible. Of central importance is the REMPI work by Pino *et al.* as it provides useful information on the \tilde{A}^2E_2'' -state vibronic structure.

The alkoxy radicals and the Jahn-Teller-active molecules long have been favorite targets for spectroscopists and theoreticians alike. However there is one other category of molecules that is particularly challenging: the one that contains weakly bound molecular systems. In the work described in this dissertation, the interaction energy of decaborane (B₁₀H₁₄) with the Xe atom and the (isoelectronic) I⁻ is investigated. Aside from the interest in the nature of this interaction, studies of such large systems are useful as they test the efficiency of the various theoretical approaches.

Decaborane exhibits a wide range of properties, the investigation of which has previously²⁹ led to the preparation for the first time of an interesting complex ion formed between the iodide ion and decaborane, namely B₁₀H₁₄I⁻. (see Fig. 2.1).

Under certain experimental conditions, $\text{B}_{10}\text{H}_{14}\text{I}^-$ is found to be stable both in the solid state and in solution.²⁹ The X-ray crystal structure of 2,4- $\text{I}_2\text{B}_{10}\text{H}_{12}\text{I}^-$ (in Fig. 2.1 but with hydrogen atoms attached to B(10) and B(9) instead of iodine atoms) reveals C_{2v} symmetry.²⁹ The formation of the $\text{B}_{10}\text{H}_{14}\text{I}^-$ complex results in some perturbation of the $\text{B}_{10}\text{H}_{14}$ framework, as is experimentally evident from the ^{11}B and ^1H NMR, Raman, IR and visible spectra.²⁹ The unique iodide is situated at the open end of the decaborane, effectively resting on the four bridging hydrogens. Iodide presumably transfers electronic charge to the lowest unoccupied molecular orbital (LUMO) of the electron-deficient $\text{B}_{10}\text{H}_{14}$ by interacting with the positive end of decaborane. While the bridging hydrogens are believed to act as Brönsted acids, the boron atoms B(1) and B(2) become susceptible to nucleophilic attack.²⁹ However, the interaction involves distances which are consistent with van der Waals interactions. On the other hand, the polar nature of decaborane and the charge of the iodide ion suggest a charge-dipole electrostatic and charge- and dipole-induced-dipole contributions to the interaction energy of this molecular system.

The purpose of the work described in chapter 2 is to study the nature of this interaction and describe the electronic charge transfer from the iodide ion to $\text{B}_{10}\text{H}_{14}$. In doing so, we have computed the ground-state interaction energy of the iodide ion with decaborane in the complex $\text{B}_{10}\text{H}_{14}\text{I}^-$. We have focused our attention on $\text{B}_{10}\text{H}_{14}\text{Xe}$, an unknown compound isoelectronic to $\text{B}_{10}\text{H}_{14}\text{I}^-$. We have determined the ground-state interaction energy of $\text{B}_{10}\text{H}_{14}\text{Xe}$ and compared the electronic structure characteristics of it with $\text{B}_{10}\text{H}_{14}\text{I}^-$.

Chapter 3 involves itself with the analysis of the recorded experimental emission spectra of the alkoxy radicals. In chapter 4 we describe the *ab initio* calculations that we have performed with the express purpose of aiding the analysis of the experimentally observed vibronic structure of Ag₃ in its \tilde{X} and \tilde{A} states. In chapter 5 we describe first our analysis of the LIF excitation spectrum¹⁴ of the $\tilde{A}^2E'' \leftarrow \tilde{X}^2E'$ electronic transition of Ag₃. We proceed to describe LEDF spectra from several \tilde{A} -state vibronic levels. In the work presented in chapter 6, the LIF spectroscopy was combined with supersonic free-jet expansion techniques to record the wavelength dispersed fluorescence spectra from a number of \tilde{A} -state levels of the tropyl radical. In chapter 6, our observation and analysis of the LIF excitation spectrum of the $\tilde{A}^2E_3'' \leftarrow \tilde{X}^2E_2''$ electronic transition of the tropyl radical is described as well as the LEDF spectra recorded from several \tilde{A} -state vibrational levels. This is followed by the last chapter which summarizes the conclusions of the experimental and various theoretical approaches that we followed for the analysis of these molecules.

CHAPTER 2

Theoretical Investigation of the Binding Energies of the Iodide Ion and Xenon Atom with Decaborane

2.1 Introduction

In chapter 1 we gave the reasons that intrigued us to study the complex ion $B_{10}H_{14}I^-$ (see Fig. 2.1). In this chapter the ground-state interaction energy of the iodide ion with decaborane in the complex $B_{10}H_{14}I^-$ is computed and the nature of this interaction is determined. Our principal results reveal the most important term in the interaction energy of $B_{10}H_{14}I^-$ to be electrostatic. We have determined the ground-state interaction energy of $B_{10}H_{14}Xe$ and found $B_{10}H_{14}Xe$ to be weakly bound by dispersion forces.

The calculation of an accurate molecular binding energy involves the use of an accurate correlation treatment and adequate basis sets. The wave-function-based methods that we apply are restricted Hartree-Fock self-consistent-field theory (SCF), (single-reference) spin-orbit single- and double-excitation configuration interaction (SO-CISD), second-order Møller-Plesset perturbation theory (MP2), coupled-cluster theory with single and double excitations (CCSD), and CCSD(T), which also includes

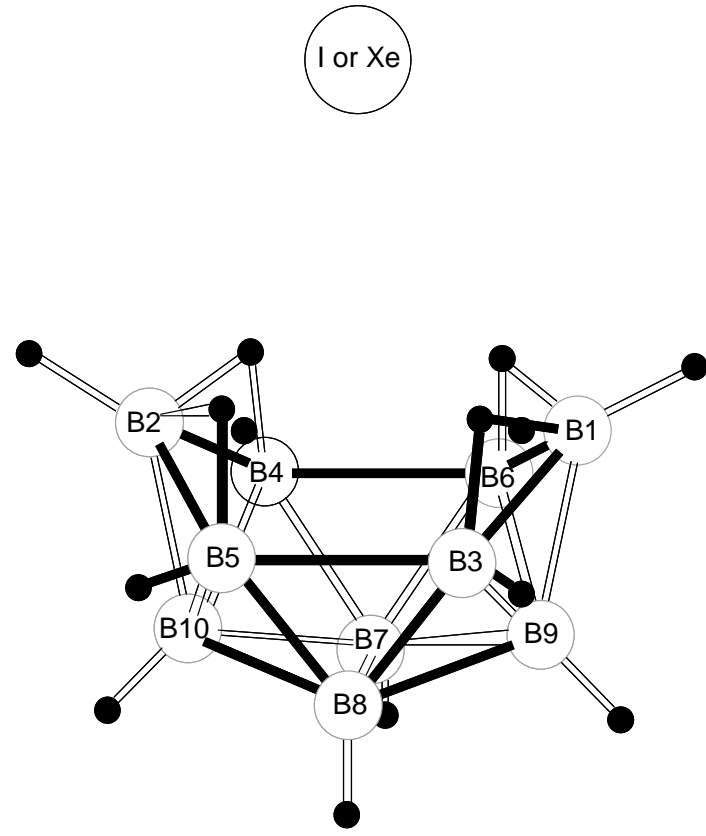


Figure 2.1: The molecular configuration and numbering scheme of $\text{B}_{10}\text{H}_{14}\text{I}^-$ and $\text{B}_{10}\text{H}_{14}\text{Xe}$. The bridging hydrogens ($\mu - H$) are between B(2), B(4,5) and B(1), B(6,3). There is no bond between B(4), B(5) and B(6), B(3) but between B(4), B(5) and B(10), and B(6), B(3) and B(9)

perturbation-theory values of the connected-triple-excitation terms. We also compare these results with density functional theory (DFT) calculations with four different exchange-correlation functionals. We apply the function counterpoise procedure (CP) for correction of basis set superposition error (BSSE). We also use relativistic effective core potentials (RECPs) and the corresponding spin-orbit operators and correlation-consistent polarized valence basis sets.

2.2 Theoretical and Computational Methods

2.2.1 Evaluation of the Interaction Energy

The method used to evaluate the interaction energy between two interacting systems (suitable for either weak or strong binding) is based on the supermolecular approach. In the case of a dimer AB, the difference between its energy and the sum of the energies of the separated monomers A and B amounts to the interaction energy:

$$\Delta E(R) = E^{\{\alpha,\beta\}}(AB, R) - E^{\{\alpha\}}(A, R = \infty) - E^{\{\beta\}}(B, R = \infty) \quad (2.1)$$

where $E^{\{\alpha,\beta\}}(AB, R)$ is the energy of the dimer AB computed with the combined basis set $\{\alpha, \beta\}$ at the geometry R (for simplicity we can consider R to be the interfragment distance between A and B; in general R denotes the coordinates that specify the geometry of the dimer), while $E^{\{\alpha\}}$ and $E^{\{\beta\}}$ are the energies of the separated fragments, each computed within its own basis set.

This approach is simple and may be extended to the inclusion of any number of fragments that each of the interacting systems may contain. The calculation of the interaction energy has the least error if the quantum mechanical method used is

size-consistent, but the above form also minimizes the error when using methods that are not size-consistent. As the interfragment distance is reduced from infinity to the equilibrium distance of the dimer AB(R_e), the basis functions centered on A assist in lowering the energy of B and those centered on B have the same effect on the energy of A. Thus, the dimer energy becomes lower than it would be otherwise. This effect introduces BSSE error in the evaluation of the interaction energy.³⁰ It is a matching or balancing error³¹ and as early as 1970 Boys and Bernardi³² proposed the CP as a way to correct for it.

According to this scheme the CP-corrected interaction energy becomes

$$\Delta E^{CP}(R) = E^{\{\alpha,\beta\}}(AB, R) - E^{\{\alpha,\beta\}}(A, R) - E^{\{\alpha,\beta\}}(B, R) \quad (2.2)$$

where the monomer energies are evaluated with the same functional space as the dimer, i.e. within the full dimer basis set defined by the union of α and β . In accord with the CP procedure, in the evaluation of the monomer energies, the partner's basis functions (or "ghost" basis functions) of each of the interacting units are centered on the same location as in the dimer, but the nuclei and RECPs are not present.

While equation 2.2 is suitable for the evaluation of the interaction energy between two monomer units, further improvement of it may become necessary in the case that A and B are molecules. In principle, the energy change for distorting the monomers from their isolated geometries to the ones in the complex (known as fragment relaxation energy or deformation energy^{33,34}) should also be included. However, as a first approximation these terms were neglected in our evaluation of the interaction energy between $B_{10}H_{14}$ and I^- ion and Xe.

2.2.2 Core Potentials

We use the RECP approximation in order to properly describe the relativistic effects of the many-electron systems that we study, and, in particular, the RECPs developed by Christiansen et al.^{35–40} These potentials are obtained directly from Dirac-Fock relativistic atomic calculations and replace inner-shell (core) electrons and orbitals by a repulsive potential. These RECP techniques^{41,42} describe the valence space in terms of pseudo-orbitals which are identical to the corresponding all-electron valence orbitals in the valence region, but go smoothly to zero in the core region. The RECP methodology is advantageous for our work because (i) more electrons can be removed from the computation, (ii) relativistic corrections are easily incorporated into RECPs, and (iii) it is possible to obtain one-electron spin-orbit operators simultaneously with the RECPs, at the same level of approximation.

With the core electrons removed from the problem, the Hamiltonian includes the nonrelativistic Hamiltonian for the valence electrons (kinetic energy and Coulomb terms) plus the RECPs and spin-orbit operators. The spin-orbit operators include the (large) spin-orbit interactions of the valence electrons with the nucleus and with the core electrons as well as an approximation⁴³ to the (small) spin-orbit interaction between the valence electrons. The boron core^{35,36} is the $1s$ shell (2 electrons), and both the iodine and xenon cores are the $1s$ through $4p$ shells (36 electrons). Thus in $\text{B}_{10}\text{H}_{14}\text{I}^-$ and $\text{B}_{10}\text{H}_{14}\text{Xe}$, 56 electrons (core) were removed from the calculations and 62 electrons (valence) were treated explicitly.

2.2.3 Basis Sets

Most atomic-orbital (AO) basis sets available for use with RECPs are those originally published with the RECPs. The basis sets we use in this work, however, include more recent improvements as described below. A common method of choosing contractions for basis sets is to use occupied atomic SCF orbitals for the basic contractions and then free up some number of the more diffuse primitive functions for additional contractions.⁴⁴ However, the RECP methodology requires the valence pseudo-orbitals to have a small amplitude in the core region and go smoothly and nodelessly to zero at the nucleus.^{42,45,46} Correspondingly, suitable additional contractions have been chosen to satisfy these properties. This is most commonly known as the one-center effect,⁴⁵ and, can be addressed in several ways.^{45,46} Christiansen uses an augmentation scheme⁴⁵ that involves the formation of two-primitive contractions with coefficients that give exact cancellation of the leading power of r at the origin. He finds that augmented (aug. in the tables) primitives are unnecessary for d and higher angular momentum orbitals.

However, orbitals centered on a neighboring atom (B) may have moderate magnitude in the core region of atom (A). This problem, known as the two-center effect,⁴⁵ requires further change in the A basis set. Christiansen adds an additional s contraction to the basis set on atom A such that the next-most-diffuse primitive function is freed. This s contraction has a large amplitude in the core region so that in the formation of the molecular orbitals (MOs), it can be used to cancel out the amplitudes of the B orbitals in the A core region. This s contraction will also lead to

orbital	primitives	contraction	contraction	contraction	contraction
s	3.072	0.048359	0.0	0.0	0.0
	0.9631	-0.806443	0.0	0.0	0.0
	0.5303	0.674366	0.0	0.0	1.0
	0.2070	0.683570	1.0	0.0	0.0
	0.09835	0.242690	0.0	1.0	0.0
p	9.624	-0.002450	0.0	0.0	
	0.9464	-0.218667	0.0	0.0	
	0.4591	0.458951	-0.298228	0.0	
	0.1744	0.582505	1.0	-0.310319	
	0.06839	0.208211	0.0	1.0	
d	31.53	-0.012148	0.0	0.0	
	4.724	0.203370	0.0	0.0	
	2.399	0.470191	0.0	0.0	
	1.100	0.378001	1.0	0.0	
	0.4419	0.101520	0.0	1.0	
f	0.701216	1.0			

Table 2.1: I cc-pVTZ Basis Set: (5s5p5d1f)/[4s3p3d1f]

a virtual MO which has such high energy that it will not contribute significantly to correlation-energy calculations and hence may be omitted from them. This additional *s* contraction makes it unnecessary to use augmented *s* functions.

We used the iodine basis set shown in Table 2.1, which, except for the *f* polarization function, was developed by Christiansen in a correlation-consistent (cc) manner^{44,47} and has polarized triple- ζ (cc-pVTZ) quality. The resulting basis set is of (5s5p5d1f)/[4s3p3d1f] size, where this notation represents (primitives)/[contractions]. It includes freed-up diffuse primitives for *s*, *p*, and *d* (augmented for *p*). We refer to this basis set in the tables as "diffuse + tight *s* + aug. *p* + *f*(0.701266)". We also wanted to find out how much valence correlation energy can be recovered using

Christiansen's contraction methods. Our results are tabulated in Table 2.2. In the same table, we include the SCF and CISD energies that result from inclusion of an f polarization function. Both choices of exponent for the f function came from cc valence basis sets for use with the Stuttgart-Dresden-Bonn (SDB) (46-electron core) RECPs.^{48,49} Similar values are available from basis sets for 28-electron RECPs.⁵⁰

primitives	E(SCF)	E(SO-CISD)	ΔE
diffuse	-0.642918	-1.578548	-0.935629
aug. s	-0.642823	-1.579481	-0.936658
diffuse + tight s	-0.642932	-1.581517	-0.938585
diffuse + tight s + aug. p	-0.643107	-1.600639	-0.957532
diffuse + tight s + aug. p + f(0.429319)	-0.643192	-1.638329	-0.995137
diffuse + tight s + aug. p + f(0.701216) ^a	-0.643158	-1.663509	-1.020351

Table 2.2: SCF and SO-CISD energies relative to -144 E_h for $\text{B}_{10}\text{H}_{14}\text{I}^-$ at its equilibrium geometry using various basis-set contraction schemes on the I atom. The ΔE values are correlation energies (in E_h).

^a Basis set in Table 2.1.

Our xenon basis set is a cc polarized double- ζ (cc-pVDZ) set and is shown in Table 2.3. The primitive functions are those provided with the RECP.³⁸ We freed up the two most diffuse s primitives and the most diffuse p (augmented) primitive, as well as adding one more d function (exponent 0.22865) to polarize the $5p$ shell since none of the primitives for the $4d$ shell were diffuse enough to serve this purpose. The two most diffuse d primitives were left uncontracted. We then performed CISD calculations using a series of f polarization functions^{48,49} and found that an exponent

of 0.801144 was best. The contractions were chosen in a way that would make the basis set similar to a cc-pVDZ basis set. Its size is (3s3p5d1f)/[3s2p3d1f]. We have

orbital	primitives	contraction	contraction	contraction
s	0.7127	-2.536570	0.0	0.0
	0.5719	2.742737	1.0	0.0
	0.1519	0.638936	0.0	1.0
p	1.2353	-0.141311	0.0	
	0.3726	0.644602	-0.249969	
	0.1229	0.511983	1.0	
d	4.5119	0.266105	0.0	0.0
	2.4799	0.385422	0.0	0.0
	1.2983	0.365995	0.0	0.0
	0.5435	0.124862	1.0	0.0
	0.22865	0.0	0.0	1.0
f	0.801144	1.0		

Table 2.3: Xe cc-pVDZ Basis Set: (3s3p5d1f)/[3s2p3d1f]

developed our own RECP basis set for boron,⁴⁷ as shown in Table 2.4. It is of cc-pVDZ size, (4s4p1d)/[3s2p1d]. The hydrogen basis set⁵¹ is also of cc-pVDZ size, (4s1p)/[2s1p].

2.2.4 Computational Methods

For both the (closed-shell) ground electronic states of $\text{B}_{10}\text{H}_{14}\text{I}^-$ and $\text{B}_{10}\text{H}_{14}\text{Xe}$, the SCF and SO-CISD calculations were performed using the COLUMBUS system of quantum chemistry programs.⁵² The SO-CISD method is implemented in COLUMBUS in combination with RECPs and spin-orbit operators.

orbital	primitives	contraction	contraction	contraction
s	14.55	-0.0103380	0.0	0.0
	2.259	-0.1368565	0.0	0.0
	0.3076	0.5752983	0.0	1.0
	0.09889	0.5324867	1.0	0.0
p	5.984	0.0355794	0.0	
	1.239	0.1982340	0.0	
	0.3358	0.5058596	0.0	
	0.09527	0.4785609	1.0	
d	0.3477	1.0		

Table 2.4: B cc-pVDZ Basis Set : (4s4p1d)/[3s2p1d]

The binding energies of $\text{B}_{10}\text{H}_{14}\text{I}^-$ and $\text{B}_{10}\text{H}_{14}\text{Xe}$ were computed at additional levels of theory with the NWChem⁵³ computational chemistry package. The wavefunction-based methods include MP2, CCSD^{54–56} and CCSD(T).^{57,58} We performed DFT calculations within the Kohn-Sham^{59,60} formalism. Several functionals were used: the Becke three-parameter exchange functional with the Lee-Yang-Parr correlation functional (B3LYP),^{61,62} the same exchange functional with the Perdew-Wang91 (PW91) correlation functional (B3PW91),^{61,63} PW91 for both exchange and correlation (PW91PW91),⁶³ and the functional PBE0.⁶⁴

In all cases we used the same basis sets and RECPs. Some of these calculations included the spin-orbit interaction. These were SO-CISD and some separate DFT calculations (SO-DFT) for the cases that the DFT functional gave binding energies close to our CCSD(T) results (most accurate correlation treatment). The SO-DFT

results were used merely as an indication of the contribution of the spin-orbit interaction to the binding energy in DFT theory. We also note that for the wave-function-based calculations, we included all occupied and virtual MOs.

For $\text{B}_{10}\text{H}_{14}\text{Xe}$, our initial effort focused on the optimization of the intermolecular distance R between $\text{B}_{10}\text{H}_{14}$ and Xe at the SO-CISD level of theory. We kept the $\text{B}_{10}\text{H}_{14}$ atoms fixed at the crystallographic geometry. The position of the minimum (R_e) of the potential surface of $\text{B}_{10}\text{H}_{14}\text{Xe}$ was obtained by fitting parabolas to three points.

2.3 Results

2.3.1 SCF Results for $\text{B}_{10}\text{H}_{14}\text{I}^-$

The ground-state SCF energy of $\text{B}_{10}\text{H}_{14}\text{I}^-$ was computed at $R_e=7.18183$ b between the center of mass of the atoms B(4,6,3,5) of $\text{B}_{10}\text{H}_{14}$ and I^- determined from the X-ray analysis (Table 2.5 and Fig. 2.1). We also made an SCF calculation at an interfragment distance of 100 b since the supermolecule is composed of two noninteracting closed-shell subsystems.

	SCF	SO-CISD
$R_e=7.18183$	-144.643158	-145.663509
$R=100$	-144.621418	-145.632860
ΔE	13.64	19.23

Table 2.5: SCF and spin-orbit CI (singles and doubles) energies (in E_h) for $\text{B}_{10}\text{H}_{14}\text{I}^-$ at R_e and at $R=100$ (both in b). ΔE is the dissociation energy (in kcal/mol).

The dissociation products are well represented by closed-shell wave functions, so closed-shell SCF calculations give the correct size-consistent behavior in the limit of large intermolecular distance. Of particular interest is the comparison of the occupied MO spectrum that is obtained at a situation of no molecular interaction with that at the equilibrium geometry.

The highest occupied MOs are I 5p and 5s orbitals (symmetries A₁, B₁, B₂, A₁) at R=100 b, but show mixing with other AOs at the equilibrium geometry of B₁₀H₁₄I⁻, particularly with AOs centered on all the B atoms and on the bridging hydrogens (see Fig. 2.1). The orbital energies (E_h) of these MOs are -0.167 (A₁), -0.164 (B₁), -0.163 (B₂), and -0.652(A₁). The partial gross atomic populations for these occupied MOs suggest electron charge transfer of ca. 0.1 electron from the iodide to the B atoms. The most important charge transfer takes place from the A₁ 5p iodide orbital. The lowest unoccupied MO of B₁₀H₁₄ (orbital energy 0.047 and A₁ symmetry) consists of orbitals mostly centered on the same atoms to which charge transfer has been noted.

Decaborane is a polar molecule with positive character at the open face of the B₄ basket. The population analysis of B₁₀H₁₄ is given in Table 2.6. The bridging hydrogens and B(2,1) atoms (Fig. 2.1) are electron deficient, and therefore Brönsted acids, and the B(2) and B(1) sites are susceptible to nucleophilic attack. A comparison of the gross atomic populations between B₁₀H₁₄ and B₁₀H₁₄I⁻ is a useful indication for the transfer of electronic charge. Table 2.7 shows the population analysis of B₁₀H₁₄I⁻.

Gross atomic populations									
atom	B(2)	B(4)	B(8)	B(10)	H(2)	$\mu - H$	H(4)	H(10)	H(8)
total	2.916	3.061	3.007	3.021	0.985	0.967	0.998	1.017	1.001

Table 2.6: Ground-state $\text{B}_{10}\text{H}_{14}$ SCF Mulliken Population Analysis. Boron has three valence electrons and the labels refer to the symmetry-distinct atoms. The labels of the hydrogens are the same as those of the borons that they are bonded to and $\mu - H$ is for the bridging hydrogens.

Gross atomic populations										I(1)
atom	B(2)	B(4)	B(8)	B(10)	H(2)	$\mu - H$	H(4)	H(10)	H(8)	
total	2.921	3.067	3.034	3.075	0.992	0.916	1.014	1.027	1.007	17.896

Table 2.7: Ground-state $\text{B}_{10}\text{H}_{14}\text{I}^-$ SCF Mulliken Population Analysis. The number of valence electrons is three for boron and eighteen for iodide. The labels refer to the symmetry-distinct atoms. The labels of the hydrogens are the same as those of the borons that they are bonded to and $\mu - H$ is for the bridging hydrogens.

The magnitude of the charge transfer from iodide is apparent and somewhat surprising in that the bridging hydrogens become more electron deficient upon the formation of $B_{10}H_{14}I^-$. The electron charge transferred is distributed among all remaining atoms of the molecule with emphasis on those of B(10,9) and B(7,8).

Our SCF results are in agreement with the experimental results.²⁹ We find that B(2) and B(1) of $B_{10}H_{14}$ are susceptible to nucleophilic attack even upon formation of $B_{10}H_{14}I^-$ and this finding is in agreement with experimental results.^{29,65,66} While population analyses are known to be particularly sensitive to basis set choice, especially when diffuse basis functions are involved, one may still assign physical significance to such results so long as the basis sets are balanced. Although the iodine basis set is larger than those of boron and of hydrogen, care has been taken that the number of basis functions describing the valence space of iodide is proportional to the number of valence electrons. In an analogous way, the same proportionality is kept, approximately, for boron and hydrogen. In this way, we try to keep a proper balance among the basis sets of the system. The alternative of using pVDZ basis sets for both B and I would probably lead to less balanced results.

2.3.2 Single-Reference S0-CISD Results for $B_{10}H_{14}I^-$

We performed single-reference SO-CISD calculations for the ground state of $B_{10}H_{14}I^-$, using the SCF MOs and including excitations from all occupied MOs to all unoccupied MOs, generating a total of 4.3×10^7 configuration state functions (CSFs). The reference configuration of $B_{10}H_{14}I^-$ at the equilibrium geometry has a CI coefficient close to 0.88. Three of the four highest contributing doubly excited configurations

are also basic doubly excited configurations for the CI expansion of decaborane with almost the same CI coefficients as those in the CI expansion of $B_{10}H_{14}I^-$ at its equilibrium geometry. We examined the SCF MOs from which the electrons are excited along with the MOs that the electrons go into. The excitations go from the $6b_1$ and $7b_2$ occupied MOs to the lowest energy virtual MOs of A_1 symmetry and A_2 symmetry. The principal coefficients for $6b_1$ come from the $2p$ orbitals on the B(10) group of atoms and also those on the B(4) group of atoms. The $7b_2$ MO has significant mixing of the $2p$ orbitals from the B(10), B(8), and B(2) groups of atoms. The lowest virtual of A_1 symmetry has its principal coefficients from the $2p$ and $2s$ orbitals on the B(4) and B(2) group of atoms, and the lowest virtual MO of A_2 symmetry has its principal coefficients from the $2s$ and $2p$ orbitals on the B(4,6,3,5) group of atoms. The fourth excited configuration has excitation from $7b_1$ to an A_1 symmetry virtual MO and from $8b_2$ to an A_2 symmetry virtual MO. The $7b_1$ and $8b_2$ MOs are the highest energy occupied MOs and have iodide 5p character. The principal coefficients for the A_1 virtual MO are for $2s$ and $2p$ orbitals on the B(8) group of atoms and for $2s$ orbitals on the B(10) group of atoms. The A_2 virtual MO has principal coefficients from $1s$ orbitals on the bridging hydrogens and also from $2p$ orbitals on the B(4) group of atoms and from $4d$ orbitals on the iodide ion. At the supermolecular separation of 100 b, we notice the same doubly excited configurations of decaborane with almost the same CI coefficients and with excitations from the same types of occupied MOs

to the same types of virtual orbitals. There are also a significant number of doubly excited configurations involving excitations from $5s$, $5p$ and $4d$ orbitals on iodide to higher energy s and p MOs on iodide.

According to Table 2.5 the binding energy between decaborane and the iodide ion has been calculated as 19.23 kcal/mol at the SO-CISD level, which is 5.59 kcal/mol more than the corresponding SCF result. This additional contribution to the binding energy upon inclusion of correlation and spin-orbit effects for $B_{10}H_{14}I^-$ signifies their importance in this type of binding energy.

2.3.3 MP2, CCSD, CCSD(T) and DFT Results for $B_{10}H_{14}I^-$

Tables 2.8 and 2.9, respectively, contain the binding energies from all the theoretical methods, both without and with the CP corrections. In Table 2.8 we note the importance of the triple excitations as a correction to the CCSD approximation. The CCSD(T) results have the most accurate correlation treatment, but do not include spin-orbit effects. However, the CCSD binding energy is close to the SO-CISD result already mentioned. Also, the MP2 result shows close agreement with the CCSD(T) calculations, so it provides a relatively good estimate of the binding energy. This has been seen previously; perturbation theory methods (even at a second-order level) provide an adequate description of weakly bonded systems whose binding is mostly electrostatic.⁶⁷ Table 2.9 shows that the B3LYP method underestimates the binding energy of $B_{10}H_{14}I^-$, while PW91PW91 and PBE0 for the CP-corrected binding energies show the opposite effect, a result owing possibly to fortuitous cancellations of inaccuracies in the exchange and correlation functionals being used. In contrast, B3PW91

Method	BE, ΔE^{CP}	BE, ΔE^{noCP}
CCSD(T)	19.84	25.30
CCSD	18.95	23.96
MP2	20.75	26.04
SO-CISD		19.23
SCF		13.64

Table 2.8: Wave-function-based results for $B_{10}H_{14}I^-$. The binding energy (BE) is in kcal/mol and CP denotes counterpoise procedure.

gives a good estimate of the binding energy, slightly lower than our CCSD(T) results. Inclusion of the spin-orbit interaction makes a difference in the case of $B_{10}H_{14}I^-$, giving a result that turns out to be the same as our CCSD(T) results (which do not include the spin-orbit interaction).

Functionals	BE, ΔE^{CP}	BE, ΔE^{noCP}
B3LYP	17.02	17.65
B3PW91	19.76	20.24
PW91PW91	21.68	22.47
PBE0	20.91	21.44
B3PW91(SO-DFT)	19.84	

Table 2.9: DFT and SO-DFT results for $B_{10}H_{14}I^-$. The binding energy (BE) is in kcal/mol and CP denotes counterpoise procedure.

2.3.4 SCF Results for $\text{B}_{10}\text{H}_{14}\text{Xe}$

$\text{B}_{10}\text{H}_{14}\text{Xe}$ is also a closed-shell system that at large distance ($R=100$ b), separates into closed-shell subsystems. This makes the closed-shell SCF calculation applicable to the whole potential surface characterizing the separation of fragments, giving a convenient reference configuration for several correlation methods.

We compared the ground-state occupied MOs for $\text{B}_{10}\text{H}_{14}\text{Xe}$ at the equilibrium distance at $R_e=8.73293$ b and at $R=100$ b and noticed differences for energetically neighboring occupied MOs. The MO 10a_1 (orbital energy -0.491 E_h) at R_e has Xe 5p as its largest coefficient. It has smaller coefficients on the 2p AOs of the B(2), B(4), B(8) and B(10) groups of atoms (see Fig. 2.1) and 1s AOs of the bridging hydrogens, H(10) and H(8) atoms. However, at 100 b, this MO is entirely on the $\text{B}_{10}\text{H}_{14}$. The 11a_1 (-0.475 E_h) is composed mostly of xenon 5p at both distances. At R_e , this MO has smaller coefficients on the 2p orbitals of atoms B(2), B(4), B(8), B(10) and the 1s orbitals of the bridging hydrogens. The total populations for the 11a_1 and 10a_1 (at R_e) is approximately independent of distance. The same behavior holds for the 6b_2 (-0.490 E_h) and 7b_2 (-0.476 E_h) MOs, but with less change for the individual MOs. Table 2.10 shows the gross atomic populations for all atoms for $\text{B}_{10}\text{H}_{14}\text{Xe}$ at equilibrium and at $R=100$ b. The total electronic charge of Xe suggests no significant electron charge transfer from this atom. The polar decaborane induces a dipole moment in the Xe atom, which interacts with the permanent dipole moment of $\text{B}_{10}\text{H}_{14}$.

Gross atomic populations										
R	B(2)	B(4)	B(8)	B(10)	H(2)	$\mu - H$	H(4)	H(10)	H(8)	Xe
R_e	2.923	3.061	3.005	3.022	0.985	0.965	0.998	1.017	1.001	17.992
100	2.917	3.061	3.007	3.020	0.986	0.967	0.998	1.017	1.001	18

Table 2.10: Ground-state $\text{B}_{10}\text{H}_{14}\text{Xe}$ SCF Mulliken Population Analysis at $R_e=8.73293$ and at $R=100$ b. The number of valence electrons is three for boron and eighteen for xenon. The labels refer to the symmetry-distinct atoms. The labels of the hydrogens are the same as those of the borons that they are bonded to and $\mu - H$ is for the bridging hydrogens.

2.3.5 Single-Reference S0-CISD Results for $\text{B}_{10}\text{H}_{14}\text{Xe}$

Single-reference SO-CISD calculations were carried out on the ground state of $\text{B}_{10}\text{H}_{14}\text{Xe}$, requiring a total of ca. 4.2×10^7 CSFs. The reference configuration of $\text{B}_{10}\text{H}_{14}\text{Xe}$ at R_e has a CI coefficient close to 0.88. The three characteristic doubly excited configurations of $\text{B}_{10}\text{H}_{14}$ appear in the same manner as before. Most of the double excitations come from 6b_1 (-0.476 E_h) and 7b_2 (-0.476 E_h). Both of these MOs have mostly Xe 5p atomic character. Excitation from orbitals with Xe 4d character is noticeable but not very significant. The virtual MOs that contribute the most to the correlation energy have as contributing AOs the 2s on the B(2), B(4) and B(8) atoms, the 2p on B(2), B(4), B(8) and B(10) and the 4d type on Xe to some extent. At $R=100$ b, some single excitations with approximately the same magnitude CI coefficients appear. Some of these are for CSFs with different spatial symmetry than the reference CSF and are due to spin-orbit mixing,⁶⁸ commonly observed for both xenon and iodide.

The SO-CISD method gives the binding energy of decaborane with xenon as 0.96 kcal/mol (see Table 2.11). Whereas at the SCF level of theory $B_{10}H_{14}Xe$ appears

	SCF	SO-CISD
R=R _e	-160.936594	-161.926417
R=100	-160.936959	-161.924894
ΔE	-0.23	0.96

Table 2.11: SCF and spin-orbit CI (singles and doubles) energies (in E_h) for $B_{10}H_{14}Xe$ at $R_e=8.73293$ b. and at $R=100$ b. ΔE denotes the dissociation energy (in kcal/mol).

to be slightly unbound, the singles and doubles correlation treatment of the system shows that it is in fact very weakly bound.

2.3.6 MP2, CCSD, CCSD(T) and DFT Results for $B_{10}H_{14}Xe$

Tables 2.12 and 2.13 summarize our wave-function-based and DFT results, respectively, for $B_{10}H_{14}Xe$. Table 2.12 indicates that the inclusion of triple excitations in CCSD(T) has a larger effect on the binding energy when the system is bound mostly by dispersion forces. Since the dispersion interaction is due to electron correlation, triple excitations contribute significantly in addition to the double excitations.^{69–73} Along the same lines, methods like MP2 (and MP3) are less suitable for the quantitative description of dispersion effects. Table 2.13 shows that the B3LYP and B3PW91 functionals completely fail to describe the binding of $B_{10}H_{14}Xe$, while the PW91PW91 and PBE0 functionals underestimate the binding energy with the latter deviating

Method	BE, ΔE^{CP}	BE, ΔE^{noCP}
CCSD(T)	1.09	1.94
CCSD	0.91	1.70
MP2	1.51	2.33
SO-CISD		0.96
SCF		-0.23

Table 2.12: Wave-function-based results for $B_{10}H_{14}Xe$. The binding energy (BE) is in kcal/mol and CP denotes counterpoise procedure.

significantly from our CCSD(T) result. The spin-orbit corrections do not contribute much to the binding energy within the PW91PW91 framework.

Functionals	BE, ΔE^{CP}	BE, ΔE^{noCP}
B3LYP	-0.37	-0.11
B3PW91	-0.57	-0.37
PW91PW91	0.74	1.02
PBE0	0.41	0.62
PW91PW91(SODFT)	0.75	

Table 2.13: DFT and SO-DFT results for $B_{10}H_{14}Xe$. The binding energy (BE) is in kcal/mol and CP denotes counterpoise procedure.

2.4 Discussion

The results in Tables 2.8, 2.9, 2.12, and 2.13 indicate several things. Some wavefunction-based and DFT methods for $B_{10}H_{14}I^-$ give reliable binding energies, but at

the level of chemical accuracy, small discrepancies appear. The energy values are also strongly affected by the BSSE, which corrects overestimates of the binding energy. Since the CCSD(T) results have the most accurate correlation treatment, we compare the results of other calculations to them, in the absence of any relevant experimental information. The CP binding energy was calculated to be 19.84 kcal/mol whereas the corresponding energy without the BSSE correction was calculated to be 25.30 kcal/mol. Hence, the error in the calculation due to BSSE is 5.46 kcal/mol, approximately the same size as the correlation-energy contribution to the binding. The CCSD method gives a value of 18.95 kcal/mol, and, by comparison with the corresponding CCSD(T) result, gives 0.89 kcal/mol as the contribution of the connected triple excitations to the binding energy. An alternative highly correlated wave-function-based method is SO-CISD, which gave a value of 19.23 kcal/mol, quite close to the CCSD(T) value. Finally, MP2 did a good job in giving a relatively close (20.75 kcal/mol) value to the CCSD(T) binding energy for $B_{10}H_{14}I^-$, overshooting it by 0.91 kcal/mol. The BSSE for CCSD(T), CCSD, and MP2 was approximately 5 kcal/mol, showing the need for its inclusion. In terms of decreasing quality of calculated binding energy, the DFT functionals used were ordered as B3PW91, PBE0, PW91PW91, B3LYP (Table 2.9). It is also notable that the BSSE does not play an important role in the DFT results. These calculations suggest that the electrostatic nature of the binding energy can be adequately described by DFT methods.

$B_{10}H_{14}Xe$ is stabilized by weaker intermolecular forces (dispersion and dipole-induced-dipole). As a correlation effect, dispersion interactions are one of the most

difficult interactions to calculate and cannot be described at the Hartree-Fock level. The accurate calculation of dispersion interactions necessitates the use of highly correlated wave-function-based techniques. Our CCSD(T) result of 1.09 kcal/mol shows that $B_{10}H_{14}Xe$ is indeed a very weakly bound system. The corresponding CCSD result (0.91 kcal/mol) shows that the triple excitations contribute 0.18 kcal/mol. The SO-CISD method does a good job in giving a binding energy of 0.96 kcal/mol. The MP2 method, as with $B_{10}H_{14}I^-$, provides an overly large value of 1.51 kcal/mol. As expected, the Hartree-Fock result gives no binding. In $B_{10}H_{14}Xe$ the contamination due to BSSE is considerably higher than in $B_{10}H_{14}I^-$; the values for the CCSD(T), CCSD and MP2 methods are 0.85, 0.79 and 0.82 kcal/mol, respectively (compared to the CP-corrected binding energy of 1.09 kcal/mol).

One goal of the present study is to test a number of (computationally cheaper) DFT methods and determine if any of them can be used to describe dispersion forces sufficiently well for practical studies of similar systems. Approximate DFT functionals do not necessarily include all correlation effects well enough to describe dispersion interactions.^{74,75} Exchange correlation functionals of the LDA and GGA types do not describe them at all,⁷⁶ and some of the hybrid type, such as B3LYP, do not either.^{74,77-79} However, for the weakly bound van der Waals complex of $B_{10}H_{14}Xe$, the PW91PW91 and PBE0 functionals generate values for the interaction energy that are comparable with higher-level wave-function-based methodologies. It has been pointed out that the PW91 functional is the most reliable for treating benzene van der Waals complexes.^{80,81} Perdew and Wang⁸² stated that the PW exchange

functional is best used with the corresponding correlation functional (PWPW), since in this case the errors in exchange and correlation contributions tend to cancel. The similarity of the CP binding energy between the CCSD(T) method (1.09 kcal/mol) and PW91PW91 method (0.74 kcal/mol) is consistent with this. The PBE0 functional (the PBE exchange functional with the PBE correlation functional) has previously been found to give a good description of noble gas dimers,⁷⁹ but the PW91 and PBE0 functionals also give binding with the correlation potential excluded, indicating that the exchange functionals contain some correlation. The calculation of the CP binding energy of B₁₀H₁₄Xe with the PBE0 functional predicts a weakly bound complex (with a CP binding energy of 0.41 kcal/mol) but is not accurate. The B3LYP and B3PW91 DFT methods, as expected, give unbound complexes. Their CP binding energies are computed to be -0.37 kcal/mol and -0.57 kcal/mol, respectively. Lastly, it needs to be emphasized that the BSSE error for the most reliable functionals PW91PW91 (0.28 kcal/mol) and PBE0 (0.21 kcal/mol) is relatively large, however less than that found for the wave-function-based methods.

2.5 Conclusions

The substantially larger binding energy for the I⁻ complex compared to the Xe complex shows that the charge (and polarizability) of I⁻ play the largest role in the interaction with B₁₀H₁₄. Significant improvement was made on the RECP basis sets of I and Xe and care was taken for the use of balanced basis sets. Although early reports were justifiably pessimistic about the ability of DFT to describe dispersion

interactions, the present study has found that DFT methods with certain exchange-correlation functionals do describe this interaction. In particular, the PW91PW91 and PBE0 functionals are the better choices for studying weak-interaction systems. Other functionals also gave realistic descriptions of the interaction energy in $B_{10}H_{14}I^-$. If one takes the high-level wave-function-based estimates as a reliable reference, we can conclude that selected DFT methods can be efficient alternatives when dealing with very large systems. It has also been found that the CP for BSSE is necessary when comparing different computational approaches.

CHAPTER 3

Dispersed Fluorescence Spectroscopy of Primary and Secondary Alkoxy Radicals

3.1 Introduction

The important role of the alkoxy radicals in chemical processes was described in Chapter 1. In this chapter, the analysis of the LEDF spectra recorded from a number of \tilde{B} state levels of the 1- and 2- isomers of propoxy and butoxy radicals is given. Emission was observed primarily to the CO vibrationless level and excited stretch and CCO vibrational modes (or modes coupled with these motions) of both the \tilde{X} and \tilde{A} states. The LEDF data also serve to support the identification of multiple conformations of the alkoxy radicals.

Extensive quantum chemical computations were carried out as an aid to the assignment of the observed vibronic bands. Both the $\tilde{A}-\tilde{X}$ energy gap and the \tilde{X} and \tilde{A} vibrational frequencies can be used as benchmarks against which theoretical treatments of these complex radicals can be measured. Information about the $\tilde{A}-\tilde{X}$ energy separation is important for a better understanding of the vibronic interactions between these close-lying, lowest energy states. The $\tilde{A}-\tilde{X}$ separation is also very important for understanding the kinetics and detailed dynamics of the alkoxy radicals

as the degree of \tilde{A} state participation in thermal reactions is dependent upon its excitation energy. The separation is also critical to an understanding of the ground state spin-rotation splittings.

The remainder of this chapter is organized as follows. In Sec. 3.2 an outline of the experimental technical details is given. The analysis of the experimental spectra takes place in Sec. 3.3. Section 3.4 centers on a number of aspects pertaining to the structure and spectra of the primary and secondary alkoxies. The chapter is completed with the conclusions presented in Sec. 3.5.

3.2 Experimental Details

The alkyl nitrite precursor molecules were prepared by the dropwise addition of the concentrated sulfuric acid to a saturated solution of NaNO_2 and the corresponding alcohol.⁸³ A few torr of the alkyl nitrite vapor was entrained into the jet flow by passing helium at a suitable backing pressure over the liquid contained in a stainless steel reservoir maintained at a suitable temperature depending upon the vapor pressure. A summary of the experimental conditions is given in Table 3.1. The seeded flow was then expanded through a $300\ \mu\text{m}$ standard pulsed nozzle (general valve) into the jet chamber which was evacuated by a mechanical booster pump backed by an oil rotary pump. To produce the alkoxy radicals, photolysis of the precursors just above the throat of the nozzle was performed using the output of a tripled Nd:yttrium aluminum garnet(YAG) laser (Quanta-Ray DCR-2, 355 nm). This produced the desired

Alkoxies	Primary	Secondary
Temperature of the sample bomb (°C)	-5	10
Backing pressure (psi)	90	40,80 ^a
Slit width (μm)	60	150 ^b
Resolution (cm^{-1})	15	30-35
Accumulation time (min)	40	60 ^c
Grating (grooves/mm)	1800	1800

Table 3.1: Summary of the conditions used for the experiments with the primary and secondary alkoxies.

^a The backing pressure in the 2-propoxy experiment was kept at 40 psi and for 2-butoxy at 80 psi. ^b The LEDF emission following the LIF excitation of the first member of the CO stretch progression of 2-propoxy was collected with an entrance slit width of 50 μm . ^c For 2-butoxy, the accumulation time for the LEDF collection via bands A through D was extended at least 3 hours for the first 2000 cm^{-1} redshifted from the pumping frequency.

alkoxy radicals which were then probed about 10 mm downstream from the photolysis laser. The probe beam was the frequency doubled output (Inrad Autotracker II) of a tunable dye laser (SpectraPhysics PDL-3) pumped by the second harmonic of a Nd:YAG (Quanta-Ray DCR) laser at 532 nm. This work required the use of three laser dyes (LDS 698, 750, and 751) which spanned appropriate spectral regions for the LEDF excitation frequencies. The delay time between the firing of the photolysis and dye lasers, along with the time delay and the opening time of the nozzle, were controlled by a pulse generator (Stanford Research, DG535).

The photolysis and probe beams counterpropagated through the vacuum chamber. The fluorescence signal was collected perpendicularly to the laser beams. On

one side of the chamber, the fluorescence emission was collimated by an 1 in. diameter lens ($f/1$) and a second lens focused the radiation onto the photocathode of the photomultiplier tube (EMI 9659Q) connected to an amplifier. The amplified LIF signal was integrated by a boxcar averager, digitized by an A/D converter and fed into a personal computer for further data processing. On the other side of the chamber, the fluorescence emission was dispersed by a Spectra Pro 300i monochromator using a 1800 grooves/mm grating and then imaged onto an intensified charge-coupled device. The detection of the dispersed photons for the secondary alkoxies was done exclusively with the Princeton Instruments PI-MAX512HB camera. In the case of the primary alkoxies two cameras were used, the above one and a second one, Princeton Instruments PI-MAX512RB. The emission frequencies reported for the LEDF spectra of the alkoxies were obtained by calibrating them against a Fe-Ne lamp, or known laser frequencies.

3.3 Results

The alkoxy radicals can be viewed as derivatives of methoxy. While the nominal point-group symmetry of methoxy is C_{3v} , for all other alkoxy radicals the symmetry is lower (except possibly for *t*-butoxy). Upon the lowering of the point-group symmetry, the ground electronic state of methoxy, 2E , is resolved into a pair of states with the ground state designated as \tilde{X} and the lowest lying excited state as \tilde{A} . The first excited state of methoxy is electronically non-degenerate and corresponds to a state designated as \tilde{B} for the alkoxies larger than methoxy (except *t*-butoxy). The LIF

excitation spectrum involves the $\tilde{B} \leftarrow \tilde{X}$ transition while the LEDF spectra involve the $\tilde{B} \rightarrow \tilde{A}$ and $\tilde{B} \rightarrow \tilde{X}$ emission. The \tilde{B} state excitation is well known to be nominally a one-electron excitation of a p- σ bonding electron to fill the half-filled p- π orbital localized on the O atom.

There are two isomers for propoxy; the linear chain isomer, 1-propoxy, and the branched chain one denoted as 2-propoxy, often referred to as isopropoxy. In the case of the buoxy radicals, there exist four possible isomers two of which will be the focus of this chapter, namely the 1-butoxy and 2-butoxy species.

It is known that different conformations can exist for a given structural isomer. Therefore, theoretically speaking, one should anticipate two different conformers for 1-propoxy and one possible conformation for isopropoxy. Five conformations are possible for 1-butoxy and three for 2-butoxy. High-resolution spectroscopic studies have identified,^{6,7} via detailed analysis of the rotational structure of the vibronic bands, both conformers of 1-propoxy and three of 1-butoxy populated in the free-jet expansion. The conformers for 1-propoxy are denoted as *gauche* (*G*) and *trans* (*T*). *G* is a C₁-symmetry structure and *T* is of C_s symmetry. For 1-butoxy the corresponding conformations (point-group symmetries) are *G₁T₂* (C₁), *T₁T₂* (C_s), and *T₁G₂* (C₁). The reflection plane of symmetry in 2-propoxy classifies it as a C_s-symmetry structure. 2-Butoxy possesses the *gauche clockwise* conformer *G+* (C₁), the *trans T* (C₁) conformer, and the *gauche counterclockwise* conformation *G-* (C₁) (See Fig. 3.1).

Because of the chiral stereocenter in 2-butoxy, enantiomers are expected in each conformer. They should give identical spectra, thus there are three conformer spectra possible for 2-butoxy.

3.3.1 Quantum Chemistry Calculations

To aid the assignment process we have carried out a number of quantum chemistry calculations. These included (i) the geometry optimization of the different conformers of the primary and secondary radicals and the determination of their relative energy difference in their ground electronic states; (ii) the calculation of the energy separations of the close-lying \tilde{A} and \tilde{X} states for each conformer; (iii) the calculation of the harmonic vibrational frequencies of the conformers in their ground state. These calculations have been performed by the GAUSSIAN 98 program package⁸⁴ at the B3LYP/6-31+G* level of theory. The geometry optimization of all of the conformers was done at C₁ symmetry. Tables 3.2, 3.3 and 3.4-3.12 summarize the computational results (i), (ii) and (iii), respectively. Table 3.3 also includes some results (obtained by the ACESII program package⁸⁵) for selected alkoxy radicals performed at the equation-of-motion excitation energy coupled cluster singles and doubles (EOM-EE-UCCSD)⁸⁶ level of theory using the cc-pVDZ basis set. Tables 3.4-3.12 include all frequencies lower than $\approx 1500\text{ cm}^{-1}$ labeled following the Mulliken notation scheme⁸⁷ for a C₁ molecule. These lower frequency vibrations are the ones relevant to the interpretation of the LEDF spectra.

The first two columns of the tables label and give the value of the harmonic frequencies obtained at the C₁-symmetry minimum while their vibrational character is

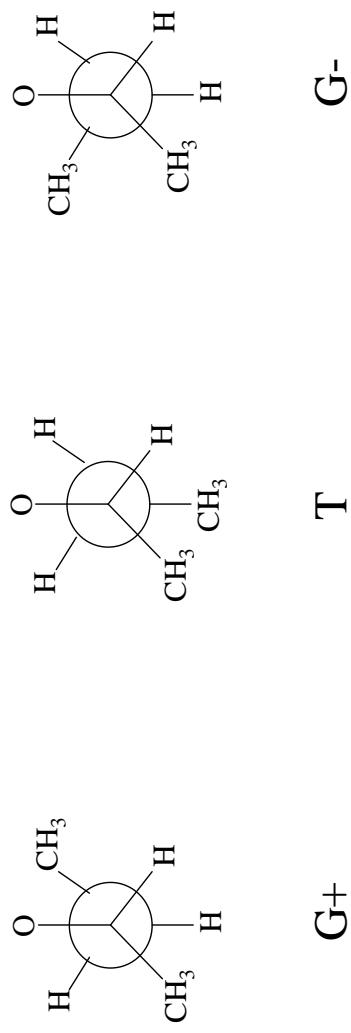


Figure 3.1: Newman projections of three unique conformational structures of 2-butoxy at their local minima. The designation of the conformers is based on the value of the dihedral angle ϕ which is formed by C₂-C₁-O and C₁-C₂-C₃ planes; rotation about the C₁-C₂ bond changes ϕ from 60° (*gauche clockwise* G+), to 180° (*trans* T) and -60° (*gauche counterclockwise* G-).

Alkoxy	conformer	E ^a
1-propoxy	<i>G</i>	0
	<i>T</i>	20
1-butoxy	<i>G</i> ₁ <i>T</i> ₂	0
	<i>T</i> ₁ <i>T</i> ₂	62
	<i>T</i> ₁ <i>G</i> ₂	339
2-propoxy		0
2-butoxy	<i>G</i> +	0
	<i>T</i>	254
	<i>G</i> -	314

Table 3.2: Energy differences (in cm^{-1}) relative to the energy of the lowest energy conformation of the primary and secondary radicals in their ground electronic state as obtained at the B3LYP/6-31+G* level of theory.

^a No zero-point energy correction was applied. For all of the alkoxy radicals, the geometry optimization led to distinct unique conformations and was done with C_1 symmetry.

described in terms of (i) CO stretch and (ii) CCO deformations, and (iii) other motions in the remaining three columns. These determinations are based upon visual inspections of the vibrational motion as displayed by GAUSSVIEW (Gaussian, Inc.). It is a useful guide for the assignment process to approximately know the degree of participation of the CO stretch and the CCO deformation in the vibrational character of each mode, since for these directions alone are there substantial differences in the \tilde{X} and \tilde{B} geometry leading to significant Franck-Condon factors for progressions in modes containing these motions. There appear to be few pronounced differences among the vibrational frequencies of the possible conformers for the alkoxy radicals.

Past and Present Studies		
Alkoxies ^a	Calculated ^b	Experimental
Ethoxy (² A')	314 [380]	364, ^c 355(10) ^d
1-Propoxy, <i>T</i> (² A'')	225 [369]	321(10) ^e
1-Propoxy, <i>G</i> (² A)	[8]	214(10) ^{e,f}
2-Propoxy (² A')	101	68(10), ^{e,f} 1225(65) ^{d,f}
1-Butoxy, <i>T</i> ₁ <i>G</i> ₂ (² A)	...	271(10) ^e
1-Butoxy, <i>T</i> ₁ <i>T</i> ₂ (² A'')	169	292(10) ^e
1-Butoxy, <i>G</i> ₁ <i>T</i> ₂ (² A)	...	129(10) ^{e,f}
2-Butoxy, "B" (² A)	...	55(10) ^{e,g}
2-Butoxy, "A" (² A)	...	125(10) ^{e,g}

Table 3.3: Experimental and calculated $\tilde{A}-\tilde{X}$ energy separation (in cm^{-1}) of a number of open-chain alkoxy radicals.

^a The symmetries of the computed ground electronic states of the alkoxy radicals are included in parentheses. The primed symmetry labels refer to the nominal C_s point-group whereas the unprimed are under C_1 symmetry. ^b The adiabatic $\tilde{A}-\tilde{X}$ energy separations were calculated at the B3LYP/6-31+G* level of theory, except for those included in brackets which were done at the EOM-EE-CCSD/cc-pVDZ level of theory. The energy separation is calculated as the difference between the C_1 energy minimum of the \tilde{X} state and the C_s energy minimum of the \tilde{A} state. ^c See Ref.9. We have reassigned the transition previously assigned to ν_{18} to the vibrationless level of the \tilde{A} state. The average value of the frequency was recalculated using the raw data in Table 2 of the reference. ^d See ref.88. ^e The $\tilde{A}-\tilde{X}$ separation obtained from the present LEDF experiments. ^f See text for possible caveats. ^g Average of two values, see text for details.

Table 3.2 gives the calculated energies of the conformers. It is worthwhile noting that the conformer that is calculated to be lowest in energy for each isomer has always been observed experimentally. However, the conformer populations are certainly not in equilibrium at the rotational temperature (1.0-1.5 K).

Table 3.3 includes experimentally determined \tilde{A} - \tilde{X} energy separations. The smallness of these separations for the C_s -symmetry structures calls for further investigation about possible pseudo-Jahn-Teller interactions, since it is possible for the two potential energy surfaces (PESs) to distort substantially upon consideration of such vibronic effects. For 2-propoxy, the T conformer of 1-propoxy and the $T_1 T_2$ conformer of 1-butoxy the geometry optimizations started from C_1 -symmetry structures and resulted in 0.4, 1.9, and 7.4 cm^{-1} stabilization, respectively, as compared to the optimized C_s -symmetry point of the \tilde{X} potential energy curve. Although single-reference theories are not accurate enough to reliably calculate the stabilization energy, owing to artificial symmetry breaking problems,^{89,90} these results may be used as a means to obtain a rough qualitative picture of trends in the alkoxy radicals. Methodologies like the equation-of-motion ionization potentials coupled cluster singles and doubles (EOMIP-CCSD)^{91,92} avoid problems of artificial symmetry breaking but they become computationally expensive as the size of the molecule increases. For the aforementioned C_s structures, we conclude from the calculations that no serious distortion of the PES of the ground state is expected, hence one would not expect vibrational progressions other than the totally symmetric ones to be promoted significantly in the excited electronic state.

Assignment	\tilde{X}, T	B3LYP ^a	CO stretch	CCO deformation ^b	Q^c
ν_{13}	1377 (a')		Small	Small	CH_3, CH_2 rock
ν_{14}	1328 (a')		Small		CH_3, CH_2 rock
ν_{15}	1305 (a'')				CH_3, CH_2 rock
ν_{16}	1238 (a'')				CH_3, CH_2 rock, CH_2 torsion
ν_{17}	1128 (a')				CH_3, CH_2 rock, CC stretch, CCC motion
ν_{18}	1074 (a')	Large			CH_3, CH_2 rock, CC stretch, CCC motion
ν_{19}	1034 (a')	Medium			CH_3, CH_2 rock, CC stretch
ν_{20}	967 (a'')				CC stretch
ν_{21}	889 (a')		Medium		CH_3, CH_2 rock
ν_{22}	771 (a'')				CH_3, CH_2 rock, CC stretch
ν_{23}	475 (a')				CH_3, CH_2 rock, CH_2 torsion
ν_{24}	307 (a'')	Large			CCC bend
ν_{25}	270 (a')				CH_2 torsion
ν_{26}	230 (a'')	Medium			CCC bend
ν_{27}	119 (a'')				CH_3, CH_2 torsion
					Backbone flex

Table 3.4: The calculated lowest 15 vibrational frequencies (in cm^{-1}) of the T conformer of 1-propoxy radical in its ground electronic state as obtained at the B3LYP/6-31+G* level of theory.

^a The unscaled harmonic frequencies were obtained at the C_1 -symmetry minimum and their symmetries under the C_s point group are included in parentheses. The labeling of the vibrational modes follows the Mulliken notation scheme⁸⁷ assuming C_1 symmetry. ^b For a' symmetry modes the CCO deformation is an in-plane bend and for a'' symmetry modes it is an out-of-plane twist. ^c The contributions of various internal coordinates Q to the normal mode indicated in the first column are listed, other than the CO stretch or CCO deformation which are listed in the preceding two columns with a qualitative indication of their magnitude.

\tilde{X}, G	B3LYP ^a	CO stretch	CCO deformation	Q^b
ν_{11}	1437	Small		CH_3,CH_2 rock, CC stretch
ν_{12}	1397	Small		CH_3,CH_2 rock
ν_{13}	1372	Small		CH_3,CH_2 rock, CC stretch
ν_{14}	1363	Small		CH_3,CH_2 rock
ν_{15}	1300			CH_3,CH_2 rock
ν_{16}	1219			CH_3,CH_2 rock
ν_{17}	1114			CH_3,CH_2 rock, CH_2 torsion
ν_{18}	1092	Large		CH_2 rock, CC stretch
ν_{19}	995	Medium		CH_3,CH_2 rock
ν_{20}	973	Small		CH_3,CH_2 rock, CC stretch
ν_{21}	867			CH_3,CH_2 rock, CC stretch
ν_{22}	788	Small		CH_3,CH_2 rock, CH_2 torsion
ν_{23}	496			CCC bend
ν_{24}	305			CCC bend
ν_{25}	286			CH_3,CH_2 torsion
ν_{26}	209			CH_3,CH_2 torsion
ν_{27}	125			Backbone flex

Table 3.5: The calculated lowest 17 vibrational frequencies (in cm^{-1}) of the G conformer of 1-propoxy radical in its ground electronic state as obtained at the B3LYP/6-31+G* level of theory.

^a Unscaled harmonic frequencies. The labeling of the vibrational modes follows the Mulliken notation scheme.⁸⁷

^b The contributions of various internal coordinates Q to the normal mode indicated in the first column are listed, other than the CO stretch or CCO deformation which are listed in the preceding two columns with a qualitative indication of their magnitude.

	\tilde{X}, T_1T_2	B3LYP ^a	CO stretch	CCO deformation ^b	Q^c
ν_{22}	1133(a')		Medium	CH ₃ , CH ₂ rock, CCC bend	
ν_{23}	1079(a')	Large		CH ₃ , CH ₂ rock, CC stretch	
ν_{24}	1061(a')	Small		CC stretch	
ν_{25}	1006(a'')		Small	CH ₃ , CH ₂ rock, CC stretch	
ν_{26}	995(a')	Medium	Large	CH ₃ , CH ₂ rock, CC stretch	
ν_{27}	914(a')		Medium	CH ₃ , CH ₂ rock, CC stretch	
ν_{28}	849(a'')			CH ₃ , CH ₂ rock	
ν_{29}	746(a'')			CH ₃ , CH ₂ rock	
ν_{30}	467(a')	Large		CH ₂ torsion, CCC bend	
ν_{31}	391(a')	Medium		CH ₂ torsion, CCC bend	
ν_{32}	361(a'')	Medium		CH ₃ , CH ₂ torsion	
ν_{33}	244(a'')			CH ₃ , CH ₂ torsion	
ν_{34}	185(a')			Backbone flex	
ν_{35}	114(a'')			Backbone flex	
ν_{36}	106(a'')			Backbone flex	

Table 3.6: The calculated lowest 15 vibrational frequencies (in cm^{-1}) of the T_1T_2 conformer of 1-butoxy radical in its ground electronic state as obtained at the B3LYP/6-31+G* level of theory.

^a The unscaled harmonic frequencies were obtained at the C₁-symmetry minimum, and their symmetries under the C_s point group are included in parentheses. The labeling of the vibrational mode follows the Mulliken notation scheme.⁸⁷ ^b For a' symmetry modes the CCO deformation is an in-plane bend and for a'' symmetry modes it is an out-of-plane twist. ^c The contributions of various internal coordinates Q to the normal mode indicated in the first column are listed, other than the CO stretch or CCO deformation which are listed in the preceding two columns with a qualitative indication of their magnitude.

Assignment	$\tilde{X}, T_1 G_2$			Q^b
	B3LYP ^a	CO stretch	CCO deformation	
ν_{21}	1192	Small		CH_3, CH_2 rock, CCC bend
ν_{22}	1110	Medium		CH_3, CH_2 rock, CCC bend, CC stretch
ν_{23}	1078	Small		CH_3, CH_2 rock, CC stretch
ν_{24}	1068	Large		CH_3, CH_2 rock
ν_{25}	1040			CH_3, CH_2 rock, CC stretch
ν_{26}	957	Medium	Large	CH_3, CH_2 rock, CC stretch
ν_{27}	887		Medium	CH_3, CH_2 rock, CC stretch
ν_{28}	869		Medium	CH_2 rock, CC stretch
ν_{29}	766			CH_3, CH_2 rock, CC stretch
ν_{30}	667			CH_2 rock
ν_{31}	474	Large		CCC bend
ν_{32}	346	Large		CCC bend
ν_{33}	286			CH_3, CH_2 torsion, CCC bend
ν_{34}	208			CH_3 torsion, CCC bend
ν_{35}	117			Backbone flex
ν_{36}	97			Backbone flex

Table 3.7: The calculated lowest 16 vibrational frequencies (in cm^{-1}) of the $T_1 G_2$ conformer of 1-butoxy radical in its ground electronic state as obtained at the B3LYP/6-31+G* level of theory.

^a Unscaled harmonic frequencies. The labeling of the vibrational modes follows the Mulliken notation scheme⁸⁷ for a C₁ molecule. ^b The contributions of various internal coordinates Q to the normal mode indicated in the first column are listed, other than the CO stretch or CCO deformation which are listed in the preceding two columns with a qualitative indication of their magnitude.

Assignment	\tilde{X}, G_1T_2			Q^b
	B3LYP ^a	CO stretch	CCO deformation	
ν_{21}	1204			CH_3, CH_2 rock, CCC bend, CC stretch
ν_{22}	1135			CH_3, CH_2 rock, CC stretch
ν_{23}	1089	Large		CH_3, CH_2 rock, CC stretch
ν_{24}	1050	Medium		CH_3, CH_2 rock, CC stretch
ν_{25}	1030	Small		CH_3, CH_2 rock, CC stretch
ν_{26}	960	Medium		CH_3, CH_2 rock, CC stretch
ν_{27}	873	Small		CH_3, CH_2 rock, CC stretch
ν_{28}	855	Small		CH_3, CH_2 rock, CC stretch
ν_{29}	754			CH_3, CH_2 rock, CC stretch
ν_{30}	559			CH_3, CH_2 rock, CC stretch
ν_{31}	426			CH_3, CH_2 torsion, CCC bend
ν_{32}	341			CH_3, CH_2 torsion, CCC bend
ν_{33}	253			CCC bend
ν_{34}	242			CH_3, CH_2 torsion, CCC bend
ν_{35}	127			CH_3, CH_2 torsion, CCC bend
ν_{36}	99			Backbone flex
				Backbone flex

Table 3.8: The calculated lowest 16 vibrational frequencies (in cm^{-1}) of the G_1T_2 conformer of 1-butoxy radical in its ground electronic state as obtained at the B3LYP/6-31+G* level of theory.

^a Unscaled harmonic frequencies. The labeling of the vibrational modes follows the Mulliken notation scheme⁸⁷ for a C₁ molecule. ^b The contributions of various internal coordinates Q to the normal mode indicated in the first column are listed, other than the CO stretch or CCO deformation which are listed in the preceding two columns with a qualitative indication of their magnitude.

	\tilde{X}			
Assignment	B3LYP ^a	CO stretch	$(C)_2CO$ deformation ^b	Q^c
ν_{13}	1404(a'')			CH_3 , CH rock, CC stretch
ν_{14}	1261(a')	Large		CH_3 , CH rock
ν_{15}	1207(a')	Medium		CH_3 , CH rock
ν_{16}	1165(a'')			CH_3 , CH rock
ν_{17}	1069(a'')			CH_3 rock, CC stretch
ν_{18}	1054(a')	Small		CH_3 , CH rock
ν_{19}	984(a')	Large		CH_3 rock
ν_{20}	921(a'')			CH_3 rock, CC stretch
ν_{21}	888(a'')			CH_3 , CH rock
ν_{22}	809(a')	Medium		CC stretch
ν_{23}	453(a')			CCC bend
ν_{24}	390(a'')			CH_3 rock, CC stretch
ν_{25}	359(a')			CCC bend
ν_{26}	244(a')			CH_3 torsion
ν_{27}	197(a'')			CH_3 torsion

Table 3.9: The calculated lowest 15 vibrational frequencies (in cm^{-1}) of 2-propoxy radical in its ground electronic state as obtained at the B3LYP/6-31+G* level of theory.

^a The unscaled harmonic frequencies were obtained at the C_1 -symmetry minimum and their symmetries under the C_s point group are included in parentheses. The labeling of the frequencies follows the Mulliken notation scheme.

^b For a' symmetry modes the $(C)_2CO$ (or HCO) deformation is an in-plane bend and for a'' symmetry modes it is an out-of-plane twist. ^c The contributions of various internal coordinates Q to the normal mode indicated in the first column are listed, other than the CO stretch or CCO deformation which are listed in the preceding two columns with a qualitative indication of their magnitude.

	$\tilde{X}, G+$	B3LYP ^a	CO stretch	(C') ₂ CO deformation	Q^b
ν_{20}	1194	Large			CH_3, CH_2 rock, CCC bend
ν_{21}	1165	Small			CH_3, CH_2 rock, CC stretch
ν_{22}	1067	Small			CH_3, CH_2 rock, CC stretch
ν_{23}	1059				CH_3, CH_2 rock, CC stretch
ν_{24}	1030	Large			CH_3, CH_2 rock, CC stretch
ν_{25}	1000				CH_3, CH_2 rock, CC stretch
ν_{26}	936	Large			CH_3, CH_2 rock, CC stretch
ν_{27}	927	Medium			CH_3, CH_2 rock, CC stretch
ν_{28}	794				CH_3, CH_2 rock, CC stretch
ν_{29}	773	Medium			CH_3, CH_2 rock, CC stretch
ν_{30}	468		Large		CCC bend
ν_{31}	431		Large		CCC bend
ν_{32}	365		Large		CCC bend
ν_{33}	247				CCC bend
ν_{34}	216				CH_3 torsion, CCC bend
ν_{35}	208				CH_3 torsion
ν_{36}	95				Backbone flex

Table 3.10: The calculated lowest 17 vibrational frequencies (in cm^{-1}) of the $G+$ conformer of 2-butoxy radical in its ground electronic state as obtained at the B3LYP/6-31+G* level of theory.

^a Unscaled harmonic frequencies. The labeling of the vibrational modes follows the Mulliken notation scheme⁸⁷ for a C₁ molecule. ^b The contributions of various internal coordinates Q to the normal mode indicated in the first column are listed, other than the CO stretch or CCO deformation which are listed in the preceding two columns with a qualitative indication of their magnitude.

	\tilde{X}, T	B3LYP ^a	CO stretch	$(C')_2CO$ deformation	Q^b
ν_{20}	1203	Medium			CH_3, CH_2 rock, CCC bend
ν_{21}	1163				CH_3, CH_2 rock, CCC bend, CC stretch
ν_{22}	1090		Large		CH_3, CH_2 rock, CC stretch
ν_{23}	1046	Large			CH_3, CH_2 rock, CC stretch
ν_{24}	1033				CH_3, CH_2 rock, CC stretch
ν_{25}	989	Large			CH_3, CH_2 rock, CC stretch
ν_{26}	936	Small			CH_3, CH_2 rock, CC stretch
ν_{27}	915	Medium			CH_3, CH_2 rock, CC stretch
ν_{28}	793				CH_3, CH_2 rock, CC stretch
ν_{29}	762	Small	Medium		CH_3, CH_2 rock, CC stretch
ν_{30}	474		Large		CCC bend
ν_{31}	406				CCC bend
ν_{32}	360				CCC bend
ν_{33}	268				CCC bend
ν_{34}	241				CH_3 torsion, CCC bend
ν_{35}	199				CH_3 torsion
ν_{36}	90				Backbone flex

Table 3.11: The calculated lowest 17 vibrational frequencies (in cm^{-1}) of the T conformer of 2-butoxy radical in its ground electronic state as obtained at the B3LYP/6-31+G* level of theory.

^a Unscaled harmonic frequencies. The labeling of the vibrational modes follows the Mulliken notation scheme⁸⁷ for a C₁ molecule. ^b The contributions of various internal coordinates Q to the normal mode indicated in the first column are listed, other than the CO stretch or CCO deformation which are listed in the preceding two columns with a qualitative indication of their magnitude.

$\tilde{X}, G-$					
Assignment	B3LYP ^a	CO stretch	$(C')_2CO$ deformation	Q^b	
ν_{20}	1186	Medium		CH_3, CH_2 rock, CCC bend	
ν_{21}	1151	Small		CH_3, CH_2 rock, CC stretch	
ν_{22}	1100		Large	CH_3, CH_2 rock, CC stretch	
ν_{23}	1064	Small		CH_3, CH_2 rock, CCC bend, CC stretch	
ν_{24}	1009	Large		CH_3, CH_2 rock, CC stretch	
ν_{25}	991	Small		CH_3, CH_2 rock, CC stretch	
ν_{26}	933	Large	Large	CH_3, CH_2 rock, CC stretch	
ν_{27}	917	Medium		CH_3, CH_2 rock, CC stretch	
ν_{28}	784	Small		CH_3, CH_2 rock, CC stretch	
ν_{29}	765	Medium		CH_3, CH_2 rock, CC stretch	
ν_{30}	573		Large	CCC bend	
ν_{31}	392		Large	CCC bend	
ν_{32}	368		Large	CCC bend	
ν_{33}	256			CCC bend	
ν_{34}	230			CH_3 torsion, CCC bend	
ν_{35}	205			CH_3 torsion	
ν_{36}	96			Backbone flex	

Table 3.12: The calculated lowest 17 vibrational frequencies (in cm^{-1}) of the $G-$ conformer of 2-butoxy radical in its ground electronic state as obtained at the B3LYP/6-31+G* level of theory.

^a Unscaled harmonic frequencies. The labeling of the vibrational modes follows the Mulliken notation scheme⁸⁷ for a C₁ molecule. ^b The contributions of various internal coordinates Q to the normal mode indicated in the first column are listed, other than the CO stretch or CCO deformation which are listed in the preceding two columns with a qualitative indication of their magnitude.

Finally it is worth mentioning a possibly obvious but quite important point. In percentage terms we expect the calculation of the vibrational frequencies of both the \tilde{X} and \tilde{A} states to be much more accurate than the $\tilde{A}-\tilde{X}$ separation. The problem with the latter prediction, of course, is that the $\tilde{A}-\tilde{X}$ difference is very small compared to the computed absolute energies of the states, which means that even if the absolute error in the states' energies is small, the error in the difference can be relatively large. To get accurate $\tilde{A}-\tilde{X}$ values would require a very large basis set with high-quality (correlation) methods.

3.3.2 LEDF Observations

Figures 3.2 and 3.3 show survey scans of LIF spectra of the primary and secondary alkoxy radicals, respectively. LEDF spectra were recorded for a number of vibronic bands labeled by the letters shown in the corresponding LIF traces

In principle, the LEDF spectra provide a direct experimental way of obtaining the energy difference between the \tilde{A} and \tilde{X} states. However, to accurately determine the origin of the \tilde{A} state, one needs to uniquely identify the $\tilde{B}-\tilde{A}$ origin band among bands belonging to the vibrationally excited levels of the \tilde{X} (\tilde{A}) states, the latter of course giving valuable information about the vibrational frequencies of these states. Our assignments were aided with quantum chemical predictions of both the energy separation of these two states and the vibrational levels for the ground electronic state. From present and previous⁸⁶ computational work, we have found the PES for the close-lying \tilde{A} state to be similar to that of the ground state. Hence the vibrational

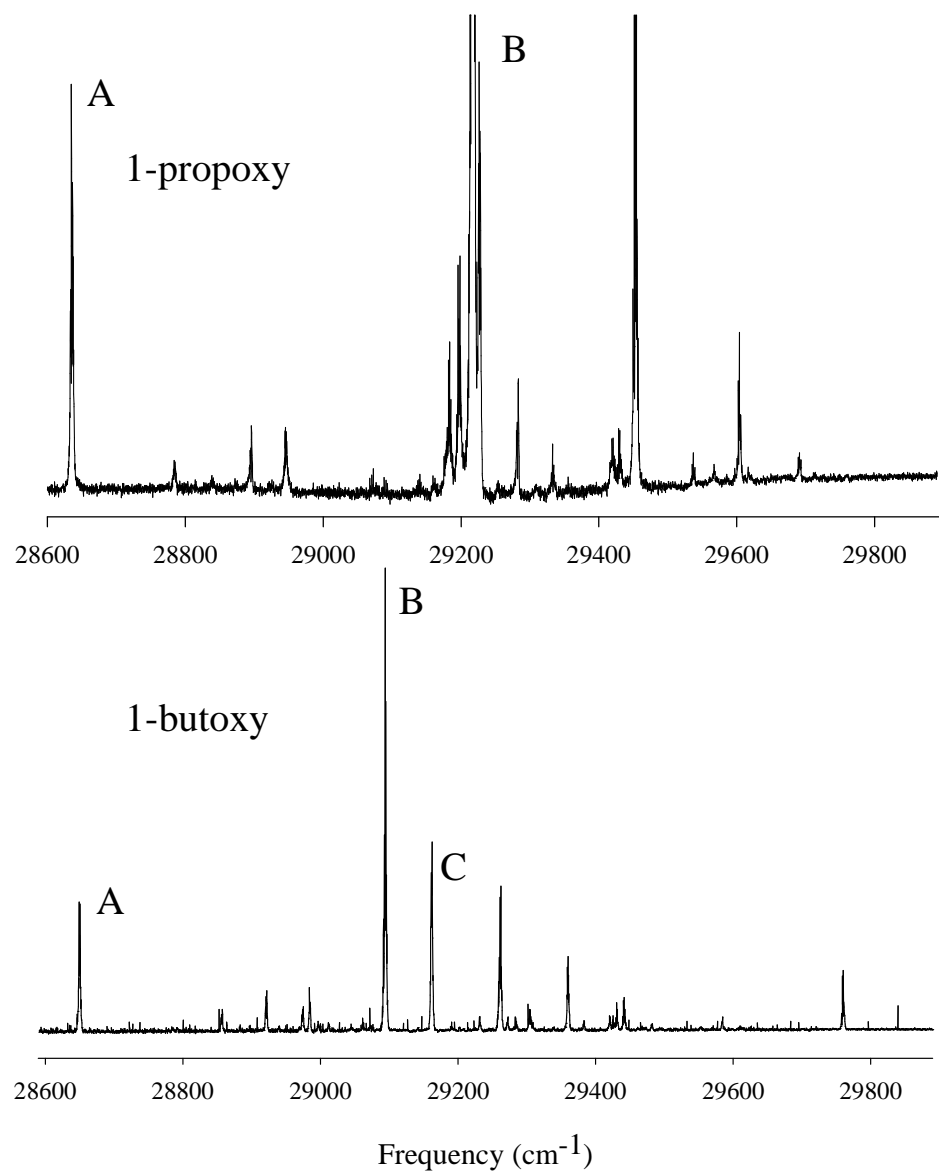


Figure 3.2: Survey scans of the LIF spectra of the primary radicals. The line labeled B in 1-propoxy extends off-scale so as to show more clearly the weaker transitions.

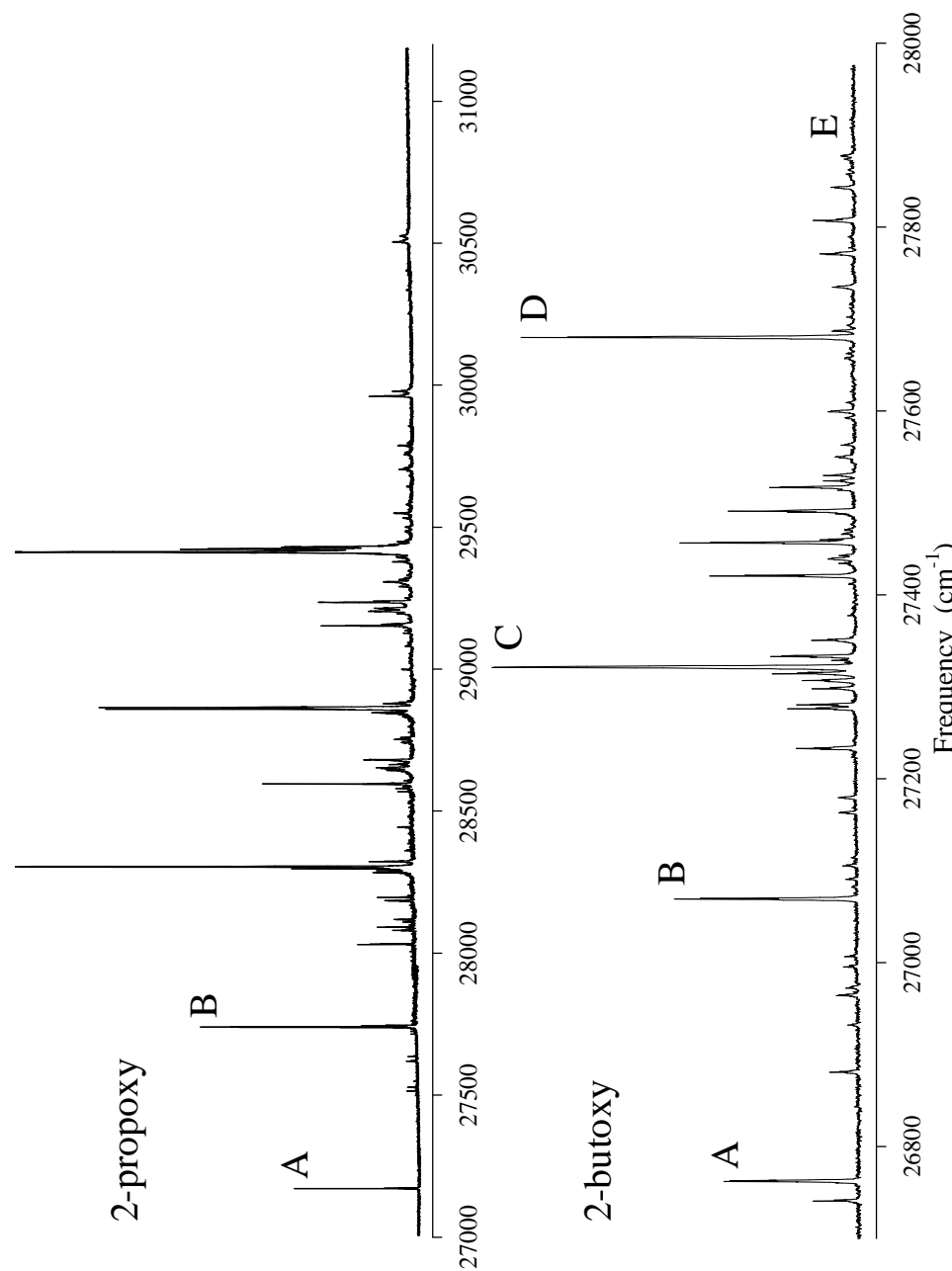


Figure 3.3: Survey scans of the LIF spectra of the secondary alkoxyes. Note the difference in frequency scales.

frequencies are not expected to differ greatly between these two electronic states, with the exception of some possible frequencies that exhibit pseudo-Jahn-Teller activity for the C_s conformers.⁸⁶

It is pertinent to mention the following additional principles upon which we base our assignments of the vibrational levels of the \tilde{X} and \tilde{A} states:(i) under C_s -symmetry (or near C_s -symmetry), only the totally symmetric fundamentals are electronically allowed and therefore these are expected to exhibit the strongest fluorescence intensity; (ii) only vibrations of CO stretch or CCO deformation (bend or twist), or vibrations coupled to those, are anticipated to have significant nondiagonal Franck-Condon factors, since the \tilde{B} , \tilde{A} and \tilde{X} potentials are quite similar along other modes, as the electronic transition is localized on the O atom.

3.3.3 1-Propoxy

For 1-propoxy, the LEDF spectra were recorded by pumping bands A and B shown in Fig. 3.2. Band A has been identified by detailed rotational analysis⁶ as the origin of the G conformer and band B is the origin of the T conformer. These LEDF spectra are shown in Fig. 3.4, while Fig. 3.5 shows an expanded view of their LEDF spectra within 1700 cm^{-1} redshifted from the pumping frequency.

The T conformer of 1-propoxy is a nominally C_s -symmetry structure and therefore one would expect the totally symmetric fundamental frequencies to dominate in the LEDF spectrum. It is the CO stretch motion that is expected to exhibit the strongest fluorescence intensity, thus the strongest transitions should be assigned to CO stretch vibrations. A strong progression in the \tilde{X} state of the T conformer can immediately

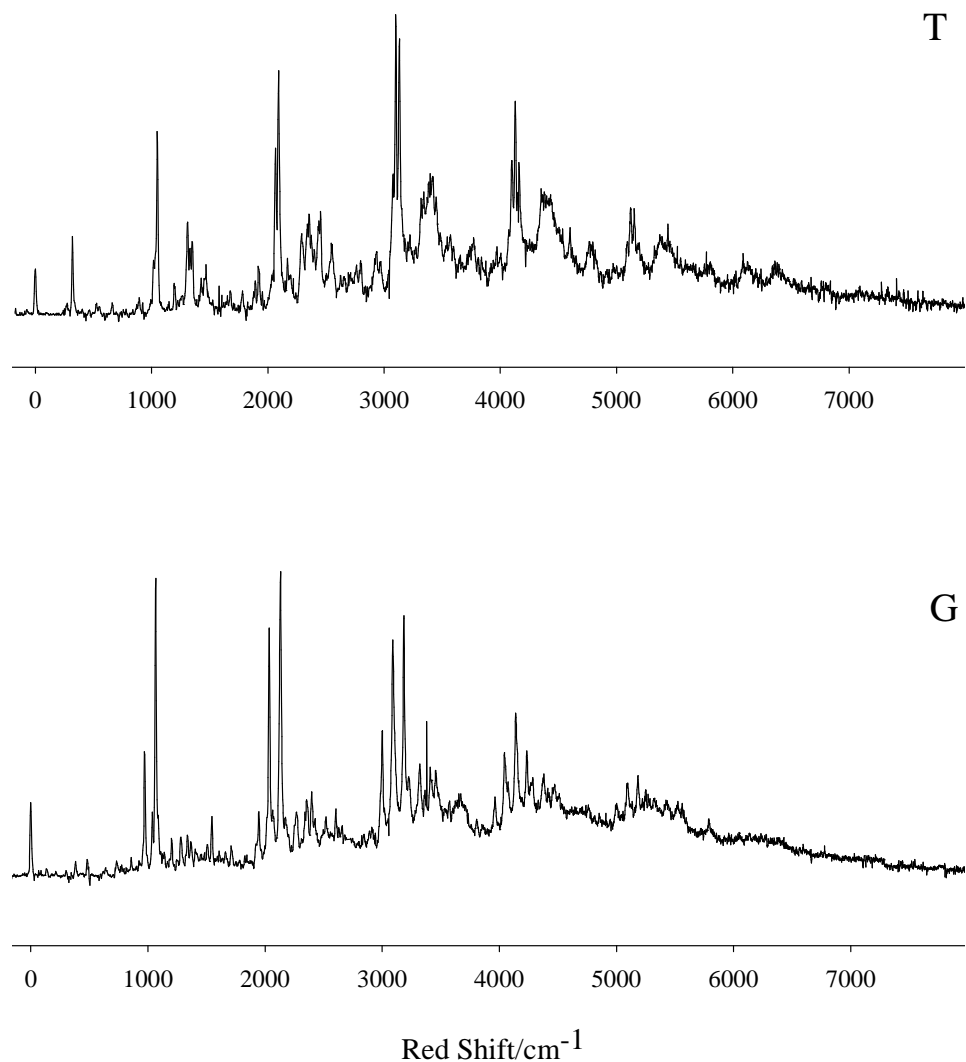


Figure 3.4: LEDF spectra of the *T* and *G* conformations of 1-propoxy radical. The top trace was obtained by pumping band B (Fig. 3.2), the origin of the *T* conformer, at 29218 cm^{-1} while the bottom trace was obtained by pumping band A (Fig. 3.2), the origin of the *G* conformer, at 28634 cm^{-1} . The x axis indicates (red) shift from the pump frequency. The intensities are not corrected for the grating efficiency and the camera sensitivity curves. The experimental resolution was 15 cm^{-1} .

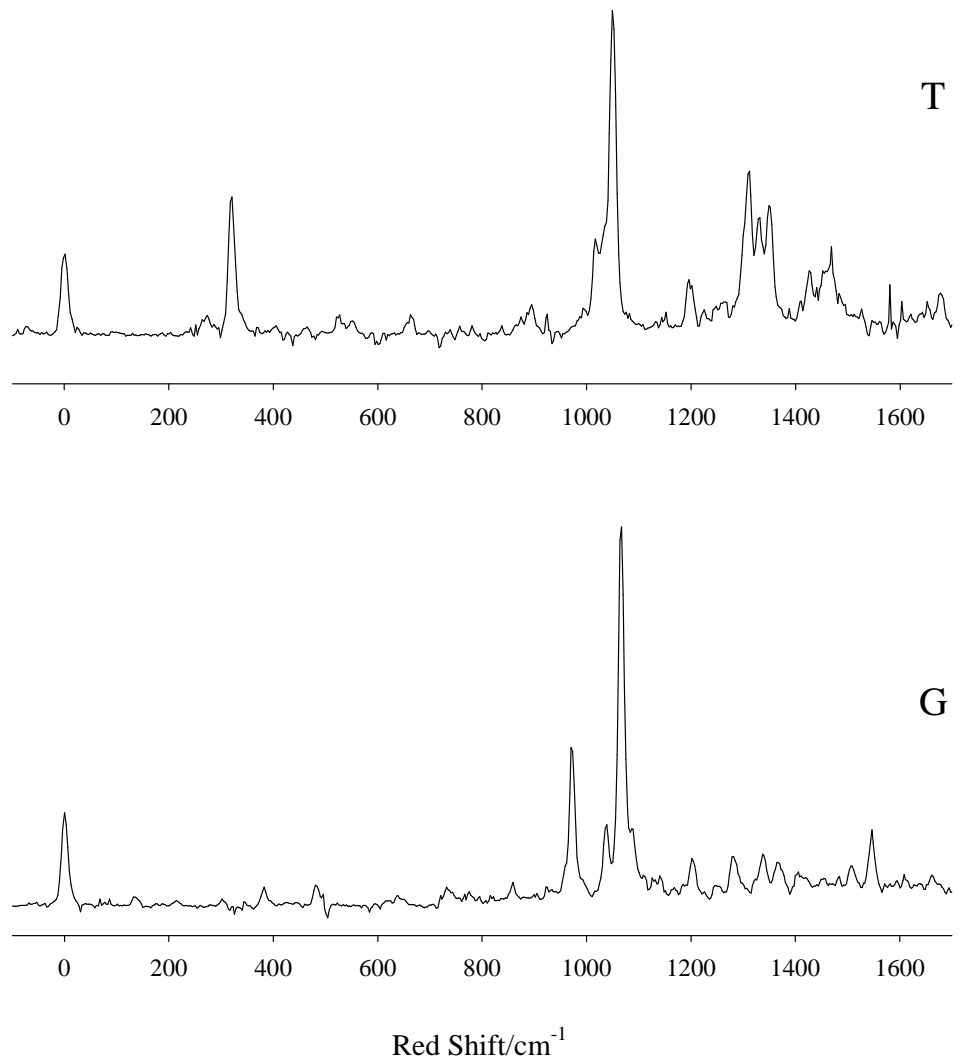


Figure 3.5: An expanded view of the LEDF spectra of the *T* and *G* conformations of 1-propoxy radical. The top trace was obtained by pumping band B (Fig. 3.2), the origin of the *T* conformer, at 29218 cm^{-1} while the bottom trace was obtained by pumping band A (Fig. 3.2), the origin of the *G* conformer, at 28634 cm^{-1} . The x axis indicates (red) shift from the pump frequency. The intensities are not corrected for the grating efficiency and the camera sensitivity curves. The experimental resolution was 15 cm^{-1} .

be identified with a 1-0 vibrational interval of 1050 cm^{-1} redshifted from the \tilde{X} state origin located at 0 cm^{-1} . We attribute this main vibrational progression to ν_{18} , as this mode has the strongest CO stretch character among all of the modes (see Table 3.4). Mode ν_{19} involves significant but less participation of the CO stretch motion than ν_{18} and that is analogously reflected in the LEDF spectrum via the fluorescence intensity of the corresponding 1-0 band assigned to the 1017 cm^{-1} peak in Table 3.13.

Based upon the match with the theoretically calculated frequencies (see Table 3.13), we have assigned several other, lower intensity, totally symmetric fundamentals to the \tilde{X} state. The bands at $274\text{ }(\nu_{25}^X)$, $527\text{ }(\nu_{23}^X)$, $895\text{ }(\nu_{21}^X)$, and $1060\text{ }(\nu_{17}^X)\text{ cm}^{-1}$ have been assigned to levels with reasonably large CCO internal coordinate contribution. This assigns all totally symmetric fundamentals calculated to be below 1200 cm^{-1} . The theoretical calculations have shown that within $1300\text{-}1450\text{ cm}^{-1}$ there are four totally symmetric vibrational modes that all involve some CO stretch and/or CCO bend movement in their motion. Only two of those, likely ν_{12}^X (theoretically calculated frequency at 1414 cm^{-1}) and ν_{11}^X (1436 cm^{-1}), appear obviously in the spectrum and their peaks are at 1426 and 1460 cm^{-1} , respectively. Their proximity may result in intensity borrowing between these bands. Nontotally symmetric fundamentals are not allowed by symmetry considerations, and their overtones, though are not prohibited, are expected to be generally weak. However, the first overtone of ν_{24}^X , which is the most pseudo-Jahn-Teller-active vibrational mode, may be a suitable candidate for the band appearing at 662 cm^{-1} .

Assignment	Frequency	
	Predicted ^a	Experimental ^b
ν_0^X	\tilde{X}	0
ν_{25}^X	270	274
ν_0^A		321
		340 ^c
ν_{23}^X	475	527
$\nu_{25}^A + \nu_0^A$		552
$2\nu_{24}^X$	614	662
$\nu_{23}^A + \nu_0^A$		844
ν_{21}^X	889	895
ν_{19}^X	1034	1017
ν_{18}^X	1074	1050
ν_{17}^X	1128	1060
$\nu_{21}^A + \nu_0^A$		1193
$\nu_{19}^A + \nu_0^A$		1311
$\nu_{18}^A + \nu_0^A$		1332
$\nu_{17}^A + \nu_0^A$		1352
ν_{12}^X	1414	1426
ν_{11}^X	1436	1460

Table 3.13: Assignment of the LEDF spectrum of the T conformer of 1-propoxy radical. The vibrational assignment is made for the emission pumping bands shown in Fig. 3.5.

^a Unscaled frequencies computed at the B3LYP/6-31+G* level of theory (in cm^{-1}). The vibrational levels of the \tilde{A} state were estimated by adding the experimentally observed vibrationless level of the \tilde{A} state (denoted as ν_0^A) to the corresponding theoretically predicted frequencies under the column of assignment. The assignment was made on the grounds that the PES for the lowest two energy states does not change considerably. ^b Experimentally observed vibrational bands (in cm^{-1}) relative to the vibrationless level of the \tilde{X} state ν_0^X . ^c Possible shoulder.

By analogy with the reasoning for the \tilde{X} state assignments, we anticipate the totally symmetric CO stretch modes to have large fluorescence intensities in the transition to the \tilde{A} state as well. However, the identification of the vibrationless level of the \tilde{A} state is the first step for assignments of the \tilde{A} state vibrational levels. As Fig. 3.4 shows, we have identified the band at 321 cm^{-1} as the vibrationless level of the \tilde{A} state. The two theoretically calculated \tilde{X} state vibrational frequencies closest to this value that are expected to show fluorescence intensity correspond to 270 and 475 cm^{-1} (see Table 3.4). In addition to the mismatch in frequency (which is large but not impossible given possible computational errors), the magnitude of the observed fluorescence intensity discourages the assignment of this band to either of these two vibrations. Our theoretically calculated \tilde{A} - \tilde{X} separation quoted in Table 3.3, while subject to considerable uncertainty, is consistent with this assignment. Similar to the \tilde{X} state, a vibrational progression associated with the ν_{18} mode appears in the \tilde{A} state, with an energy interval of 1011 cm^{-1} from the above identified \tilde{A} state origin. Using the other \tilde{X} state assignments as a guide, we have assigned the bands at 552 , 844 , 1193 , 1311 and 1352 cm^{-1} to the following modes of the \tilde{A} state: ν_{25}^A , ν_{23}^A , ν_{21}^A , ν_{19}^A and ν_{17}^A , respectively. It should be pointed out that there are vibrational progressions associated with ν_{17} and ν_{19} in both the \tilde{X} and \tilde{A} states, probably arising via intensity borrowing among the closely energy spaced totally symmetric ν_{17} , ν_{18} and ν_{19} levels.

The *G* conformer of 1-propoxy is a C_1 -symmetry structure and hence one may not preclude the appearance of any of its vibrations in the LEDF spectrum. However,

again it is the CO stretch character that carries most of the oscillator strength, therefore the strongest transitions should be connected with the CO stretch vibrations. In the LEDF spectrum of the *G* conformer (see Fig. 3.5), a strong progression in the \tilde{X} state can immediately be identified with a vibrational spacing of 1066 cm^{-1} , which as in the *T* conformer, we attribute to ν_{18} (see Table 3.5). The second strongest transition below 1700 cm^{-1} peaks at 973 cm^{-1} and is assigned to ν_{19} , which also has significant CO stretch character. Table 3.14 presents a number of assigned vibrational bands based upon matches with calculated frequencies. Indeed in this C_1 -symmetry molecule, there appears to be a peak assignable to every vibrational mode expected below 1200 cm^{-1} .

The bands appearing at 1337 , 1365 , and 1546 cm^{-1} have been assigned as combination bands of one quantum of excitation of ν_{18}^X with, respectively, two quanta of ν_{27}^X , one quantum of ν_{25}^X and one quantum of ν_{23}^X . The corresponding combination bands but with two quanta of excitation of ν_{18}^X lead to the appearance of the following peaks in the LEDF spectrum: 2399 , 2427 , and 2603 cm^{-1} . This repeated pattern of observed frequencies in the energy region higher than 2000 cm^{-1} of redshift strongly validates our previous assignments of the combination bands with ν_{18}^X .

One notes that unlike the *T* conformer in the *G* conformer the \tilde{A} state origin (nor excited vibrations) does not distinctly appear in the spectrum. The theoretical predictions (see Table 3.3) indicate that the \tilde{A} state origin lies very close to the \tilde{X}

Assignment	Frequency	
	Predicted ^a	Experimental ^b
	\tilde{X}	\tilde{A}
ν_0^X		0
ν_{27}^X	125	135
ν_0^A		214
ν_{25}^X	286	302
ν_{24}^X	305	383
ν_{23}^X	496	485
$\nu_{23}^X + \nu_{27}^X$	621	650
ν_{22}^X	788	743
ν_{21}^X	867	859
ν_{19}^X	995	973
ν_{17}^X	1114	1039
ν_{18}^X	1092	1066
$\nu_{19}^A + \nu_0^A$		1204
$\nu_{17}^A + \nu_0^A$		1254
$\nu_{18}^A + \nu_0^A$		1282
$\nu_{18}^X + 2\nu_{27}^X$	1342	1337
$\nu_{18}^X + \nu_{25}^X$	1378	1365
$\nu_{18}^X + \nu_{23}^X$	1588	1546
$2\nu_{19}^X$	1990	1947
$2\nu_{17}^X$	2228	2033
$2\nu_{18}^X$	2184	2132
$2\nu_{19}^A + \nu_0^A$		2168
$2\nu_{17}^A + \nu_0^A$		2251
$2\nu_{18}^A + \nu_0^A$		2350
$2\nu_{18}^X + 2\nu_{27}^X$	2434	2399
$2\nu_{18}^X + \nu_{25}^X$	2470	2427
$2\nu_{18}^X + \nu_{23}^X$	2680	2603

Table 3.14: Assignment of the LEDF spectrum of the *G* conformer of 1-propoxy radical. The vibrational assignment is made for the emission pumping bands shown in Fig. 3.5.

^a Unscaled harmonic frequencies computed at the B3LYP/6-31+G* level of theory (in cm⁻¹). ^b Experimentally observed vibrational bands (in cm⁻¹) relative to the vibrationless level of the \tilde{X} state ν_0^X .

state origin. The experimental resolution could be insufficient to resolve the $\tilde{B} - \tilde{A}$ and $\tilde{B} - \tilde{X}$ transitions. In this case the experimental resolution places an upper limit on the $\tilde{A} - \tilde{X}$ separation of $\lesssim 15 \text{ cm}^{-1}$.

A second possibility would be that the \tilde{A} state origin appears at a resolvable separation from that of the \tilde{X} state but with considerably diminished intensity. Whereas in the *T* conformation one can easily identify the \tilde{A} state origin as well as the vibrational structures built upon the bands belonging to it, in the *G* conformer it is difficult to make comparable assignments. What is different in the latter case is that the symmetry is lower. A single argument shows that a strongly diminished \tilde{A} state origin intensity is possible. Assume for the $C_s(T)$ conformer the $\tilde{B} - \tilde{A}$ and $\tilde{B} - \tilde{X}$ intensities are exactly the same. Further assume that the electronic eigenfunctions of the *G* conformer are just the symmetric and anti-symmetric linear combinations of the *T* state eigenfunctions. Both assumptions are qualitatively reasonable and together yield the result that the $\tilde{B} - \tilde{X}$ intensity increases by a factor of 2 going from the *T* to *G* conformer while the $\tilde{B} - \tilde{A}$ intensity exactly goes to zero.

Of course we do not expect this simple model to be completely correct and we also expect some variation in the $\tilde{B} - \tilde{X}$ and $\tilde{B} - \tilde{A}$ intensities along the strong CO stretch progression. Indeed for the alkoxies as a whole the $\tilde{B} - \tilde{A}$ transition seems to slightly increase in intensity for higher CO stretch quanta. It therefore seems reasonable to look for $\tilde{B} - \tilde{A}$ CO stretch bands in the vicinity of the corresponding $\tilde{B} - \tilde{X}$ bands.

The triplet of bands ν_{19}^X , ν_{18}^X and ν_{17}^X exhibit high fluorescence intensities in the \tilde{X} state, hence they are good candidates for the assignment of their analog in the \tilde{A} state.

Indeed, the peaks appearing at 1204, 1254 and 1282 cm⁻¹ could possibly be identified as ν_{19}^A , ν_{17}^A and ν_{18}^A , respectively. All three of these \tilde{A} state bands show a profile of intensities that appears decreased in a proportional way with respect to corresponding \tilde{X} state ones. From these lines one would deduce an \tilde{A} - \tilde{X} separation of 214 cm⁻¹. Moreover a peak displaced from the \tilde{B} - \tilde{X} origin by 214 cm⁻¹ actually appears in the LEDF spectrum albeit with a very low intensity. Going to a higher-frequency region, we identified the first overtones of ν_{19}^X , ν_{17}^X and ν_{18}^X peaking at the frequencies of 1947, 2033, and 2132 cm⁻¹, respectively. The same pattern as before in the \tilde{X} state is consistently reproduced in the \tilde{A} state, i.e. the peaks at 2168, 2251 and 2350 cm⁻¹ may be assigned as their corresponding \tilde{A} state bands. The second overtones of the same modes appearing at 3000 (ν_{19}^X , theoretically calculated frequency at 2985 cm⁻¹), 3089 (ν_{17}^X , 3342) and 3183 (ν_{18}^X , 3276) cm⁻¹ exhibit fluorescence intensity, with corresponding bands in the \tilde{A} state at 3223 (3199), 3316 (3556), and 3409 (3490) cm⁻¹, respectively. Obviously the poor Franck-Condon factors for the \tilde{A} state make it impossible for the majority of the vibrational modes to appear in the spectrum save for the strongest modes identified in the \tilde{X} state. We consider the determination of the \tilde{A} - \tilde{X} separation of 214 cm⁻¹ as likely to be correct. However, the large number of vibrational modes possibly active in the G conformer makes it impossible to definitely affirm this value or rule out that the \tilde{A} - \tilde{X} separation is just too small to be resolved.

The largest discrepancies between the calculated harmonic frequencies and the experimentally observed anharmonic frequencies lie, for the T conformer, with ν_{17}^X , ν_{18}^X and ν_{17}^A while for the G conformer with ν_{24}^X and ν_{17}^X . We need to recognize that while

the B3LYP methodology is generally a cost-effective procedure for predicting reliable vibrational frequencies, its results are obtained by use of the harmonic approximation. Neither possible anharmonicity effects (probably ν_{17}^X of T and G conformers) nor vibronic coupling interactions between the \tilde{X} and \tilde{A} states (ν_{25}^A and $2\nu_{24}^X$ of the T conformer) are incorporated in the vibrational frequency calculations. In addition, mechanisms like intensity borrowing between energetically closely spaced bands (e.g. ν_{19}^A , ν_{18}^A and ν_{17}^A of the T conformer) of the same symmetry may not be completely described by the output of such calculations.

3.3.4 1-Butoxy

For 1-butoxy, the LEDF spectra were recorded by pumping bands A, B, and C shown in Fig. 3.2. Band A has been identified⁷ as the origin of the $G_1 T_2$ conformer, band B is that of $T_1 T_2$, and band C is that of $T_1 G_2$. The LEDF spectra of these species are shown in Fig. 3.6, while Fig. 3.7 shows an expanded view of their LEDF spectra up to $\approx 1600 \text{ cm}^{-1}$ redshifted from the pumping frequency.

Using our experience with the T conformer of 1-propoxy, the vibrational interval of 1052 cm^{-1} measured from the \tilde{X} state origin may be associated with the CO stretch progression in the \tilde{X} state for the $T_1 T_2$ conformation of 1-butoxy. Since the vibrational mode ν_{23} encompasses the largest CO stretch character we assign this band and the higher members of the progression to this mode. On the grounds of matching well with the theoretically calculated frequencies (see Table 3.15), the following low-intensity, totally symmetric fundamentals were assigned in the \tilde{X} state: the bands at 395 (ν_{31}^X), 950 (ν_{27}^X) and 1116 (ν_{22}^X) cm^{-1} involve medium CCO deformation in

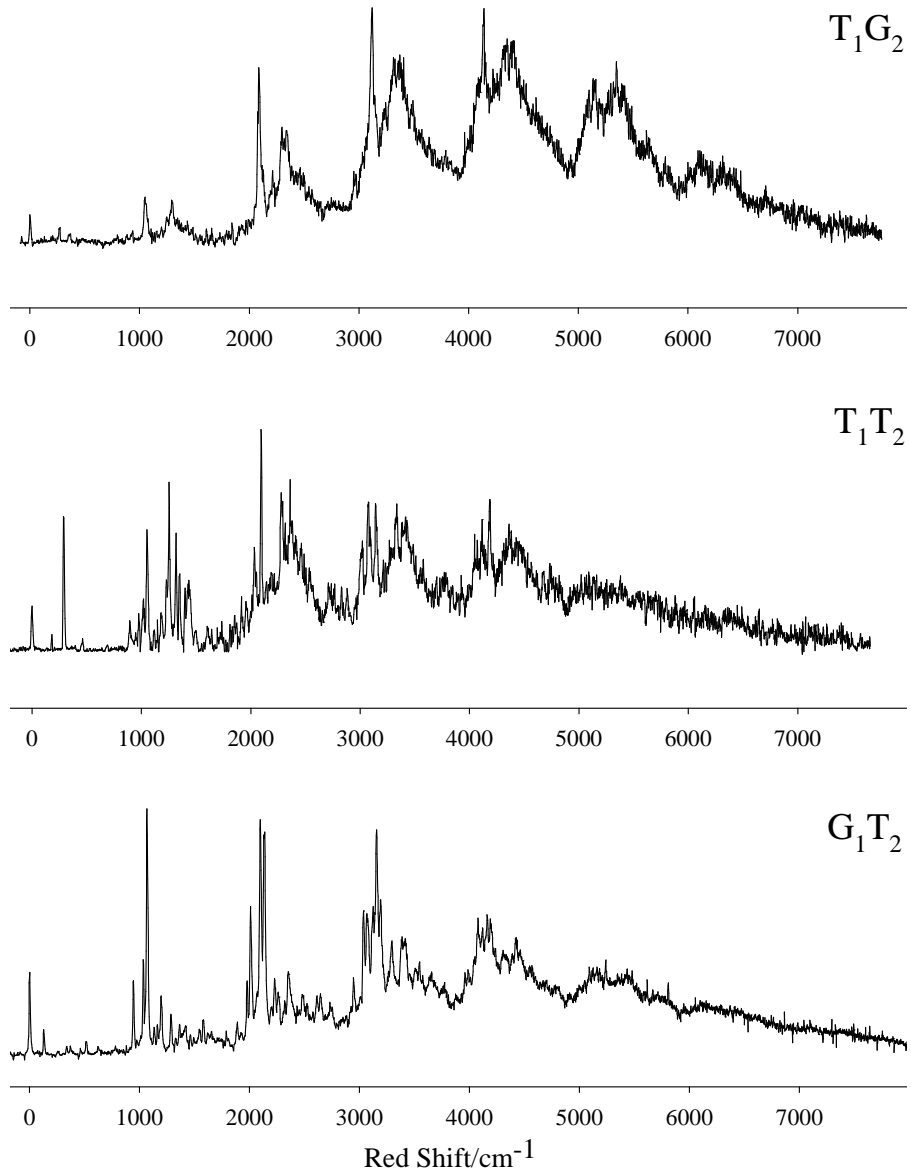


Figure 3.6: LEDF spectra of the T_1G_2 , T_1T_2 , and G_1T_2 conformations of 1-butoxy radical. The top trace was obtained by pumping band C (Fig. 3.2), the origin of the T_1G_2 conformer, at 29164 cm^{-1} , the middle trace was obtained by pumping band B (Fig. 3.2), the origin of the T_1T_2 conformer, at 29095 cm^{-1} while the bottom trace by pumping band A (Fig. 3.2), the origin of the G_1T_2 conformer, at 28649 cm^{-1} . The x axis indicates (red) shift from the pump frequency. The intensities are not corrected for the grating efficiency and the camera sensitivity curves. The experimental resolution was 15 cm^{-1} .

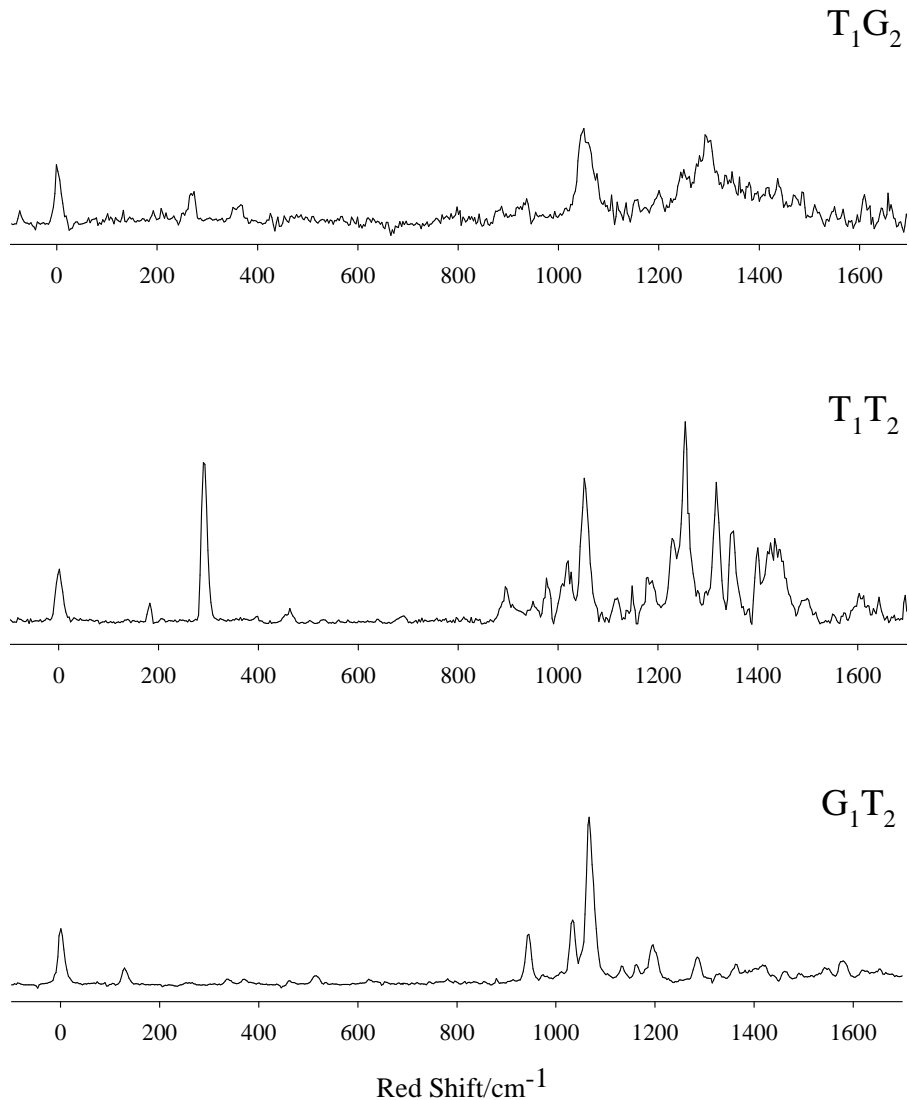


Figure 3.7: An expanded view of the LEDF spectra of the T_1G_2 , T_1T_2 , and G_1T_2 conformations of 1-butoxy radical. The top trace was obtained by pumping band C (Fig. 3.2), the origin of the T_1G_2 conformer, at 29164 cm^{-1} , the middle trace was obtained by pumping band B (Fig. 3.2), the origin of the T_1T_2 conformer, at 29095 cm^{-1} while the bottom trace by pumping band A (Fig. 3.2), the origin of the G_1T_2 conformer, at 28649 cm^{-1} . The x axis indicates (red) shift from the pump frequency. The intensities are not corrected for the grating efficiency and the camera sensitivity curves. The experimental resolution was 15 cm^{-1} .

their motion, and the band at 463 (ν_{30}^X) cm^{-1} large CCO deformation. The band at 976 cm^{-1} is identified as ν_{26}^X , a mode with moderate CO stretch and large CCO bend character. The band at 183 cm^{-1} was assigned to ν_{34}^X and is a backbone flex mode. The vibration ν_{24} involves a small amount of CO stretch character and is assigned to the peak at 1017 cm^{-1} in the \tilde{X} state. Finally, the bands peaking at 1279 (ν_{20}^X , theoretically calculated frequency at 1282 cm^{-1}), 1425 (ν_{17}^X , 1369), and 1437 (ν_{16}^X , 1393) cm^{-1} likely correspond to modes involving small CO and small CCO deformation.

Following the same arguments for the assignment of the \tilde{A} state origin in the T conformer of 1-propoxy (and within the expectedly large interval of uncertainty of our theoretical calculations quoted in Table 3.3), we have identified the peak at 292 cm^{-1} as the vibrationless level of the \tilde{A} state. The band redshifted from it by 1056 cm^{-1} (at 1348 cm^{-1}) is correlated with the strong CO stretch character vibration ν_{23} , a mode that also leads a vibrational progression in the \tilde{A} state. By reference to our \tilde{X} state assignments, we make similar assignments in the \tilde{A} state, as detailed in Table 3.15.

While the $T_1 T_2$ conformer of 1-butoxy is a near- C_s symmetry structure, the geometry of the $T_1 G_2$ conformation is characterized by significant departure from the C_s -symmetry reference structure. The CO stretch progression in the \tilde{X} state is easily identifiable in Fig. 3.6. The vibrational 1-0 spacing of the first number of this relatively strong CO stretch progression is 1050 cm^{-1} and we associated ν_{24} with strong CO stretch character mode with this band. (See Table 3.7.) Using the calculated

Assignment	Frequency	
	Predicted ^a	Experimental ^b
ν_0^X	\tilde{X}	0
ν_{34}^X	185	183
ν_0^A		292
ν_{31}^X	391	395
$(\nu_{30}^X \text{ and } \nu_{34}^A + \nu_0^A)^c$	467	463
$\nu_{31}^A + \nu_0^A$		683
$\nu_{30}^A + \nu_0^A$		895
ν_{27}^X	914	950
ν_{26}^X	995	976
ν_{24}^X	1061	1017
ν_{23}^X	1079	1052
$(\nu_{22}^X \text{ and } \nu_{27}^X + \nu_{34}^X)^c$	1133 and 1099	1116
$\nu_{26}^X + \nu_{34}^X$	1180	1148
$\nu_{24}^X + \nu_{34}^X$	1246	1191
$\nu_{27}^A + \nu_0^A$		1206
$\nu_{26}^A + \nu_0^A$		1287
ν_{20}^X	1282	1279
$\nu_{24}^A + \nu_0^A$		1353
$\nu_{23}^A + \nu_0^A$		1371
$\nu_{22}^A + \nu_0^A$		1425
$(\nu_{17}^X \text{ and } \nu_{27}^A + \nu_{34}^A + \nu_0^A)^c$	1369	1425
ν_{16}^X	1393	1437
$(\nu_{15}^X \text{ and } \nu_{26}^A + \nu_{34}^A + \nu_0^A)^c$	1413	1445
$\nu_{24}^A + \nu_{34}^A + \nu_0^A$		1538
$\nu_{20}^A + \nu_0^A$		1574

Table 3.15: Assignment of the LEDF spectrum of the $T_1 T_2$ conformer of 1-butoxy radical. The vibrational assignment is made for the emission pumping bands shown in Fig. 3.7.

^a See footnote a of Table 3.13. ^b Experimentally observed vibrational bands (in cm^{-1}) relative to the vibrationless level of the \tilde{X} state ν_0^X . ^c The experimental bands may have dual assignments.

frequencies for comparison, we made additional assignments of the lower intensity bands in the \tilde{X} state. The weak peaks at 79 (ν_{36}^X) and 101 (ν_{35}^X) cm^{-1} are characterized as vibrations that exhibit backbone flex motions, and the peak at 208 (ν_{34}^X) cm^{-1} is characterized by a mode of CH_3 torsion and CCC bend. The bands peaking at 351 (ν_{32}^X) and 484 (ν_{31}^X) cm^{-1} are attributed to modes involving large CCO deformation in their motion, the peaks at 798 (ν_{28}^X), 886 (ν_{27}^X), and 930 (ν_{26}^X) cm^{-1} correspond to modes containing the internal coordinates of medium-sized CCO and small-sized CO movement, medium CCO deformation and medium CO/large CCO motion, respectively. Mode ν_{23}^X involves medium CCO and small CO movements and reasonably correlates with a peak at 1071 cm^{-1} and mode ν_{22}^X is characterized by a medium CO movement and corresponds to the peak appearing at 1117 cm^{-1} . The bands centered at 1135 (ν_{21}^X), 1244 (ν_{20}^X , theoretically calculated frequency at 1256 cm^{-1}), 1300 (ν_{19}^X , 1307) and 1338 (ν_{18}^X , 1338) are built upon vibrational modes that include small amounts of CO stretch character in their motion.

The assignment of the \tilde{A} state origin is based on the consideration that the strong CO stretch progression appearing in the \tilde{X} state should also appear in the \tilde{A} state. The band at 1300 cm^{-1} is most likely the first member of the CO stretch progression in the \tilde{A} state, and is likewise assigned to ν_{24}^A . This assignment identifies the origin of the \tilde{A} state at 271 cm^{-1} above the \tilde{X} state. Other observed peaks at frequencies lower than 1600 cm^{-1} that may be assigned to the \tilde{A} state are given in Table 3.16.

For the $G_1 T_2$ conformation, a pronounced vibrational progression with a 1-0 interval of 1067 cm^{-1} is attributed to the CO stretch motion in the \tilde{X} state and is assigned

Assignment	Frequency	
	Predicted ^a	Experimental ^b
ν_0^X	\tilde{X}	0
ν_{36}^X	97	79
ν_{35}^X	117	101
ν_{34}^X	208	208
ν_0^A		271
$(\nu_{32}^X \text{ and } \nu_{36}^A + \nu_0^A)^c$	346	368
$\nu_{35}^A + \nu_0^A$		388
$(\nu_{31}^X \text{ and } \nu_{34}^A + \nu_0^A)^c$	474	479
$\nu_{32}^A + \nu_0^A$		617
$\nu_{31}^A + \nu_0^A$		745
ν_{28}^X	869	798
ν_{27}^X	887	886
ν_{26}^X	957	930
$(\nu_{24}^X \text{ and } \nu_{28}^A + \nu_0^A)^c$	1068	1140
ν_{23}^X	1078	1071
ν_{22}^X	1110	1117
ν_{21}^X	1192	1135
$\nu_{27}^A + \nu_0^A$		1158
$\nu_{26}^A + \nu_0^A$		1228
ν_{20}^X	1256	1244
$(\nu_{19}^X \text{ and } \nu_{24}^A + \nu_0^A)^c$	1307	1339
ν_{18}^X	1338	1338
$\nu_{23}^A + \nu_0^A$		1349
$\nu_{22}^A + \nu_0^A$		1381
$\nu_{21}^A + \nu_0^A$		1463
$\nu_{20}^A + \nu_0^A$		1527
$\nu_{19}^A + \nu_0^A$		1578
$\nu_{18}^A + \nu_0^A$		1609
		1610

Table 3.16: Assignment of the LEDF spectrum of the $T_1 G_2$ conformer of 1-butoxy radical. The vibrational assignment is made for the emission pumping bands shown in Fig. 3.7.

^a See footnote a of Table 3.13. ^b Experimentally observed vibrational bands (in cm^{-1}) relative to the vibrationless level of the \tilde{X} state ν_0^X . ^c The experimental bands may have dual assignments.

to ν_{23} , the character of which is predominantly the CO stretch movement (see Table 3.8). Based upon the match with the calculated frequencies, we assigned the following low-intensity bands: 259 (ν_{33}^X) cm^{-1} corresponds to a CH_3/CH_2 torsion and CCC bend mode, 337 (ν_{32}^X) cm^{-1} involves large CCO motion, 374 (ν_{31}^X) cm^{-1} is characterized by medium-sized CCO motion, 510 (ν_{30}^X) cm^{-1} includes large contribution from the CCO internal coordinate, 850 (ν_{28}^X) cm^{-1} contains a small-sized CO stretch character, 879 (ν_{27}^X) cm^{-1} is described by small CCO and small CO participation, 946 (ν_{26}^X) cm^{-1} may be attributed to medium CCO and medium CO participation, 1033 (ν_{25}^X) cm^{-1} involves a small CO stretch activity in its motion, 1061 (ν_{24}^X) cm^{-1} includes the internal coordinate of a medium character CO stretch motion, 1132 (ν_{22}^X) cm^{-1} refers to a medium character CCO deformation, 1285 (ν_{20}^X , theoretically calculated frequency at 1271 cm^{-1}) cm^{-1} and 1329 (ν_{18}^X , 1337) cm^{-1} correspond to a small contribution of the CCO deformation internal coordinate in their modes, and 1362 (ν_{17}^X , 1370) cm^{-1} includes a small CO stretch character in its motion.

In the $T_1 T_2$ conformation the \tilde{A} state origin band appears relatively strong while it is somewhat diminished in the $G_1 T_2$ conformer. In this sense the conformers of the 1-butoxy show the same trend with respect to $\tilde{B} - \tilde{A}$ origin intensity as was suggested for 1-propoxy. However in $G_1 T_2$ 1-butoxy there is an observable band at 129 cm^{-1} which is likely the \tilde{A} state origin. It then follows that there is a CO stretch progression in the \tilde{A} state starting with the 1-0 line at 1196 cm^{-1} which we again associate

with the mode ν_{23}^A . By comparison with the \tilde{X} state assignments and having identified the \tilde{A} state origin in the $T_1 G_2$ conformer, it is a straightforward task to complete our assignments in the \tilde{A} state. Other observed peaks are assigned in Table 3.17.

3.3.5 2-Propoxy

The LEDF spectra for the unique conformer of 2-propoxy were recorded via two bands (A and B in Fig. 3.3), namely the origin band and the first member of the CO stretch progression. Fig. 3.8 includes, in the top trace, the extended LEDF spectrum recorded via the first member of the CO progression in the \tilde{B} state, and in the bottom trace an expanded view of the region redshifted up to $\approx 1300 \text{ cm}^{-1}$ from the pumping frequency. The LEDF spectrum through the origin is almost identical with the spectrum recorded by pumping one quantum of CO stretch excitation but the latter has better signal/noise and we focus our analysis on it.

Our assignments for the nominally C_s 2-propoxy are necessarily built upon the same principles as for the primary alkoxies. For the \tilde{X} state, we have identified a vibrational progression starting at 932 cm^{-1} redshifted from the pumping frequency (see Fig. 3.8) with ν_{19} , a mode that bears significant CO stretch character (see Table 3.9). However as Table 3.9 shows in 2-propoxy, unlike the primary alkoxy radicals, there is a second mode, ν_{14} , that has comparable CO stretch character. Referring to Table 3.18 we see that ν_{14} is assigned to a band at 1169 cm^{-1} . Clearly the 932 and 1169 cm^{-1} frequencies are much lower and higher, respectively, than the CO stretch frequencies deduced above for the primary alkoxies. We propose that when discussing CO stretch motion in 2-propoxy, and comparing it with other alkoxies, the average

Assignment	Frequency	
	Predicted ^a	Experimental ^b
ν_0^X	\tilde{X}	0
ν_0^A	\tilde{A}	129
ν_{33}^X	253	259
ν_{32}^X	341	337
ν_{31}^X	426	374
$\nu_{33}^A + \nu_0^A$	382	387
$\nu_{32}^A + \nu_0^A$	470	466
$(\nu_{30}^X \text{ and } \nu_{31}^A + \nu_0^A)^c$	559	510
$\nu_{30}^A + \nu_0^A$	688	640
ν_{28}^X	855	850
ν_{27}^X	873	879
ν_{26}^X	960	946
$\nu_{28}^A + \nu_0^A$	984	979
$\nu_{27}^A + \nu_0^A$	1002	1008
ν_{25}^X	1030	1033
ν_{24}^X	1050	1061
$(\nu_{23}^X \text{ and } \nu_{26}^A + \nu_0^A)^c$	1089	1067
ν_{22}^X	1135	1132
$\nu_{25}^A + \nu_0^A$	1159	1162
$\nu_{24}^A + \nu_0^A$	1179	1190
$\nu_{23}^A + \nu_0^A$	1218	1196
$\nu_{22}^A + \nu_0^A$	1264	1260
ν_{20}^X	1271	1285
ν_{18}^X	1337	1329
ν_{17}^X	1370	1362
$\nu_{20}^A + \nu_0^A$	1400	1414
$\nu_{18}^A + \nu_0^A$	1466	1460
$\nu_{17}^A + \nu_0^A$	1499	1491

Table 3.17: Assignment of the LEDF spectrum of the $G_1 T_2$ conformer of 1-butoxy radical. The vibrational assignment is made for the emission pumping bands shown in Fig. 3.7.

^a See footnote a of Table 3.13. ^b Experimentally observed vibrational bands (in cm^{-1}) relative to the vibrationless level of the \tilde{X} state ν_0^X . ^c The experimental bands may have dual assignments.

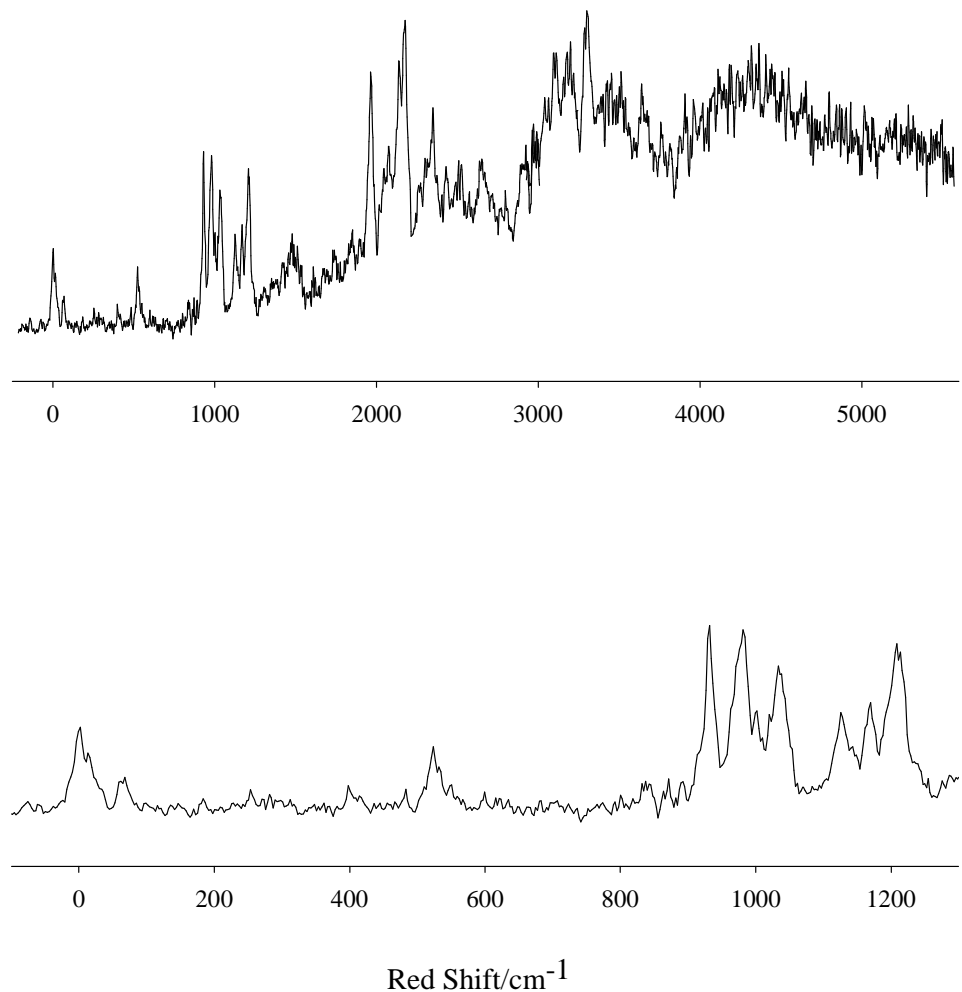


Figure 3.8: LEDF spectra of 2-propoxy radical. The top trace was obtained by pumping band B (Fig. 3.3), the frequency of the first member of the CO stretch progression, at 27734 cm^{-1} . The bottom trace corresponds to an expanded view of the LEDF data shown in the top trace. The x axis indicates (red) shift from the pump frequency. The intensities are not corrected for the grating efficiency and the camera sensitivity curves. The experimental resolution was $30\text{--}35 \text{ cm}^{-1}$.

value, 1050 cm^{-1} , of these two frequencies be considered. Based upon the match (see Table 3.18) with the calculated frequencies, we have assigned the other bands shown in the spectrum $\lesssim 1200\text{ cm}^{-1}$ to the vibrational modes placed within the parentheses (in cm^{-1}): $254(\nu_{26}^X)$, $398(\nu_{24}^X)$, $483(\nu_{23}^X)$, $837(\nu_{22}^X)$, $1002(\nu_{18}^X)$, $1033(\nu_{17}^X)$, and $1125(\nu_{15}^X)$. The character of each of the assigned modes in terms of its constituent internal coordinates is shown in Table 3.9.

The assignment of the \tilde{A} state origin is somewhat challenging. After the above fairly straightforward \tilde{X} state assignments, there are two relatively strong bands, in the low-frequency region at 68 and 524 cm^{-1} , which are plausible candidates. We favor the assignment of the $\tilde{B} - \tilde{X}$ origin to the 68 cm^{-1} band for a couple of reasons. First there seems no other explanation for a band at such a low frequency, as Table 3.9 indicates the lowest vibrational frequency should be $\approx 200\text{ cm}^{-1}$. In addition as Table 3.3 shows, both the calculated and experimental trends for the $\tilde{A} - \tilde{X}$ separation would indicate a value of $\lesssim 150\text{ cm}^{-1}$, clearly inconsistent with an assignment to 524 cm^{-1} . As Table 3.18 indicates there is a good frequency match for the 524 cm^{-1} band to $\nu_0^A + \nu_{23}^A$ assuming the ν_0^A assignment of 68 cm^{-1} . The main problem with the assignment is that there seems no particularly good reason for the relatively strong appearance of this band, although a very small $\tilde{A} - \tilde{X}$ separation may facilitate significant vibronic perturbations between the \tilde{A} and \tilde{X} states with resulting intensity anomalies. Using 68 cm^{-1} as the value for ν_0^A , the vibrational interval of the CO stretch progression formed in the \tilde{A} state (attributed to ν_{19}^A) is, for the LEDF spectrum pumped via the origin of the $\tilde{B}-\tilde{X}$ LIF excitation, 904 cm^{-1} and

Assignment	Frequency	
	Predicted ^a	Experimental ^b
ν_0^X	\tilde{X}	0
ν_0^A		68
ν_{26}^X	244	254
ν_{24}^X	390	398
ν_{23}^X	453	483
$\nu_{23}^A + \nu_0^A$	521	524
ν_{22}^X	809	837
$\nu_{22}^A + \nu_0^A$	877	892
ν_{19}^X	984	932
$\nu_{19}^A + \nu_0^A$	1052	981
ν_{18}^X	1054	1002
ν_{17}^X	1069	1033
$\nu_{18}^A + \nu_0^A$	1122	1054
ν_{15}^X	1207	1125
ν_{14}^X	1261	1169
$(\nu_{14}^A + \nu_0^A \text{ and } \nu_{15}^A + \nu_0^A)^c$	1329 and 1275	1208

Table 3.18: Assignment of the LEDF spectrum pumped via the first member of the CO stretch progression of the excitation spectrum of 2-propoxy radical. The vibrational assignment is made for the emission pumping bands shown in Fig. 3.8.

^a See footnote a of Table 3.13. ^b Experimentally observed vibrational bands (in cm^{-1}) relative to the vibrationless level of the \tilde{X} state ν_0^X . ^c The experimental bands may have dual assignments.

for the spectrum pumped through its first CO stretch 913 cm^{-1} , making an average of 908 cm^{-1} . Having the assignments to the \tilde{X} state as a guide, we make corresponding assignments to the \tilde{A} state as follows (in cm^{-1}): 892 (ν_{22}^A), 981 (ν_{19}^A), 1054 (ν_{18}^A) and 1208 (ν_{14}^A and ν_{15}^A unresolved).

3.3.6 2-Butoxy

There are some important differences between the 2-butoxy spectra and the other species that we have observed. Like most of the other species there are multiple conformers, denoted $G+$, $G-$, and T (see Fig. 3.1) for a total of 3. However, unlike the other species there are no rotational analyses that assign a group of lines in the LIF spectrum to a given conformer. However, Figs. 3.9 and 3.10 show that the LEDF spectra from lines A and C and separately B and D are nearly identical. Thus we believe that the LIF lines A and C likely belong to a given conformer, which we call A, and lines B and D belong to a second conformer, which we call B.

In addition to the conformer assignment issue, the general appearance of the 2-butoxy LEDF spectra is significantly different from the other species. Clearly there are fewer individual lines observed in the low-frequency, redshift region and as the frequency increases, the lines become broader and congestion becomes greater. There is also a tendency, as we will see below, not to see a precise repetition of fundamental frequencies in the combinations, nor a precise repetition between the $\tilde{A} - \tilde{X}$ intervals. We believe all of these effects stem from two factors: (i) the increasing size of the

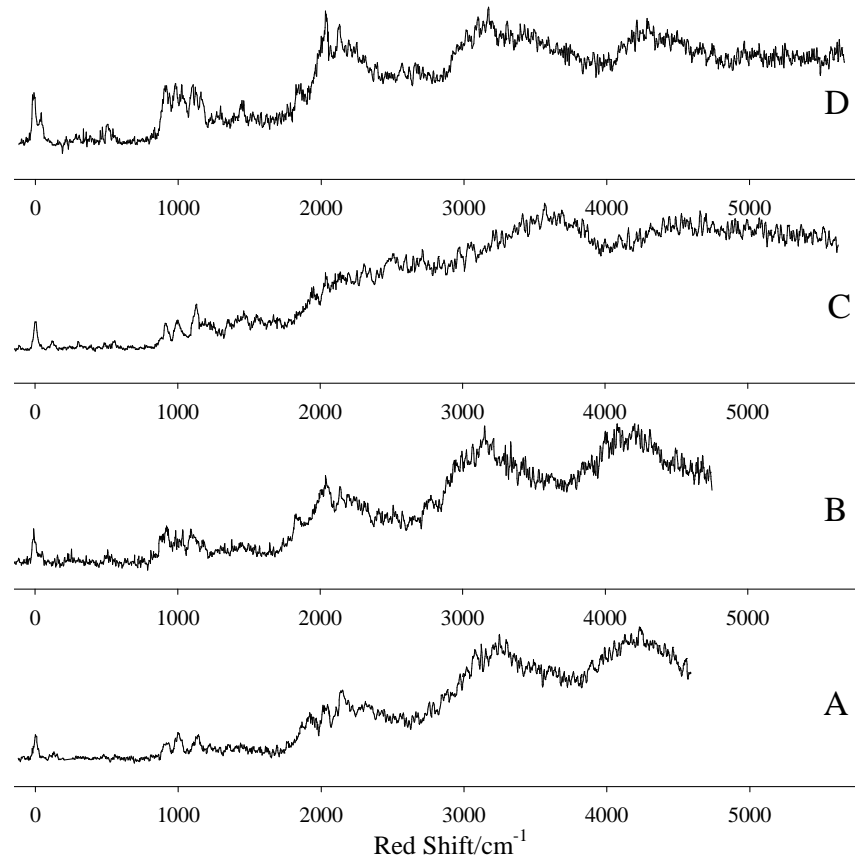


Figure 3.9: LEDF spectra of the A and B conformations of 2-butoxy radical. The lowest trace was obtained by pumping band A (Fig. 3.3), the origin of the A conformer at 26760 cm^{-1} while the next to the lowest trace was obtained by pumping band B (Fig. 3.3), the origin of the B conformer, at 27068 cm^{-1} . The trace obtained by pumping band C, at 27321 cm^{-1} , corresponds to the transition which includes one quantum of the CO stretch vibration of the A conformer in the \tilde{B} state, while the trace through D, at 27682 cm^{-1} , to the same type of excitation but for the B conformer. The x axis indicates (red) shift from the pump frequency. The intensities are not corrected for the grating efficiency and the camera sensitivity curves. The experimental resolution was $30\text{-}35\text{ cm}^{-1}$.

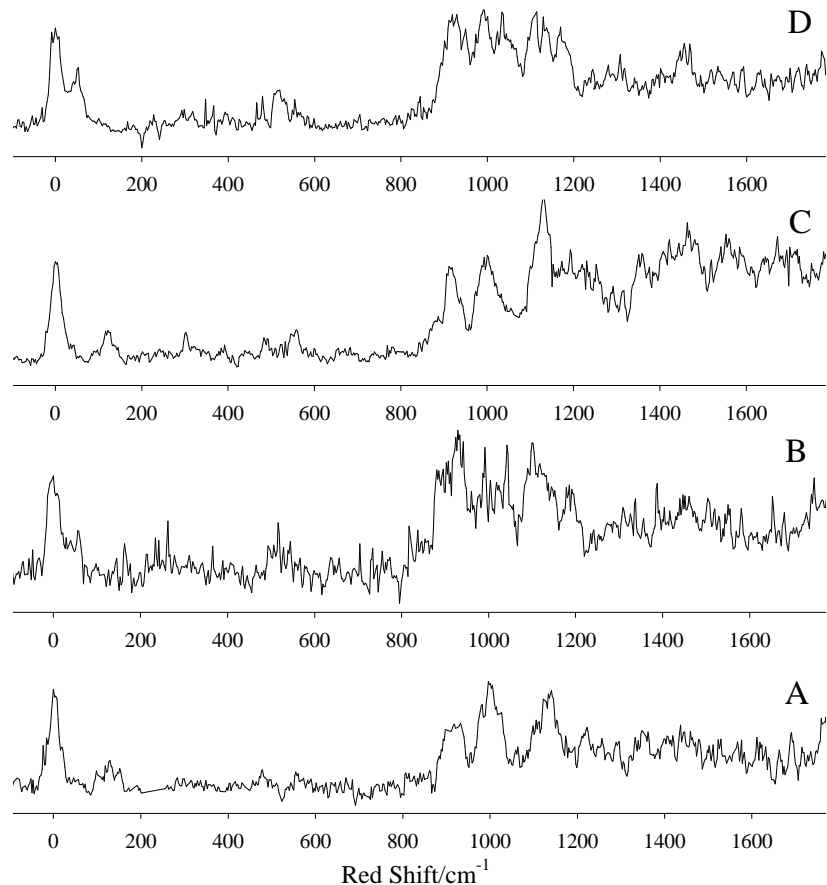


Figure 3.10: An expanded view of the LEDF spectra of the A and B conformations of 2-butoxy radical. The lowest trace was obtained by pumping band A (Fig. 3.3), the origin of the A conformer at 26760 cm^{-1} while the next to the lowest trace was obtained by pumping band B (Fig. 3.3), the origin of the B conformer, at 27068 cm^{-1} . The trace obtained by pumping band C, at 27321 cm^{-1} , corresponds to the transition which includes one quantum of the CO stretch vibration of the A conformer in the \tilde{B} state, while the trace through D, at 27682 cm^{-1} , to the same type of excitation but for the B conformer. The x axis indicates (red) shift from the pump frequency. The intensities are not corrected for the grating efficiency and the camera sensitivity curves. The experimental resolution was $30\text{-}35\text{ cm}^{-1}$.

molecule with additional vibrational degrees of freedom and (ii) a small $\tilde{A} - \tilde{X}$ separation which combined with (i) engenders extensive vibronic interactions between the \tilde{A} and \tilde{X} states.

As a consequence of the above we limit ourselves to a somewhat less quantitative and less extensive analysis for 2-butoxy. Nonetheless, some quantitative information can be obtained from the spectra and is summarized in Tables 3.19 and 3.20. Using these Tables and Figs. 3.9 and 3.10 as a guide we can make the following observations. For conformer A there is a band at 125 cm^{-1} , much like the 68 cm^{-1} band in 2-propoxy. There is only one vibrational mode (see Tables 3.10-3.12), a backbone flex for which little intensity would be expected in the LEDF spectrum, at anywhere near this low a frequency. Hence like 2-propoxy, we assign this band to the $\tilde{B} - \tilde{A}$ origin. Turning to conformer B, a corresponding band appears at 55 cm^{-1} , which can be identified as the $\tilde{B} - \tilde{A}$ origin with even greater confidence.

As one would expect for both conformers there is a relatively long CO stretch progression but only the first member of it has significantly resolved structure. In conformer A, it appears that there are four discernible lines (see Table 3.20), which we assign to the two bands with strongest CO stretch character for each the \tilde{A} and \tilde{X} states. Referring to Table 3.20 we note the $\tilde{A} - \tilde{X}$ separations do not match those of the origin region all that well, but we attribute this to the strong vibronic interactions among the multiple levels in this region. For conformer B, the pattern is even more complex in the CO stretch region, but it is again at least consistent with that expected.

Assignment	Frequency			
	Experimental ^a (B)	Experimental ^a (D)	Average ^b	Predicted ^c
ν_0^X	0	0	0	\tilde{X}
ν_0^A	58	53	55	\tilde{A}
$\nu_{30}^A + \nu_0^A$	509	509	509	529
ν_{25}^X	929	929	929	989
$\nu_{25}^A + \nu_0^A$	992	993	992	1044
ν_{23}^X	1045	1044	1044	1046
$\nu_{23}^A + \nu_0^A$	1105	1104	1104	1101
ν_{20}^X	1142	1142	1142	1203
$\nu_{20}^A + \nu_0^A$	1188	1187	1187	1258

Table 3.19: Assignment of the LEDF spectrum of the “B” conformer of 2-butoxy radical. The vibrational assignment is made for the emission pumping bands shown in Fig. 3.10.

^a Experimentally observed vibrational bands (in cm^{-1}) relative to the excitation frequency of the vibrationless level of the \tilde{X} state ν_0^X . ^b The average values between the observed vibrational bands shown under the second and third column of the experimental results. ^c Unscaled frequencies computed at the B3LYP/6-31+G* level of theory (in cm^{-1}). The vibrational levels of the \tilde{A} state were estimated by adding the average of the two experimentally observed vibrationless levels of the \tilde{A} state (denoted as ν_0^A) to the corresponding theoretically predicted frequencies under the column of assignment. The predicted frequencies were obtained for the T conformer which possibly correlates with bands B and D. See text for details. The assignment was made on the grounds that the PES for the lowest two energy states does not change considerably.

Assignment	Frequency			
	Experimental ^a (A)	Experimental ^a (C)	Average ^b	Predicted ^c
ν_0^X	0	0	0	\tilde{X}
ν_0^A	129	121	125	\tilde{A}
$\nu_0^A + \nu_0^A$	484	493	488	490
$\nu_{32}^A + \nu_0^A$	555	553	554	556
$\nu_{31}^A + \nu_0^A$	916	916	916	936
ν_{26}^X				
$(\nu_{24}^X \text{ and } \nu_{26}^A + \nu_0^A)^d$	1000	1000	1000	1061
$(\nu_{24}^X \text{ and } \nu_{24}^A + \nu_0^A)^d$	1136	1134	1135	1155
$\nu_{20}^A + \nu_0^A$	1253	1252	1252	1319

Table 3.20: Assignment of the LEDF spectrum of the “A” conformer of 2-butoxy radical. The vibrational assignment is made for the emission pumping bands shown in Fig. 3.10.

^a Experimentally observed vibrational bands (in cm^{-1}) relative to the vibrationless level of the \tilde{X} state ν_0^X .

^b The average values between the observed vibrational bands shown under the second and third column of the experimental results. ^c See footnote c of Table 3.19. The predicted frequencies were obtained for the G+ conformer which possibly correlates with bands A and C. See text for details. ^d The experimental bands may have multiple assignments.

To this point, except for the \tilde{A} state origin band, we have ignored the region redshifted 0-900 cm⁻¹. As the figures and tables show there is little activity in this region in our 2-butoxy spectra. Nonetheless there is one band around 500 cm⁻¹ (554 cm⁻¹ in conformer A and 509 cm⁻¹ in conformer B). These are somewhat similar to a corresponding trend in this region for 2-propoxy, which we suggested was a possible, but not particularly likely, $\tilde{B} - \tilde{A}$ origin. The same must be said for the above bands in 2-butoxy. However, we feel the most likely assignment of this band is to ν_{31}^A for the A conformer and ν_{30}^A for the B conformer, although like 2-propoxy the reason for the relatively strong intensity for a band in this region is not obvious.

Before closing this section it is worth speculating a moment upon the correlation between the conformer labels A and B assigned to various spectral bands and the actual conformers, $G+$, $G-$, and T which have been the subject of our quantum chemistry calculations. The proper way of making this correlation will be via the rotational analyses. However, the present studies at least provide some hints as to what the correlation may be.

It is useful to compare C₁ symmetry 2-butoxy to 2-propoxy which has C_s symmetry. As we have previously observed the “local” symmetry around the O chromophore is the most important thing for determining the electronic structure and spectrum. Referring to Fig. 3.1, it is reasonable to argue that the local symmetry of T 2-butoxy is rather similar to 2-propoxy while $G+$ and $G-$, while having similar structures among themselves, are both somewhat distinguished from the T conformer. The qualitative observation is supported by the calculated vibrational frequencies of the

three conformers in Tables 3.10-3.12. While the vibrational frequencies of all three conformers are collectively rather similar, some distinctions appear. For example all three conformers have two modes sharing the CO stretch character, but the lower frequency ones are almost identical (933 and 936 cm^{-1}) for the $G-$ and $G+$ conformer while it is 989 cm^{-1} for the T conformer.

We note that there appear to be noticeable differences between the spectra of the A and B conformers. Based upon the above we expect one to be the T conformer while the other is either the $G+$ or $G-$ conformer, with the $G+$ conformer more likely since it is computed to be the lowest energy and for the primary alkoxies the lowest energy conformer has always been observed.

If one accepts the above reasoning, it remains to suggest how A and B correlate to $G+$ and T . We argued earlier that the T conformer seems structurally more similar in the local O environment to 2-propoxy. Hence it may follow that the 55 cm^{-1} $\tilde{A}-\tilde{X}$ separation of the B conformer, being very similar to the 68 cm^{-1} value for 2-propoxy, makes it more likely correlated to the T conformer structure, leaving the A band for the $G+$ conformer. No band was observed corresponding to the $G-$ conformer. While we believe the analysis to be reasonable, we stress that definitive correlation must await rotational analyses of the A and B conformer bands.

3.4 Discussion

There are two primary kinds of quantitative information that result from our LEDF studies of the alkoxy radicals, namely, the $\tilde{A}-\tilde{X}$ separations and the vibrational

frequencies of the two states. We discuss these in turn and wrap up this section of the chapter with some observations on qualitative aspects of the LEDF spectra.

It is important first to comment on the reliability of the $\tilde{A} - \tilde{X}$ separations from the LEDF data. The precision of these values is $\lesssim 10\text{ cm}^{-1}$ but given the inherent spectral complexity there is always the possibility of assignment error. For example we now report a value of the $\tilde{A} - \tilde{X}$ separation for ethoxy although none was reported by Zhu, Kamal, and Misra⁹ in their analysis of the LEDF spectrum. We have reassigned to the $\tilde{B} - \tilde{A}$ origin the line assigned by them to the fundamental vibration ν_{18} of the \tilde{X} state. We believe that this is very reasonable given the fact that this vibrational frequency agreed least well of any they reported, when compared to those of similar molecules. It also is a relatively strong transition, consistent with the $\tilde{B} - \tilde{X}$ origin, but does not show a progression as expected for a strong vibrational band. Finally it is in good agreement with a value from a photoelectron detachment study⁸⁸ and qualitatively with quantum chemistry calculations.⁸⁶

On the other hand, for 2-propoxy, the only other of these alkoxy radicals studied by electron detachment,⁸⁸ there is a marked discrepancy. However, if our value is correct, then it is fairly easy to understand an error in the electron detachment work. It is unlikely that an $\tilde{A} - \tilde{X}$ separation of 68 cm^{-1} would have been resolved in those studies. Therefore, an average $\approx 1225\text{ cm}^{-1}$ of two strong peaks was previously assigned as the \tilde{A} state origin. We believe that transition corresponds to the CO stretch fundamental. In the report on the photodetachment work, the authors pointed out that their \tilde{A} state assignment in 2-propoxy did not have the support of

polarization data as did their assignment for ethoxy. We have pointed out the possibility of assigning our observed line at 524 cm^{-1} to the $\tilde{B} - \tilde{A}$ origin, but if the $\tilde{A} - \tilde{X}$ separation were this large it would be hard to understand why it was not observed in the photodetachment studies and it would be rather inconsistent with the quantum chemistry calculations, which as noted earlier are admittedly not very accurate for the $\tilde{A} - \tilde{X}$ separation. Finally we pointed out that for 2-butoxy again it is possible to assign a transition, giving a much larger $\tilde{A} - \tilde{X}$ separation ($\gtrsim 500\text{ cm}^{-1}$) but the preponderance of the evidence favors the $\lesssim 130\text{ cm}^{-1}$ values.

With these comments we now turn to the discussion of the values of the $\tilde{A} - \tilde{X}$ separation in Table 3.3. Several trends are apparent. For a given species the conformer with the C_s plane always has the largest $\tilde{A} - \tilde{X}$ separation and it appears the stronger the deviation from symmetry near the O atom chromophore, the more pronounced the decrease in splitting. For a given 1-alkoxy conformer, T_1 or G_1 near the oxygen atom, increasing the alkyl chain decreases the $\tilde{A} - \tilde{X}$ separation. Finally in going from a primary to a secondary alkoxy radical isomer, the $\tilde{A} - \tilde{X}$ separation decreases significantly.

These experimental results are quite valuable, since the energy of the excited \tilde{A} state is quite important with respect to its participation in thermal reaction chemistry. Moreover, as we discussed earlier, the most advanced quantum chemistry calculations today can only give a qualitative idea at best as to its value.

The ability of calculations to predict vibrational frequencies is of course much better and we have strongly relied upon them for our vibrational assignments. However experiment clearly provides the “gold standard” for the frequencies as well. As we have shown the LEDF experiments measure a fairly large number of \tilde{X} (and \tilde{A}) state vibrational frequencies for the alkoxies. Since modes involving the CO stretch character are the strongest we have the most information for them.

Table 3.21 summarizes the experimentally determined \tilde{X} and \tilde{A} state CO stretching frequencies of the alkoxy radicals investigated thus far. The CO stretching frequency of the \tilde{X} state will be larger than that of the \tilde{B} state. The lowering of the frequency upon excitation is due to the expansion of the CO bond upon the electronic transition, as a consequence of exciting a bonding σ electron to a nonbonding orbital localized on the O atom. Comparing the CO frequencies between the \tilde{X} and \tilde{A} states we notice an obvious similarity, a fact that is not surprising owing to the theoretically predicted similarity of the corresponding PESs.

The \tilde{X} state CO stretch frequencies of the T conformer of 1-propoxy, and $T_1 T_2$ and $T_1 G_2$ conformations of 1-butoxy are almost identical and very similar to methoxy. The G conformer of 1-propoxy shows similar CO frequencies to those of the $G_1 T_2$ conformer of 1-butoxy as well, but higher than the values for the other radicals. It seems that there is a consistent trend within the conformers of the primary alkoxies that involves a larger \tilde{X} state CO stretching frequency for the conformers that have a G local electronic environment around oxygen.

Alkoxies	Conformers	\tilde{X}			\tilde{A}		
		ω_0	ω_e	ω_{ex_e}	ω_0	ω_e	ω_{ex_e}
methoxy		1047(2) ^a	1057(3) ^a	7.0(7) ^a			
ethoxy		1068 ^b	1078(2) ^b	6.2(4) ^b	991 ^b		
1-propoxy	T	1050(10)	1055.8(5)	2.8(1)	1011(10)	1010.3(5)	-0.3(1)
	G	1066(10)	1072(3)	2.6(7)	1068(10)	1080(4)	3.9(8)
1-butoxy	$T_1 T_2$	1052(10)	1055(1)	2.0(4)	1056(10)	1063(9)	6(2)
	$T_1 G_2$	1051(10)	1058(2)	4.7(4)	1029(10)	1031(1)	0.4(2)
	$G_1 T_2$	1067(10)	1093(15)	10(4)	1067(10)	1092(16)	10(4)
2-propoxy		1050(10) ^c			1026(10) ^c		
2-butoxy	B	1044(10) ^d			1049(10) ^d		
	A	1000(10) ^d			1010(10) ^d		

Table 3.21: Summary (in cm^{-1}) of experimentally determined \tilde{X} and \tilde{A} state vibrational fundamental frequencies of the CO stretch mode of the primary and secondary alkoxy radicals. The table summarizes the results of this work unless noted otherwise. The reported standard deviation of ω_{ex_e} is determined by the fit and it does not include the uncertainties of ω_0 .

^a Taken from Refs. 93 and 94. ^b See Ref. 9. We have refitted the data of Table II for the CO stretch progressions in the \tilde{X} and \tilde{B} states and include the errors of ω_e and ω_{ex_e} in parentheses. Based on our assignment of the \tilde{A} state origin, we determined ω_0 of the CO stretch progression in the \tilde{A} state. ^c The frequency of 1050 cm^{-1} (\tilde{X} state) is the average of 932 (ν_{19}^X) and 1169 (ν_{14}^X) cm^{-1} . The frequency of 1026 cm^{-1} (\tilde{A} state) is the average of 913 (ν_{19}^A) and 1140 (ν_{14}^A) cm^{-1} . All of these values were determined from the LEDF spectrum that corresponds to emission from the $\nu=1$ CO stretch vibrational level of the \tilde{B} state. ^d The unresolved structure of the 2-butoxy LEDF spectra above 1500 cm^{-1} allowed only for the determination of the fundamental frequencies with any precision.

We conclude our discussion with a few words about the general appearance of the LEDF spectra. As expected, as the energy in the \tilde{X} (or \tilde{A}) state increases, the spectra become more congested and eventually discrete lines are not observed. It is also expected that this phenomenon occurs at progressively lower energy as the size of the radical increases.

However, what is not particularly expected is significantly different behavior for different isomers and conformers which is most clearly indicated for propoxy in Figs. 3.5 and 3.8. The degree of difference for the C_s conformers of 1- and 2-propoxy is striking. Even more interesting is how different the spectra of the T and G conformers of 1-propoxy appear. Consider also the vast difference in the congestion in the T and G 1-propoxy spectra for the \tilde{X} and \tilde{A} states at nearly the same energy. These results indicate the vibronic coupling must be rather isomer and conformer specific with possible implications for interval vibrational redistribution and dynamics in these species.

3.5 Conclusions

LEDF spectra of the alkoxy radicals have been observed in a free-jet expansion environment. Analysis of the spectra yields the energy separation between the vibrationless levels of the \tilde{X} and \tilde{A} states for most of the isomers and conformers of $C_nH_{2n+1}O$ for $n=3$ and 4. These studies also provide considerable insight into the \tilde{X} and \tilde{A} state vibrational structures. The CO stretch progression dominates for all LEDF

spectra providing the ν_{CO} stretching frequency for the \tilde{X} state and in most cases for the \tilde{A} state as well as numerous other vibrations. Quantum chemical calculations have been performed and compared with the experimental observations. Generally speaking, the experimental results agree well with the theoretical calculations. Observations are made concerning the degree of congestion of the LEDF spectra as the radical size increases.

CHAPTER 4

The *Ab Initio* Calculation of Spectroscopically Observable Parameters for the \tilde{X} $^2\text{E}'$ and \tilde{A} $^2\text{E}''$ Electronic States of the Silver Trimer

4.1 Introduction

Metal clusters are of considerable interest due to their role as a bridge between the atomic and solid states. The stabilities of small clusters and the evolution of bulk properties from cluster properties is the subject of nanoscience. Small clusters play an important role in homogeneous and heterogeneous catalysis, solid-state physics, crystal growth, and surface science.⁹⁵

Silver is important in photographic and catalytic processes.^{10,95} There is also an intriguing contrast among the bonding in silver with that in copper and gold. Among the simplest metal clusters are the homonuclear coinage metal trimers (Cu_3 , Ag_3 and Au_3). While their ground-state electronic structure essentially corresponds to three metal atoms each with a single s electron, the d orbitals also play a role, particularly in electron correlation. The orbitally degenerate \tilde{X} $^2\text{E}'$ D_{3h} state of Ag_3 can undergo Jahn-Teller distortion to $^2\text{A}_1$ and $^2\text{B}_2$ states in C_{2v} symmetry. The spin-orbit splitting may partially quench this distortion. Thus silver trimer is an interesting candidate for the study of the interplay of the Jahn-Teller and spin-orbit effects.

Silver clusters have been a favorite target of theoreticians for nearly 30 years. Their primary focus was to understand and predict the molecule's geometries and electronic structures. Ag_3 has received special attention. Ionization energies, electron affinities, vertical detachment energies, electronic transition energies, and ground-state geometries for Ag_3 have been studied by previous workers.⁹⁵ Previous theoretical work on Ag_3 has not produced, however, any conclusive information about the Jahn-Teller effects.^{17, 18, 96}

Ag_3 has also stimulated experimental¹⁰ interest, and considerable research was conducted in parallel to the theoretical work. Although experimentally it is possible to directly investigate the Jahn-Teller conical intersection, very little experimental work concerned itself with answering this central question. The vibronic spectrum of Ag_3 in the range 370-365 nm was first reported and interpreted by Cheng and Duncan.^{19, 97} The spectrum was assigned as the $\tilde{A}^2\text{E}'' \leftarrow \tilde{X}^2\text{E}'$ transition. Miller *et al.*¹⁴ studied the fluorescence excitation of the $\tilde{A}^2\text{E}''$ state. They recorded the laser induced, dispersed fluorescence spectra of Ag_3 by pumping several vibronic bands of the excited state. One year later, the same vibronic spectrum was remeasured and analyzed by Duncan *et al.*¹⁷ These authors empirically fitted the lower vibronic levels of the excited state to a theoretical spectrum generated from an $E \otimes e$ vibronic coupling scheme using two different methods. These included either spin-orbit coupling and linear-only Jahn-Teller coupling or linear and quadratic Jahn-Teller coupling and no spin-orbit coupling. While the excited-state vibronic structure was relatively well understood, the corresponding information for the ground-state was not. Riley *et*

*al.*¹⁸ applied the one-color resonant two-photon ionization (R2PI) technique to measure the $\tilde{A} \ ^2\text{E}'' \leftarrow \tilde{X} \ ^2\text{E}'$ transition of Ag_3 . There was a Jahn-Teller analysis that included linear and quadratic terms along with the spin-orbit interaction term. The fitting of the excited-state levels was empirical and led to a set of spectral parameters dramatically different than the previous values.¹⁷ The spin-orbit coupling parameter for the \tilde{A} state was found to be one order of magnitude higher. The excited-state intensity pattern was best simulated using a set of ground-state spectral parameters which, however, were not equally good for the ground state. Raman spectroscopy of matrix-isolated, mass-selected Ag_3 was reported by Moskovits *et al.*⁹⁶ The spectrum displayed rich vibronic structure. They derived a set of \tilde{X} -state spectral parameters similar to the previous values.¹⁷

It is difficult with experiment alone to provide a definite answer as to the nature of the Jahn-Teller distortion, dynamic or static. A suitable theoretical model needs to be constructed that characterizes the Jahn-Teller-distorted potential energy surface (PES) and is in agreement with the experimental observation. A reliable theoretical model may be constructed by use of high-level *ab initio* calculations.

In the following chapter we report and analyze previously¹⁴ acquired spectral results for Ag_3 . The resolved emission spectra from different vibronic levels of the \tilde{A} -state provide a detailed map of the \tilde{X} -state vibronic structure. These spectra have very complex vibronic structures, which require the aid of *ab initio* calculations for a proper interpretation. Previous calculations have neither reached a consensus on the nature of the Jahn-Teller distortion in Ag_3 , nor calculated many parameters

useful for spectral analysis; therefore we have undertaken a new series of calculations for the molecule with the explicit goal of predicting molecular parameters contained in the spectral analysis. Past work^{16,98} has presented theoretical approaches which we have extended⁹⁹ here with the express purpose of deriving the necessary spectral parameters for the analysis of the experimental spectra of Jahn-Teller-active molecules in their triangular configuration. In this chapter we apply these approaches for the previously observed, quite complicated, spectra of Ag₃.

Experimentally observed electronic spectra reveal not only Jahn-Teller-active vibrations but also other allowed transitions to totally symmetric fundamentals, overtones, and the like. The data in chapter 5 include emission spectra from several different \tilde{A} -state vibronic levels. These complementary spectra help assign the \tilde{X} -state vibronic levels, but only if the \tilde{A} -state vibronic assignments are known. Therefore we have performed calculations that help assign the \tilde{A} -state levels, as well as those of the \tilde{X} state.

The remainder of this chapter is arranged as follows. The Hamiltonian used to interpret the spectroscopic results is briefly reviewed. The molecular parameters contained therein are explicitly related to topographic features of the PES obtainable as cuts of C_{2v} symmetry from the *ab initio* calculations. Results from several calculations for the \tilde{A} and \tilde{X} state are given. The *ab initio* results are then used to predict specific molecular parameters relevant to the spectral analysis. Finally, the various

computational results are discussed, particularly with respect to their accuracy and usefulness for the spectral analysis. Chapter 5 contains the complete analysis of the spectra, using these calculations as the foundation of the analysis.

4.2 The Silver Trimer Potential Energy Surface and Jahn-Teller Effects

4.2.1 General Features

Jahn-Teller theory predicts that the \tilde{X}^2E' and \tilde{A}^2E'' electronic states of Ag_3 (D_{3h} symmetry) will interact with the e' vibration (see Fig. 4.1), leading to an adiabatic PES (APES) with a circular trough (the "Mexican hat") when plotted versus the two coordinates of the degenerate mode. A reduction in symmetry to C_{2v} results in vibrations of symmetry a_1 and b_2 . As the molecule vibrates along the a_1 mode, the C_{2v} symmetry is retained, but for the b_2 mode it is not.

The lowest Jahn-Teller-split PES sheet is characterized by two sets of three equivalent extrema when the quadratic Jahn-Teller effect due to the e' mode is considered. These may be either global minima or saddle points. The degeneracy point represents a local cusplike maximum of the APES and is a conical intersection. Figure 4.2 illustrates the Jahn-Teller distortion away from the D_{3h} geometry. A plot of the \tilde{X} - or \tilde{A} -state PES along the two Jahn-Teller degrees of freedom is given.

The spectroscopic problem at hand is to understand the observed structure in the $\tilde{A}^2E'' \leftarrow \tilde{X}^2E'$ electronic transition. This in turn corresponds to determining the po-

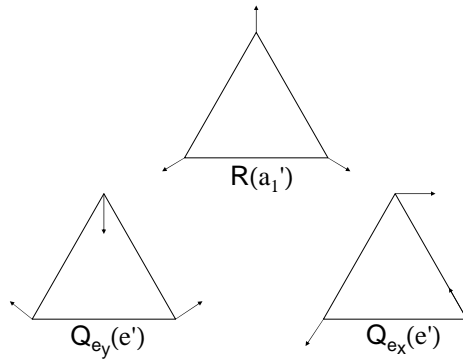


Figure 4.1: The symmetry displacements of a planar triatomic equilateral nuclear conformation. The displacements Q_{e_y} and Q_{e_x} are, respectively, the real and imaginary parts of the complex coordinate $Q_{e',\pm}$.

sitions of the vibronic levels within the \tilde{X} and \tilde{A} states. Consequently, any valid representation of the \tilde{A} and \tilde{X} state surfaces must yield vibronic structure consistent with the experimental results.

The primary computational goal is to calculate the potential energy curves along the C_{2v} cuts through the e' vibrational subspace of the ground- and excited-Jahn-Teller-split C_{2v} electronic states. These cuts will lie along the a_1 component of the e' vibration and they will also go though the potential minima of the lower APES of the \tilde{X}^2E' and \tilde{A}^2E'' states. The latter are expected to lie at opposite ends of the a_1 vibration and will correspond to C_{2v} triangular configurations with either elongated geometries or compressed ones along the in-plane z axis. The higher-energy potential

minima correspond to the saddle points and the lower ones to the global minima, while their energy difference is the barrier to pseudorotation around the moat. Of equal interest is the energy of Ag_3 at the D_{3h} cusp, since it is with reference to this energy that the total (linear and quadratic) stabilization energy is measured.

In effect, the fundamental goals of this theoretical work are to try to determine for the $\tilde{X}^2\text{E}'$ and $\tilde{A}^2\text{E}''$ states (1) the total Jahn-Teller stabilization (the energy difference between the conical intersection and the global minima); (2) the barrier to pseudorotation; (3) the geometries at the symmetric D_{3h} point, at the global minima, and at the saddle points, as well as the distances between them; and (4) the magnitude of the spin-orbit interaction.

4.2.2 Nuclear Displacement Coordinates

We start with an equilateral-triangle geometry with its vertices labeled starting from 1 at the apex of the triangle and increasing in a clockwise manner to 2 and 3 at its base.

Following ref.98, the nuclear displacement coordinates may be expressed as:

$$R[a_1] = \frac{1}{\sqrt{3}}(r_{12} + r_{13} + r_{23}), \quad (4.1)$$

$$Q_{e_x}[b_2] = \frac{1}{\sqrt{2}}(r_{12} - r_{13}), \quad (4.2)$$

$$Q_{e_y}[a_1] = \frac{1}{\sqrt{6}}(2r_{23} - r_{12} - r_{13}). \quad (4.3)$$

Their corresponding symmetries in the C_{2v} group are denoted in brackets. The nuclear displacement coordinate R describes the symmetric stretching vibration, while

Q_{e_x} and Q_{e_y} represent the bending mode with Q_{e_x} having asymmetric-stretch character at large displacements. Displacement in Q_{e_y} leads to either an obtuse or acute isosceles triangle. Distortion along Q_{e_x} leads to a structure with C_s symmetry.

The distortion of Ag_3 along the e' Jahn-Teller coordinates may be conveniently visualized if we define polar coordinates ρ and ϕ to span the e' irreducible representation:

$$Q_{e_x} = \rho \cos \phi \quad (4.4)$$

$$Q_{e_y} = \rho \sin \phi \quad (4.5)$$

where $\rho = \sqrt{(Q_{e_x})^2 + (Q_{e_y})^2}$ and $\tan \phi = (Q_{e_y}) / (Q_{e_x})$. The normal coordinates of the e' Jahn-Teller active vibrational mode $Q_{e',\pm}$ may also be taken to be the complex combinations of the (Q_{e_x}, Q_{e_y}) coordinates for this mode:

$$Q_{e',\pm} = Q_{e_y} \pm iQ_{e_x}. \quad (4.6)$$

(See also Figure 4.1.)

4.2.3 The Spectroscopic Model of the Jahn-Teller PES

The Jahn-Teller effect may be described by Q_{e_x} and Q_{e_y} , two orthogonal vectors that span the space of the single e' molecular distortion. As they constitute a subspace of the $3N-6$ normal coordinate space (Q_i), the Jahn-Teller coordinates may be completely described in terms of linear combinations of the normal coordinates. It is hence convenient to work in the normal coordinate system more specifically the normal coordinate system of the undistorted symmetric molecule.

The general Hamiltonian for our system is

$$\hat{\mathcal{H}} = \hat{\mathcal{H}}_T + \hat{\mathcal{H}}_{SO} + \hat{\mathcal{H}}_e \quad (4.7)$$

where $\hat{\mathcal{H}}_T$ is the nuclear kinetic energy, $\hat{\mathcal{H}}_{SO}$ is the spin-orbit coupling Hamiltonian, and $\hat{\mathcal{H}}_e$ is the electronic Hamiltonian. The spin-orbit coupling is expected to be non-zero for any open-shell orbitally degenerate electronic state. For Ag_3 the spin-orbit coupling is small but not negligible for the $\tilde{X}^2\text{E}'$ and $\tilde{A}^2\text{E}''$ states, so $\hat{\mathcal{H}}_{SO}$ should not be discarded. We shall confine ourselves here to an analysis that assumes a small effect for the spin-orbit coupling and we shall address its effect in the problem as a second step in Section 4.2.4.

We consider the PES for a doubly degenerate electronic state of the nominally D_{3h} Ag_3 . In ref. 100 we showed, as have others, that the PESs, V_{\pm} , of a Jahn-Teller-active molecule may be represented in terms of matrix elements of the electronic Hamiltonian, $\hat{\mathcal{H}}_e$, i.e.,

$$V_{\pm} = \left\langle \Lambda_{\pm} \left| \hat{\mathcal{H}}_e \right| \Lambda_{\pm} \right\rangle \pm \left(\left\langle \Lambda_{+} \left| \hat{\mathcal{H}}_e \right| \Lambda_{-} \right\rangle \left\langle \Lambda_{-} \left| \hat{\mathcal{H}}_e \right| \Lambda_{+} \right\rangle \right)^{1/2}, \quad (4.8)$$

where $\left\langle \Lambda_{+} \left| \hat{\mathcal{H}}_e \right| \Lambda_{+} \right\rangle = \left\langle \Lambda_{-} \left| \hat{\mathcal{H}}_e \right| \Lambda_{-} \right\rangle$ and Λ_{\pm} are complex wave functions related to the real electronic wave functions, Λ_a and Λ_b by $\Lambda_{\pm} = 1/\sqrt{2}(\Lambda_a \pm i\Lambda_b)$. The diagonal and off-diagonal terms of Eq. 4.8 for Ag_3 may be written, in a power series expansion,

$$\left\langle \Lambda_{+} \left| \hat{\mathcal{H}}_e \right| \Lambda_{+} \right\rangle = \sum_{r=+,-} \frac{1}{2} \lambda_{e'} |Q_{e',r}|^2 + \frac{1}{2} \lambda_{a'_1} |R|^2, \quad (4.9)$$

$$\begin{aligned} \left\langle \Lambda_{+} \left| \hat{\mathcal{H}}_e \right| \Lambda_{-} \right\rangle &= k_{e'} Q_{e',+} + \frac{1}{2} g_{e'} (Q_{e',-})^2 \\ &+ \frac{1}{2} b_{a'_1 e'} (Q_{e',+} R), \end{aligned} \quad (4.10)$$

where in Eqs. 4.9 and 4.10, the expansion has been truncated at second order. Equations 4.9 and 4.10 give the mathematical expressions of a parameterized spectroscopic potential. The parameters are the harmonic force constant of the e' or a'_1 mode represented, respectively, by $\lambda_{e'}$ and $\lambda_{a'_1}$, the linear Jahn-Teller coupling coefficient due to the Jahn-Teller-active e' mode, $k_{e'}$, the Jahn-Teller quadratic coupling coefficient, $g_{e'}$, and the quadratic coupling coefficient between the degenerate e' coordinate and the non-degenerate a'_1 coordinate, called¹⁰¹ the bilinear coupling coefficient, $b_{a'_1 e'}$. These parameter definitions are summarized in Table 4.1.

We mainly consider the linear Jahn-Teller term $k_{e'}$, and the quadratic Jahn-Teller term $g_{e'}$. The only remaining nonzero term is the bilinear term $b_{a'_1 e'}$, which although we have not rigorously calculated it, we have approximate estimates for it for the \tilde{X} and \tilde{A} states. It has previously been shown by Köppel *et al.*¹⁰² that this bilinear term has little effect on the vibronic spectrum of CH₃O. Additionally, the experimental results for C₅(H/D)₅¹⁰³ and for the closely related molecules C₆(H/F)₆⁺ and C₆H₃F₃⁺¹⁰⁴ have been successfully analyzed without invoking this term. The primary goal of this work is to provide reasonable estimates of the most critical molecular parameters, which are the Jahn-Teller constants. These will be used to initiate the vibronic analysis of the experimental spectra of the \tilde{A}^2E'' and \tilde{X}^2E' states.

The topography of the PES is quite dependent on the symmetry of the normal coordinate along which one views the surface. The entire PES, neglecting the bilinear Jahn-Teller term, may be defined by the following equation

$$V_{\pm} = V_{\pm, e'}^{l,q} + V_{\pm, a'_1}^h, \quad (4.11)$$

Symbol	Description	Definition
$\lambda_{e'}$	harmonic force constant of the Jahn-Teller active e' mode	$\frac{\partial^2}{\partial Q_{e',+} \partial Q_{e',-}} \left(\langle \Lambda_{\pm} \hat{\mathcal{H}}_e \Lambda_{\pm} \rangle \right)_0$
$\lambda_{a'_1}$	harmonic force constant of the Jahn-Teller inactive a'_1 mode	$\frac{\partial^2}{\partial R^2} \left(\langle \Lambda_{\pm} \hat{\mathcal{H}}_e \Lambda_{\pm} \rangle \right)_0$
$k_{e'}$	linear Jahn-Teller coupling coefficient	$\frac{\partial}{\partial Q_{e',\pm}} \left(\langle \Lambda_{\pm} \hat{\mathcal{H}}_e \Lambda_{\mp} \rangle \right)_0$
$g_{e'}$	quadratic Jahn-Teller coupling coefficient	$\frac{\partial^2}{\partial Q_{e',\pm}^2} \left(\langle \Lambda_{\pm} \hat{\mathcal{H}}_e \Lambda_{\mp} \rangle \right)_0$
$b_{a'_1 e'}$	bilinear Jahn-Teller coupling coefficient	$\frac{\partial^2}{\partial R \partial Q_{e',\pm}} \left(\langle \Lambda_{\pm} \hat{\mathcal{H}}_e \Lambda_{\mp} \rangle \right)_0$

Table 4.1: The Jahn-Teller coupling coefficients that parameterize the effective spectroscopic Hamiltonian and their relationships to the terms of the Taylor series expansion of the potential.

where

$$\begin{aligned} V_{\pm,e'}^{l,q} &= \frac{1}{2}\lambda_{e'}\rho^2 \pm k_{e'}\rho \left(1 + \frac{2g_{e'}\rho}{k_{e'}} \cos(3\phi) + \frac{g_{e'}^2\rho^2}{k_{e'}^2}\right)^{1/2} \\ &\approx \frac{1}{2}\lambda_{e'}\rho^2 \pm [k_{e'}\rho + g_{e'}\rho^2 \cos(3\phi)], \end{aligned} \quad (4.12)$$

$$V_{\pm,a'_1}^h = \frac{1}{2}\lambda_{a'_1}R^2, \quad (4.13)$$

following the polar coordinate representation of the doubly degenerate normal coordinate. In the last equality of Eq. 4.12 the expansion of the radical has been truncated at the quadratic term in ρ . With the assumption that $k_{e'}$ and $g_{e'}$ are positive, the plus sign in the above equations corresponds to the upper sheet of the PES and the minus sign to the lower sheet. Then $V_{\pm,e'}^{l,q}$ adds the linear and quadratic Jahn-Teller term to the harmonic oscillator to describe the linear and quadratic Jahn-Teller PES seen along the e' normal coordinate. V_{\pm,a'_1}^h refers to the harmonic oscillator potential seen along the single Jahn-Teller-inactive normal coordinate.

We introduce the previously defined^{100,103} $\omega_{e,e'}$, the harmonic vibrational frequency of the e' mode evaluated at the conical intersection of the PES, $D_{e'}$, the linear Jahn-Teller coupling constant, and $K_{e'}$, the quadratic Jahn-Teller coupling constant, and also define and use here the bilinear Jahn-Teller coupling constant $B_{a'_1 e'}$

$$\omega_{e,e'} = \frac{1}{2\pi c} \left(\frac{\lambda_{e'}}{M_{e'}} \right)^{1/2}, \quad (4.14)$$

$$D_{e'} = \frac{k_{e'}^2}{2\hbar} \left(\frac{M_{e'}}{\lambda_{e'}^3} \right)^{1/2}, \quad (4.15)$$

$$K_{e'} = \frac{g_{e'}}{\lambda_{e'}}, \quad (4.16)$$

and

$$B_{a'_1 e'} = \frac{b_{a'_1 e'}}{\sqrt{\omega_{e,e'} \omega_{e,a'_1}}} \quad (4.17)$$

where $M_{e'}$ corresponds to the reduced mass of the e' vibrational mode of Ag_3 . If $g_{e'}$ is positive the minima about the moat will be at $\phi = 0, \frac{2\pi}{3}, \frac{4\pi}{3}$ and the maxima will be at $\phi = \frac{\pi}{3}, \pi, \frac{5\pi}{3}$. A negative value of $g_{e'}$ (relative to $k_{e'}$) generates a $\frac{2\pi}{3}$ rotation in the e' vibrational space. This in turn leads to a reversal on the values of ϕ for the maxima and minima. We can derive the following equations¹⁶ by taking the derivative of Eq. 4.12 with respect to ρ and setting it to zero with $\phi = 0$ and $\frac{\pi}{3}$.

$$\rho_{e'}^0 = \frac{k_{e'}}{\lambda_{e'}(1 - 2K_{e'})} = \frac{1}{(1 - 2K_{e'})} \left(\frac{D_{e'} \hbar}{\pi c M_{e'} \omega_{e,e'}} \right)^{1/2} \quad (4.18)$$

$$E_{e'}^0 = -\frac{k_{e'}^2}{2\lambda_{e'}(1 - 2K_{e'})} = -\frac{2\hbar\pi c D_{e'} \omega_{e,e'}}{(1 - 2K_{e'})} \quad (4.19)$$

$$\rho_{e'}^{\pi/3} = \frac{k_{e'}}{\lambda_{e'}(1 + 2K_{e'})} = \frac{1}{(1 + 2K_{e'})} \left(\frac{D_{e'} \hbar}{\pi c M_{e'} \omega_{e,e'}} \right)^{1/2} \quad (4.20)$$

$$E_{e'}^{\pi/3} = -\frac{k_{e'}^2}{2\lambda_{e'}(1 + 2K_{e'})} = -\frac{2\hbar\pi c D_{e'} \omega_{e,e'}}{(1 + 2K_{e'})} \quad (4.21)$$

$$\Delta E_{e'}^B = \left| E_{e'}^0 - E_{e'}^{\pi/3} \right|, \quad (4.22)$$

where the superscripts 0 and $\frac{\pi}{3}$ indicate solutions at $\phi = 0$ and $\phi = \frac{\pi}{3}$, respectively. The distance from the symmetric point to the distorted potential energy minima is given by $\rho_{e'}^0$ and $\rho_{e'}^{\pi/3}$. The total linear and quadratic Jahn-Teller stabilization energy is calculated for the angles that correspond to the global minima. It is the energy distance between their positions and the conical intersection, taking the latter to be zero. The total Jahn-Teller stabilization energy is given, within this approximation,

by $E_{e'}^0$ or $E_{e'}^{\pi/3}$ depending on whether $\phi = 0$ or $\phi = \frac{\pi}{3}$ gives the largest energy, with the other angle corresponding to the saddle point. The barrier to pseudorotation around the moat is defined by $\Delta E_{e'}^B$ in Eq. 4.22.

Relationship of the Spectroscopic Model and *ab initio* Results

The slice along the \mathcal{Q}_{e_y} coordinate of the PES (Fig. 4.2) represents a cross-section of the PES that preserves the C_{2v} symmetry. It also bisects the most important regions of the PES; the global minimum and local maximum and the conical intersection. Additional information about the atomic displacements that one must apply to the symmetric configuration to reach the global minimum and saddle point may be extracted. These correspond to the distortion vectors ρ taken along the \mathcal{Q}_{e_y} coordinate. The remainder of the section will detail the mathematics used to implement this methodology.

To further simplify Equations 4.12 for this cross-section we choose for the angle $\phi = 0$. The addition and subtraction of the resultant equations lead to

$$V_+ + V_- \approx \lambda_{e'} \rho^2 \quad (4.23)$$

$$(V_+ - V_-)/2 \approx k_{e'} \rho + g_{e'} \rho^2, \quad (4.24)$$

where V_{\pm} is measured relative to the energy at the conical intersection, and the distortion parameter ρ measures the atomic displacements from the same point. The barrier to pseudorotation around the moat, $\Delta E_{e'}^B$, may be obtained from

$$\Delta E_{e'}^B \approx \frac{1}{2} \lambda_{e'} (\rho_{max}^2 - \rho_{min}^2) + k_{e'} (\rho_{max} + \rho_{min}) + g_{e'} (\rho_{max}^2 + \rho_{min}^2), \quad (4.25)$$

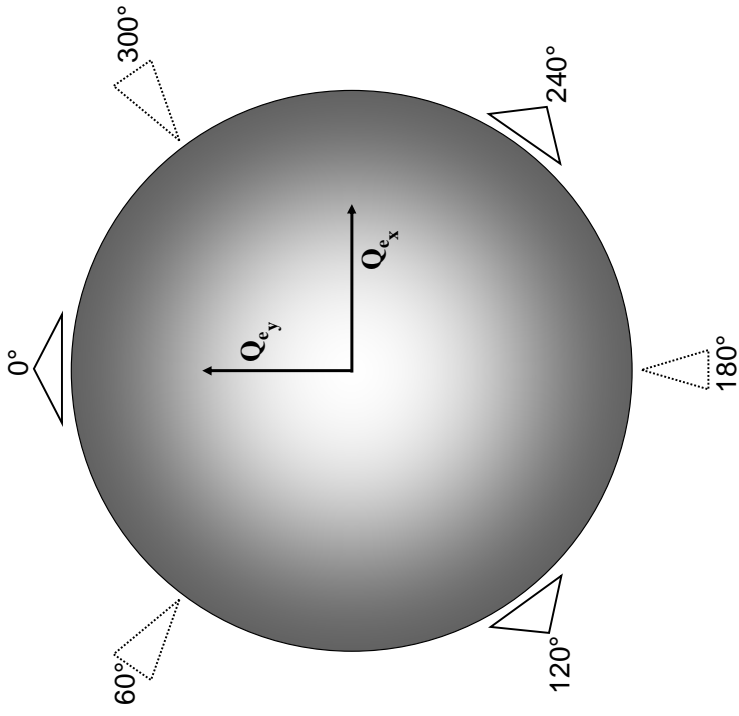


Figure 4.2: Downward-looking view of the linear and quadratic Jahn-Teller distorted lower PES appropriate for Ag_3 . The coordinates Q_{e_x} and Q_{e_y} denote the two unique dimensions along which motion resolves the degeneracy of the conical intersection corresponding to the $^2\text{E}'$ or $^2\text{E}''$ state. Around the perimeter of the figure are pictures of the distorted Ag_3 geometries for the corresponding value of the pseudo-rotation phase angle ϕ . The quadratic Jahn-Teller effect introduces a ϕ dependence in the energy. The radius of the pseudo-rotation circle is given by the magnitude of the distortion parameter ρ . The pictures are schematic only and do not attempt to represent all details of the distortion, e.g., the exact positions of the Ag atoms.

where ρ_{min} and ρ_{max} point to the global minimum and local maximum of the Jahn-Teller distorted PES. (Notice that in this formalism ρ_{max} may now attain a negative sign.)

Equations 4.23 and 4.24 will result in reliable estimates for $\lambda_{e'}$ and $k_{e'}$, based on a grid of PES points lying in the vicinity of the conical intersection. Equation 4.25 may be used for the calculation of the quadratic Jahn-Teller coefficient. It gives the barrier to pseudorotation from the energy difference between the extrema points of the Jahn-Teller distorted PES. This energy difference is a known parameter from our *ab initio* calculations. It builds up mainly due to the quadratic Jahn-Teller effect. It makes use of directly available topographical characteristics of the PES like ρ_{min} and ρ_{max} which can be calculated with greater reliability within our approach. Use of this equation avoids the inherently greater computational errors arising in using regions of the PES that are farther from the symmetric point; $g_{e'}$, as a quadratic constant, is normally smaller relative to $k_{e'}$ and is susceptible to greater error especially when it attains values that are at or near the limit of the reliability of the calculations. We place greater confidence in calculating the quadratic Jahn-Teller constant in this way. Also, by computing the ratio of Eqs. 4.19 and 4.21 we can calculate the value of its unitless expression $K_{e'}$, i.e.,

$$\frac{E_{e'}^0}{E_{e'}^{\pi/3}} = \left(\frac{1 + 2K_{e'}}{1 - 2K_{e'}} \right). \quad (4.26)$$

An obvious last alternative would be to undergo a direct evaluation of the constants using the definitions given in Table 4.1. In principle this is possible with very high

accuracy wave functions, however one should not underestimate the extreme difficulty of such calculations basically due to the wave-function error and therefore failure to obey the Hellmann-Feynman theorem.^{105,106}

We sampled points of D_{3h} symmetry. As the breathing mode of Ag_3 does not lower the symmetry of the molecule the potential along the a'_1 vibration that crosses the conical intersection necessarily corresponds to a hypothetical D_{3h} cut of the PES. The harmonic force constant of a'_1 at the conical intersection was calculated based on a quadratic fit and by using a grid of points lying in the vicinity of the conical intersection.

To estimate $b_{a'_1e'}$ in the \tilde{X} and \tilde{A} states, we computed the potential energy surface along Q_{e_y} and R. In this approach we imposed the geometry restriction that the sum of the sides of the isosceles triangle equals the sum of the sides of the equilateral triangle.

With the theoretically calculated values of $\lambda_{a'_1}$, $\lambda_{e'}$, $k_{e'}$, $g_{e'}$ and $b_{a'_1e'}$ at hand we can easily calculate the harmonic frequencies of the a'_1 and e' modes based on Eq. 4.14 as well as the Jahn-Teller molecular parameters $D_{e'}$, $K_{e'}$ and $B_{a'_1e'}$ using Eqs. 4.15, 4.16 and 4.17. The frequencies of the a'_1 and e' modes at the stationary points were not estimated since they are not directly related to the analysis of the experimental spectra. While the harmonic frequency of the totally symmetric mode at the conical intersection could be useful in such analyses, the one due to the Jahn-Teller active mode is of little direct value owing to the convoluted topology of its vibronic space.

4.2.4 Spin-Orbit Interaction

Ag_3 is a heavy molecule and hence subject to relativistic effects which makes $\hat{\mathcal{H}}_{SO}$ non-negligible. The spin-orbit coupling interaction partially quenches the Jahn-Teller effect (and vice versa), thus a suitable theoretical treatment is needed to account for it. Following Barckholtz's and Miller's methodology¹⁶ the potentials in the presence of linear and quadratic Jahn-Teller effects and spin-orbit coupling for a degenerate mode, $V_{\pm,e'}^{l,q,SO}$, are given by

$$\begin{aligned} V_{\pm,e'}^{l,q,SO} &= \frac{1}{2}\lambda_{e'}\rho^2 \pm \frac{1}{2}\left[(\alpha\zeta_e)^2 + 4k_{e'}^2\rho^2 + 8g_{e'}k_{e'}\rho^3\cos(3\phi)\right]^{\frac{1}{2}} \\ &\approx \frac{1}{2}\lambda_{e'}\rho^2 \pm \left[\frac{1}{2}(\alpha\zeta_e) + \frac{k_{e'}^2\rho^2}{(\alpha\zeta_e)} + \frac{2g_{e'}k_{e'}\cos(3\phi)\rho^3}{(\alpha\zeta_e)}\right], \end{aligned} \quad (4.27)$$

where in the last equality the expansion of the radical has been truncated at terms cubic in ρ . Due to the fact that the projection Σ of the electron spin S on the C_3 axis is still approximately preserved, the eigenvalues $V_{\pm,e'}^{l,q,SO}$ are each degenerate. The product $\alpha\zeta_e$ corresponds to a parameterized expression for the spin-orbit Hamiltonian $\hat{\mathcal{H}}_{SO}$, where ζ_e is the projection of the electronic orbital angular momentum on the principal axis and α is the spin-orbit coupling constant.¹⁶

Relationship of the Spectroscopic Model and *ab initio* Results

We outline here the approach that we follow to theoretically calculate the effect of the spin-orbit interaction in Ag_3 . It is effectively represented by the traditional spectroscopic spin-orbit coupling parameter $\alpha\zeta_e$. We discuss the relationship between the theoretically determined and spectroscopically approximated expressions for the spin-orbit interaction. The primary objective is to obtain a theoretically calculated

estimate for the spin-orbit coupling that is also, in essence, compatible with the parameterized expression $\alpha\zeta_e$ and hence to make use of this in our spectroscopic model.

Once the the spin-orbit coupling is considered in the problem, the two surfaces of the Jahn-Teller distorted PES no longer intersect at $\rho = 0$; they become separated by an energy difference that is directly dependent upon the magnitude of the spin-orbit coupling. The two curves present the characteristics of an avoided crossing. Assuming a moderate spin-orbit interaction in the presence of Jahn-Teller effects, one would anticipate the upper surface to exhibit a minimum at the symmetric configuration and the lower one to have a maximum at the same point of the PES.

The addition and subtraction of Eqs. 4.27, for $\phi = 0$, give

$$V_+ + V_- \approx \lambda_{e'}\rho^2 \quad (4.28)$$

$$(V_+ - V_-) \approx (\alpha\zeta_e) + \frac{1}{(\alpha\zeta_e)} [2k_{e'}^2\rho^2 + 4g_{e'}k_{e'}\rho^3]. \quad (4.29)$$

Equation 4.28 suggests that the e' harmonic force constant may be calculated independent of the presence of the spin-orbit coupling. Equation 4.29 clearly suggests that the energy difference between the Jahn-Teller-split potential energy curves due to the presence of the spin-orbit interaction corresponds in principle to $\alpha\zeta_e$. While this statement is in general strictly true only at a first approximation, it is almost exactly applicable between the \tilde{X}^2E' - and \tilde{A}^2E'' -state-Jahn-Teller-split PESs of Ag_3 ; a reduction by $\alpha\zeta_e$ in the energy difference between the theoretically calculated (in the presence of spin-orbit effects) Jahn-Teller PESs readily verifies the above observation. The spin-orbit interaction that we report in Section 4.4 for the \tilde{X}^2E' and \tilde{A}

$^2\text{E}''$ states refers to $\alpha\zeta_e$. It will be used as an effective spin-orbit parameter in the calculation of the spin-vibronic levels in the $\tilde{X}\ ^2\text{E}'$ and $\tilde{A}\ ^2\text{E}''$ states of Ag_3 in chapter 5.

The spin-orbit coupling in the valence shell of Ag_3 is addressed by the valence spin-orbit operators and was calculated by the COLUMBUS suite of programs.⁵² The spin-orbit operators include the (large) spin-orbit interactions of the valence electrons with the nucleus and with the core electrons as well as an approximation to the (small) spin-orbit interaction between the valence electrons. To include or omit the spin-orbit operators in the calculation is an option for the user in COLUMBUS. To estimate the spin-orbit effects of Ag_3 one simply needs to carry out the calculation twice, i.e. in the absence and in the presence of the spin-orbit operators. Once they have been included, the calculation may be carried out in a single step, with no implicit or explicit assumptions about the size of the spin-orbit interaction compared to the other interactions, and within a larger configuration space.

4.3 Calculational Details

4.3.1 Electronic Structure Calculations

All of the computations were carried out with relativistic effective core potentials (RECPs) that retained the outer $4s^24p^64d^{10}5s^1$ shells of the silver atoms in the valence space, replacing the remaining 28 electrons by RECPs. Hence 57 electrons were explicitly treated in the calculations for Ag_3 . The AREPs and spin-orbit operators

were taken from the work of Christiansen and coworkers.³⁵ We used our newly developed basis set of Ag which corresponds to a generally contracted valence Gaussian basis set. (See Section 4.3.2.)

The ground- and excited-state electronic structures are characterized by 28 doubly occupied MOs. These orbitals span 11 a_1 , 4 a_2 , 5 b_1 , and 8 b_2 orbitals in C_{2v} symmetry. This leaves a total of 87 other MOs to be used by the unpaired electron and in describing correlation. Although the \tilde{X}^2E' state of Ag_3 arises from the $4d^{10}5s^1$ shells of the silver atoms, \tilde{A}^2E'' arises from the promotion of 1 electron from an e' MO predominantly $5s$ in atomic character to an e'' MO predominantly $5p$ in character. All calculations were performed in the C_{2v} group and C_{2v}^2 double group. Single-point calculations were conducted at the SCF, CISD and SOCISD levels of theory with the COLUMBUS suite of programs.⁵² The MOs for the \tilde{X}^2E' state were determined by carrying out an SCF calculation using the average energy expression for the $a_1^1 2A_1$ and $b_2^1 2B_2$ states so that the MOs would be of equal quality for the Jahn-Teller-split states. The same approach was used for the \tilde{A}^2E'' state. This approach avoids symmetry breaking problems in the electronic wave functions; the absolute energies of the Jahn-Teller-split PESs can now be directly compared, as a consequence of the fact that they may be represented (or theoretically calculated) in an equivalent manner.

The PES points of the potential energy curves were determined after a Hartree-Fock geometry optimization for a C_{2v} triangular configuration, hence Figures 4.3, 4.4 and 4.5 for the \tilde{X}^2E' state, and 4.6 and 4.7 for the \tilde{A}^2E'' state. Figure 4.6 presents similar information but for a CISD geometry optimization.

Ag_3 $^2\text{E}'$ -State e' potentials along the C_{2v} PES cut at the CISD level

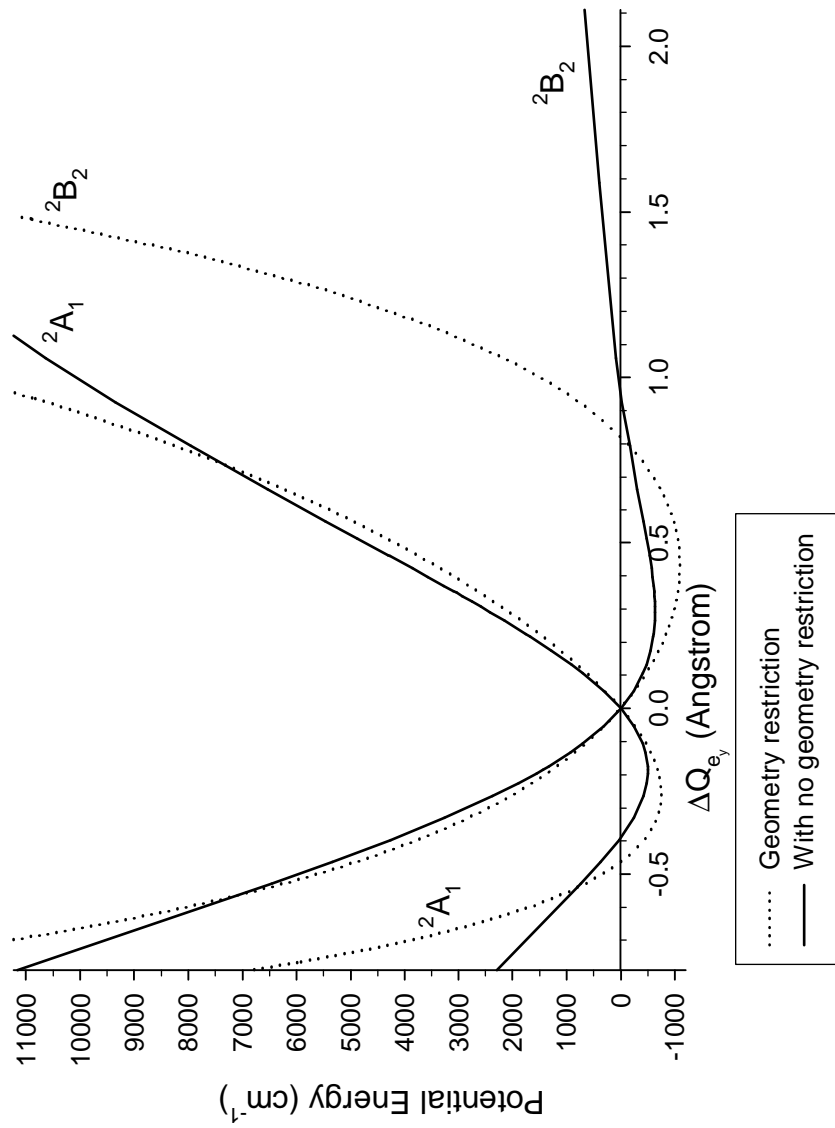


Figure 4.3: Ag_3 potential energy curves for the $^2\text{A}_1$ and $^2\text{B}_2$ components of the \tilde{X} $^2\text{E}'$ state along the C_{2v} coordinate Q_{e_y} of the single Jahn-Teller active \tilde{X} -state e' vibrational mode.

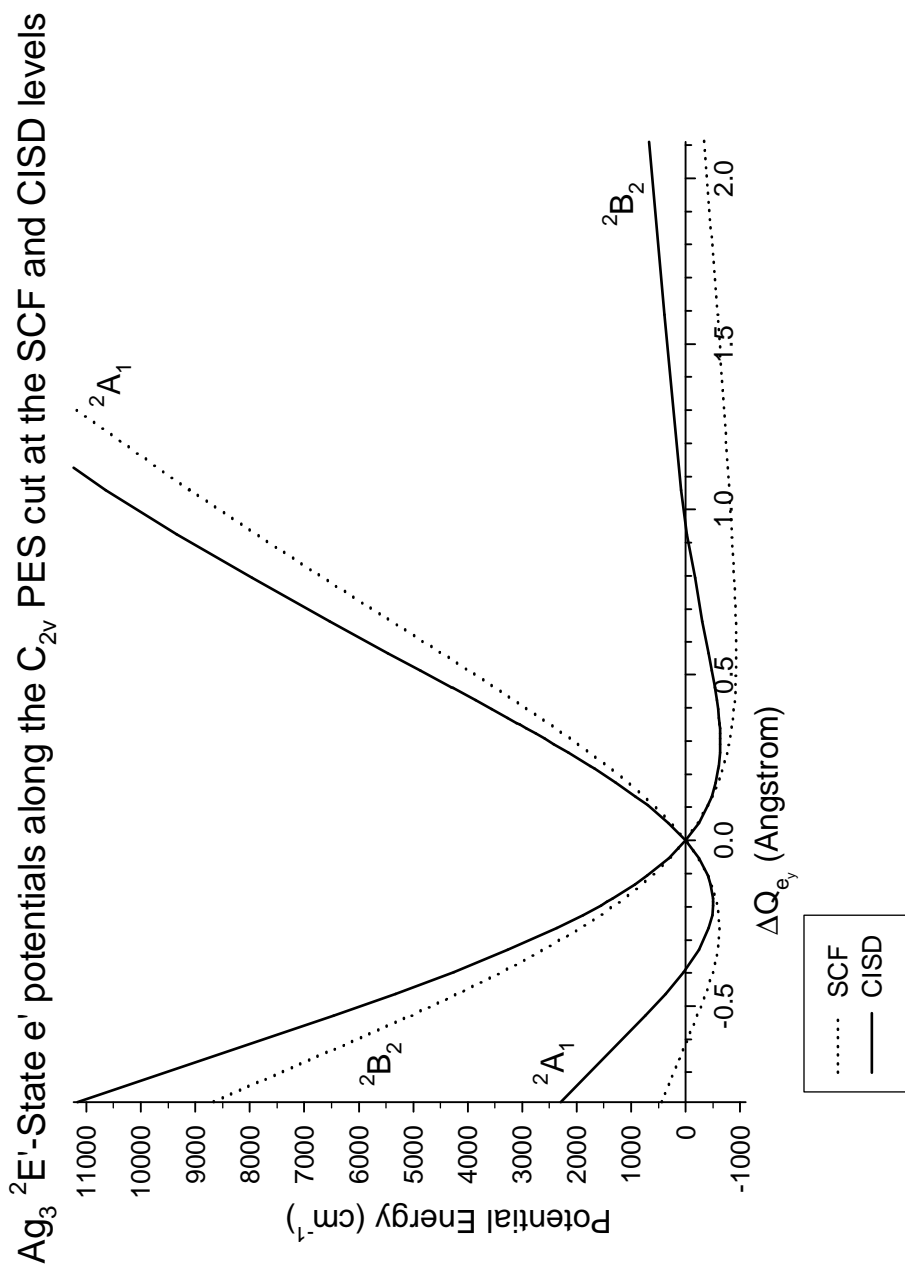


Figure 4.4: Ag₃ potential energy curves at the SCF and CISD levels of theory for the ²A₁ and ²B₂ components of the \tilde{X} ²E' state along the C_{2v} coordinate Q_{e_y} of the single Jahn-Teller active \tilde{X} -state e' vibrational mode.

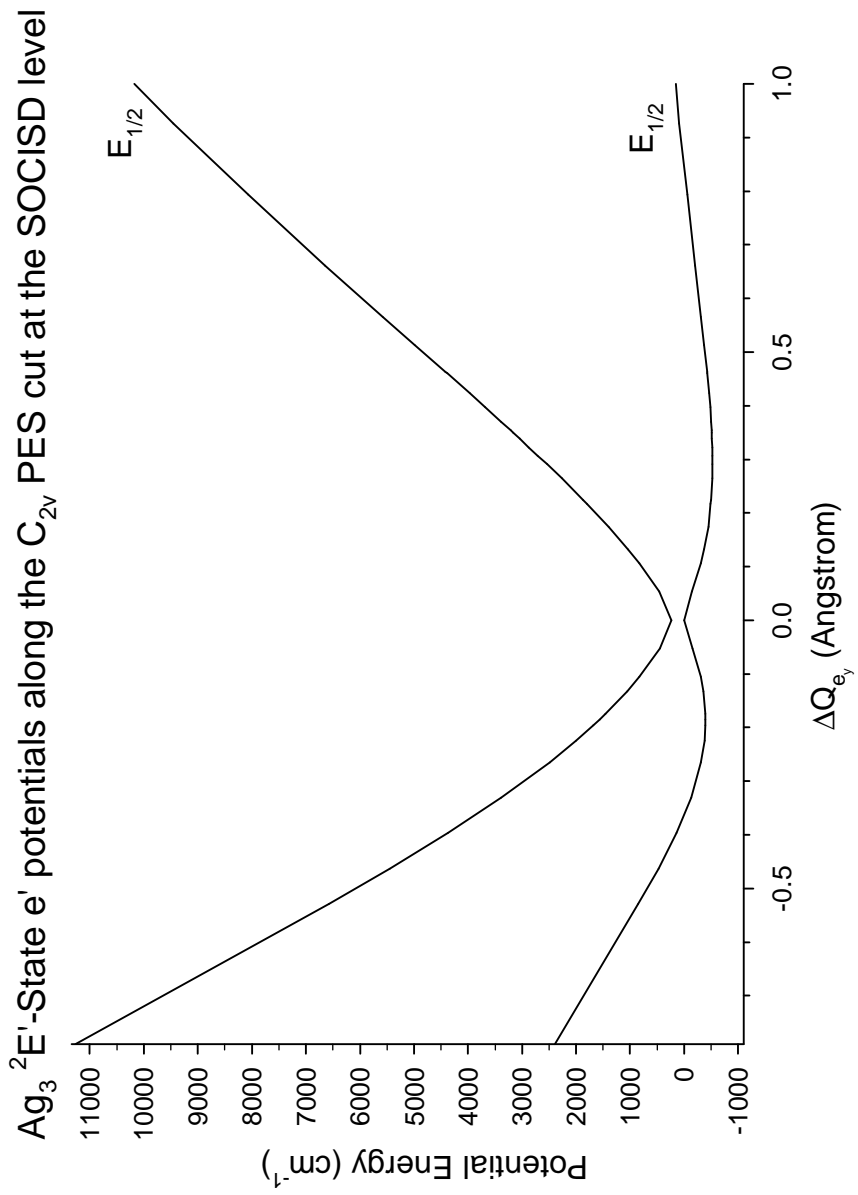


Figure 4.5: Ag_3 potential energy curves at the SOCISD level of theory for the $^2\text{A}_1$ and $^2\text{B}_2$ Jahn-Teller components of the $\tilde{X}^2\text{E}'$ state along the C_{2v} coordinate Q_{e_y} of the single Jahn-Teller active \tilde{X} -state e' vibrational mode.

Ag_3 $^2\text{E}''$ -State e' potentials along the C_{2v} PES cut at the SCF and CISD levels

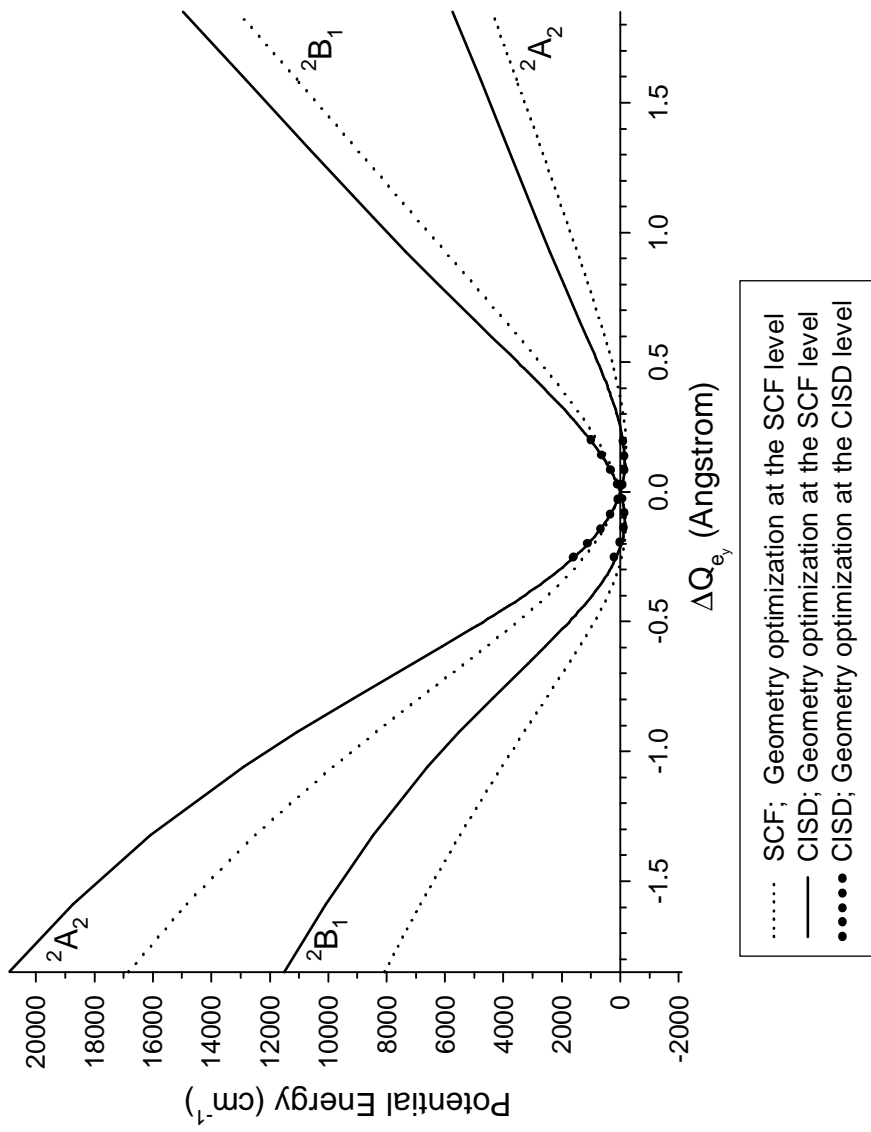


Figure 4.6: Ag_3 potential energy curves at the SCF and CISD levels of theory for the $^2\text{A}_2$ and $^2\text{B}_1$ components of the \tilde{A} $^2\text{E}''$ state along the C_{2v} coordinate Q_{e_y} of the single Jahn-Teller-active \tilde{A} -state e' vibrational mode.

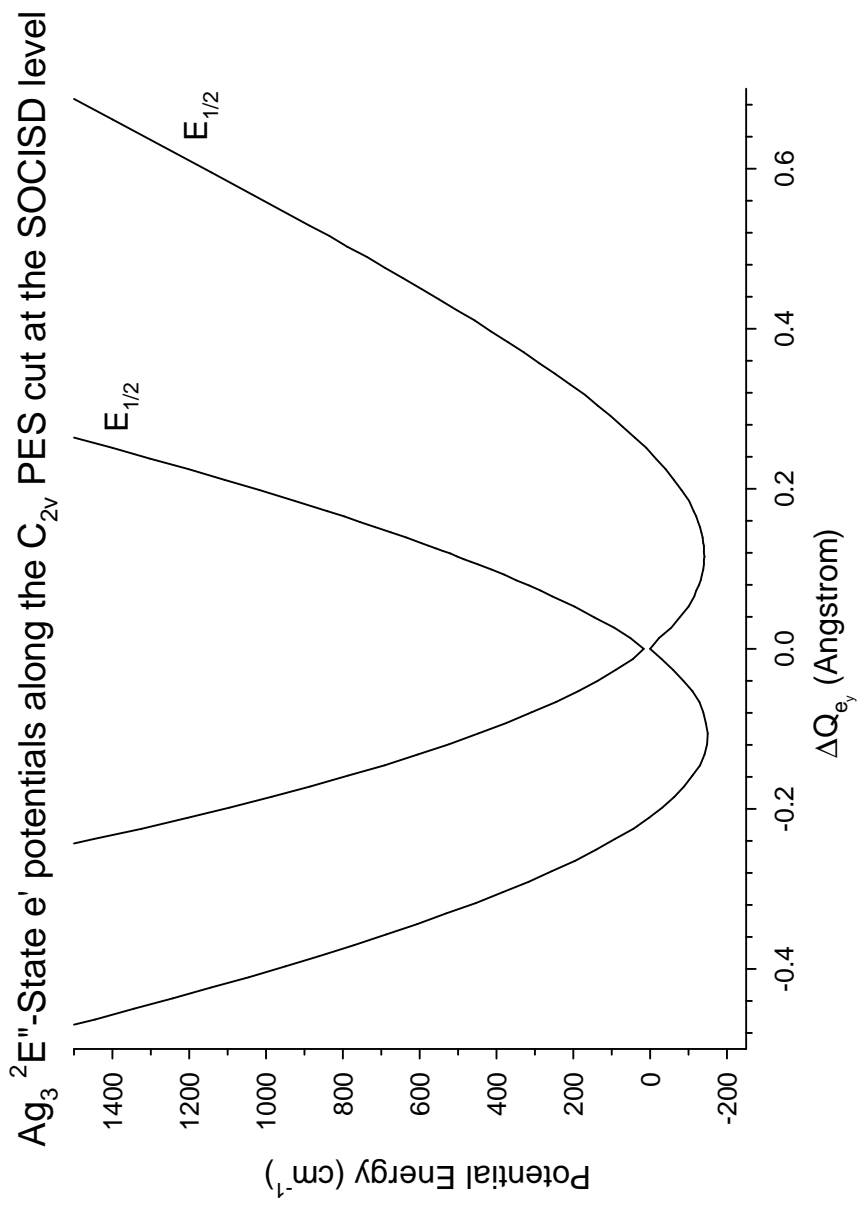


Figure 4.7: Ag_3 potential energy curves at the SOCISD level of theory for the $^2\text{A}_2$ and $^2\text{B}_1$ Jahn-Teller components of the $\tilde{A}^2\tilde{\text{E}}''$ state along the C_{2v} coordinate Q_{e_y} of the single Jahn-Teller-active \tilde{A} -state e' vibrational mode.

The single-point calculations at the energy minima were done with the MRSDCI (Multireference Singles and Doubles Configuration Interaction) method leading to correlated relative energies. The CI wave functions were optimized in a direct-CI iterative approach,^{107,108} employing the Davidson diagonalization method.¹⁰⁹ The Davidson correction^{110–114} was not incorporated. All 57 electrons were correlated by including all single and double excitations from the reference electron configurations, leading to ≈ 3.9 million configuration state functions (CSFs). No virtual orbitals were omitted. Either one or two roots were converged per calculation.

A fair number of additional single-point CISD calculations were performed with the express purpose of investigating the possibility of pseudo-Jahn-Teller mixing between the \tilde{X}^2E' state and nearby excited electronic states of Ag_3 . These may only exhibit $^2A'_1$, $^2A'_2$ and $^2E'$ symmetries. They all correspond to molecular analogues of the atomic $5s \rightarrow 5p$ electron excitation. The Type II potential energy curves of Fig. 4.8 were calculated to include this correlation. No virtual MOs were deleted prior to the CI step. Two roots were converged per calculation. Approximately 16 million CSFs were used. No symmetry-breaking problems occurred.

Additional CISD energy calculations were performed for the \tilde{A}^2E'' state; the list of references was expanded to include one additional MO of b_1 symmetry. This MO effectively corresponds to the C_{2v} symmetry analogue of the only excited electronic state lying lower than \tilde{A}^2E'' that exhibits common C_{2v} spatial symmetry with one of

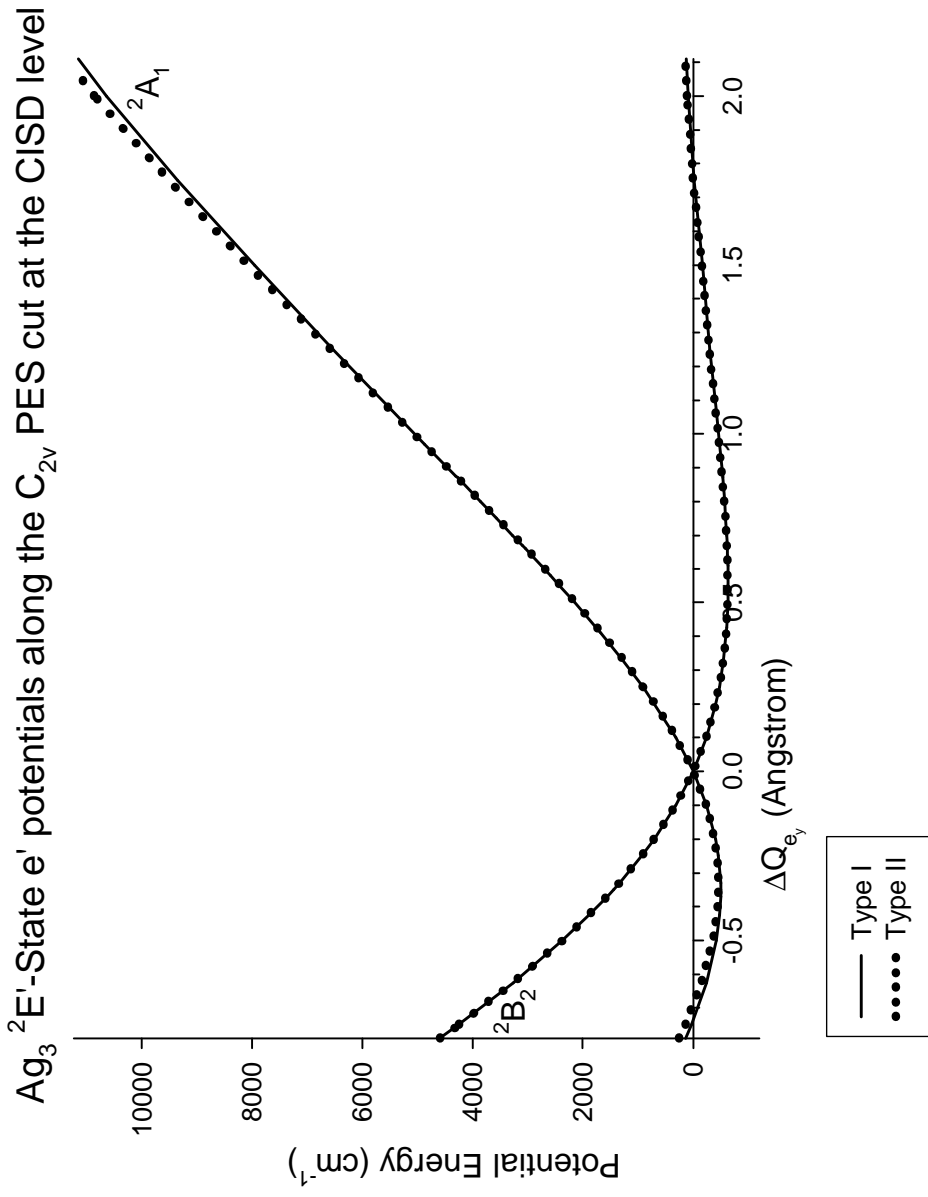


Figure 4.8: Ag₃ potential energy curves for the ²A₁ and ²B₂ components of \tilde{X} ²E' along the coordinate Q_{e_y} of the e' vibrational mode. The curves Type I and Type II correspond, in respect, to CISD energy calculations that explicitly include or omit in the list of correlating MOs those that give rise to ²A'₁, ²E', ²E', ²A'₂ and ²A'₁.

the Jahn-Teller-split electronic components arising from it. Approximately 9 million CSFs were used. To reach the excited state of interest, at least two roots were requested for the ${}^2\text{B}_1$ calculation. No symmetry-breaking problems occurred.

The spin-orbit CISD methodology (SOCISD) was used to measure the effect of the spin-orbit interaction on the $\tilde{X} \, {}^2\text{E}'$ - (Fig. 4.5) and $\tilde{A} \, {}^2\text{E}''$ -state (Fig. 4.7) Jahn-Teller-split potential energy curves. The SOCISD calculations include electron correlation and spin-orbit effects variationally in a multireference configuration space constructed in the C_{2v} double group of Ag_3 . The SOCISD calculations extracted at least two roots. A number of ≈ 48 million CSFs is generated for the spin-orbit relativistic computations for the $\tilde{X} \, {}^2\text{E}'$ and $\tilde{A} \, {}^2\text{E}''$ states.

The a'_1 vibrational force constants (harmonic frequencies) of the $\tilde{X} \, {}^2\text{E}'$ and $\tilde{A} \, {}^2\text{E}''$ states were calculated at the CISD level of theory imposing an equilateral geometry constraint. The two Jahn-Teller-split-state-averaged MOs were correlated in each case. In a second step we considered mixing between the $\tilde{X} \, {}^2\text{E}'$ state and several other energetically close excited states. For the $\tilde{X} \, {}^2\text{E}'$ state, the CISD calculations were repeated correlating electrons in an additional number of MOs; these span the following electronic states ${}^2\text{A}''_2$ (${}^2\text{B}_1$), ${}^2\text{A}'_1$ (${}^2\text{A}_1$), ${}^2\text{E}'$ (${}^2\text{A}_1 \oplus {}^2\text{B}_2$), ${}^2\text{E}''$ (${}^2\text{A}_2 \oplus {}^2\text{B}_1$), ${}^2\text{E}'$ (${}^2\text{A}_1 \oplus {}^2\text{B}_2$), ${}^2\text{A}'_1$ (${}^2\text{A}_1$), and ${}^2\text{A}'_2$ (${}^2\text{B}_2$). (The spatial electronic symmetries within parentheses are for the C_{2v} symmetry reduction.) The Hartree-Fock ground-state MOs were used as an initial guess to describe the excited-state MOs. No virtual orbitals were omitted. The length of the CI expansion now reached ca. 16 million. No symmetry-breaking problems were observed. We repeated the same calculations

for the two excited states of $^2E'$ symmetry that lie the closest to $\tilde{A} \ ^2E''$, correlating the electron in the excited-state MOs particular to each case. For the $\tilde{A} \ ^2E''$ state, similar work was not undertaken; while electron excitation from the atomic $4d$ shells of Ag may lead to excited electronic states with $^2E''$ symmetry, the correlation of MOs with principal or significant $4d$ atomic character was not pursued.

A large series of single-point calculations was carried out at geometries along the previously described normal mode vectors. To that effect, and to further speed up the calculations, the hundreds of input files necessary for the calculation of the potential energy curves were run as batch jobs.

4.3.2 Basis-Set Construction

The basis set for Ag was constructed having in mind three general considerations; (1) the p-set should be sufficiently flexible to adequately describe the $\tilde{A} \ ^2E''$ state, (2) the d-set may be important in treating electron correlation, and (3) the basis set should have an economical size.

The excited-state of interest arises from an electron excitation from the $5s$ to the $5p$ atomic orbital (AO) of Ag. Our effort focused on the development of a basis set that would be adequate to describe the $\tilde{A} \ ^2E''$ and $\tilde{X} \ ^2E'$ states and at an equivalent level of approximation.

The final form of the basis set for silver is displayed in Table 4.2. We have developed a (contracted Gaussian) AO basis set in a correlation-consistent (cc) manner^{44,47} and it corresponds to a polarized valence double- ζ quality (cc-pVDZ) set. The resulting Ag basis set is of $(5s5p5d1f)/[5s4p3d1f]$ size, where this notation represents

(primitives)/[contractions]. It was developed for use with an RECP,¹¹⁵ which replaces the atomic core electronic shells $1s^2 2s^2 2p^6 3s^2 3p^6 3d^{10}$ of Ag. The core orbitals are removed from such calculations and the valence orbitals are replaced by pseudo-orbitals, which are unchanged in the valence region, but go smoothly and nodelessly to zero in the core region with no oscillatory behavior.⁴² This published RECP contained a suggested basis set developed at the double- ζ level which was used to test the RECP and compare with all-electron calculations.

Orbital	Primitives	Contraction	Contraction	Contraction	Contraction
s	1.080794	-1.5658625	0.3275119	0.0	0.0
	0.869444	1.8261032	-0.5525424	0.0	0.0
	0.096476	0.0187219	0.6138649	1.0	0.0
	0.036342	-0.0061177	0.5095764	0.0	1.0
3s	2.442376	1.0			
p	5.367865	-0.1536624	0.0216393	0.0	0.0
	1.772321	0.6847692	-0.1155315	-0.2966970	0.0
	0.670491	0.4587971	-0.0698728	1.0	0.0
	0.118685	0.0239507	0.3070103	0.0	-0.1842908
	0.030676	-0.0050129	0.7992705	0.0	1.0
d	2.448778	0.2978670	0.0	0.0	
	1.042491	0.4498545	0.0	0.0	
	0.418454	0.3466049	0.0	0.0	
	0.151913	0.1327947	1.0	0.0	
	0.050700	0.0000000	0.0	1.0	
f	1.541074	1.0			

Table 4.2: Ag core cc-pVDZ Basis Set:(5s5p5d1f)/[5s4p3d1f]

We used this basis set as an initial guess and made further modifications, starting by minimizing the energy of the $5s^1$ 2S ground state. In optimizing the set of s

primitive functions for the pVDZ set,¹¹⁶ two of them "collapsed", i.e., their exponents approached each other closely and their coefficients became very large and equal in magnitude but opposite in sign. Carrying out this limiting procedure analytically results in one $1s$ function and one $3s$ function, both with the same exponent. We made that change and reoptimized all s exponents, d exponents, and the three inner p exponents, keeping the two most diffuse p exponents (suitable for the description of the $5p^1\ ^2P$ state of Ag) fixed. Following this optimization, we optimized the outer two p exponents keeping now the s , d and three inner p exponents fixed to their previous values. These optimizations were done with the program ATMSCF,¹¹⁶ and followed many cycles of iteration till convergence. We then added one more d primitive and optimized it for a two-configuration MCSCF wave function. This calculation was done in the D_{2h} point group for $\tilde{X}\ ^1\Sigma_g^+$ of Ag_2 at the experimental¹¹⁷ bond length of 2.5303(2) Å. The two configurations that were included in the MCSCF wave function were of closed-shell type. They differed by a double electron replacement from the a_g bonding MO to the corresponding b_{1u} antibonding MO. We added this additional d function to polarize the $5p$ shell since none of the primitives for the $4d$ shell were diffuse enough to serve this purpose. The two most diffuse d primitives were left uncontracted. Then an f set was added and optimized for the SOCISD wave function for $5s^1\ ^2S_{1/2}$ Ag in the D_{2h} point group. We included the f polarization function to polarize mainly the silver's $4d$ shell. We point out that the final basis set includes

freed-up diffuse s , p , and d primitives in the same manner used in all-electron work. To avoid two-center RECP problems, we followed Christiansen's scheme⁴⁵ in modifying the s and p contractions.

An assessment of the accuracy of our Gaussian basis is afforded by direct comparison with experimental results.¹¹⁸ We used our final basis set to calculate the energies of the three lowest energy states of Ag, since the energetics of these states at the atomic level set the foundation for the reliable calculation of the excitation in question at the molecular level in Ag₃. The results are tabulated in Table 4.3 and

States ^a	SCF Energies	SOCISD Energies	Exp ^b
² S _{1/2}	0 ^c	0 ^c	0.00
² P _{1/2}	24899	27458	29552.05
² P _{3/2}	24899	28122	30472.71
ΔE[² P _{3/2} - ² P _{1/2}]		664	920.66

Table 4.3: Theoretically calculated lowest three energy states of Ag based on our newly constructed cc-pVDZ basis set and comparison with corresponding experimental values.

^a The theoretical and experimental energies are in cm⁻¹. ^b See Ref.118 for a complete list of the experimentally determined excitation energies for Ag. ^c The absolute energy of the silver atom in its ²S_{1/2} ground spin-orbit state at the SCF level of theory is -145.300491 hartree and at the SOCISD level -145.623883 hartree.

are compared with the corresponding experimental values. One may immediately identify a < 10% deviation between the theoretically calculated excitation energies for the spin-orbit states of ²P_{1/2} and ²P_{3/2} and the experimentally observed ones. The

SOCISD calculations recover $\approx 72\%$ of the experimentally determined energy separation between $^2P_{1/2}$ and $^2P_{3/2}$ due to the spin-orbit coupling. One thus may anticipate reasonable errors in the actual calculation of the excitation energies for Ag_3 , mostly due to the basis set truncation. (See Section 4.5 for a detailed error analysis for this work.) Despite its moderate size, this basis set should give reliable results for the relative energies of the various conformations about the equilateral triangle geometry on the Ag_3 PES surface, which is the main subject of the present work. Hence, we did not pursue the construction of a larger basis set for Ag which could refine the excitation energies for Ag but at an additional computational expense.

4.4 Results

With the side opposite the apical Ag atom and the two equal sides of the isosceles triangle being the only two geometric factors that uniquely determine any C_{2v} structure of Ag_3 , Eq. 4.3 becomes

$$Q_{e_y}[\alpha_1] = \frac{2}{\sqrt{6}}(\beta - \alpha), \quad (4.30)$$

where $\beta = r_{23}$ and $\alpha = r_{12} = r_{13}$. For any given Q_{e_y} value there may only be a single pair of (α, β) for which the potential energy of Ag_3 becomes a minimum. The geometrically optimized C_{2v} structures for each Q_{e_y} value along the PES cuts were determined as the energy minima from the polynomial fits of second-order of approximately 10 (α, β) pairs. The majority of the PES points were placed in the vicinity of the conical intersection and at the global minima and local maxima.

We examined the possibility that the sum of the sides of a C_{2v} geometric conformation may not significantly deviate from that defined at the optimum D_{3h} geometry. In doing so we assumed the geometry restriction $2\alpha + \beta = 3c$, where c corresponds to the Ag-Ag bond at the molecule's optimum D_{3h} geometry.

4.4.1 The \tilde{X} State

The SCF-, CISD-, and SOCISD-energy calculations for Ag_3 in its equilateral triangle geometry led, respectively, to Ag-Ag bond lengths and total energies of $5.4535a_0$ (-435.915590 E_h), $5.1985a_0$ (-436.824408 or -436.824926 E_h when more correlating MOs are used), and $5.1950a_0$ (-436.845269 E_h). (See Table 4.4) The CI leads to a bond length contraction of $0.255a_0$ in going from the SCF to the CI results, as has previously been observed in other triatomic systems.¹¹⁹ There is an additional contraction of $0.0035a_0$ in going from the CI to the SOCISD results.

Table 4.5 summarizes the computed geometries and symmetric-stretch frequencies for the $\tilde{X}^2\text{E}'$ state and a number of low-lying excited electronic states of Ag_3 in D_{3h} geometry. Note that there is little variation in the bond distances for these states and that the excited states are all considerably closer to each other in energy than they are to the ground state. This further raises the question as to whether part of the vibronic structure in the $\tilde{A}^2\text{E}''$ excitation spectrum of Ag_3 (Chapter 5) is due to interactions with neighboring electronic states, given the limited reliability of their calculated excitation energies. (See Section 4.5.)

In comparison to the $\tilde{X}^2\text{E}'$ -state's totally symmetric mode frequency, the corresponding frequencies for the excited states appear to deviate very little assuming a

	Electronic Symmetry ^a	$R_e(12)/\text{\AA}$	$R_e(23)/\text{\AA}$	θ_e/deg	$(\Delta E/\text{cm}^{-1})^b$
$\tilde{X}^2\text{E}'$ State	$(^2\text{E}')^c$	2.8859	2.8859	60	0 (0)
	$(^2\text{E}')^d$	2.7509	2.7509	60	
	$(^2\text{E}')^e$	2.7491	2.7491	60	
	$^2\text{B}_2$	2.8161 (2.8161)	3.1725 (3.1725)	69 (69)	-633 (-628)
	$^2\text{A}_1$	2.9849 (2.9779)	2.7581 (2.7640)	55 (55)	-504 (-465)
$\tilde{A}^2\text{E}''$ State	$(^2\text{E}'')^c$	2.8857	2.8857	60	0
	$(^2\text{E}'')^{d,e}$	2.7564	2.7564	60	
	$^2\text{A}_2$	2.8483	2.9901	63	-150
	$^2\text{B}_1$	2.9353	2.8057	57	-158

Table 4.4: Geometries and energy separation of the $\tilde{X}^2\text{E}'$ - and $\tilde{A}^2\text{E}''$ -Jahn-Teller-split states of Ag_3 .

^a The geometries at the stationary points and at the high-symmetry point of the $\tilde{X}^2\text{E}'$ and $\tilde{A}^2\text{E}''$ Jahn-Teller distorted PESs of Ag_3 . The positions of the stationary points (Hartree-Fock geometry optimized structures) do not change upon inclusion of the spin-orbit correction. For the \tilde{X} -state PES, the global minimum is predicted at $\rho_{min}(\text{\AA}) = 0.29$ (it remains 0.29 when the calculations incorporate pseudo-Jahn-Teller mixing) and the saddle point at $\rho_{max}(\text{\AA}) = -0.18$ (-0.17). For the \tilde{A} -state PES, the global minimum and saddle point are found at $\rho_{min}(\text{\AA}) = -0.11$ and $\rho_{max}(\text{\AA}) = 0.12$, respectively.^b The zero energy corresponds to the Hartree-Fock geometry optimized D_{3h} structure of Ag_3 in its $\tilde{X}^2\text{E}'$ and $\tilde{A}^2\text{E}''$ states. For the \tilde{X} -state, the absolute value of energy at the conical intersection (CISD level) is -436.821540 hartree. For the \tilde{A} -state, it becomes -436.698733 hartree. For the \tilde{X} -state, the additional values in parentheses correspond to calculations that incorporate pseudo-Jahn-Teller mixing; the zero energy becomes -436.822061 hartree. The barrier to pseudorotation for the $\tilde{X}^2\text{E}'$ state is 129 cm^{-1} (163 cm^{-1} with pseudo-Jahn-Teller mixing in the calculations) while for the $\tilde{A}^2\text{E}''$ state it is 8 cm^{-1} .^c Geometry optimization for a D_{3h} structure at the SCF level of theory.^d Geometry optimization for a D_{3h} structure at the CISD level of theory.^e Geometry optimization for a D_{3h} structure at the SOCISD level of theory.

State	$R_e,^a \alpha_0$ CISD	$\omega_e,^b \text{cm}^{-1}$ & Calc	Energy, E_h CISD
${}^2\text{A}'_1$	5.1555	172	-436.654215
${}^2\text{A}'_2$	5.2355	158	-436.655824
${}^2\text{E}'^c$	5.1915 (5.1905)	163 (164)	-436.679465 (-436.683068)
$\tilde{\text{A}} {}^2\text{E}''$	5.2089	162	-436.701399
${}^2\text{E}'^c$	5.2465 (5.2255)	161 (163)	-436.721876 (-436.728154)
${}^2\text{A}'_1$	5.1855	168	-436.739044
$\tilde{\text{X}} {}^2\text{E}'^d$	5.1985	161,165	-436.824408 or -436.824926

Table 4.5: Summary of geometries and symmetric stretch frequencies for the $\tilde{\text{X}} {}^2\text{E}'$ state and a number of low-lying excited electronic state of Ag_3 .

^a Ag-Ag distance in atomic units for an equilateral triangle geometry calculated at the CISD level of theory. ^b Harmonic frequencies, in cm^{-1} , estimated from quadratic fits to energies computed at the CISD level of theory. The a'_1 potentials of the $\tilde{\text{X}} {}^2\text{E}'$ and $\tilde{\text{A}} {}^2\text{E}''$ states were found to be slightly anharmonic ($\omega_e \chi_e \leq 1 \text{ cm}^{-1}$). ^c The values in parentheses were based on CISD-energy calculations where the SCF MOs converged to the excited-state in question. ^d The frequency of 161 cm^{-1} arises from a CISD-energy quadratic fit where the Jahn-Teller-split MOs are correlated, while the frequency of 165 cm^{-1} from a corresponding calculation with an extended reference list of correlating MOs.

D_{3h} triangle geometry for Ag_3 . The single occupation of antibonding orbitals would in general lead to longer Ag-Ag bond lengths for the D_{3h} structures. This in turn would indicate lower vibrational frequencies. This happens for several of the excited states. However, the bond lengths of the $\tilde{X}^2\text{E}'$ state and the excited $^2\text{E}'$ state above the $\tilde{A}^2\text{E}''$ state are comparable which further suggests that the bond order of Ag_3 is in this case little affected by the higher MO occupation. The bond lengths for the D_{3h} Ag_3 structures of the other excited states near $\tilde{A}^2\text{E}''$ are comparable and the symmetric-stretch frequencies are similar.

Figure 4.3 presents the Jahn-Teller-split potential energy curves of $^2\text{A}_1$ and $^2\text{B}_2$ symmetries as a function of the displacement coordinate ΔQ_{e_y} in units of Å, calculated at the CISD level of theory. Note that the $^2\text{E}'$ point is a local maximum on the PES with distortion to C_{2v} symmetry leading to a lowering in the energy for both $^2\text{A}_1$ (local minimum) and $^2\text{B}_2$ (global minimum) symmetries. The $^2\text{A}_1$ symmetry favors acute angle geometries while the $^2\text{B}_2$ symmetry favors obtuse angle geometries. The zero energy point corresponds to -436.821540 E_h . A comparison between the dotted (with geometry restriction) and straight (with no geometry restriction) lines suggests that the approximation of keeping the totally symmetric coordinate R constant at its value at the molecule's equilibrium point is valid only for areas of the PES that lie close to the conical intersection. The $^2\text{B}_2$ surface shows a marked asymmetry (straight line) leading to a linear $^2\Sigma_u^+$ state as ΔQ_{e_y} becomes larger. The $^2\text{A}_1$ and $^2\text{B}_2$ surfaces appear to be relatively shallow. Based on the straight-line results, the obtuse structure obtains an apex angle of 69° (global minimum and $^2\text{B}_2$ in symmetry)

while the acute C_{2v} conformation obtains an apex angle of 55° (saddle point and 2A_1 in symmetry.) A summary of the Ag-Ag bond lengths for the apical side $R_e(23)$ and the two equal sides $R_e(12)$ of the isosceles triangle at the stationary points of the Jahn-Teller-distorted \tilde{X} -state PES is given in Table 4.4.

While the qualitative characteristics of the SCF potential energy curves remain the same upon inclusion of CI, the same cannot be said in quantitative terms. This becomes more apparent in Fig. 4.4 where the potential energy curves calculated at the SCF and CISD levels are presented. The CISD calculations clearly suggest that smaller displacements in the Q_{e_y} coordinate are required to reach the stationary points relative to those calculated at the SCF level of theory. What is also apparent is that the 2B_2 surface becomes considerably less shallow upon inclusion of the CI corrections. The energy separation between the conical intersection and the global minimum of the 2B_2 state corresponds to 633 cm^{-1} , while the value for the saddle point of the 2A_1 state is 504 cm^{-1} . The barrier to pseudorotation around the moat of the \tilde{X} -state-Jahn-Teller-distorted PES is 129 cm^{-1} . Note that, in general, the MRSDCI energies along the potential energy curves are much lower than the SCF results. This indicates that the SCF methodology is not adequate to properly describe the \tilde{X} -state electronic structure of Ag_3 .

Fig. 4.5 shows the theoretically calculated Jahn-Teller-split potential energy curves of Ag_3 in the presence of spin-orbit coupling. The Jahn-Teller and spin-orbit couplings should be considered simultaneously in the calculation of the Jahn-Teller-split PES, as they both involve electron angular momentum. The two effects have

opposite actions on the geometry; the spin-orbit coupling may quench the Jahn-Teller distortion if it is considerably greater than the latter. We noted earlier that for the \tilde{X} $^2E'$ (D_{3h}) state of Ag_3 , the Ag-Ag bond length is subject to a relativistic contraction. One may conclude that the effect of spin-orbit interaction on the geometry is minimal for Ag_3 in its \tilde{X} -state. When considering spin-orbit coupling, the D_{3h} symmetry at the conical intersection turns into the D_{3h}^2 double group symmetry, hence the $^2E'$ electronic state in D_{3h} symmetry is split into the $E_{3/2}$ and $E_{5/2}$ spin-orbit components, with the latter having lower energy. Both of these spin components transform like $E_{1/2}$ in the C_{2v}^2 double group symmetry. In Figure 4.5, the zero of energy was arbitrarily chosen to correspond to the energy of -436.842319 E_h . The energy separation at the symmetric configuration point of the \tilde{X} -state PES due to spin-orbit coupling is 232 cm^{-1} . A comparison between the CISD-calculated potential energy curves of Figure 4.4 with the ones of Figure 4.5 after having subtracted out their energy difference at the symmetric configuration due to the spin-orbit interaction i.e. 232 cm^{-1} leads to approximately a set of overlapping potential energy curves. The positions of the stationary points in the Jahn-Teller-distorted PES of the \tilde{X} state do not change upon inclusion of the spin-orbit interaction, nor does their relative energy difference since the PES points along the potential energy curves have been determined after a geometry optimization at the Hartree-Fock level and not at the SOCISD level. So the spin-orbit coupling is merely incorporated as a final correction to these potential energy curves.

Figure 4.8 presents the Type II and Type I CISD-potential-energy-surface calculations for the Jahn-Teller-split components of the \tilde{X}^2E' state. These correspond, respectively, to energy calculations that explicitly include or omit in the list of references at the CI step the MOs that give rise to the next five excited states. Any pseudo-Jahn-Teller mixing between the \tilde{X} state and low-lying excited states should be reflected in the calculated \tilde{X} -state PES. For the Type II calculations the energy at “zero” corresponds to -436.822061 E_h . The Type II curves appear to almost completely overlap the Type I curves. Only a minimal change is observed for the 2A_1 component; the local maximum corresponds now to a smaller displacement from the symmetric configuration, with its energy lowering from the D_{3h} point being reduced also. With reference to the conical intersection, the Type II calculations predict the energy at the global minimum (2B_2 state) to be -628 cm^{-1} and that at the local maximum (2A_1 state) to be -465 cm^{-1} . Hence the barrier to pseudorotation is found to be 163 cm^{-1} .

In Section 4.2.3 we gave our general theoretical methodology which was based on a second-order truncated expression for the general Hamiltonian given in Equation 4.7. This approximation led to Equation 4.12 which pertains to the cut of the global PES along the Q_{e_y} coordinate. Such an approach is based on what has traditionally and historically in the Jahn-Teller analysis been classified as the most dominant vibronic interactions. To follow up on this methodology, we utilized Eqs. 4.23-4.25

and calculated a set of parameters, i.e.,

$$\lambda_{e'}(cm^{-1}/\text{\AA}^2) = 25951$$

$$k_{e'}(cm^{-1}/\text{\AA}) = 5253$$

$$g_{e'}(cm^{-1}/\text{\AA}^2) = 1908.$$

With passing reference to Eqs. 4.14-4.16 we obtain

$$\omega_{e,e'}(cm^{-1}) = 156$$

$$D_{e'} = 3.41$$

$$K_{e'} = 0.07.$$

The quadratic Jahn-Teller constant compares well with the one calculated from Eq. 4.26; with $E_{e'}^0(cm^{-1}) = -633$ and $E_{e'}^{\pi/3}(cm^{-1}) = -504$, Eq. 4.26 predicts $K_{e'} = 0.06$.

By using Eqs. 4.18-4.22 we obtain

$$\rho_{e'}^o(\text{\AA}) = 0.23$$

$$E_{e'}^o(cm^{-1}) = -613$$

$$\rho_{e'}^{\pi/3}(\text{\AA}) = -0.18$$

$$E_{e'}^{\pi/3}(cm^{-1}) = -469$$

$$\Delta E_{e'}^B(cm^{-1}) = 144.$$

(The minus sign in $\rho_{e'}^{\pi/3}$ is due to the $\cos \phi$ dependence.) The above set of parameters

compares well with the Type I CISD calculated results of Fig. 4.3

$$\begin{aligned}\rho_{e'}^o(\text{\AA}) &= 0.29 \\ E_{e'}^o(cm^{-1}) &= -633 \\ \rho_{e'}^{\pi/3}(\text{\AA}) &= -0.18 \\ E_{e'}^{\pi/3}(cm^{-1}) &= -504 \\ \Delta E_{e'}^B(cm^{-1}) &= 129.\end{aligned}$$

However, other workers⁹⁹ have recently pointed out that for Ag₃ not only linear and quadratic but cubic and pseudo-Jahn-Teller contributions become important to the warping of the APES of the $\tilde{X}^2\text{E}'$ state. It is worthwhile to investigate this possibility further.

García-Fernández *et al.*⁹⁹ derived general formulas that take into consideration linear, quadratic, cubic, and pseudo-Jahn-Teller contributions to the APES. We shall make use of these formulas as adjusted to our nomenclature and mathematical symbols. What we find from our *ab initio* calculations is that the dominant mechanism of warping in the $\tilde{X}^2\text{E}'$ -state-Jahn-Teller $E \otimes e$ problem of Ag₃ is due to linear terms and we prove this later on in our analysis. If all terms up to ρ^3 are included in the effective Hamiltonian, Equation 4.12 becomes

$$\begin{aligned}V_{\pm,e'}^{l,q} &= \frac{1}{2}\lambda_{e'}\rho^2 + \frac{1}{2}c_{e'}\rho^3 \cos(3\phi) \pm k_{e'}\rho \left(1 + \frac{2g_{e'}\rho}{k_{e'}} \cos(3\phi) + \frac{g_{e'}^2\rho^2}{k_{e'}^2} + \frac{2m_{e'}\rho^2}{k_{e'}}\right)^{1/2} \\ &\approx \frac{1}{2}\lambda_{e'}\rho^2 + \frac{1}{2}c_{e'}\rho^3 \cos(3\phi) \pm [k_{e'}\rho + g_{e'}\rho^2 \cos(3\phi) + m_{e'}\rho^3].\end{aligned}\quad (4.31)$$

In the above Equations $c_{e'}$ and $m_{e'}$ represent⁹⁹ the cubic anharmonicity and the cubic Jahn-Teller coupling constant of the e' mode, respectively. In the last equality

terms that involve $\cos(6\phi)$ have been neglected, as no evidence of significant contribution from such terms has previously been documented.⁹⁹ This assumption is also confirmed from the fit of our own *ab initio* results to such expressions, which also suggests that the contribution from the $m_{e'}$ terms is negligible.

Based on the fact that the positions of the stationary points of the \tilde{X} -state PES do not change upon explicit inclusion of interactions with nearby excited electronic states (the global minimum remains at 0.29 \AA whereas the local maximum becomes -0.17 \AA from -0.18 \AA when the additional interactions of pseudo-Jahn-Teller nature are explicitly introduced in the calculations, see also Table 4.4) it is safe to use Eqs. 4.31, which do not incorporate terms of pseudo-Jahn-Teller activity,

$$\left(\frac{dV_+}{d\rho} \right)_{max} = 0 \quad (4.32)$$

and

$$\left(\frac{dV_-}{d\rho} \right)_{min} = 0. \quad (4.33)$$

We obtain

$$\lambda_{e'} \rho_{min} + \frac{3}{2} c_{e'} \rho_{min}^2 - k_{e'} - 2g_{e'} \rho_{min} = 0 \quad (4.34)$$

$$\lambda_{e'} \rho_{max} + \frac{3}{2} c_{e'} \rho_{max}^2 + k_{e'} + 2g_{e'} \rho_{max} = 0. \quad (4.35)$$

By adding Eqs. 4.34 and 4.35, the following equation is generated

$$\lambda_{e'} (\rho_{min} + \rho_{max}) + \frac{3}{2} c_{e'} (\rho_{min}^2 + \rho_{max}^2) + 2g_{e'} (\rho_{max} - \rho_{min}) = 0. \quad (4.36)$$

Hence with the Type I CISD calculated values for the positions of the stationary points of the \tilde{X} -state ($\rho_{min} = 0.29 \text{ \AA}$ and $\rho_{max} = -0.18 \text{ \AA}$ in Fig. 4.3) given, and

once $\lambda_{e'}$ and $c_{e'}$ are calculated, then Eq. 4.36 can be used to calculate $g_{e'}$. Although $\lambda_{e'}$ and $c_{e'}$ may be calculated at a satisfactory level of confidence, the fitting error may primarily affect $c_{e'}$ and it unavoidably propagates into $g_{e'}$.

Upon inclusion of the e' cubic anharmonicity, and after neglecting the contribution from $m_{e'}$ terms based on the fact that their effect is negligible, Eqs. 4.23 and 4.24 become

$$V_+ + V_- \approx \lambda_{e'} \rho^2 + c_{e'} \rho^3 \quad (4.37)$$

$$(V_+ - V_-)/2 \approx k_{e'} \rho + g_{e'} \rho^2. \quad (4.38)$$

By fitting the Type I CISD energies to the PES points lying at the vicinity of the conical intersection we derive

$$\lambda_{e'}(cm^{-1}/\text{\AA}^2) = 25951$$

$$c_{e'}(cm^{-1}/\text{\AA}^3) = -6202$$

$$k_{e'}(cm^{-1}/\text{\AA}) = 5253.$$

The linear Jahn-Teller constant $k_{e'}$ remains practically the same when a larger grid of PES points is utilized for the fit, i.e., the space of PES points connecting the stationary points. The only new calculated parameter here is $c_{e'}$ with $\lambda_{e'}$ and $k_{e'}$ remaining the same. With $\lambda_{e'}$ and $c_{e'}$ at hand, we go back to Eq. 4.36 and calculate the quadratic Jahn-Teller constant $g_{e'}$

$$g_{e'}(cm^{-1}/\text{\AA}^2) = 1720. \quad (4.39)$$

If we go back to Eqs. 4.14-4.16 and Eqs. 4.18-4.22 we obtain the same set of fit values with before. Eqs. 4.14-4.22 were derived assuming a second-order truncation

for the Taylor series expansion of the electronic Hamiltonian. These equations, hence, strictly represent the linear and quadratic contributions to the topology of the APES in the $E \otimes e$ problem. The fit values do not change when we further consider the cubic contribution. The cubic contribution is admittedly small enough to have practically no significant effect on the PES. The major contributions to the topology of the APES is due to the linear contribution and in part due to the quadratic contribution, since these alone suffice to adequately represent the topographic characteristics of the Jahn-Teller distorted potential energy surface. The Type I CISD calculations contain in part some degree of pseudo-Jahn-Teller mixing, which could affect to some extent the values of the fit parameters $\lambda_{e'}$, $c_{e'}$ and $g_{e'}$. To properly account for the pseudo-Jahn-Teller mixing, we refer to the Type II CISD calculations that were based on an extended reference space of correlating MOs. The calculated positions and relative energies of the stationary points with reference to the conical intersection (see also Tab. 4.4) are

$$\begin{aligned}\rho_{e'}^o(\text{\AA}) &= 0.23 \\ E_{e'}^o(cm^{-1}) &= -628 \\ \rho_{e'}^{\pi/3}(\text{\AA}) &= -0.17 \\ E_{e'}^{\pi/3}(cm^{-1}) &= -465.\end{aligned}$$

To calculate the energies at the stationary points when linear, quadratic, cubic and pseudo-Jahn-Teller contributions to the APES are taken into consideration⁹⁹ the following equations may be used (within parentheses are the known from the previous

fit contributions, in cm^{-1})

$$V_- = \frac{1}{2}\lambda_{e'}\rho_{min}^2(1099) + \frac{1}{2}c_{e'}\rho_{min}^3(-76) - k_{e'}\rho_{min}(-1529) - g_{e'}\rho_{min}^2(-146) + V_{PJT}\rho_{min}^2 \quad (4.40)$$

$$V_+ = \frac{1}{2}\lambda_{e'}\rho_{max}^2(396) + \frac{1}{2}c_{e'}\rho_{max}^3(16) + k_{e'}\rho_{max}(-917) + g_{e'}\rho_{max}^2(52) - V_{PJT}\rho_{max}^2. \quad (4.41)$$

In Eqs. 4.40 and 4.41, the term V_{PJT} represents the pseudo-Jahn-Teller effects with other electronic states⁹⁹ and if we assume the value of $283 \text{ cm}^{-1}/\text{\AA}^2$ for it we obtain

$$V_-(\text{cm}^{-1}) = -628$$

$$V_+(\text{cm}^{-1}) = -462.$$

Clearly, the contribution due to the pseudo-Jahn-Teller mixing is minimal for the $\tilde{X}^2\text{E}'$ state of Ag_3 ; for V_- , $V_{PJT}\rho_{min}^2(\text{cm}^{-1}) = 24$ and for V_+ , $V_{PJT}\rho_{max}^2(\text{cm}^{-1}) = 9$. The PES fit along R and \mathcal{Q}_{e_y} gave $b_{a'_1 e'}(\text{cm}^{-1}) = -1$, which corresponds to $B_{a'_1 e'} = -0.01$ based on Eq. 4.17. Table 4.6 summarizes all of the theoretically derivable parameters for the $\tilde{X}^2\text{E}'$ state of Ag_3 .

Table 4.7 shows the SCF Mulliken population analysis of Ag_3 calculated at the stationary points of the Jahn-Teller-distorted $\tilde{X}^2\text{E}'$ PES. In the ${}^2\text{B}_2$ state a total charge transfer of 0.08e from the apex Ag atom to the base Ag atoms is observed whereas in the ${}^2\text{A}_1$ state 0.13e have moved from the base Ag atoms to the apex Ag atom. Hence, in the ${}^2\text{B}_2$ state the apex Ag atom carries a positive charge while in the ${}^2\text{A}_1$ state it carries a negative charge. One would expect for the dipole moment of the ${}^2\text{E}'$ state (D_{3h} geometry) to be exactly zero. The dipole moments of the two

Variable (units) ^a	
Atomic weight of Ag (a.u.)	107.8682
Force constant $\lambda_{e'}$ ($\text{cm}^{-1}/\text{\AA}^2$)	25951
Force constant $\lambda_{e'}$ (mdyn/ \AA)	0.52
Frequency of $\nu_2(e')$ (cm^{-1})	156
Cubic anharmonicity $c_{e'}$ ($\text{cm}^{-1}/\text{\AA}^3$)	-6206
Cubic anharmonicity $c_{e'}$ (mdyn/ \AA^2)	-0.12
Linear Jahn-Teller constant $k_{e'}$ ($\text{cm}^{-1}/\text{\AA}$)	5253
Linear Jahn-Teller constant $k_{e'}$ (mdyn)	0.10
Linear Jahn-Teller constant $D_{e'}$	3.41
Quadratic Jahn-Teller constant $g_{e'}$ ($\text{cm}^{-1}/\text{\AA}^2$)	1720
Quadratic Jahn-Teller constant $g_{e'}$ (mdyn/ \AA)	0.034
Quadratic Jahn-Teller constant $K_{e'}$	0.07
Bilinear Jahn-Teller constant $b_{a'_1 e'}$ (cm^{-1})	-1
Bilinear Jahn-Teller constant $B_{a'_1 e'}$	-0.01
Pseudo-Jahn-Teller constant V_{PJT} ($\text{cm}^{-1}/\text{\AA}^2$)	283
Pseudo-Jahn-Teller constant V_{PJT} (mdyn/ \AA)	0.0056
^b Force constant of $\lambda_{a'_1}$ ($\text{cm}^{-1}/\text{\AA}^2$)	28955
^b Force constant of $\lambda_{a'_1}$ (mdyn/ \AA)	0.57
^b Frequency of $\nu_1(a'_1)$ (cm^{-1})	165
Spin-orbit coupling (cm^{-1})	232

Table 4.6: Molecular parameters of the \tilde{X} $^2\text{E}'$ electronic state of Ag_3 .

^a The conversion factor used is 1 mdyn=50341.1762 $\text{cm}^{-1}/\text{\AA}$. ^b Derived based on a CISD wave function with an extended reference space of correlating MOs.

State	Gross							
	M	M ₂	M(s)	M ₂ (s)	M(p)	M ₂ (p)	M(d)	M ₂ (d)
$\tilde{X}^{\text{2E}'}$	² B ₂	18.91	38.08	2.693	5.820	6.245	12.30	9.975
	² A ₁	19.13	37.87	3.006	5.489	6.145	12.43	9.980
$\tilde{A}^{\text{2E}''}$	² B ₁	19.28	37.72	2.534	5.241	6.835	12.57	9.915
	² A ₂	18.71	38.29	2.654	5.120	6.103	13.31	9.955

Table 4.7: Mulliken population analysis for Ag₃.^a

^a M₂ refers to the two base atoms of the isosceles triangle of Ag₃. These results pertain to the position of the stationary points in the Jahn-Teller distorted PES of the $\tilde{X}^{\text{2E}'}$ and $\tilde{A}^{\text{2E}''}$ states.

\tilde{X} -state Jahn-Teller components of Ag₃ should be of opposite sign. Indeed, our observations from the charge distribution in the isosceles triangles confirm the above, and are in agreement with previous work.^{11,95}

Table 4.7 also indicates that for the $\tilde{X}^{\text{2E}'}$ -state-Jahn-Teller-split electronic states of Ag₃, the bonding is mainly due to the 5s-5p electrons. The deviation of the total *d* populations from the expected valence value of 30 suggests that the 4*d* electrons participate in the bonding to some extent. The contributions from *d* electrons in both of the $\tilde{X}^{\text{2E}'}$ -Jahn-Teller-split electronic states of Ag₃ are similar. The participation of the 5p shell is indeed important here. This is readily explained based on the atomic states of Ag.¹¹⁸ While the first excited state of Ag is due to the 4*d*¹⁰5p configuration and lies ca. 30000 cm⁻¹ above the ground electronic state, the excited states due to

the $4d^95s^2$ configuration are ca. 30300-35000 cm⁻¹, while the $5p$ orbitals have a similar radial extent as the $5s$. Thus, as others have previously noticed,^{11,15} the $5p$ orbital is expected to participate more in the bonding of Ag₃ than the $4d$ orbital.

4.4.2 The \tilde{A} State

The \tilde{A} $^2E''$ -state-SHF- and CISD-energy calculations have determined for the Ag-Ag bond length of Ag₃ (D_{3h} geometry) respectively 5.4532 a_0 and 5.2089 a_0 . The spin-orbit interaction had no effect on the geometry. The bond length contraction in going from SCF to CI or SOCISD was 0.2443 a_0 . The symmetric stretch frequency is calculated to be 162 cm⁻¹. (Table 4.5.)

Fig. 4.6 shows the \tilde{A} $^2E''$ -state-Jahn-Teller-split potential energy curves of 2A_2 and 2B_1 symmetries, expressed in units of cm⁻¹, as a function of the displacement coordinate ΔQ_{e_y} , in units of Å. The dotted lines were calculated at the SCF level of theory after an SCF geometry optimization. The CISD-energy calculations gave the straight lines and the intensely dotted lines which respectively are based on the SCF and CISD geometry optimizations.

While the 2A_2 electronic symmetry favors obtuse-angle geometries, 2B_1 favors acute-angle geometries. Based on the “straight-line” calculations, the global minimum is located in the potential of the 2B_1 state and is characterized by an acute structure with an apex angle of 57°, while the saddle point of the 2A_2 -state potential corresponds to an obtuse configuration with an apex angle of 63°. The energy of the global minimum (relative to the conical intersection) is at $\rho_{min}(\text{\AA}) = -0.11, -158$

cm^{-1} and that of the saddle point at $\rho_{max}(\text{\AA}) = 0.12, -150 \text{ cm}^{-1}$. The barrier to pseudorotation is 8 cm^{-1} . The Ag-Ag bond lengths $R_e(12)$ and $R_e(23)$ of the molecule's C_{2v} configurations at the stationary points of the Jahn-Teller distorted $\tilde{A}^2\text{E}''$ -state PES are presented in Table 4.4. No significant quadratic Jahn-Teller activity is expected based on the $\tilde{A}^2\text{E}''$ -state's theoretically calculated topological characteristics of the Jahn-Teller distorted PES; the stationary points are almost isoenergetic and at a nearly equal displacement from the conical intersection. We also note that smaller displacement vectors are required to reach the stationary points with the CI results compared to the SCF results. We checked the approximation of using Hartree-Fock geometry optimization and conducted a CISD geometry optimization but only for a limited section of the PES, the region in the immediate vicinity of the conical intersection. In comparing our newly acquired potential lines (intensely dotted) with the "straight-line" CISD curves, we found no significant deviation.

Some additional calculations were conducted. We compared our geometry- and non-geometry-restricted potential lines and found that for the CISD calculations following an SCF geometry optimization, it is not a good approximation to assume R to be a constant along the Q_{e_y} cut of the $\tilde{A}^2\text{E}''$ -state PES. We also investigated the possibility of pseudo-Jahn-Teller mixing between $\tilde{A}^2\text{E}''$ and the excited electronic state ${}^2\text{A}_2''$. In comparing the two different sets of curves we found that these completely overlapped so there is negligible pseudo-Jahn-Teller mixing between $\tilde{A}^2\text{E}''$ and ${}^2\text{A}_2''$. We examined the CI expansions of the \tilde{A} -state-Jahn-Teller-split and "pseudo-Jahn-Teller-mixed" wave functions calculated at the stationary points of the PES. They

were found to be mixed from several basic configurations. It is likely that higher-order correlations may be important for the \tilde{A}^2E'' -Jahn-Teller-split states. Some of the virtual-space MOs involve d -orbital participation to some extent.

Fig. 4.7 shows the \tilde{A}^2E'' -state-Jahn-Teller-split potentials of Ag_3 in the presence of spin-orbit coupling. When considering spin-orbit coupling, the $^2E''$ electronic state in D_{3h} symmetry is split into the $E_{3/2}$ and $E_{1/2}$ spin-orbit components. They both transform like $E_{1/2}$ in the C_{2v}^2 double group symmetry. The energy separation between the Jahn-Teller-split- \tilde{A}^2E'' -state lines at the symmetric configuration point in the presence of the spin-orbit interaction is 17 cm^{-1} . Such a small energy separation is consistent with the observation of a negligible effect of the spin-orbit interaction on the geometry of Ag_3 in its \tilde{A}^2E'' state.

Based on Eqs. 4.23-4.25 the following set of parameters is calculated for the \tilde{A}^2E'' state

$$\lambda_{e'}(\text{cm}^{-1}/\text{\AA}^2) = 25613$$

$$k_{e'}(\text{cm}^{-1}/\text{\AA}) = 2801$$

$$g_{e'}(\text{cm}^{-1}/\text{\AA}^2) = -247.$$

Eqs. 4.14-4.16 give

$$\omega_{e,e'}(\text{cm}^{-1}) = 155$$

$$D_{e'} = 0.99$$

$$K_{e'} = -0.01.$$

Eq. 4.26 (given $E_{e'}^o(cm^{-1}) = -150$ and $E_{e'}^{\pi/3}(cm^{-1}) = -158$) predicts $K_{e'} = -0.01$.

By using Eqs. 4.18-4.22 we obtain

$$\rho_{e'}^o(\text{Å}) = 0.11$$

$$E_{e'}^o(cm^{-1}) = -150$$

$$\rho_{e'}^{\pi/3}(\text{Å}) = -0.11$$

$$E_{e'}^{\pi/3}(cm^{-1}) = -156$$

$$\Delta E_{e'}^B(cm^{-1}) = 6.$$

(The minus sign in $\rho_{e'}^{\pi/3}$ is due to the $\cos \phi$ dependence.) The above set of parameters is in agreement with the “straight line” CISD results

$$\rho_{e'}^o(\text{Å}) = 0.12$$

$$E_{e'}^o(cm^{-1}) = -150$$

$$\rho_{e'}^{\pi/3}(\text{Å}) = -0.11$$

$$E_{e'}^{\pi/3}(cm^{-1}) = -158$$

$$\Delta E_{e'}^B(cm^{-1}) = 8.$$

As a final remark, we note that the major contribution to the topology of the APES of the $\tilde{A}^2\text{E}''$ state comes from the linear Jahn-Teller term; the quadratic and cubic contributions are indeed negligible. Pseudo-Jahn-Teller mixing between $\tilde{A}^2\text{E}''$ and excited electronic states is possible but this was not examined further in the present work. The PES fit along R and \mathcal{Q}_{e_y} gave $b_{a'_1 e'}(cm^{-1}) = -1$, which corresponds to $B_{a'_1 e'} = -0.01$ based on Eq. 4.17. Table 4.8 summarizes all of the theoretically derivable parameters for the $\tilde{A}^2\text{E}''$ state of Ag_3 .

Variable (units) ^a	
Atomic weight of Ag (a.u.)	107.8682
Force constant $\lambda_{e'}$ ($\text{cm}^{-1}/\text{\AA}^2$)	25613
Force constant $\lambda_{e'}$ (mdyn/ \AA)	0.51
Frequency of $\nu_2(e')$ (cm^{-1})	155
Linear Jahn-Teller constant $k_{e'}$ ($\text{cm}^{-1}/\text{\AA}$)	2801
Linear Jahn-Teller constant $k_{e'}$ (mdyn)	0.06
Linear Jahn-Teller constant $D_{e'}$	0.99
Quadratic Jahn-Teller constant $g_{e'}$ ($\text{cm}^{-1}/\text{\AA}^2$)	-247
Quadratic Jahn-Teller constant $g_{e'}$ (mdyn/ \AA)	-0.005
Quadratic Jahn-Teller constant $K_{e'}$	-0.01
Bilinear Jahn-Teller constant $b_{a'_1 e'}$ (cm^{-1})	-1
Bilinear Jahn-Teller constant $B_{a'_1 e'}$	-0.01
^b Force constant of $\lambda_{a'_1}$ ($\text{cm}^{-1}/\text{\AA}^2$)	28135
^b Force constant of $\lambda_{a'_1}$ (mdyn/ \AA)	0.56
^b Frequency of $\nu_1(a'_1)$ (cm^{-1})	162
Spin-orbit coupling (cm^{-1})	17

Table 4.8: Molecular parameters of the $\tilde{A}^2\text{E}''$ electronic state of Ag_3 .

^a The conversion factor used is 1 mdyn=50341.1762 $\text{cm}^{-1}/\text{\AA}$. ^b Derived based on a CISD wave function with an extended reference space of correlating MOs.

Table 4.7 presents the SCF Mulliken population analysis at the stationary points of the Jahn-Teller distorted \tilde{A}^2E'' PES. A charge transfer of 0.29e from the apex Ag atom to the base Ag atoms is observed in the 2A_2 state. In the 2B_1 state, 0.28e moves from the base Ag atoms to the apex Ag atom. The charge distribution confirms the center of gravity rule with respect to the signs of the dipole moments arising from the \tilde{A} -state Jahn-Teller components. The bonding involves principally $5s$ - $5p$ electrons. The involvement of $4d$ electrons is now greater than in the \tilde{X}^2E' state. There are similar contributions from d electrons in the \tilde{A}^2E'' Jahn-Teller split states of Ag_3 . The participation of the $5p$ shell is important.

4.5 Discussion

The primary focus of this theoretical investigation was to calculate reliable Jahn-Teller parameters which can be used as starting points for the Jahn-Teller spectral simulations. The theoretically calculated Jahn-Teller parameters can in turn be refined by using experimental data. From the comparison of our theoretically calculated Jahn-Teller parameters with the experimental ones (see Chapter 5), we find that they are generally in good agreement for the \tilde{X}^2E' and \tilde{A}^2E'' states. However, it is possible that the \tilde{A}^2E'' state does not conform to the model that we detailed in Section 4.2.3 in that it may also involve pseudo-Jahn-Teller-quadratic-interaction terms.⁹⁸ Since the \tilde{A} state has more electronic states nearby than the \tilde{X} state, it is likely that the pseudo-Jahn-Teller interaction will be more important here, resulting in a contribution to the quadratic term, but not the linear term. Since it is difficult to distinguish

between the two contributions to the quadratic term, which is small for the \tilde{A} state, we did not try to make this distinction. However, based on the above simple approximation and as will be seen in chapter 5, the Jahn-Teller calculations are successful in reproducing the pattern of the experimentally observed vibronic energy levels only when the quadratic Jahn-Teller constant is fit experimentally. This value of the effective quadratic Jahn-Teller constant is useful since it provides some insight into the nature of the vibronic coupling involved in the \tilde{A}^2E'' state. The calculation of the pseudo-Jahn-Teller electronic matrix elements⁹⁸ for the \tilde{A} state was not attempted in this work. The quadratic pseudo-Jahn-Teller interactions with nearby excited electronic states in principle may be fully addressed by the theoretical calculations so long as enough CFSs are included; as the excitation energy increases, the congestion among the excited states naturally increases.

Upon inclusion of relativistic effects, all electronic states span the same irreducible representation in the C_{2v}^2 spin-double group i.e. $E_{1/2}$. All these can mix into the spin-orbit wave function, and this mixing becomes more important in energy regions where the congestion is high. It may also be that higher-order excitations become important for the \tilde{A}^2E'' -state PES. Although we didn't find them to have a significant impact, it is possible that extending the virtual space (using a larger basis set) would reveal stronger mixing. Also, one would need to include in the list of correlating MOs all of the basic references that give rise to excited electronic states (pseudo-Jahn-Teller active for \tilde{A}^2E'' or not) that mix with the Jahn-Teller electronic components of \tilde{A} .

$^2\text{E}''$ in C_{2v} symmetry. Among those excited states are states that are based on atomic configurations that arise from excitation from the $4d$ shell. Describing such states well would also require a better quality d basis set.

Of particular interest is the consideration of the possible errors in our theoretical calculations. There are errors due to the incompleteness of the basis set, the computational methodology, and the description of the relativistic effects in the system. A central question is how accurate the relative energies of the C_{2v} structural isomers of Ag_3 are.

Our fundamental approach was to conduct a geometry optimization at the Hartree-Fock level, then as a second step include the correlation effects and at the end incorporate the effect of the spin-orbit interaction (which is admittedly the least important factor in Ag_3^{11}). Although the energies of the potential energy curves relative to the conical intersection are not expected to significantly deviate upon inclusion of correlation effects at the geometry optimization step (we rigorously tested this assumption for the $\tilde{\text{A}}^2\text{E}''$ -state Jahn-Teller split potentials and it was proven correct), the minimum energy geometries themselves along the potentials will be different. The singles and doubles CI methodology is bound by the size-consistency effects, as in the MRSDCI wave function higher-order excitations are not fully accounted for. The magnitude of the error for Ag_3 may be estimated from its effect on the Ag-Ag bond lengths; we may, hence, easily get an idea about the importance of higher-order

correlation effects. Indeed, we applied small changes in the minimum energy geometries (located at the CISD level of theory), and found that the size-consistency effects do not substantially distort the \tilde{X}^2E' - and \tilde{A}^2E'' -state PESs. We believe that our theoretical calculations on Ag_3 treat the electron correlation to a high order for a molecule containing 57 electrons. Experience with similar systems¹¹⁹ also suggests that the size-consistency error is not the major computational error here. We believe that our relativistic SCF plus singles and doubles CI methodology adequately described the electronic structure of Ag_3 , as the main features of the Ag_3 PES were readily confirmed from the experiment. The relativistic effects are mainly introduced by the RECPs and by the use of the spin-orbit operators in our calculations; it has earlier been shown that the effect of spin-orbit interaction is underestimated here. The spin-orbit splitting in the \tilde{X}^2E' and \tilde{A}^2E'' states is predicted to be small; furthermore is effectively quenched in both states by the Jahn-Teller activity. Hence, any errors in its calculation do not lead to significantly different results from those obtained in our experimental analysis of chapter 5.

The size-consistency effects will not greatly affect the calculated excitation energies, since the size-consistency error remains approximately constant when comparing the energies between the \tilde{X}^2E' state and several excited electronic states for Ag_3 in its D_{3h} geometry. (See Table 4.5.) A larger basis set is needed for a more accurately predicted excitation energy spectrum for Ag_3 . The good prediction for the $\tilde{X}^2E' \rightarrow \tilde{A}^2E''$ excitation energy is most probably result of a fortuitous cancelation of errors. Our calculated excited-state energies may still be useful; based on our excitation-spectrum

experimental results (Chapter 5), a pattern of increasing vibronic-level congestion is observed in the spectral region to the blue of the $\tilde{A}^2E'' \leftarrow \tilde{X}^2E'$ origin which may be due to the vibronic energy level structure of the $^2E'$ electronic state lying higher than the \tilde{A}^2E'' state.

In this chapter we focused our attention on C_{2v} cross-sections of the \tilde{X}^2E' - and \tilde{A}^2E'' -state PESs without performing additional calculations for non- C_{2v} potential energy points. Although this kind of information is important to determine whether the C_{2v} local minima are true global minima or saddle points of the trimer's global PES, it is likely that this is the case since the interpretation of the experimental observation is based on this assumption. (See chapter 5.) In the pseudorotation process, it is very probable that only C_{2v} structures are involved at the stationary points. A similar situation held in the pseudorotation path around the moat of the \tilde{X}^2E' -state's Jahn-Teller distorted PES of Cu_3 .¹¹⁹ Table 4.9 summarizes the present and past work regarding the geometries of Ag_3 at the global minima and saddle points as well as at the conical intersection of the Jahn-Teller distorted PES of the \tilde{X}^2E' electronic state. Our work's calculated apex angles for the C_{2v} structures of the 2B_2 and 2A_1 electronic states are in good agreement with previous studies, as well as the Ag - Ag bond lengths, which will probably contract somewhat further if correlation is incorporated into the geometry-optimization process, which we only slightly included in our work.

The $4d$ shell of Ag is expected to remain atomic-like, but the $4d$ electrons are not inert, since correlating them shortens the bonds of Ag_3 . (See Table 4.4.) This finding

	² B ₂		² A ₁		⁽²⁾ E' ^a
	R _e (12)/Å	θ _e /deg	R _e (12)/Å	θ _e /deg	
Present work	2.8161	69	2.9779	55	2.7509
Ref. 99	-	-	-	-	2.771
Ref. 95	2.593	70.45	2.758	55.08	2.670
Ref. 120	2.774	68.54	2.948	54.92	2.849
Ref. 10	2.695	67.88	2.846	55.43	-
Ref. 121	2.687	69.1	2.892	54.1	-
Refs. 122, 123	2.709	69.2	-	-	-
Ref. 11	2.72	63.7	2.88	54.2	-
Ref. 15	2.709	69.2	2.885	55.2	-
Ref. 124	2.582	67.5	2.725	55.2	-

Table 4.9: Geometries of Ag₃ at the global minima and saddle points as well as at the conical intersection of the Jahn-Teller distorted PES of the \tilde{X} ²E' electronic state. Comparison of the present work's results with past theoretical studies in reverse chronicle order.

^aThe Ag-Ag bond distance at the D_{3h} geometry.

is consistent with previous work on similar systems.^{11,119,125,126} The bond lengths are expected to shorten further due to higher-order excitations which were not included in the MRSDCI methodology. We have observed a relativistic contraction on the Ag-Ag bond lengths of the equilateral Ag_3 triangle in its $\tilde{X}^2\text{E}'$ state, but not in its $\tilde{A}^2\text{E}''$ state. This is expected; orbitals that have significant density near the nucleus are subject to an increased relativistic contraction. Hence s orbitals are expected to contract the most. Ag_3 in its $\tilde{X}^2\text{E}'$ state (D_{3h} symmetry) has a shorter bond length (2.7491 Å in Table 4.4, larger totally symmetric vibrational frequency expected) than in its $\tilde{A}^2\text{E}''$ state (2.7564 Å), since the $5s$ orbital is less diffuse than the $5p$ orbital. The small magnitude of the relativistic effects in Ag_3 also explains the relatively small contraction of the bond length in the D_{3h} configuration of the $\tilde{X}^2\text{E}'$ state and the lack of any additional contraction due to relativity for the corresponding one of $\tilde{A}^2\text{E}''$.

Ag_3 is among the Ag clusters that have shown the greatest ambiguity. Previous gas-phase and matrix-isolation experimental studies have reported on the frequencies of Ag_3 in its $\tilde{X}^2\text{E}'$ and $\tilde{A}^2\text{E}''$ states.¹²⁷ Briefly, one observes a discrepancy between the gas-phase and the matrix-isolation values for the totally symmetric and degenerate bend frequencies. However, it must be pointed out that the totality of the suggested gas-phase values for the totally symmetric frequency converges mostly to $\approx 160 \text{ cm}^{-1}$ for the $\tilde{X}^2\text{E}'$ and $\tilde{A}^2\text{E}''$ states.

Lombardi and Davis¹²⁷ have taken a somewhat different approach on the matter of calculating a reliable frequency for the totally symmetric mode of Ag_3 ; they estimated

the force constants (hence the totally symmetric frequencies) of Ag_3 and various other silver clusters based on actual experimental data, having in mind the scheme proposed by Ozin and McIntosh,¹²⁸ which predicts the force constants of higher clusters from that of the dimer. Using the information that for the ground state¹²⁹ of Ag_2 , i.e. ${}^1\Sigma_g^+$ (0_g^+), $\omega_e(\text{cm}^{-1}) = 192.4(5)$ or the force constant is 1.18 mdyne/ \AA ($59403 \text{ cm}^{-1}/(\text{\AA})^2$), Lombardi and Davis estimated the ground-state bond stretching force constants of Ag_n with $n=5,7,9,13$ based on the existing spectra.¹²⁷ They also applied Ozin and McIntosh's scheme and were able to predict the bond stretching force constants for these species as well as the one for the ambiguous Ag_3 . There was good correlation between the experimentally found and predicted values for the force constants. It is likely, thus, that the predicted value of 0.59 mdyne/ \AA ($29701 \text{ cm}^{-1}/(\text{\AA})^2$ or 167 cm^{-1}) for the ground-state force constant of Ag_3 , which also agrees with the gas-phase results and our theoretical results, is indeed the correct stretching force constant. It must be noticed that this predicted value for the ground-state totally symmetric frequency of Ag_3 is meant for a D_{3h} configuration. Any deviations in the geometry from the D_{3h} geometry will lead to larger force constants, i.e., the force constants for an isosceles trimer are expected to lie between those for the equilateral triangle and those of the linear configuration.¹²⁷ Although its experimental confirmation from the ground-state emission spectra seems to be difficult, our predicted value sets a good foundation for the experimental analysis (see chapter 5).

While the e' frequency is not readily apparent from the spectra due to the convoluted topography of the PES near the e' vibrational cusp, its value is critical for the

experimental analysis in chapter 5. The a'_1 mode is orthogonal to the e' subspace, and is predicted to have a reasonable frequency. It is of central importance to obtain a reliable degenerate bend frequency (for the equilateral triangle of Ag_3 in D_{3h}). If we consider the central force approximation, as have others,¹²⁷ the following general relations¹³⁰ come into play:

$$\nu_1^2 = 3(k_{eq}/m) \quad (4.42)$$

$$\nu_2^2 = 2 \cos^2(\phi/2)(k_{eq}/m) \quad (4.43)$$

$$\nu_3^2 = (3 - 2 \cos^2(\phi/2))(k_{eq}/m), \quad (4.44)$$

where m is the atomic mass of the homonuclear trimer, and k_{eq} is the bond stretching force constant. In the equilateral triangle limit ($\phi = 60^\circ$), k_{eq} becomes $k_{eq} = m\nu_{a'_1}^2/3$, the breathing mode $\nu_{a'_1}$ and the degenerate bend mode $\nu_{e'}$ become $\nu_{a'_1} = \nu_1$ and $\nu_{e'} = \nu_2 = \nu_3$, and $\nu_{a'_1}/\nu_{e'} = \sqrt{2}$. Assuming that the central force field approximation holds and that the totally symmetric frequency is 167 cm^{-1} then one would anticipate for the frequency of the degenerate bend mode $\approx 120 \text{ cm}^{-1}$, a value in agreement with our theoretically calculated ground-state result.

4.6 Conclusions

From comparisons with experiment, one may conclude that the present electronic structure calculations have accurately described the ground electronic state and the excited electronic state. A possible difficulty unobserved here is that the pseudo-Jahn-Teller quadratic interactions in the \tilde{A}^2E'' state were not fully addressed in this work, due to the formidable computational cost. However, the analysis of the

excitation spectrum would not have proceeded unambiguously unless there was some initial information about the vibronic coupling interactions in the \tilde{A}^2E'' state. The equilibrium Ag triangle defined at the conical intersection of the \tilde{X}^2E' and \tilde{A}^2E'' states of Ag_3 increases by a small but important amount in going from the \tilde{X}^2E' to the \tilde{A}^2E'' state. The single e' mode of Ag_3 results in a greater linear and quadratic Jahn-Teller stabilization in the \tilde{X}^2E' state than in the \tilde{A}^2E'' state.

CHAPTER 5

Vibrational Analysis of the $\tilde{A}^2E''\text{-}\tilde{X}^2E'$ Electronic Transition of the Silver Trimer

5.1 Introduction

The importance of Ag_3 in industrial processes and various fields of science was described in chapter 1 and the introduction of chapter 4. Therein is also included previous experimental and theoretical work on the \tilde{X}^2E' and \tilde{A}^2E'' states of Ag_3 .

The previous analyses for the \tilde{X} - and \tilde{A} -state vibronic structures of Ag_3 are summarized in Table 5.1 which shows the vast diversity of the molecular parameters reported.

In this chapter we describe first our analysis of the LIF excitation spectrum¹⁴ of the $\tilde{A}^2E'' \leftarrow \tilde{X}^2E'$ electronic transition of Ag_3 . We proceed to describe LEDF spectra from several \tilde{A} -state vibronic levels. The analysis of the LIF and LEDF spectra establishes the positions of the \tilde{A} - and \tilde{X} -state vibronic levels. We apply the results of chapter 4 to help assign and analyze the vibronic structure observed in the \tilde{X}^2E' and \tilde{A}^2E'' states, which results from the single Jahn-Teller active vibrational mode e' (ν_2) and the non-Jahn-Teller active vibrational mode a'_1 (ν_1).

	$\tilde{X}^2\text{E}'$ State ^a						$\tilde{A}^2\text{E}''$ State ^a					
	Exp			Calc			Exp			Calc		
	Ref. 17	Ref. 18	Our work ^b	Chapter 4	Ref. 17	Ref. 18	Ref. 17	Ref. 18	Our work ^b	Chapter 4	Ref. 17	Ref. 18
ω_{e,a'_1}	121	157.9	185(5)	165	158.2,158.2 ^c	157.9	158.5(5)	158.5(5)		162		
$\omega_{e,e'}$	99	140.0	180(10)	156	96,98 ^c	139.1	139(3)[0.9 ^d (1 ^d)]			155		
$D_{e'}$	1.86	3.20	3.0(5)	3.41	0.018,0.04 ^c	5.028	2.0(1)			0.99		
$K_{e'}$	0.25	0.12	0.08(2)	0.07	0.02,0.0 ^c	0.354	-0.17(1)			-0.005		
$B_{a'_1 e'}$	0.00	0.00	-0.01 ^e	-0.01	0.00,0.00 ^c	0.01	-0.03 ^f			-0.01		
$\alpha\zeta_e$	0.0	0.0	-232 ^e	-232	0.0,190 ^c	1500.0	-30 ^f			-17		

Table 5.1: Jahn-Teller and Spin-Orbit interaction parameters of the $\tilde{X}^2\text{E}'$ and $\tilde{A}^2\text{E}''$ electronic states of Ag₃.

^a ω_{e,a'_1} , $\omega_{e,e'}$ and $\alpha\zeta_e$ in cm⁻¹. ^b The experimental error is included within parentheses. See text for details. ^c In Ref. 17, there was a second Jahn-Teller coupling scheme that was proposed for the $\tilde{A}^2\text{E}''$ state. ^d The e' -mode anharmonicity constant $\omega_e\chi_e$ in cm⁻¹. ^e Fixed at calculated values. ^f See text for method of determination and approximate error limits.

5.2 Theoretical

5.2.1 Vibronic Eigenvalues and Eigenfunctions

In chapter 4 we applied the general theory for Jahn-Teller distortions specifically to the case of Ag_3 . We defined $\omega_{e,e'}$ and ω_{e,a'_1} as the vibrational frequency of the e' normal mode, $Q_{e',\pm}$, and the a'_1 normal mode, R, respectively, at the D_{3h} conical intersection of the potential energy surfaces (PES). $D_{e'}$ was defined as the linear Jahn-Teller coupling parameter, $K_{e'}$ as the quadratic Jahn-Teller coupling parameter, and $B_{a'_1 e'}$ as the bilinear Jahn-Teller coupling parameter. We also defined $\alpha\zeta_e$ as the spin-orbit coupling parameter. A summary of our calculated PES parameters from chapter 4 is given in Table 5.1.

A high-data throughput computer program called SPEC-SOCJT¹³¹ was specifically designed to compute eigenvalues and functions of $\hat{\mathcal{H}}_e$ for the \tilde{A} - and \tilde{X} -state Ag_3 spectral analysis. It was implemented in Fortran and C++ and enabled fast computational methods for the construction of the Hamiltonian matrix and the solution of the Schrödinger equation. The data input and output interfaces were developed using Microsoft Visual C++ tools and allow for a quick exchange of information between the computational core and the user. The totality of the extracted information from the LIF and LEDF spectra of Ag_3 should be represented by a unique set of \tilde{X} $^2\text{E}'$ - and \tilde{A} $^2\text{E}''$ -state PES parameters. The graphic user interface part of the program was developed to easily test this requirement by displaying and comparing in one step all pairs of experimental and simulated spectra. Each fit set of \tilde{X} and \tilde{A} PES parameters

therefore reflects all available experimental data. To facilitate ease of use the data input can be made in dialog boxes, and the user can also perform a one-dimensional parameter scan with the simple touch of the mouse wheel.

SPEC-SOCJT can be used to numerically solve for the $\tilde{X}^2\text{E}'$ - and $\tilde{A}^2\text{E}''$ -state vibronic energy levels based on the Hamiltonian matrix. Using the known¹⁶ matrix elements of $\hat{\mathcal{H}}$, in terms of the experimental parameters, $\omega_{e,e'}$, $D_{e'}$, $K_{e'}$, $B_{a'_1 e'}$ and $\alpha\zeta_e$, SPEC-SOCJT can construct this matrix in a suitable basis set and find its eigenpairs. The basis set used in SPEC-SOCJT is a product of spin, electronic and vibrational wave functions represented by

$$|\Lambda, \nu_{1i}, \nu_{2i}, l_{2i}, \Sigma\rangle = |\Lambda\rangle |\nu_{1i}\rangle |\nu_{2i}, l_{2i}\rangle |\Sigma\rangle \quad (5.1)$$

with quantum numbers $\Lambda = \pm 1$, $\nu_{1i(2i)} = 0, 1, 2, \dots$, $l_{2i} = v_i, v_i - 2, \dots, -v_i + 2, -v_i$, and $\Sigma = \pm \frac{1}{2}$. $\Lambda = \pm 1$ refers to the two electronic components of the doubly degenerate electronic state, v_{1i} and v_{2i} are respectively the principal vibrational quantum numbers of the a'_1 and e' modes, which also have vibrational angular momentum quantum number l_{2i} , and Σ is the electron spin angular momentum quantum number. Since the linear Jahn-Teller term in the Hamiltonian is off-diagonal in the Λ , v_{2i} , l_{2i} quantum numbers it is useful to define a quantum number, j , that is conserved, and is given by¹⁶

$$j = l + \frac{1}{2}\Lambda. \quad (5.2)$$

It is obvious that there will be multiple energy levels with identical values of j , hence we define a second quantum number, n_j , which takes on the values 1, 2, 3, ..., ∞

and serves only to provide unique labels to the eigenvalues of the same j , ordered by increasing energy. Thus we denote eigenkets as $|j, n_j\rangle$. When quadratic Jahn-Teller effects are considered, even j is no longer a good quantum number, although Σ still is. However j may still be a useful descriptor of the states if $K_{e'}$ is not too large.

The e' vibronic levels of the \tilde{X} state become $e_{3/2}$ and $e_{5/2}$ spin-vibronic levels in the double group, D_{3h}^2 , when the spin is considered. The a'_1 and a'_2 levels become $e_{1/2}$. Likewise in the \tilde{A} state, the e'' vibronic levels become $e_{1/2}$ and $e_{3/2}$ while the a''_1 and a''_2 levels are $e_{5/2}$. We denote the spin-vibronic eigenfunctions as $|j, n_j\rangle |\Sigma\rangle$, where j and Σ are approximately good quantum numbers. Figs. 5.1 and 5.2 illustrate the energy level pattern of a single e' vibrational mode with and without spin-orbit coupling in the \tilde{X}^2E' and \tilde{A}^2E'' states of Ag_3 , respectively.

As the basis set is infinite in size, obviously one must truncate the basis set to some reasonable size before diagonalizing the Hamiltonian matrix. In practice the calculated eigenvalues were tested for convergence by systematically increasing the number of basis functions until the change in the eigenvalues was less than 0.1 cm^{-1} . For Ag_3 , the final matrices used were of order 10^5 .

5.2.2 Line Intensities and Selection Rules

The spin-vibronic eigenfunctions may be expressed as linear combinations of the basis-set functions, i.e.,

$$|j'^{(n)}, n_j'^{(n)}, \Sigma'^{(n)}\rangle = \sum_k \left(C_k^{n_j'^{(n)}} |\Lambda'^{(n)}\rangle |\nu_{1i}'^{(n)}\rangle |\nu_{2i}'^{(n)} l_{2i}'^{(n)}\rangle |\Sigma'^{(n)}\rangle \right), \quad (5.3)$$

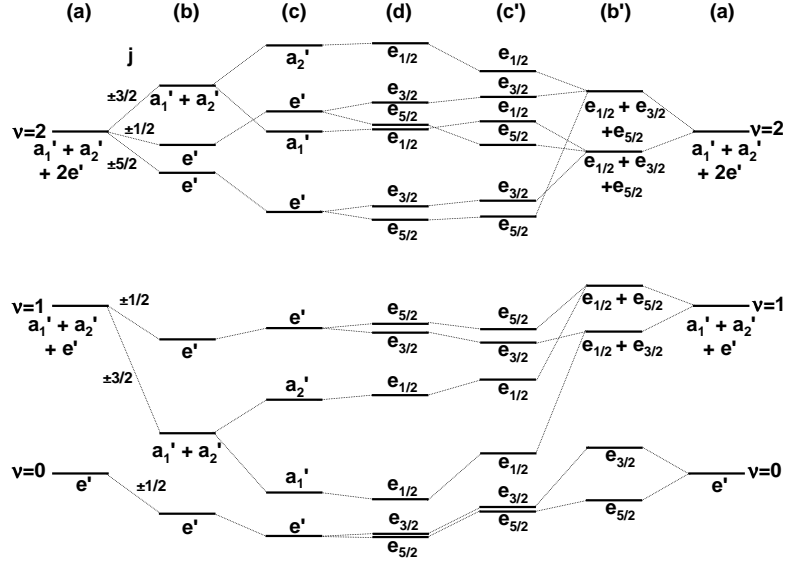


Figure 5.1: Qualitative energy level scheme of the vibronic energy levels of a $^2E'$ state under D_{3h} symmetry, with a single Jahn-Teller active mode of e' symmetry, for the following Hamiltonians.

(a) $\hat{\mathcal{H}}_{h,e}$; (b) $\hat{\mathcal{H}}_{h,e} + \hat{\mathcal{H}}_1$; (c) $\hat{\mathcal{H}}_{h,e} + \hat{\mathcal{H}}_1 + \hat{\mathcal{H}}_q$; (d) $\hat{\mathcal{H}}_{h,e} + \hat{\mathcal{H}}_1 + \hat{\mathcal{H}}_q + \hat{\mathcal{H}}_{SO}$; (c') $\hat{\mathcal{H}}_{h,e} + \hat{\mathcal{H}}_{SO} + \hat{\mathcal{H}}_1$; (b') $\hat{\mathcal{H}}_{h,e} + \hat{\mathcal{H}}_{SO}$; (a) $\hat{\mathcal{H}}_{h,e}$. The far left and far right columns are identical. Column (d) is a representative ordering of the energy levels when linear and quadratic Jahn-Teller coupling and spin-orbit coupling are included in the calculation. The left hand side of the diagram derives the energy levels of (d) via addition of the Jahn-Teller terms and then spin-orbit coupling, while the right hand side takes the opposite approach. They do, however, have a common result (d). The symmetry labels for (a)-(c) correspond to the irreducible representations of the D_{3h} group while those for (b'), (c') and (d) are for D_{3h}^2 .

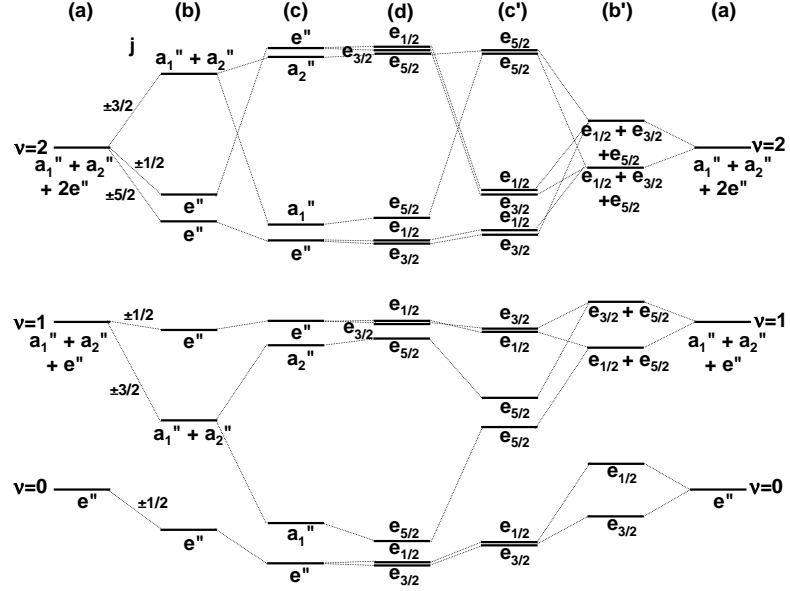


Figure 5.2: Qualitative energy level scheme of the vibronic energy levels of a $^2E''$ state under D_{3h} symmetry, with a single Jahn-Teller active mode of e' symmetry, for the following Hamiltonians.

(a) $\hat{\mathcal{H}}_{h,e}$; (b) $\hat{\mathcal{H}}_{h,e} + \hat{\mathcal{H}}_1$; (c) $\hat{\mathcal{H}}_{h,e} + \hat{\mathcal{H}}_1 + \hat{\mathcal{H}}_q$; (d) $\hat{\mathcal{H}}_{h,e} + \hat{\mathcal{H}}_1 + \hat{\mathcal{H}}_q + \hat{\mathcal{H}}_{SO}$; (c') $\hat{\mathcal{H}}_{h,e} + \hat{\mathcal{H}}_{SO} + \hat{\mathcal{H}}_1$; (b') $\hat{\mathcal{H}}_{h,e} + \hat{\mathcal{H}}_{SO}$; (a) $\hat{\mathcal{H}}_{h,e}$. The far left and far right columns are identical. Column (d) is a representative ordering of the energy levels when linear and quadratic Jahn-Teller coupling and spin-orbit coupling are included in the calculation. The left hand side of the diagram derives the energy levels of (d) via addition of the Jahn-Teller terms and then spin-orbit coupling, while the right hand side takes the opposite approach. They do, however, have a common result (d). The symmetry labels for (a)-(c) correspond to the irreducible representations of the D_{3h} group while those for (b'), (c') and (d) are for D_{3h}^2 .

where the index k of the expansion coefficients $C_k^{n_j'('')}$ represents all combinations, although not all have non-vanishing coefficients, of the basis-set quantum numbers $\Lambda'^{(\prime\prime)}$, $\nu_{1i}^{\prime(\prime\prime)}$, $\nu_{2i}^{\prime(\prime\prime)}$, $l_{2i}^{\prime(\prime\prime)}$ and $\Sigma'^{(\prime\prime)}$ and ' and " denote respectively the excited \tilde{A} and ground \tilde{X} states.

The expansion of the transition electric-dipole moment operator $T(r, Q)$ is truncated to include only the constant term $T(r, Q)_0 = T(r)_0$, where r and Q are the electronic and nuclear coordinates. The line intensity $I(j', n'_j, \Sigma'; j'', n''_j, \Sigma'')$ of the transition between any two spin-vibronic eigenstates is given by

$$\begin{aligned}
I(j', n'_j, \Sigma'; j'', n''_j, \Sigma'') &= |\langle j', n'_j, \Sigma' | T(r)_0 | j'', n''_j, \Sigma'' \rangle|^2 \\
&= \left| \left(\sum_k C_k^{n'_j} \langle \Lambda'_{E''}, \nu'_{1k}, \nu'_{2k} l'_{2k}, \Sigma' | T(r)_0 | \sum_i C_i^{n''_j} \Lambda''_{E'}, \nu''_{1i}, \nu''_{2i} l''_{2i}, \Sigma'' \rangle \right) \right|^2 \\
&= \left| \left(\sum_k \sum_i C_k^{n'_j} C_i^{n''_j} \langle \Lambda'_{E''} | T(r)_0 | \Lambda''_{E'} \rangle \langle \nu'_{1k} | \nu''_{1i} \rangle \langle \nu'_{2k} l'_{2k} | \nu''_{2i} l''_{2i} \rangle \delta_{\Sigma', \Sigma''} \right) \right|^2 \\
&= |\langle \Lambda'_{E''} | T(r)_0 | \Lambda''_{E'} \rangle|^2 \left(\sum_k \sum_i C_k^{n'_j} C_i^{n''_j} \langle \nu'_{1k} | \nu''_{1i} \rangle \langle \nu'_{2k} l'_{2k} | \nu''_{2i} l''_{2i} \rangle \right)^2 \delta_{\Sigma', \Sigma''} \quad (5.4)
\end{aligned}$$

Since the $\hat{\mathcal{H}}_e$ Hamiltonian is diagonal in S_z and $T(r)_0$ is independent of S , transitions can occur only between \tilde{X} - and \tilde{A} -state levels with the same projection of spin, S_z , i.e. $\delta_{\Sigma', \Sigma''} = 1$. Since $T(r)_0$ does not have a vibrational coordinate dependence, the term $\langle \Lambda'_{E''} | T(r)_0 | \Lambda''_{E'} \rangle$ may be factored out from the summation. The z component of the space vector in D_{3h} transforms as A''_1 and the (x, y) components as E' . Therefore the z component of the matrix element $\langle \Lambda'_{E''} | T(r)_0 | \Lambda''_{E'} \rangle$ will not vanish although the (x, y) components do.

The summation of Eq. 5.4 may be carried out numerically in SPEC-SOCJT, once the vibrational integrals $\langle \nu'_{1k} | \nu''_{1i} \rangle$ and $\langle \nu'_{2k} l'_{2k} | \nu''_{2i} l''_{2i} \rangle$ are estimated. The parameters

$$FC_{ki} = \langle \nu'_{1k} | \nu''_{1i} \rangle \quad (5.5)$$

are the a'_1 vibrational-function overlaps, and may be independently fit in SPEC-SOCJT for $i, k \leq 4$. In chapter 4 we found from our *ab initio* calculations that there is an equilibrium geometry difference of $\Delta R = 0.013 \text{ \AA}$ between $\tilde{X}^2\text{E}'$ (side of the D_{3h} triangle(\AA)=2.7491) and $\tilde{A}^2\text{E}''$ (side of the D_{3h} triangle(\AA)=2.7564). We also calculated the a'_1 frequencies of the \tilde{X} and \tilde{A} states to be 165 cm^{-1} and 162 cm^{-1} respectively. Using this information we calculate the FC_{ki} parameters with a program¹³² which assumes a one-dimensional oscillator along a'_1 . The resulting FC_{ki} parameters are shown in the second column of Table 5.2, labelled by their integral expression given in the first column of the same Table. Based on these values, we calculated the a'_1 Franck-Condon intensity profile of the \tilde{X} and \tilde{A} states and found it to be close but not exactly the same as the one observed experimentally. We adjusted the FC_{ki} parameters to obtain closer agreement with experiment and were led to the set of FC_{ki} parameters shown in the third column of Table 5.2. This set of FC_{ki} parameters is even more consistent with a set that is calculated¹³² if we assume that $\Delta R = 0.017 \text{ \AA}$ and use the experimentally fit a'_1 frequencies of 185 and 158.5 cm^{-1} of the \tilde{X} and \tilde{A} states respectively. We calculate $\langle \nu'_{2k} l'_{2k} | \nu''_{2i} l''_{2i} \rangle$ based on the approximation that only their diagonal terms retain non-zero value, i.e., $\langle \nu'_{2k} l'_{2k} | \nu''_{2i} l''_{2i} \rangle = \delta_{\nu'_{2k}, \nu''_{2i}} \delta_{l'_{2k}, l''_{2i}}$. The latter combined with the fact that only μ_z may be non-vanishing impose a strict

Integral ^a	Calc.I ^b	Fit ^c	Calc.II ^d
$\langle 0 0 \rangle$	0.8	0.7	0.7
$\langle 0 1 \rangle$	0.5	0.6	0.6
$\langle 0 2 \rangle$	0.2	0.5	0.3
$\langle 0 3 \rangle$	0.1	0.1	0.1
$\langle 1 0 \rangle$	0.5	0.6	0.6
$\langle 1 1 \rangle$	0.5	0.1	0.2
$\langle 1 2 \rangle$	0.6	0.6	0.6
$\langle 1 3 \rangle$	0.3	0.3	0.5
$\langle 2 0 \rangle$	0.2	0.3	0.3
$\langle 2 1 \rangle$	0.6	0.5	0.5
$\langle 2 2 \rangle$	0.3	0.1	0.1
$\langle 2 3 \rangle$	0.6	0.5	0.5
$\langle 3 0 \rangle$	0.1	0.2	0.2
$\langle 3 1 \rangle$	0.3	0.4	0.4
$\langle 3 2 \rangle$	0.6	0.3	0.3
$\langle 3 3 \rangle$	0.1	0.3	0.3

Table 5.2: Fitted and calculated spectral parameters, FC_{ki} , relevant to the determination of the Franck-Condon factors along the totally symmetric mode for Ag_3 .

^a Integrals written in the form $\langle \nu''_{1i} | \nu'_{1k} \rangle$, where ν''_{1i} and ν'_{1k} are the vibrational quantum numbers of a'_1 of $\tilde{X}^2\text{E}'$ and $\tilde{A}^2\text{E}''$. The Franck-Condon factors along the a'_1 mode would be proportional to the square of these integrals. ^b The FC_{ki} parameters under the column Calc. I were computed¹³² based on the *ab initio* predicted equilibrium geometry difference of 0.013 Å between $\tilde{X}^2\text{E}'$ and $\tilde{A}^2\text{E}''$ (see chapter 4), and the *ab initio* calculated frequencies $\omega_{e,a'_1}^{\tilde{X}}(\text{cm}^{-1}) = 165$ and $\omega_{e,a'_1}^{\tilde{A}}(\text{cm}^{-1}) = 162$, assuming a one-dimensional oscillator along a'_1 . ^c The experimentally fit FC_{ki} parameters. ^d Same with footnote b of this Table but for an equilibrium geometry difference of 0.017 Å and for the experimentally fit frequencies $\omega_{e,a'_1}^{\tilde{X}}(\text{cm}^{-1}) = 185$ and $\omega_{e,a'_1}^{\tilde{A}}(\text{cm}^{-1}) = 158.5$.

selection rule on the Jahn-Teller quantum number j : $\Delta j = 0$. The selection rule may relax to $\text{mod}(j, 3) = 0$ only when there is no orthogonality between the basis sets $|\nu'_{2k}l'_{2k}\rangle$ and $|\nu''_{2i}l''_{2i}\rangle$.

In the above formulation, the selection rule for j is given by $\Delta j = 0$ and for Σ by $\Delta\Sigma = 0$. In terms of D_{3h} point-group symmetry labels, the excitation from the vibrationless level of $\tilde{X}^2\text{E}'$ with e' symmetry can only terminate on levels in the $\tilde{A}^2\text{E}''$ state with e'' symmetry and vice versa. (Based on the electric-dipole moment component μ_z .) If one wanted to consider the general set of electric dipole-allowed selection rules in the D_{3h}^2 spin-double group then $E_{1/2} \longleftrightarrow E_{3/2}$ (allowed by $\text{E}'(\mu_x, \mu_y)$), $E_{1/2} \longleftrightarrow E_{5/2}$ (allowed by either $\text{E}'(\mu_x, \mu_y)$ or $A_2''(\mu_z)$), $E_{3/2} \longleftrightarrow E_{3/2}$ (allowed by $A_2''(\mu_z)$), and $E_{3/2} \longleftrightarrow E_{5/2}$ (allowed by $\text{E}'(\mu_x, \mu_y)$). Those spin-double-group transitions that are allowed by $A_2''(\mu_z)$ are the ones for which $\Delta j = 0$ and $\Delta\Sigma = 0$, which we only consider later on in the analysis.

5.2.3 Theoretical Simulations

The first simulations of the $\tilde{A} \longleftrightarrow \tilde{X}$ excitation spectrum used the *ab initio* calculated parameters of $\tilde{X}^2\text{E}'$ as initial input (Table 5.1.) The Hamiltonian matrix was diagonalized, and the eigenvalues and eigenvectors obtained showed that the lowest two spin-vibronic levels, i.e. $\Sigma = \pm \frac{1}{2}$, were nearly degenerate. We therefore adopted as a working hypothesis that the excitation spectrum arises by pumping both of these levels, which as we will later determine have eigenvalues of 0 and 2 cm^{-1} . Next, the matrix elements of the \tilde{A} -state Hamiltonian matrix were computed using the *ab initio*

calculated parameters of \tilde{A}^2E'' as an initial estimate. (Table 5.1.) After the diagonalization, the eigenvalues and eigenvectors of the lowest 25 vibronic energy levels from each spin-symmetry block of the spin-double group (i.e. with symmetries $e_{1/2}$, $e_{3/2}$, and $e_{5/2}$) were obtained for the \tilde{A}^2E'' state. (75 solutions total.) The frequencies and intensities of the resulting $\tilde{X}^2E' \rightarrow \tilde{A}^2E''$ spectrum were then calculated generating a simulated excitation spectrum. The spacings between the experimentally observed lines (as well as their intensity) was directly compared to the simulated spectrum. The spectral parameters of the \tilde{A}^2E'' state were adjusted to reproduce the frequencies and intensities of the experimentally observed spectrum. A satisfactory $\tilde{A} \leftarrow \tilde{X}$ simulation was obtained, which primarily was used to determine \tilde{A} state parameters.

Employing the experimentally determined spectral parameters of the \tilde{A}^2E'' state, the frequency and intensity simulations for the $\tilde{A} \rightarrow \tilde{X}$ emission spectrum began, which primarily depended upon the \tilde{X} state parameters. The above procedure followed many cycles of iteration until convergence. The experimentally determined spectral parameters from the global fit of the \tilde{X} - and \tilde{A} -state vibronic levels are summarized in Table 5.1. The FC_{ki} factors that were found as best to describe transitions involving the a'_1 levels are given in the second column of Table 5.2. The vibronic structure, assuming the fit constants, of both the \tilde{A} and \tilde{X} states is shown in Fig. 5.3.

The following procedure was used to provide the uncertainties in the fit parameters of the model as shown in Table 5.1. Using the calculated line positions from the best fit parameters determined according to the procedure described above, the

standard deviation was computed for all the experimental lines and the corresponding frequencies from the simulation. After that a particular constant was selected from the set of molecular parameters describing the electronic state and varied until the constantly monitored standard deviation of the simulation reached the value of $\sqrt{2}\sigma_0$, where σ_0 is the standard deviation of the optimal simulation. The error bars obtained by this method relate to the diagonal elements of the covariance matrix, and give 68% confidence limit for each of the constants. Although the intensities of the lines were considered while making line assignments, the error bars in Table 5.1 were derived solely from the analysis of the line frequencies.

5.3 Results

5.3.1 Assignment of the $\tilde{A}^2\text{E}''$ State

Although the REMPI^{17–20} and LIF spectra¹⁴ of “cold” Ag₃ have been known for quite some time, there are still open questions as to the complete assignment of the spectra. Table 5.3 lists the experimental frequencies of the $\tilde{A} \leftarrow \tilde{X}$ spectrum. The values were taken from Ref. 14, but are also consistent with the REMPI^{17–20} frequencies.

We first consider spectral assignments of the observed levels in the LIF spectrum lower than 370 cm⁻¹. (See Fig. 5.4.) The assignments are guided by our $\tilde{A}^2\text{E}''$ -state *ab initio* calculated Jahn-Teller and spin-orbit parameters from chapter 4. However, as these calculations did not fully account for pseudo-Jahn-Teller mixing with other

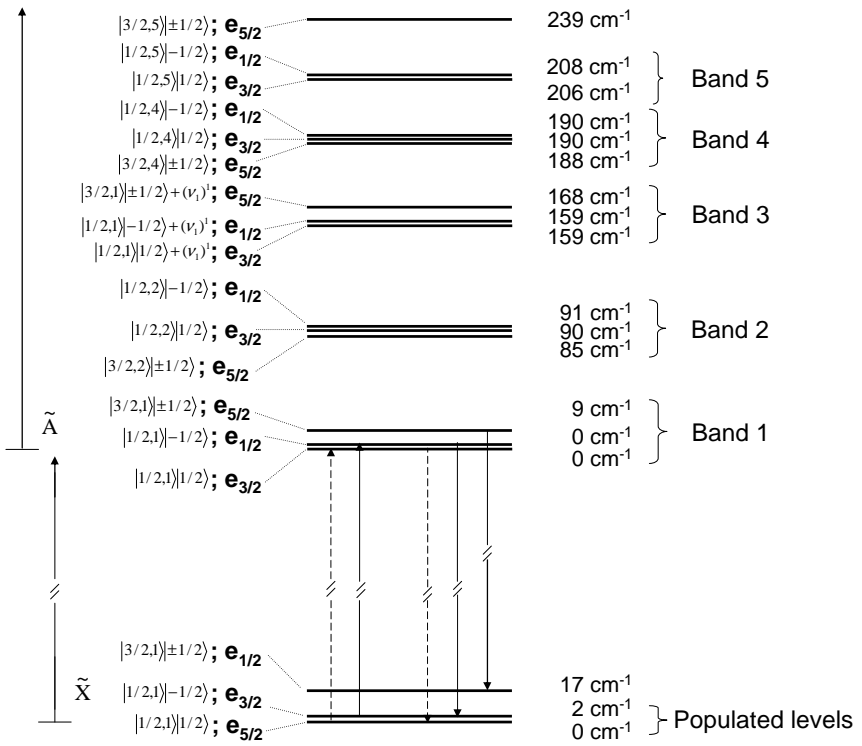


Figure 5.3: Energy level diagram of the lowest three spin-vibronic levels of the \tilde{X} state and those that characterize bands 1-5 of the \tilde{A} state. The ordering of the energy levels is not in scale. Their labels based on the $|j, n_j\rangle|\Sigma\rangle$ and the spin-double group notations are given at the left side of the Figure. Their energies (relative to the lowest level of the \tilde{X} and \tilde{A} states) were computed using the best-fit spectral parameters of the \tilde{X} and \tilde{A} states, and are shown at the right side of the Figure, in cm^{-1} . The dashed line at the left corresponds to the simulation's origin transition of the excitation spectrum depicted by 0 cm^{-1} in the fifth column of Table 5.3, and the star on top of it means that the spin-double group symmetry of the terminating level in the excitation has $e_{3/2}$. The transition with excitation frequency -2 cm^{-1} refers to $|\frac{1}{2}, 1\rangle| - \frac{1}{2}\rangle$ of $\tilde{X} \rightarrow |\frac{1}{2}, 1\rangle| - \frac{1}{2}\rangle$ of \tilde{A} . The terminating level in this transition has $e_{1/2}$ symmetry. The dashed line at the right corresponds, for the simulation of the emission spectrum laser excited to the origin of \tilde{A} , to the transition with the emission frequency of 0 cm^{-1} depicted in the fourth column of Table 5.4, and the star on top of it means that the terminating level in the emission has $e_{5/2}$ symmetry. The transition $|\frac{1}{2}, 1\rangle| - \frac{1}{2}\rangle$ of $\tilde{A} \rightarrow |\frac{1}{2}, 1\rangle| - \frac{1}{2}\rangle$ of \tilde{X} has an emission frequency of 2 cm^{-1} and terminates to a level of the \tilde{X} state with $e_{3/2}$ symmetry.

Assignment ($ j, n_j\rangle \Sigma\rangle$) ^a	Symmetry	Ag ₃ Frequency (cm ⁻¹)		
		Absolute ^b	Relative to 0 ₀ ⁰ ^b	Calc
$ \frac{1}{2}, 1\rangle \pm\frac{1}{2}\rangle$ (1)	$e_{1/2}, e_{3/2}$	26969.0	0.0	-2,0*
$ \frac{1}{2}, 2\rangle \pm\frac{1}{2}\rangle$ (2)	$e_{1/2}, e_{3/2}$	27069.5	100.5	89,90*
$ \frac{1}{2}, 3\rangle \pm\frac{1}{2}\rangle$	$e_{1/2}, e_{3/2}$	d	d	120,122*
$ \frac{1}{2}, 1\rangle \pm\frac{1}{2}\rangle + (\nu_1)^1$ (3)	$e_{1/2}, e_{3/2}$	27127.5	158.5	157,159*
$ \frac{1}{2}, 4\rangle \pm\frac{1}{2}\rangle$ (4)	$e_{1/2}, e_{3/2}$	27163.0	194.0	188,190*
$ \frac{1}{2}, 5\rangle \pm\frac{1}{2}\rangle$ (5)	$e_{1/2}, e_{3/2}$	27169.5	200.5	206,206*
$ \frac{1}{2}, 2\rangle \pm\frac{1}{2}\rangle + (\nu_1)^1$ (α)	$e_{1/2}, e_{3/2}$	27225.0	256.0	247,249*
$ \frac{1}{2}, 6\rangle \pm\frac{1}{2}\rangle$	$e_{1/2}, e_{3/2}$	d	d	248,250*
...	...	27245.5	276.5	...
$ \frac{1}{2}, 3\rangle \pm\frac{1}{2}\rangle + (\nu_1)^1$ (β)	$e_{1/2}, e_{3/2}$	27253.9	284.9	279,281*
$ \frac{1}{2}, 7\rangle \pm\frac{1}{2}\rangle$	$e_{1/2}, e_{3/2}$	27267.9	298.9	308,308*
$ \frac{1}{2}, 1\rangle \pm\frac{1}{2}\rangle + (\nu_1)^2$	$e_{1/2}, e_{3/2}$	27283.3	314.3	316,318*
$ \frac{1}{2}, 8\rangle \pm\frac{1}{2}\rangle$	$e_{1/2}, e_{3/2}$	d	d	317,319*
...	...	27299.0	330.0	...
$ \frac{1}{2}, 9\rangle \pm\frac{1}{2}\rangle$	$e_{1/2}, e_{3/2}$	27312.2	343.2	345,346*
$ \frac{1}{2}, 4\rangle \pm\frac{1}{2}\rangle + (\nu_1)^1$ (γ)	$e_{1/2}, e_{3/2}$	27322.9	353.9	347,349*
$ \frac{1}{2}, 5\rangle \pm\frac{1}{2}\rangle + (\nu_1)^1$ (δ)	$e_{1/2}, e_{3/2}$	27328.4	359.4	365,365*

Table 5.3: Frequencies and $\tilde{A}^2E''-\tilde{X}^2E'$ transition assignments of Ag₃.

^a We denote with numbers (1-5) those bands of the \tilde{A} state from which we have collected emission spectra. The labels (α - δ) refer to transitions to combination levels in the \tilde{A} state between the totally symmetric a'_1 fundamental and the e' Jahn-Teller active levels. See also footnote for Fig. 5.3. Note that in the first column under assignment we give the spectroscopic designation of the spin-vibronic terminating levels of the transitions originating in $|\frac{1}{2}, 1\rangle|\pm\frac{1}{2}\rangle$ of the \tilde{X} state. The calculated excitation frequencies are given in the fifth column, where asterisks distinguish transitions to $e_{3/2}$ levels of the \tilde{A} state from transitions to $e_{1/2}$ levels. ^b d stands for dark and refers to transitions with predicted intensity $\leq 5\%$ of the strongest intensity transition of the simulation.

states, we had to significantly adjust the \tilde{A}^2E'' parameters, thereby generating a set of preliminary experimental parameters. They were refined based on the methodology outlined in Section 5.2.3.

We first identified the fundamental a'_1 band in the $\tilde{A}^2E''-\tilde{X}^2E'$ spectrum shown in Fig. 5.4. The band peaking at 158 cm^{-1} to the blue of the origin was assigned to the fundamental of a'_1 based on our *ab initio* value of 162 cm^{-1} . (As labelled in Fig. 5.4 this band is hereafter referred to as band 3, with band 1, the lowest frequency band assumed to be the origin.) Also its laser excited, dispersed fluorescence spectrum qualitatively matches the one collected from the origin as expected for the totally symmetric vibrational mode. Hence all other bands located lower than 200 cm^{-1} must involve e' Jahn-Teller levels. Thus we assign band 2 near 100 cm^{-1} to the lowest ($n_j = 2$) e' vibration excitation. The band at 256 cm^{-1} may be assigned to a combination band of the fundamental of a'_1 with the $n_j = 2, e'$ level. Correspondingly bands 4 and 5 must be assigned to the next two allowed transitions to e' levels with $n_j = 4$ and 5. (See also Table 5.3.)

The first overtone of a'_1 may be assigned to either the band at 299 cm^{-1} or at 314 cm^{-1} depending on the degree of anharmonicity along the a'_1 direction of the potential. From the *ab initio* calculations of chapter 4 we expect for $\omega_e \chi_e$ of a'_1 to be $\leq 1\text{ cm}^{-1}$. Hence the feature at 299 cm^{-1} arises from a transition to an e' Jahn-Teller level and the one at 314 cm^{-1} must be the first overtone of a'_1 . Moving further to the blue from the origin, we note a partially resolved structure with excitation frequencies of 354 and 359 cm^{-1} . This doublet may be assigned as combination bands between the

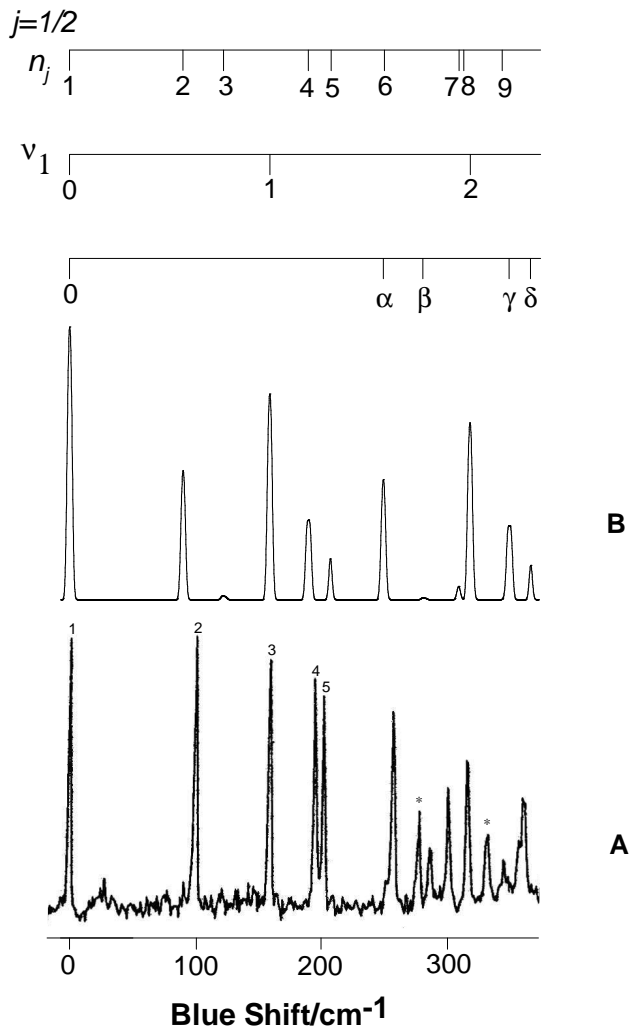


Figure 5.4: Excitation spectrum of Ag_3 , from $|\frac{1}{2}, 1\rangle \pm \frac{1}{2}\rangle$ of the $\tilde{X}^2\text{E}'$ state.

(A) Experimental trace. (bottom trace). The origin transition is at 26969.0 cm^{-1} . The x-axis indicates (blue) shift from the origin transition. The experimental resolution is $\approx 3 \text{ cm}^{-1}$. (B) Positions of the transitions to the e' Jahn-Teller active levels (labelled 1...9), the totally symmetric a'_1 level and its overtone (labelled 1,2) as well as their combinations (labelled $\alpha, \beta, \gamma, \delta$) with the Jahn-Teller active levels, with $j = 1/2$ symmetry, computed with SPEC-SOCJT using the best-fit spectral parameters of the $\tilde{X}^2\text{E}'$ and $\tilde{A}^2\text{E}''$ states. (top trace).

fundamental of a'_1 with the e' bands 4 and 5. We examined whether the corresponding combinations with the first overtone of a'_1 appear in the spectrum. This is confirmed from previously recorded experimental excitation frequencies.¹⁸

Our assignments for the levels $\leq 256 \text{ cm}^{-1}$ are in agreement with past work^{14,17}. There was dispute about whether the first overtone of a'_1 should be attributed to the peak at 314^{17} or 299^{14} cm^{-1} . The bands at 354 and 359 cm^{-1} were previously assigned as either e' Jahn-Teller levels¹⁴ or as combinations of a'_1 with e' levels.¹⁷

We simulated the vibronic structure of the $\tilde{A}^2\text{E}''-\tilde{X}^2\text{E}'$ excitation spectrum using the above assignments and according to the methodology of Section 5.2.3. Our assumption is that the lowest two spin-vibronic wave functions of the \tilde{X} state, i.e. $|\frac{1}{2}, 1\rangle |\Sigma = \pm 1/2\rangle$, are equally populated in the jet expansion and both excited within the laser bandwidth. (See Fig. 5.3. It should be noted that the experimental excitation spectrum is insensitive to the assumption of whether the upper spin component is excited or not.)

We expect transitions to the \tilde{A} state that satisfy $\Delta j = 0$ and $\Delta\Sigma = 0$, as shown in Fig. 5.3. Table 5.3 presents the experimental (third and fourth columns) and calculated (fifth column) excitation frequencies. The latter were based on the fit \tilde{A} -state spectral parameters of Table 5.1, assuming that the transition $|\frac{1}{2}, 1\rangle |\frac{1}{2}\rangle$ of $\tilde{X} \rightarrow |\frac{1}{2}, 1\rangle |\frac{1}{2}\rangle$ of \tilde{A} is the origin of our simulated excitation spectrum, with excitation frequency 0 cm^{-1} as noted in the Table. Hence the transition $|\frac{1}{2}, 1\rangle | - \frac{1}{2}\rangle$ of $\tilde{X} \rightarrow |\frac{1}{2}, 1\rangle | - \frac{1}{2}\rangle$ of \tilde{A} has an excitation frequency of -2 cm^{-1} . The asterisks in Table 5.3 distinguish transitions to spin-vibronic levels with $e_{3/2}$ spin-double group symmetries.

from transitions to $e_{1/2}$ levels of the \tilde{A} state. (See second column of Table 5.3 and Fig. 5.2.) In the first column of Table 5.3, under assignment, the terminating spin-vibronic levels of such transitions to the \tilde{A} state are given. Note also that the spin-orbit coupling in the \tilde{A} state is largely quenched from the Jahn-Teller effect. The spin-vibronic transitions to the \tilde{A} state are not experimentally resolved. Fig. 5.4B presents our simulation of the excitation spectrum. It was based on the \tilde{X}^2E' - and \tilde{A}^2E'' -state final spectral parameters of Table 5.1. (The calculated intensity pattern of \tilde{A}^2E'' is dependent on the \tilde{X}^2E' -state spectral parameters. See Section 5.3.2 for \tilde{X} -state assignments.)

The origin of the excited-state spectrum has been experimentally identified to peak at 26969.0 cm^{-1} . The next intense feature is at 100 cm^{-1} and may be attributed to $|j, n_j\rangle|\Sigma\rangle = |\frac{1}{2}, 2\rangle|\pm 1/2\rangle$. The final two prominent features in the spectrum that gain intensity due to a Jahn-Teller coupling mechanism peak at 27163.0 cm^{-1} and 27169.5 cm^{-1} . They are assigned in respect to $|\frac{1}{2}, 4\rangle|\pm 1/2\rangle$ and $|\frac{1}{2}, 5\rangle|\pm 1/2\rangle$. The features at 299 cm^{-1} and 343 cm^{-1} are assigned respectively to transitions to $|\frac{1}{2}, 7\rangle|\pm 1/2\rangle$ and $|\frac{1}{2}, 9\rangle|\pm 1/2\rangle$ but their calculated intensity does not match well with experiment. Note that little or no intensity is predicted to the levels with $j = \frac{1}{2}$ and $n_j = 3, 6$ and 8 corresponding to bands at $\approx 121, 249$ and 318 cm^{-1} . This completes the assignments of all Jahn-Teller active levels lower than 370 cm^{-1} . They are shown in Fig. 5.4B where also the fundamental and first overtone of a'_1 ($\nu_1 = 1, 2$) as well as its combinations with Jahn-Teller levels $(\alpha, \beta, \gamma, \delta)$ are presented, although β is predicted to have little intensity.

While the majority of the most pronounced features of the \tilde{A} -state's vibronic structure lower than 370 cm^{-1} has been predicted by our model, the bands at 276 and 330 cm^{-1} have not. (These are denoted with an asterisk in Fig. 5.4A.) Although there are hypotheses as to their nature, no straightforward assignments may be given to them at this point. These can not be attributed to $j = 3/2$ levels, since under such an assumption additional vibronic structure is predicted that is not experimentally observed in the excitation spectrum.

It has been suggested^{15, 133} that the linear structural isomer of Ag_3 ($\tilde{X}^2\Sigma_u^+$ in $D_{\infty h}$) lies 800 cm^{-1} above the Jahn-Teller stabilized \tilde{X}^2B_2 electronic state. It is possible that, with the bent isomer, the linear geometrical configuration of Ag_3 is also produced and populated under jet-cooling conditions in the various experiments.^{14, 17–20} The Franck-Condon intensity of the vibrational origin for a linear-to-bent transition is expected to be very weak, due to the extreme change in the geometry. However, there could be a transition between a linear $^2\Sigma_u^+$ ground state and a linear excited state. One would expect activity only for the symmetric stretch or even-only quanta in an asymmetric stretch or bend. Previous experimental work¹³⁴ has determined the following neutral excited states at linear geometry above $\tilde{X}^2\Sigma_u^+$ which lie the closest to the origin of the $\tilde{A}\text{ }^2\text{E}'' \leftarrow \tilde{X}\text{ }^2\text{E}'$ excitation spectrum: $^2\Pi_g^+$ with an energy at 25326 cm^{-1} above $\tilde{X}^2\Sigma_u^+$ (3.14 eV) and $^2\Sigma_u^+$ with an energy at 27180 cm^{-1} above $\tilde{X}^2\Sigma_u^+$ (3.37 eV). Whereas the transition from the ground to $^2\Sigma_u^+$ is symmetry forbidden, the transition $^2\Sigma_u^+ \rightarrow ^2\Pi_g^+$ is electronically allowed. Depending on the degree of the accuracy of the theoretically determined energy minimum of the linear structural

isomer of Ag_3 , which also determines the accuracy of the molecule's energy above the \tilde{X}^2E' -state's vibrationless level of the bend isomer, and the experimentally determined transition energy between $\tilde{X}^2\Sigma_u^+$ and ${}^2\Pi_g^+$, it is possible that linear-to-linear transitions may be manifested in the energy region of interest and farther to the blue from the $\tilde{A}^2\text{E}''$ -state origin of Ag_3 .

Probably more likely is that the additional lines in the $\tilde{A}^2\text{E}'' \leftarrow \tilde{X}^2\text{E}'$ excitation spectrum may be part of the vibronic structure of other nearby optically bright electronic states of Ag_3 in its bent geometrical configuration. Previous experimental work¹⁸ observed a dense but resolvable excitation spectrum between 370 and 1000 cm^{-1} above the $\tilde{A}^2\text{E}''$ -state origin. There appear to be too many lines to assign to the $\tilde{A}^2\text{E}'' \leftarrow \tilde{X}^2\text{E}'$ spectrum and part of this structure may be due to a different electronic state. Our theoretical computations (see chapter 4) suggest the next highest electronic state (${}^2\text{E}'$ symmetry) should be considered a reasonable candidate. It is an optically bright electronic state via the $E'(x, y)$ electric dipole moment component in D_{3h} and lies the closest in energy to the $\tilde{A}^2\text{E}''$ state. (Our calculations from chapter 4 predict as a best estimate an excitation energy to the higher excited state (${}^2\text{E}'$) of approximately 31000 cm^{-1} , and to $\tilde{A}^2\text{E}''$ 27000 cm^{-1} , assuming a D_{3h} geometry for Ag_3 . We noted that the calculated energy difference between these states decreases in higher order calculations.) This electronic state, Jahn-Teller active via a linear and quadratic mechanism, may be responsible for much of the irregular pattern of vibronic energy levels observed between 370 and 1000 cm^{-1} above the origin. However, it should be mentioned that our model predicts an increasing congestion of energy

levels, proportional to the extent of departure to the blue from the origin and higher in energy than 370 cm^{-1} that is due to combinations of the overtones of the totally symmetric mode with the Jahn-Teller active levels. The plethora of bands, though strong and resolved, in the energy region between 370 and 1000 cm^{-1} above the origin makes it difficult to pursue their assignment and their classification as $\tilde{A}\text{ }^2\text{E''-state-}$ or excited $^2\text{E'-state}$ vibronic structure. (See chapter 4 for a discussion about the accuracy of the theoretical calculations of the adiabatic transition energies for the excited states of D_{3h} structures of Ag_3 .)

5.3.2 Assignment of the $\tilde{X}\text{ }^2\text{E'}$ State

Laser excited, wavelength resolved emission (LEDF) spectra were collected from each of the five labelled bands shown in the Ag_3 excitation spectrum in Fig. 5.4. The $\tilde{A}\text{ }^2\text{E''-state}$ assignments are critical to the interpretation of the LEDF spectra. Our initial assignments for the emission frequencies particularly with respect to intensities were based on our *ab initio* spectral parameters for the ground state, which we believe are more reliable than for the \tilde{A} state.

5.3.3 Emission from Band 1 of the \tilde{A} State of Ag_3

The experimental LEDF spectrum from band 1 of $\tilde{A}\text{ }^2\text{E''}$ is shown in Fig. 5.5A. Transitions involving the Jahn-Teller active levels $|1/2, n_j\rangle|\Sigma = +1/2\rangle$ are shown in Figs. 5.5B-5.5E and 5.5G. The emission intensities are calculated by SPEC-SOCJT assuming that all oscillator strength results from the Jahn-Teller mixing for the e' mode. The intensities derived from Table 5.2 for the a'_1 mode Franck-Condon envelope

are included in Figs. 5.5D-5.5G. We first make assignments to transitions to the e' Jahn-Teller spectrum and then consider the transitions to a'_1 levels and finally their combinations with the Jahn-Teller levels.

The assignment of the transitions to the e' Jahn-Teller spin-vibronic levels started with a simulation of the spectrum using the *ab initio* calculated parameters of the \tilde{X}^2E' state. (Fig. 5.5B.) The most intense feature to the red of the origin of the simulation in Fig. 5.5B must reasonably correlate with either the first or second feature of the experimental spectrum. Assignment to the first feature above the origin of the experimental trace of this feature proved to produce simulations of the other four emission traces inconsistent with the experimental observation. Thus the feature is assigned to the second experimental band and the Jahn-Teller parameters adjusted accordingly. (See Fig. 5.5C.)

Fig. 5.5D presents the transitions to the $j = 1/2$ levels plus those terminating in the a'_1 level and its combinations with the Jahn-Teller levels. The calculations were based on the *ab initio* spectral parameters of the \tilde{X}^2E' state. The only logical experimental candidate for assignment to the fundamental of a'_1 is the third feature to the red from the origin. By making this assignment, and further adjustment of its position to the experiment, a good match in intensity and position is achieved for all other predicted features of 5.5D. Fig. 5.5E shows these results. It is constructed from $j = 1/2$ levels, a'_1 levels and their combinations with Jahn-Teller levels and is calculated based on the experimental spectral parameters of \tilde{X}^2E' .

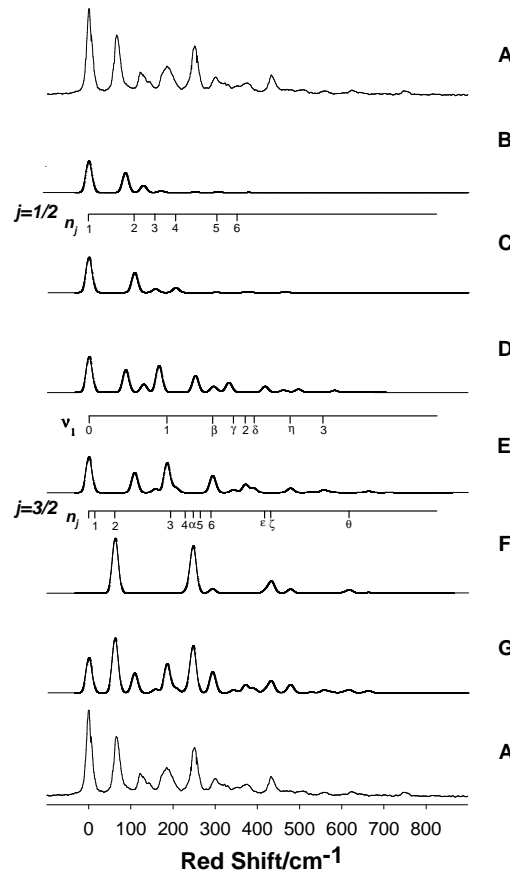


Figure 5.5: Emission spectrum of Ag_3 , laser excited to the vibrationless level of the $\tilde{A}^2\text{E}''$ state.

(A) Experimental trace from ref. 14 (top and bottom traces.); (B) Positions of the transitions to the e' Jahn-Teller active levels with $j = 1/2$ symmetry, computed using the *ab initio* calculated Jahn-Teller parameters of the $\tilde{X}^2\text{E}'$ state; (C) Same as (B) but using the best-fit Jahn-Teller parameters of the $\tilde{X}^2\text{E}'$ state; (D) Same as (B) plus the positions of the transitions to the totally symmetric a'_1 level and its overtones (labelled in E as 1-3), as well as their combinations (labelled in E as $\beta, \gamma, \delta, \eta$) with the Jahn-Teller active levels; (E) Same as (D) but using the experimentally determined parameters of the $\tilde{X}^2\text{E}'$ state; (F) Positions of the transitions to the e' $j = 3/2$ Jahn-Teller active levels as well as their combinations (labelled $\alpha, \varepsilon, \zeta, \theta$) with the totally symmetric a'_1 level and its overtones as computed with SPEC-SOCJT based on the parameters of the $\tilde{X}^2\text{E}'$ state experimentally determined from steps (B)-(E); (G) Simulated emission spectrum obtained by summing traces (E) and (F).

However the structure in 5.5E only accounts for part of the experimental spectrum. We examined the possibility of emission from the \tilde{A} -state spin component of $|\frac{3}{2}, 1\rangle$, as this transition previously explained part of the $\tilde{X}^2\text{E}'$ -state experimental data of a homologous system, Cu₃.¹³⁵ (See Figs. 5.2 and 5.3.) We found that the structure missing from the simulation of Fig. 5.5E is indeed consistent with transitions to the $j = 3/2 e'$ Jahn-Teller levels in the \tilde{X} state, as is shown in Fig. 5.5F. The calculation of the emission frequencies is based on the Jahn-Teller parameters for the $\tilde{X}^2\text{E}'$ state determined in the steps illustrated in Figs. 5.5B-D. The intensities of the spectra in steps 5.5E and F were calculated assuming that the spin components of $|\frac{1}{2}, 1\rangle$ and $|\frac{3}{2}, 1\rangle$ are equally excited in the \tilde{A} state. As was previously noted,¹³⁵ Coriolis interactions involving in-plane rotation will mix these levels.

As we will see later in the analysis of the emission spectra through bands 2-4, the contribution from the transitions to the $j = 3/2$ levels of the \tilde{X} state will continue to be important. However, the simulation of the emission from band 5 of the \tilde{A} state does not predict any clearly observable $\tilde{A} \rightarrow \tilde{X} j = 3/2$ transitions and none are observed. This is consistent with Fig. 5.3 which clearly shows that the $j = 3/2$ level of band 5 lies approximately 3.5 times higher in energy than the two $j = 1/2$ spin-vibronic levels of the same band, relative to the corresponding energy separation between the same levels but for bands 1-4. The excitation spectrum does not show any evidence of a resolved transition to the lowest $j = 3/2$ level of the \tilde{A} state. However it could be contained within the 3 cm^{-1} of the experimental linewidth of the excitation spec-

trum since we expect a computational error of approximately 5-10 cm⁻¹ for the calculated energies of the $j=1/2$ and $j=3/2$ levels of the \tilde{A} state, which likely are a lot closer than is shown in Fig. 5.3. (See Section 5.4.)

The “combs” in Figs. 5.5C and 5.5F mark the progressions in $j = 1/2$ and $j = 3/2$ e' levels. Only the first 6 members are shown. Except the trivial assignment of the origin, there are 2 assignments to experimental transitions; the band at 121 cm⁻¹ may be attributed to $|\frac{1}{2}, 2\rangle| \pm \frac{1}{2}\rangle$ and the level $|\frac{3}{2}, 2\rangle| \pm \frac{1}{2}\rangle$ may be assigned to the intense feature at 67 cm⁻¹. (Note that since the $j = 3/2$ levels transform as the same $e_{1/2}$ symmetry in the \tilde{X} state under the spin double group, they will be mixed with each other by the spin-orbit coupling. Hence their spin wave functions are linear combinations of $|\Sigma = \pm \frac{1}{2}\rangle$.) The levels $|\frac{1}{2}, 3\rangle| \pm \frac{1}{2}\rangle$, $|\frac{1}{2}, 4\rangle| \pm \frac{1}{2}\rangle$, $|\frac{3}{2}, 4\rangle| \pm \frac{1}{2}\rangle$ and $|\frac{3}{2}, 6\rangle| \pm \frac{1}{2}\rangle$ exhibit fluorescence intensity in the emission but at frequencies that may not be experimentally resolved from other features in the spectrum. All other $j = 1/2$ and $j = 3/2$ levels up to $n_j = 13$ are predicted to have negligible intensity.

The transitions to the energy levels of the first three quanta of excitation of a'_1 as well as to their combination with $j = 3/2$ levels are included in 5.5F. Our final simulated emission spectrum (Fig. 5.5G) is constructed by adding the vibronic structures of Figs. 5.5E and 5.5F. Notice the particular contribution that the $j = 3/2$ vibronic structure has to the overall simulation presented in Fig. 5.5G; the most intense fea-

tures, though fewer in number in comparing with the $j = 1/2$ structure, are due to the $j = 3/2$ transitions to the \tilde{X} state. There seems to be a one-to-one correspondence between the experimentally observed features and the simulated ones in 5.5G.

Table 5.4 presents the “assignments” to the terminating energy levels of the transitions to the \tilde{X} state (first column) to the experimentally observed lines (third column) of the emission from band 1 of \tilde{A}^2E'' . Their corresponding calculated emission frequencies (see Fig. 5.3) are given in the fourth column of Table 5.4, and were based on the experimental spectral parameters of the \tilde{X}^2E' state. Asterisks distinguish transitions to $e_{5/2}$ levels of the \tilde{X} state from transitions to $e_{3/2}$ levels for the $j = 1/2$ e' levels. The symmetry of the $j = 3/2$ e' levels is $e_{1/2}$. The spin double group symmetries of all levels are given in the second column. The emission frequency of 0 cm^{-1} in the simulated emission spectrum corresponds to the transition from $|\frac{1}{2}, 1\rangle|\frac{1}{2}\rangle$ of \tilde{A}^2E'' to $|\frac{1}{2}, 1\rangle|\frac{1}{2}\rangle$ of \tilde{X}^2E' . Note that the calculated emission frequencies of the transitions to the $|\frac{1}{2}, n_j\rangle|\pm\frac{1}{2}\rangle$ levels of the \tilde{X} state are not the same for a given n_j value since the spin-orbit coupling in the \tilde{X} state is not completely quenched from the Jahn-Teller interaction as it is in the \tilde{A} state. This may explain, in part, the observed broadness of the emission spectrum. (The $j = 1/2$ Jahn-Teller spectra of Figs. 5.5B-5.5E and 5.5G were artificially broadened to take into account the transitions to the $|1/2, n_j\rangle|\Sigma = -1/2\rangle$ Jahn-Teller active levels of the \tilde{X} state.)

Bands ^a 1 and 3			
Assignment ($ j, n_j\rangle \Sigma\rangle$)	Symmetry	Exp ^b	Calc
$ 1/2, 1\rangle \pm 1/2\rangle$	$e_{5/2}, e_{3/2}$	0 [0]	0*,2
$ 3/2, 1\rangle \pm 1/2\rangle$	$e_{1/2}$	d [d]	8
$ 3/2, 2\rangle \pm 1/2\rangle$	$e_{1/2}$	67 [67]	62
$ 1/2, 2\rangle \pm 1/2\rangle$	$e_{3/2}, e_{5/2}$	121 [121]	103,108*
$ 1/2, 3\rangle \pm 1/2\rangle$	$e_{5/2}, e_{3/2}$	u [151]	157*,164
$ 1/2, 1\rangle \pm 1/2\rangle + (\nu_1)_1$	$e_{5/2}, e_{3/2}$	184 [d]	185*,187
$ 3/2, 3\rangle \pm 1/2\rangle$	$e_{1/2}$	d [d]	193
$ 1/2, 4\rangle \pm 1/2\rangle$	$e_{5/2}, e_{3/2}$	u [215]	205*,213
$ 3/2, 4\rangle \pm 1/2\rangle$	$e_{1/2}$	u [243]	233
$ 3/2, 2\rangle \pm 1/2\rangle + (\nu_1)_1$	$e_{1/2}$	250 (α) [d]	247
$ 3/2, 5\rangle \pm 1/2\rangle$	$e_{1/2}$	d [d]	263
$ 1/2, 2\rangle \pm 1/2\rangle + (\nu_1)_1$	$e_{3/2}, e_{5/2}$	302 (β) [d]	288,293*
$ 3/2, 6\rangle \pm 1/2\rangle$	$e_{1/2}$	u [302]	292
$ 1/2, 5\rangle \pm 1/2\rangle$	$e_{3/2}, e_{5/2}$	d [d]	298,301*
$ 1/2, 3\rangle \pm 1/2\rangle + (\nu_1)_1$	$e_{5/2}, e_{3/2}$	350 (γ) [d]	342*,349
$ 1/2, 6\rangle \pm 1/2\rangle$	$e_{5/2}, e_{3/2}$	d [d]	349*,357
$ 1/2, 1\rangle \pm 1/2\rangle + (\nu_1)_2$	$e_{5/2}, e_{3/2}$	367 [367]	370*,372
$ 1/2, 4\rangle \pm 1/2\rangle + (\nu_1)_1$	$e_{5/2}, e_{3/2}$	u (δ) [d]	390*,398
$ 3/2, 4\rangle \pm 1/2\rangle + (\nu_1)_1$	$e_{1/2}$	u (ε) [d]	418
$ 3/2, 2\rangle \pm 1/2\rangle + (\nu_1)_2$	$e_{1/2}$	430 (ζ) [430 (α)]	432
$ 1/2, 2\rangle \pm 1/2\rangle + (\nu_1)_2$	$e_{3/2}, e_{5/2}$	481 ^c (η) [481 (β)]	473,478*
$ 1/2, 3\rangle \pm 1/2\rangle + (\nu_1)_2$	$e_{5/2}, e_{3/2}$	520 [520 (γ)]	527*,534
$ 1/2, 1\rangle \pm 1/2\rangle + (\nu_1)_3$	$e_{5/2}, e_{3/2}$	548 [548]	555*,557
$ 1/2, 4\rangle \pm 1/2\rangle + (\nu_1)_2$	$e_{5/2}, e_{3/2}$	d [u (δ)]	575*,583
$ 3/2, 4\rangle \pm 1/2\rangle + (\nu_1)_2$	$e_{1/2}$	d [u (ε)]	603
$ 3/2, 2\rangle \pm 1/2\rangle + (\nu_1)_3$	$e_{1/2}$	611 (θ) [611 (ζ)]	617
$ 3/2, 6\rangle \pm 1/2\rangle + (\nu_1)_2$	$e_{1/2}$	d [u]	662
$ 1/2, 2\rangle \pm 1/2\rangle + (\nu_1)_3$	$e_{5/2}, e_{3/2}$	d [665 (η)]	663*,658

Table 5.4: Calculated and experimentally observed spectral transitions to the $\tilde{X}^2\text{E}'$ state originating in bands 1 and 3 of the $\tilde{A}^2\text{E}''$ state of Ag_3 .

^a For emission from bands 1 and 3 (in brackets), the assignments to all experimental bands lower than 665 cm^{-1} are presented. ^b u denotes unresolved transitions, and d stands for dark and refers to transitions with predicted intensity $\leq 5\%$ of the strongest intensity transition of the simulation. The estimated experimental error is $< 10 \text{ cm}^{-1}$.

^c Dual assignment; $|3/2, 6\rangle |\pm 1/2\rangle + (\nu_1)_1$, calculated energy 477.

5.3.4 Emission from Band 3 of the \tilde{A} State of Ag_3

We examine next the emission from band 3 which is the fundamental of a'_1 in the $\tilde{A}^2\text{E}''$ state. While there are many spectral features that are common with the emission through the origin, the spectrum is dominated by very strong features to the red by ca. 450 cm^{-1} . The corresponding ones in the origin emission are weaker. Two predominant bands at ca. 180 and 250 cm^{-1} in the origin emission completely disappear in the a'_1 emission.

The experimental spectrum is given in Fig. 5.6A. Our simulation is presented in Fig. 5.6B. Jahn-Teller levels of $j = 1/2$ and $j = 3/2$ symmetry are computed as well as their combinations with a'_1 levels. The Jahn-Teller active portion of the spectrum is given first, then the assignments of the fundamental and overtones of a'_1 are presented along with its combinations with the Jahn-Teller levels, finalizing the totality of the assignments lower than 665 cm^{-1} . The calculation of the energy levels is based on the experimental molecular parameters of the $\tilde{X}^2\text{E}'$ state. As with the origin emission, the most intense features of the spectrum are again due to transitions to $j = 3/2$ levels. There is a one-to-one correspondence between experiment and simulation in an extensive energy region to the red of the origin from which we can extract the a'_1 Franck-Condon factors. The reader is referred to Table 5.4 for a comparison between experimental (third column in parentheses) and calculated emission frequencies. The emission frequency of 0 cm^{-1} in the simulated emission spectrum corresponds to the transition from $|\frac{1}{2}, 1\rangle|\frac{1}{2}\rangle + (\nu_1)^1$ of $\tilde{A}^2\text{E}''$ to $|\frac{1}{2}, 1\rangle|\frac{1}{2}\rangle$ of $\tilde{X}^2\text{E}'$.

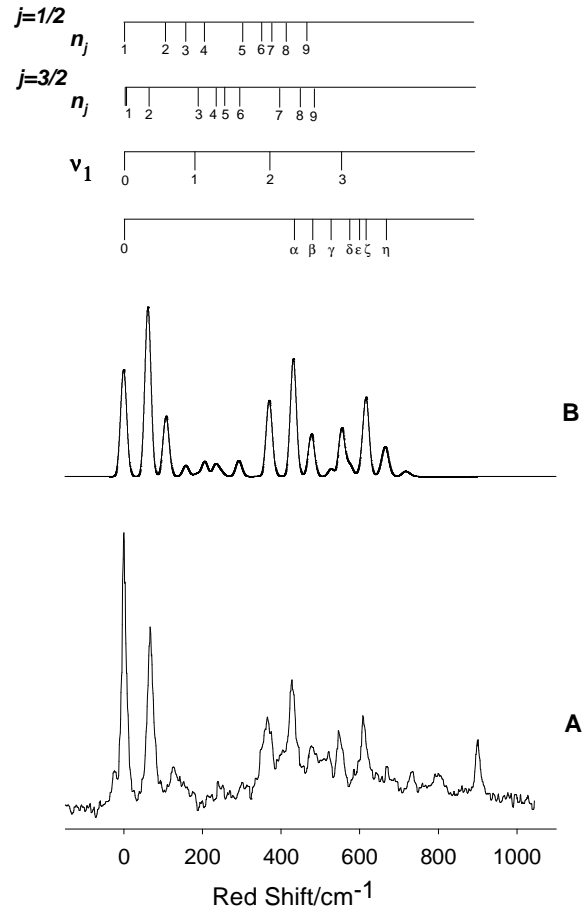


Figure 5.6: Emission spectrum of Ag_3 , laser excited to band 3 of the $\tilde{A}^2\text{E}''$ state.

(A) Experimental trace from ref. 14 (bottom trace); (B) Positions of the transitions to the $j = 1/2$ Jahn-Teller active levels and $j = 3/2$ Jahn-Teller active levels as well as their combinations (labelled $\alpha, \beta, \gamma, \delta, \varepsilon, \zeta, \eta$) with the totally symmetric a'_1 level and its overtones (labelled 1-3) as computed with SPEC-SOCJT based on the experimentally determined parameters of the $\tilde{X}^2\text{E}'$ state. (top trace.)

Based on Fig. 5.6B we add assignments for $n_j = 3, 4$ for the $j = 1/2$ levels and $n_j = 4, 6$ for the $j = \frac{3}{2}$ levels to our total set. (See Table 5.4.) Other new features arise as transitions to combinations with a'_1 . We have a nearly comprehensive assignment of the spectral lines below 655 cm^{-1} and very good agreement with the observed LEDF spectrum.

The emissions from the origin and the fundamental of a'_1 in the $\tilde{A}^2\text{E}''$ state are different in that (i) the fundamental of a'_1 exhibits little intensity in the a'_1 emission in contrast with the corresponding one in the origin emission, (ii) while the relative intensity profile of the first and second overtones of a'_1 is approximately the same in both emissions (with the first overtone exhibiting stronger intensity), their intensities are comparably greater in the a'_1 emission. Hence their combinations with Jahn-Teller levels may exhibit stronger intensity in the a'_1 emission. The Franck-Condon factors of Table 5.2 are consistent with the above experimental observations.

5.3.5 Emission from Band 4 of the \tilde{A} State of Ag_3

The experimental emission spectrum originating in band 4 of the $\tilde{A}^2\text{E}''$ -state is given in Fig. 5.7A. It is characterized by complex and broad band patterns, which are nonetheless relatively intense.

The construction of Figs. 5.7B-5.7G follows the same logic as Figs. 5.5B-5.5G. Particularly challenging was the initial assignment of the $j = 1/2$ levels. (Fig. 5.7B.) The first feature to the red from the origin in the experimental trace could likely be attributed to the first most intense feature above the origin of the calculated emission spectrum shown in Fig. 5.7B. In doing so we found no reasonable set of \tilde{X} -state

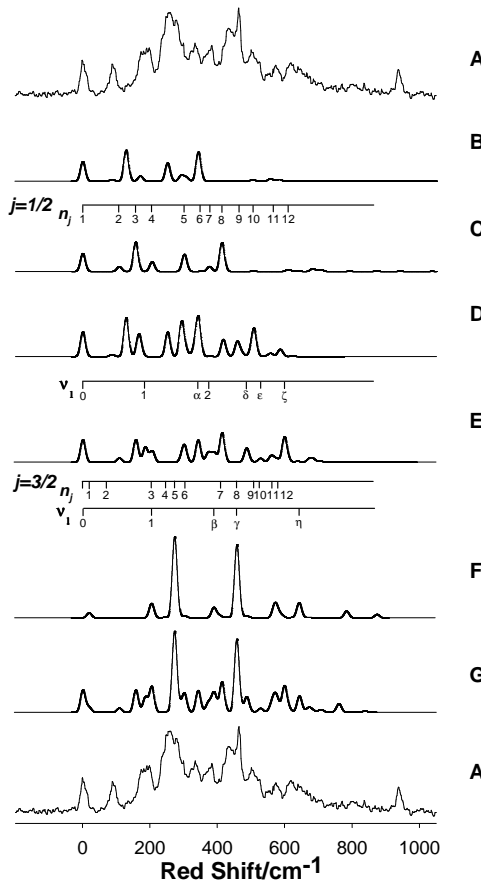


Figure 5.7: Emission spectrum of Ag_3 , laser excited to band 4 of the $\tilde{A}^2\text{E}''$ state.

(A) Experimental trace from ref. 14 (top and bottom traces); (B) Positions of the transitions to the e' Jahn-Teller active levels with $j = 1/2$ symmetry, computed using the *ab initio* calculated Jahn-Teller parameters of the $\tilde{X}^2\text{E}'$ state; (C) Same as (B) but using the best-fit Jahn-Teller parameters of the $\tilde{X}^2\text{E}'$ state; (D) Same as (B) plus the positions of the transitions to the totally symmetric a'_1 level and its first overtone (labelled in E as 1,2), as well as their combinations (labelled in E as $\alpha, \delta, \varepsilon, \zeta$) with the Jahn-Teller active levels; (E) Same as (D) but using the experimentally determined parameters of the $\tilde{X}^2\text{E}'$ state; (F) Positions of the transitions to the e' $j = 3/2$ Jahn-Teller active levels as well as their combinations (labelled β, γ, η) with the totally symmetric a'_1 level as computed with SPEC-SOCJT based on the parameters of the $\tilde{X}^2\text{E}'$ state experimentally determined from steps (B)-(E); (G) Simulated emission spectrum obtained by summing traces (E) and (F).

spectral parameters that may equally well account for the other four experimental emission spectra. When we assign this intense calculated feature to the second intense experimental feature, a set of \tilde{X} -state molecular parameters is produced that accounts for the other four emission traces. The $j = 1/2$ levels now have an extended contribution to the overall emission spectrum, especially $\leq 450 \text{ cm}^{-1}$. However, the predicted structure outlined in the simulation of Fig. 5.7E is far from sufficient to understand the totality of the emission. The most intense features of the experimental spectrum are missing. We found again that the “blanks of the simulation” may be filled with transitions to $j = 3/2$ levels. There is good correlation between our simulation in Fig. 5.7G and experiment, save the first band above the origin.

The four columns of Table 5.5 present our “assignments” to the experimental bands of Fig. 5.7, the symmetries of the levels in the spin double group, and comparisons with the calculated emission frequencies. In the first column under assignment we give the spectroscopic designation of the spin-vibronic terminating levels of the transitions originating in band 4 of the \tilde{A} state. The corresponding experimental emission frequencies, in cm^{-1} , are given in the third column and the calculated ones, in cm^{-1} , in the fourth column of the Table. Asterisks distinguish transitions to $e_{5/2}$ levels of the \tilde{X} state from transitions to $e_{3/2}$ levels, for the $j = 1/2 e'$ levels. The symmetry of the $j = 3/2 e'$ levels is $e_{1/2}$. The spin double group symmetries of all levels are given in the second column. The calculated emission frequency of 0 cm^{-1} corresponds here to the transition from $|\frac{1}{2}, 4\rangle|\frac{1}{2}\rangle$ of $\tilde{A}^2\text{E}''$ to $|\frac{1}{2}, 1\rangle|\frac{1}{2}\rangle$ of $\tilde{X}^2\text{E}'$. See also the diagrams of Fig. 5.7 for an illustrative presentation of assignments. Except

for the origin, an additional five Jahn-Teller levels may be assigned in the spectrum, namely $n_j=5,8$ for $j = 1/2$ and $n_j=3,5,11$ for $j = 3/2$. A fair number of bands may contribute in the congestion of the emission spectrum, i.e., $|\frac{1}{2}, 3\rangle| \pm \frac{1}{2}\rangle$, $|\frac{1}{2}, 7\rangle| \pm \frac{1}{2}\rangle$, $|\frac{1}{2}, 12\rangle| \pm \frac{1}{2}\rangle$, and $|\frac{3}{2}, 1\rangle| \pm \frac{1}{2}\rangle$, $|\frac{3}{2}, 7\rangle| \pm \frac{1}{2}\rangle$ and $|\frac{3}{2}, 12\rangle| \pm \frac{1}{2}\rangle$. All other calculated Jahn-Teller levels $\leq 665 \text{ cm}^{-1}$ exhibit no intensity in the spectrum.

The spin-vibronic levels $|\frac{1}{2}, 1\rangle| \pm \frac{1}{2}\rangle + (\nu_1)_1$ and $|\frac{3}{2}, 1\rangle| \pm \frac{1}{2}\rangle + (\nu_1)_1$ lie in a congested energy region. Our assignment of the partially resolved feature at ca. 178 cm^{-1} should be considered tentative. Likewise, the first and second overtones of a'_1 occupy an unresolved, as well as weak in intensity, energy region of the spectrum. Combinations of a'_1 with Jahn-Teller levels may be assigned to several experimental bands. The spin-vibronic level(s) $|\frac{1}{2}, 3\rangle| \pm \frac{1}{2}\rangle + (\nu_1)_1$ (α) may be assigned to the feature at 334 cm^{-1} , $|\frac{3}{2}, 3\rangle| \pm \frac{1}{2}\rangle + (\nu_1)_1$ (β) or $|\frac{1}{2}, 4\rangle| \pm \frac{1}{2}\rangle + (\nu_1)_1$ (β) to the feature at 381 cm^{-1} , $|\frac{3}{2}, 5\rangle| \pm \frac{1}{2}\rangle + (\nu_1)_1$ (γ) to the prominent feature at 463 cm^{-1} , $|\frac{1}{2}, 5\rangle| \pm \frac{1}{2}\rangle + (\nu_1)_1$ (δ) at the feature rising at 501 cm^{-1} , $|\frac{1}{2}, 3\rangle| \pm \frac{1}{2}\rangle + (\nu_1)_2$ (ε) tentatively to the possible shoulder at $\approx 524 \text{ cm}^{-1}$, $|\frac{1}{2}, 8\rangle| \pm \frac{1}{2}\rangle + (\nu_1)_1$ (ζ) to the relatively intense feature peaking at 614 cm^{-1} , and $|\frac{3}{2}, 5\rangle| \pm \frac{1}{2}\rangle + (\nu_1)_2$ (η) to the feature at 640 cm^{-1} . Calculated levels with non-negligible intensity in the $\tilde{X}^2\text{E}'$ state but with frequencies that may not be experimentally resolvable are $|\frac{1}{2}, 2\rangle| \pm \frac{1}{2}\rangle + (\nu_1)_1$, $|\frac{1}{2}, 7\rangle| \pm \frac{1}{2}\rangle + (\nu_1)_1$, $|\frac{1}{2}, 4\rangle| \pm \frac{1}{2}\rangle + (\nu_1)_2$, and $|\frac{3}{2}, 8\rangle| \pm \frac{1}{2}\rangle + (\nu_1)_1$.

As noted earlier, the first most pronounced experimental band appears at 92 cm^{-1} above the origin. Our model fails to predict it. However, it was previously suggested¹⁴ that this feature probably arises from collisional relaxation of the excited

Band 4 ^a			
Assignment ($ j, n_j\rangle \Sigma\rangle$)	Symmetry	Exp ^b	Calc
$ 1/2, 1\rangle \pm 1/2\rangle$	$e_{5/2}, e_{3/2}$	0	0*, 2
$ 3/2, 1\rangle \pm 1/2\rangle$	$e_{1/2}$	u	18
$ 3/2, 2\rangle \pm 1/2\rangle$	$e_{1/2}$	d	72
...	...	92 ^c	93
$ 1/2, 2\rangle \pm 1/2\rangle$	$e_{3/2}, e_{5/2}$	u	103, 108*
$ 1/2, 3\rangle \pm 1/2\rangle$	$e_{5/2}, e_{3/2}$	u	157*, 164
$ 1/2, 1\rangle \pm 1/2\rangle + (\nu_1)_1$	$e_{5/2}, e_{3/2}$	178	185*, 187
$ 3/2, 1\rangle \pm 1/2\rangle + (\nu_1)_1$	$e_{1/2}$	u	203
$ 3/2, 3\rangle \pm 1/2\rangle$	$e_{1/2}$	197	203
$ 1/2, 4\rangle \pm 1/2\rangle$	$e_{5/2}, e_{3/2}$	u	205*, 213
$ 3/2, 4\rangle \pm 1/2\rangle$	$e_{1/2}$	d	243
$ 3/2, 5\rangle \pm 1/2\rangle$	$e_{1/2}$	261	273
$ 1/2, 2\rangle \pm 1/2\rangle + (\nu_1)_1$	$e_{3/2}, e_{5/2}$	u	288, 293*
$ 1/2, 5\rangle \pm 1/2\rangle$	$e_{3/2}, e_{5/2}$	282	298, 301*
$ 3/2, 6\rangle \pm 1/2\rangle$	$e_{1/2}$	d	302
$ 1/2, 3\rangle \pm 1/2\rangle + (\nu_1)_1$	$e_{5/2}, e_{3/2}$	334 (α)	342*, 349
$ 1/2, 6\rangle \pm 1/2\rangle$	$e_{5/2}, e_{3/2}$	d	349*, 357
$ 1/2, 1\rangle \pm 1/2\rangle + (\nu_1)_2$	$e_{5/2}, e_{3/2}$	u	370*, 372
$ 1/2, 7\rangle \pm 1/2\rangle$	$e_{3/2}, e_{5/2}$	u	372, 376*
$ 3/2, 3\rangle \pm 1/2\rangle + (\nu_1)_1$	$e_{1/2}$	381 ^d (β)	388
$ 3/2, 7\rangle \pm 1/2\rangle$	$e_{1/2}$	u	405
$ 1/2, 8\rangle \pm 1/2\rangle$	$e_{5/2}, e_{3/2}$	436	413*, 425
$ 3/2, 8\rangle \pm 1/2\rangle$	$e_{1/2}$	d	456
$ 3/2, 5\rangle \pm 1/2\rangle + (\nu_1)_1$	$e_{1/2}$	463 (γ)	458
$ 1/2, 9\rangle \pm 1/2\rangle$	$e_{5/2}, e_{3/2}$	d	465*, 475
$ 1/2, 5\rangle \pm 1/2\rangle + (\nu_1)_1$	$e_{3/2}, e_{5/2}$	501 (δ)	483, 486*
$ 1/2, 3\rangle \pm 1/2\rangle + (\nu_1)_2$	$e_{5/2}, e_{3/2}$	524 ^e (ε)	527*, 534
$ 3/2, 11\rangle \pm 1/2\rangle$	$e_{1/2}$	570	568
$ 1/2, 8\rangle \pm 1/2\rangle + (\nu_1)_1$	$e_{5/2}, e_{3/2}$	614 (ζ)	598*, 610
$ 3/2, 5\rangle \pm 1/2\rangle + (\nu_1)_2$	$e_{1/2}$	640 (η)	643

Table 5.5: Calculated and experimentally observed spectral transitions to the $\tilde{X}^2\text{E}'$ state originating in band 4 of the $\tilde{A}^2\text{E}''$ state of Ag₃.

^a The assignments to all experimental bands lower than ca. 500 cm⁻¹ are presented plus a number of others of resolved features of the higher energy region. ^b See footnote b of Table 5.4. The estimated experimental error is ≈ 15 cm⁻¹. ^c See text for a tentative assignment. ^d Dual assignment; $|1/2, 4\rangle |\pm 1/2\rangle + (\nu_1)_1$, calculated energy 390*, 398. ^e Possible shoulder.

vibronic state to lower levels followed by subsequent emission. The emission intensity profile of this band relative to other bands in the spectrum does not seem to be preserved in repeated emission traces. The first level lying lower than the spin-vibronic levels $|\frac{1}{2}, 4\rangle | \pm \frac{1}{2}\rangle$ in the \tilde{A}^2E'' state is $|\frac{3}{2}, 1\rangle | \pm \frac{1}{2}\rangle + (\nu_1)^1$. If we assume that there is indeed a relaxation from $|\frac{1}{2}, 4\rangle | \pm \frac{1}{2}\rangle$ to $|\frac{3}{2}, 1\rangle | \pm \frac{1}{2}\rangle + (\nu_1)^1$ can we simulate the missing experimental band. The additional structure so predicted lies within congested energy regions of the experimental emission spectrum, in part explaining the observed broadness.

5.3.6 Emission from Bands 2 and 5 of the \tilde{A} State of Ag_3

Fig. 5.8A shows the LEDF spectrum originating from band 2 of the \tilde{A}^2E'' state. Of all the available emission spectra of Ag_3 this is the broadest, and is certainly not limited instrumentally. This broadness allows only tentative assignments for this band.

The columns of Table 5.6 contain information about “assignments”, experimental and calculated emission frequencies from band 2 of \tilde{A}^2E'' as well as the symmetries of the levels in the spin double group. In the first column under assignment we give the spectroscopic designation of the spin-vibronic terminating levels of the transitions originating in band 2 of the \tilde{A} state. The corresponding experimental emission frequencies, in cm^{-1} , are given in the third column and the calculated ones, in cm^{-1} , in the fourth column of the Table. Asterisks distinguish transitions to $e_{5/2}$ levels of the \tilde{X} state from transitions to $e_{3/2}$ levels, for the $j = 1/2 e'$ levels. The symmetry of the $j = 3/2 e'$ levels is $e_{1/2}$. The spin double group symmetries of all levels are given in

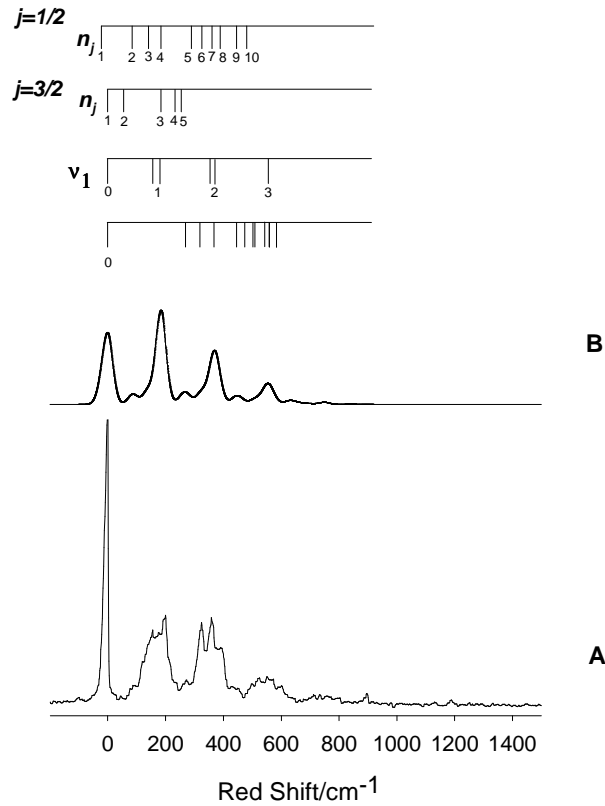


Figure 5.8: Emission spectrum of Ag_3 , laser excited to band 2 of the $\tilde{A}^2\text{E}''$ state.

(A) Experimental trace from ref. 136 (bottom trace); (B) Positions of the transitions to the e' $j = 1/2$ Jahn-Teller active levels and $j = 3/2$ Jahn-Teller active levels as well as their combinations with the totally symmetric a'_1 level and its overtones as computed with SPEC-SOCJT based on the experimentally determined parameters of the $\tilde{X}^2\text{E}'$ state. The doubled lines marked in the diagram of the totally symmetric mode, ν_1 , result from the consideration of the $j = 3/2$ e' Jahn-Teller active levels; $\nu_1 = 1$ refers to transitions, in increasing energy order, to $|1/2, 1\rangle |\pm 1/2\rangle + (\nu_1)_1$ and $|3/2, 1\rangle |\pm 1/2\rangle + (\nu_1)_1$, $\nu_1 = 2$ to $|1/2, 1\rangle |\pm 1/2\rangle + (\nu_1)_2$ and $|3/2, 1\rangle |\pm 1/2\rangle + (\nu_1)_2$, and $\nu_1 = 3$ to $|3/2, 1\rangle |\pm 1/2\rangle + (\nu_1)_3$. (See also Table 5.6.) (top trace.)

the second column. Note that the experimental frequencies now deviate significantly from those observed in the experimental emission spectra from bands 1, 3, 4 and 5 of the \tilde{A} state. This discrepancy is resolved by making the following considerations.

Based on Fig. 5.3, the transition from $|\frac{1}{2}, 1\rangle|\frac{1}{2}\rangle$ of \tilde{X}^2E' to $|\frac{1}{2}, 2\rangle|\frac{1}{2}\rangle$ of \tilde{A}^2E'' has a calculated excitation frequency of 90 cm^{-1} above the origin of the \tilde{A} state, as shown in Table 5.3, and the transition from $|\frac{1}{2}, 2\rangle|\frac{1}{2}\rangle$ of \tilde{A}^2E'' to $|\frac{1}{2}, 1\rangle|\frac{1}{2}\rangle$ of \tilde{X}^2E' is expected to have an emission frequency of 0 cm^{-1} . Not only the emission from $|\frac{1}{2}, 2\rangle|\pm\frac{1}{2}\rangle$ of the \tilde{A} state, but also the emission from $|\frac{3}{2}, 2\rangle|\pm\frac{1}{2}\rangle$ is important for the interpretation of the experimental trace in Fig. 5.8A. Based on the experimentally determined spectral parameters of the \tilde{A} and \tilde{X} states, we found that $\frac{P|\frac{3}{2}, 2\rangle|\pm\frac{1}{2}\rangle \rightarrow |\frac{3}{2}, 1\rangle|\pm\frac{1}{2}\rangle}{P|\frac{1}{2}, 2\rangle|\frac{1}{2}\rangle \rightarrow |\frac{1}{2}, 1\rangle|\frac{1}{2}\rangle} \approx 3.5$, where $P(\tilde{A}^2E'' \rightarrow \tilde{X}^2E')$ is the transition probability for emission from \tilde{A} to \tilde{X} . Also the transition $|\frac{1}{2}, 2\rangle|\frac{1}{2}\rangle$ of $\tilde{A} \rightarrow |\frac{1}{2}, 1\rangle|\frac{1}{2}\rangle$ of \tilde{X} exhibits a small intensity relative to the strongest feature of the simulation, and is experimentally unresolved. Consequently, we assigned the origin of the experimental emission spectrum to the transition $|\frac{3}{2}, 2\rangle|\pm\frac{1}{2}\rangle$ of $\tilde{A} \rightarrow |\frac{3}{2}, 1\rangle|\pm\frac{1}{2}\rangle$ of \tilde{X} , which is calculated by a difference of ca. 21 cm^{-1} from the corresponding $j = 1/2$ transition. Note that we have assumed that the $j = 1/2$ and $j = 3/2$ levels with $n_j = 2$ of the \tilde{A} state are equally populated when pumping band 2.

The energy region that we analyze expands from 0 to 615 cm^{-1} above the origin. The diagrams above Fig. 5.8B where our simulation is presented give a summary of our assignments. One general observation is that a fair amount of spectral broadness

Band 2 ^a				
Assignment ($ j, n_j\rangle \Sigma\rangle$)	Symmetry	Exp ^b	Calc	
$ 1/2, 1\rangle \pm 1/2\rangle$	$e_{5/2}, e_{3/2}$	u	-22*, -21	
$ 3/2, 1\rangle \pm 1/2\rangle$	$e_{1/2}$	0	0	
$ 3/2, 2\rangle \pm 1/2\rangle$	$e_{1/2}$	d	54	
$ 1/2, 2\rangle \pm 1/2\rangle$	$e_{3/2}, e_{5/2}$	92	80, 86*	
$ 1/2, 3\rangle \pm 1/2\rangle$	$e_{5/2}, e_{3/2}$	124	135*, 141	
$ 1/2, 1\rangle \pm 1/2\rangle + (\nu_1)_1$	$e_{5/2}, e_{3/2}$	157	163*, 164	
$ 1/2, 4\rangle \pm 1/2\rangle$	$e_{5/2}, e_{3/2}$	177	183*, 190	
$ 3/2, 3\rangle \pm 1/2\rangle$	$e_{1/2}$	u	185	
$ 3/2, 1\rangle \pm 1/2\rangle + (\nu_1)_1$	$e_{1/2}$	195	185	
$ 3/2, 4\rangle \pm 1/2\rangle$	$e_{1/2}$	d	225	
$ 3/2, 5\rangle \pm 1/2\rangle$	$e_{1/2}$	u	255	
$ 1/2, 2\rangle \pm 1/2\rangle + (\nu_1)_1$	$e_{3/2}, e_{5/2}$	267	265, 271*	
$ 1/2, 5\rangle \pm 1/2\rangle$	$e_{3/2}, e_{5/2}$	d	275, 279*	
$ 3/2, 6\rangle \pm 1/2\rangle$	$e_{1/2}$	d	284	
$ 1/2, 3\rangle \pm 1/2\rangle + (\nu_1)_1$	$e_{5/2}, e_{3/2}$	300	320*, 326	
$ 1/2, 6\rangle \pm 1/2\rangle$	$e_{5/2}, e_{3/2}$	u	327*, 334	
$ 1/2, 1\rangle \pm 1/2\rangle + (\nu_1)_2$	$e_{5/2}, e_{3/2}$	324	348*, 349	
$ 1/2, 7\rangle \pm 1/2\rangle$	$e_{3/2}, e_{5/2}$	u	349, 354*	
$ 1/2, 4\rangle \pm 1/2\rangle + (\nu_1)_1$	$e_{5/2}, e_{3/2}$	355	368*, 375	
$ 3/2, 1\rangle \pm 1/2\rangle + (\nu_1)_2$	$e_{1/2}$	u ^c	370	
$ 3/2, 7\rangle \pm 1/2\rangle$	$e_{1/2}$	d	387	
$ 1/2, 8\rangle \pm 1/2\rangle$	$e_{5/2}, e_{3/2}$	387	391*, 402	
$ 3/2, 8\rangle \pm 1/2\rangle$	$e_{1/2}$	d	438	
$ 3/2, 5\rangle \pm 1/2\rangle + (\nu_1)_1$	$e_{1/2}$	434	440	
$ 1/2, 9\rangle \pm 1/2\rangle$	$e_{5/2}, e_{3/2}$	u	443*, 452	
$ 1/2, 2\rangle \pm 1/2\rangle + (\nu_1)_2$	$e_{3/2}, e_{5/2}$	u	450, 456*	
$ 3/2, 9\rangle \pm 1/2\rangle$	$e_{1/2}$	d	479	
$ 1/2, 10\rangle \pm 1/2\rangle$	$e_{5/2}, e_{3/2}$	485	484*, 486	
$ 3/2, 10\rangle \pm 1/2\rangle$	$e_{1/2}$	d	508	
$ 1/2, 3\rangle \pm 1/2\rangle + (\nu_1)_2$	$e_{5/2}, e_{3/2}$	505	505*, 511	

Table 5.6: Calculated and experimentally observed spectral transitions to the \tilde{X}^2E' state originating in band 2 of the \tilde{A}^2E'' state of Ag_3 .

^a The assignments to all experimental bands lower than ca. 500 cm^{-1} are presented.

^b See footnote b of Table 5.4. The estimated experimental error is $\approx (15\text{-}20) \text{ cm}^{-1}$.

^c Dual assignment; $|3/2, 3\rangle |\pm 1/2\rangle + (\nu_1)_1$, calculated energy 370.

may be attributed to the fundamental and overtones of a'_1 and their combinations with the Jahn-Teller levels. Intensity borrowing mechanisms may become important here.

The experimental emission spectrum originating in band 5 of the \tilde{A}^2E'' state is given in Fig. 5.9A. The involved spin-vibronic structure manifests itself in a rather complex and broad emission pattern in the \tilde{X}^2E' state. In comparison with all previously examined emission spectra, this emission is rather “unique”. The observed broadness here seems to fall into the general pattern. The greater the energy departure to the blue from the origin of the pumped levels in the \tilde{A}^2E'' state, the greater becomes the observed congestion of their emissions in the \tilde{X}^2E' state. The spectrum’s vibronic structure involves fewer resolved bands than before. An extensive analysis of it would provide little reliable new information and hence was not pursued. However it is gratifying to observe a fairly good agreement between our simulation in Fig. 5.9B and experiment, even though this emission originates from an \tilde{A}^2E'' -state level that was not simulated the best among the emitting lines of the \tilde{A}^2E'' state. This simulation is the only one that did not include the use of any $j = 3/2$ structure, as no $j = 3/2$ levels were found to be close in energy with the levels $|\frac{1}{2}, 5\rangle |\pm \frac{1}{2}\rangle$ of the \tilde{A}^2E'' state. (See Fig. 5.3.) In the simulation, the transitions to both spin components of the \tilde{X} -state $j = 1/2$ Jahn-Teller levels are considered, as well as the contribution from a'_1 and its combinations with the Jahn-Teller levels. In the diagrams of Fig.

5.9B we denote first the transitions to the $|\frac{1}{2}, n_j\rangle|\frac{1}{2}\rangle$ levels of the \tilde{X} state, then the transitions to the totally symmetric a'_1 fundamental and overtone levels, and finally the transitions to their combinations with the $|\frac{1}{2}, n_j\rangle|\frac{1}{2}\rangle$ Jahn-Teller levels.

5.4 Discussion

Our primary goal was to understand the vibronic structures of the $\tilde{X}^2\text{E}'$ and $\tilde{A}^2\text{E}''$ states of Ag_3 . We used our *ab initio* calculated Jahn-Teller parameters as starting points for the Jahn-Teller simulations. These parameters were refined by adjusting them until the Jahn-Teller spin-vibronic-state energies and intensities matched the experimental line positions and intensities based on reasonable assignments in the \tilde{A} and \tilde{X} states. In the following, the *ab initio* calculated Jahn-Teller molecular parameters of the $\tilde{A}^2\text{E}''$ and $\tilde{X}^2\text{E}'$ states of Ag_3 are compared with the experimental ones, and their ramifications on the Jahn-Teller distorted potential energy surface in each case are discussed.

Our *ab initio* calculated and experimental spectral parameters for the $\tilde{X}^2\text{E}'$ state are generally in good agreement. The experimentally determined frequencies ω_{e,a'_1} and $\omega_{e,e'}$ for the $\tilde{X}^2\text{E}'$ state were found to be higher by approximately 15% than their corresponding calculated values. Discrepancies of this size are common at this level of theoretical treatment. Our calculated linear and quadratic Jahn-Teller coupling constants $D_{e'}$ and $K_{e'}$ are in excellent agreement with our experimental values as is clearly shown in Table 5.1. Our experimental $D_{e'}$ and $K_{e'}$ compare well with the corresponding ones suggested in the work by Wallimann *et al.*¹⁸ and less so with

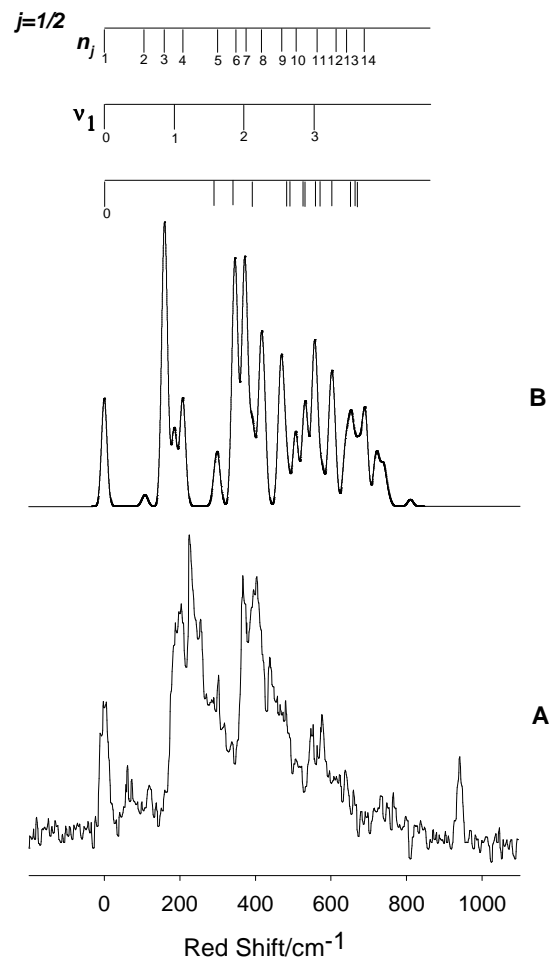


Figure 5.9: Emission spectrum of Ag_3 , laser excited to band 5 of the $\tilde{A}^2\text{E}''$ state.

(A) Experimental trace from ref. 14 (bottom trace); (B) Positions of the transitions to the e' $j = 1/2$ Jahn-Teller active levels, the totally symmetric a'_1 level and its overtones as well as their combinations with the Jahn-Teller active levels as computed with SPEC-SOCJT based on the experimentally determined parameters of the $\tilde{X}^2\text{E}'$ state. (top trace.)

the ones given by Wedum *et al.*¹⁷ The bilinear Jahn-Teller coupling, $B_{a'_1e'}$, was not incorporated in our simulations for the \tilde{X} state as any reasonable value for $B_{a'_1e'}$ had negligible effect on the simulation, so we kept it fixed to its calculated value. The spin-orbit coupling parameter $\alpha\zeta_e$ that we used in the \tilde{X} -state simulations was held at the one that we found theoretically, since the simulations were insensitive to any value below ca. 500 cm⁻¹. This calculated parameter is consistent with other workers' theoretical calculations.¹¹

The cubic anharmonicity term in the Taylor series expansion of the electronic Hamiltonian of the \tilde{X}^2E' state was found from the theoretical calculations of chapter 4 to have a small contribution. So did the pseudo-Jahn-Teller mixing in the \tilde{X}^2E' state. We did not incorporate these interactions in the description of the \tilde{X}^2E' state. These are additional degree of freedom for the simulation and the frequency match between the computed eigenvalues and the experimental positions may improve. The experimental frequency of e' would most likely be affected the most among the spectral parameters in the fit of the \tilde{X} -state vibronic structure if the effect of the cubic anharmonicity was considered.

Our *ab initio* calculated and experimental spectral parameters for the \tilde{A}^2E'' state are in fair agreement. There is a satisfactory frequency match between the experimental and *ab initio* calculated ω_{e,a'_1} and $\omega_{e,e'}$. Our experimental $D_{e'}$ was found to lie between the previous experimental values.^{17,18} Our *ab initio* calculated $D_{e'}$ value is more consistent with the experimental value that we suggest, though not exactly the same due to inadequacies in the \tilde{A} -state calculations. A value of -0.03(1) for $B_{a'_1e'}$

was found to be best based on the intensity variation in the simulation. Note that the error estimate for $B_{a'_1 e'}$ is crude and is not subject to the previously discussed approach of Section 5.2.3.

The calculated value for $\alpha\zeta_e$ is 17 cm^{-1} . We found that the \tilde{A} -state fit was practically insensitive to any value for $\alpha\zeta_e$ below ca. 50 cm^{-1} . Based on intensity variations we found an experimental value of $30(10) \text{ cm}^{-1}$ to best reproduce the spectrum, a value in reasonable agreement with our calculations. Previous work¹⁸ has suggested a value of 1500.0 cm^{-1} for $\alpha\zeta_e$. This value is dramatically higher than 229 cm^{-1} that is found for the same parameter for the heavier relativistic system of Au_3 .¹³⁷ One would normally expect a lower value for $\alpha\zeta_e$ for the lighter Ag_3 .

Our theoretical prediction of the quadratic Jahn-Teller constant $K_{e'}$ suggests that there is no significant quadratic Jahn-Teller effect within the electronic components of the $\tilde{A}^2\text{E}''$ state. Since the e' mode is pseudo-Jahn-Teller active we expect that there may be additional interactions between the $\tilde{A}^2\text{E}''$ state with the pseudo-Jahn-Teller coupled electronic states of ${}^2A_1''$, ${}^2A_2''$ and ${}^2E''$ symmetries. Limited by the fact that our Jahn-Teller software cannot describe any pseudo-Jahn-Teller interactions (it was not implemented to explicitly include the pseudo-Jahn-Teller-interaction electronic matrix elements that connect ${}^2E''$ with ${}^2A_1''$, ${}^2A_2''$ and ${}^2E''$), we chose to use $K_{e'}$ to account for all quadratic-in-nature interactions in the \tilde{A} state and found it be -0.17.

The Jahn-Teller molecular parameters contain valuable information about the topographic characteristics of the Jahn-Teller distorted potential energy surfaces. The experimental negative sign of $K_{e'}$ of the \tilde{A} state places the three global minima of

the lower sheet of the \tilde{A} $^2\text{E}''$ -state PES in positions rotated by 60° in the e' vibrational space compared to the corresponding ones of the \tilde{X} $^2\text{E}'$ state. Assuming the correctness of the prediction that the global-energy-minimum geometry of Ag_3 in its \tilde{X} state is an obtuse triangle, the corresponding minimum in the \tilde{A} state must be an acute triangle.

In Table 5.7 the *ab initio* calculated and experimentally determined Jahn-Teller stabilization energies ($E_{e'}^0$ and $E_{e'}^{\pi/3}$) and barriers to pseudorotation ($\Delta E_{e'}^B$) of the \tilde{X} - and \tilde{A} -state PESs of Ag_3 are given. The calculated values are taken from chapter

	\tilde{X} $^2\text{E}'$ State ^a			\tilde{A} $^2\text{E}''$ State ^a		
	$E_{e'}^0$	$E_{e'}^{\pi/3}$	$\Delta E_{e'}^B$	$E_{e'}^0$	$E_{e'}^{\pi/3}$	$\Delta E_{e'}^B$
Calc ^b	628	465	163	150	158	8
Exp	643	465	178	207	421	214

Table 5.7: Calculated and experimental stabilization energies and barriers to pseudorotation of the \tilde{X} $^2\text{E}'$ - and \tilde{A} $^2\text{E}''$ -state potential energy surfaces of Ag_3 .

^a All values in cm^{-1} . ^b The calculated values were taken from chapter 4, where we defined $E_{e'}^0$ and $E_{e'}^{\pi/3}$ as the energies at the stationary points of the potential energy surface of the \tilde{X} and \tilde{A} states, i.e., at $\phi = 0$ and $\phi = \pi/3$, respectively, and $\Delta E_{e'}^B$ is the barrier to pseudorotation around the moat of the potential energy surface. While the global-energy-minimum geometry of Ag_3 in its \tilde{X} state corresponds to an obtuse triangular configuration ($\phi = 0$), the corresponding one in the \tilde{A} state involves an acute angle configuration ($\phi = \pi/3$).

4. We used equations (19), (21), and (22) of chapter 4 to estimate the experimental values of Table 5.7. The calculated stabilization energies and experimental ones for the \tilde{X} state are in nearly complete agreement. The global minimum lies 643 cm^{-1}

below the D_{3h} conical intersection, and 178 cm^{-1} below the saddle point. For the \tilde{A} state we notice some discrepancy between the calculated and experimental values. However, useful information may still be extracted about the \tilde{A} -state Jahn-Teller potential energy surface; the global minimum lies 421 cm^{-1} below the D_{3h} point, and 214 cm^{-1} below the saddle point.

5.5 Conclusions

The laser induced, dispersed fluorescence emission spectra and the lower energy region of the laser induced, fluorescence excitation spectrum of the silver trimer have been successfully analyzed utilizing the *ab initio* molecular parameters. The agreement between experimental and theoretical Jahn-Teller parameters is better for the $\tilde{X}\text{ }^2\text{E}'$ state than for the $\tilde{A}\text{ }^2\text{E}''$ state. The vibronic structures of the $\tilde{A}\text{ }^2\text{E}''$ and $\tilde{X}\text{ }^2\text{E}'$ states reveal the Jahn-Teller distortion of their potential energy surfaces. The contributions from the totally symmetric a'_1 level and its overtones as well as their combinations with the Jahn-Teller levels are important in the spectra. The Franck-Condon factors between the \tilde{X} and \tilde{A} states along the totally symmetric mode also have an important effect on the spectra. The spin-orbit coupling is largely quenched in both the \tilde{X} and \tilde{A} states.

CHAPTER 6

Computational and Experimental Investigation of the Jahn-Teller Effect in the Ground and Excited States of the Tropyl Radical: Vibrational Analysis of the $\tilde{A}^2\text{E}_3''-\tilde{X}^2\text{E}_2''$ Electronic Transition

6.1 Introduction

The importance of studying the vibrational properties of the tropyl radical was expounded in section 1. Therein was also given the previous experimental and theoretical work on its $\tilde{X}^2\text{E}_2''$ and $\tilde{A}^2\text{E}_3''$ states. In the work presented in this chapter, the laser induced fluorescence spectroscopy was combined with supersonic free-jet expansion techniques to record the wavelength dispersed fluorescence spectra from a number of \tilde{A} -state levels of the tropyl radical for the first time.

In Section 6.2 of this chapter we describe the *ab initio* calculations that we have performed with the express purpose of aiding the analysis of the experimentally observed vibronic structure of the tropyl radical in its \tilde{X} and \tilde{A} states. In Section 6.5 we describe first our observation and analysis of the LIF excitation spectrum of the $\tilde{A}^2\text{E}_3'' \leftarrow \tilde{X}^2\text{E}_2''$ electronic transition of the tropyl radical. We proceed to describe the LEDF spectra from several \tilde{A} -state vibrational levels. The analysis of the LEDF spectra establishes the positions of the \tilde{X} -state vibronic levels. We apply the results

of Section 6.2 to help assign and analyze the \tilde{X} - and \tilde{A} -state vibronic structures, which consist of both Jahn-Teller active and Jahn-Teller inactive vibrational modes.

The spectroscopic analysis of the \tilde{X} - and \tilde{A} -state vibronic structures of C₇H₇ provides a complete set of linear Jahn-Teller coupling constants for the linear Jahn-Teller active vibrational modes of each state. It also gives information about their Jahn-Teller distorted potential energy surfaces and their energy stabilizations.

6.2 The Tropyl Potential Energy Surface

6.2.1 General Features

The PES of tropyl is a function of its $3N - 6 = 36$ vibrational degrees of freedom. Fig. 6.1 shows the linear Jahn-Teller (JT) distortion away from the D_{7h} geometry. The figure represents a plot of the \tilde{X} - or \tilde{A} -state PES along the two degrees of freedom that resolve the degeneracy. Fig. 6.2 gives a slice through the PES of Fig. 6.1.

In D_{7h} symmetry (which corresponds to the point labeled X₀ in Fig. 6.2), the \tilde{X} and \tilde{A} states are electronically doubly degenerate. The Jahn-Teller theorem dictates that the degeneracy at the conical intersection of the \tilde{X} - and \tilde{A} -state PESs will be removed by a suitable molecular distortion along (at most) two orthogonal coordinates, which are denoted by \mathcal{Q}_a and \mathcal{Q}_b in Fig. 6.1. (See also Ref. 16.) These may be expressed as

$$\mathcal{Q}_{\pm} = (\mathcal{Q}_a \pm i\mathcal{Q}_b) = \rho_{JT} e^{\pm i\phi_{JT}}, \quad (6.1)$$

where ρ_{JT} is the ordinate of Fig. 6.2 and ϕ_{JT} is an arbitrary angle around the moat of Fig. 6.1. (The PES is not dependent on ϕ_{JT} to the quadratic approximation.)

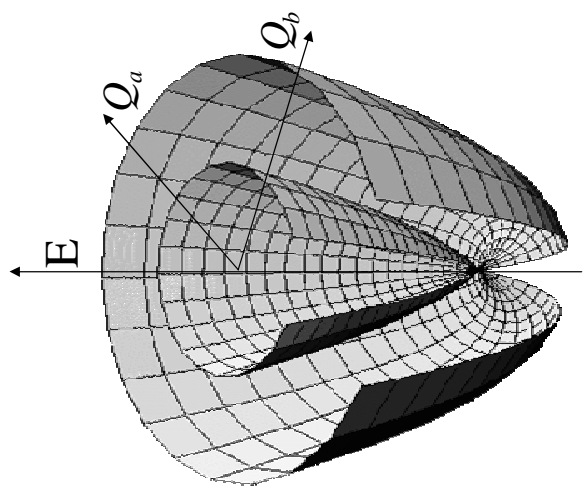


Figure 6.1: Plot of the \tilde{X} -state (or \tilde{A} -state) PES of the tropyl radical, where E is energy and Q_a and Q_b are the unique directions that lift the degeneracy present at the D_{7h} geometry.

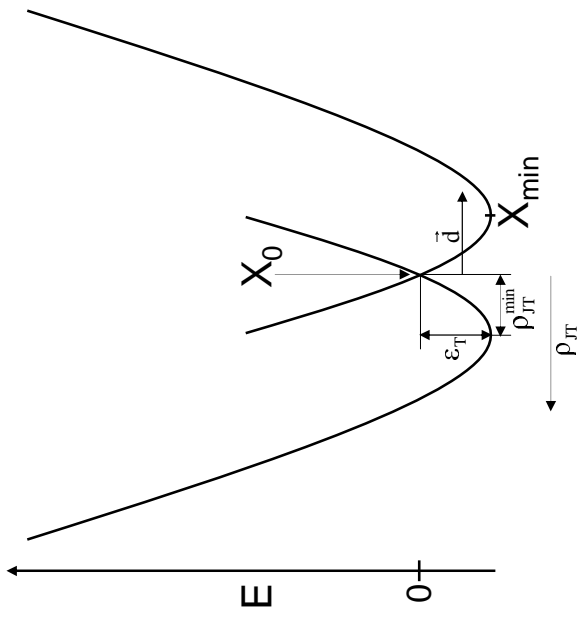


Figure 6.2: Slice through the \tilde{X} -state potential (or the \tilde{A} -state potential) at an arbitrary angle around the moat (shown in Fig. 6.1). The point X_0 defines the geometry of the symmetric D_{7h} (conical intersection) point on the \tilde{X} -state PES (or the \tilde{A} -state PES), and X_{min}^{min} is the geometry of the global minimum on the \tilde{X} -state PES (or \tilde{A} -state PES). The vector \vec{d} is the distortion vector. The parameter ε_T is the total linear Jahn-Teller stabilization energy, while ρ_{JT}^{min} is the distance from X_0 to X_{min}^{min} .

The goal of the present study is to determine the total linear Jahn-Teller stabilization ε_T of the \tilde{X} and \tilde{A} states of tropyl, which is defined as the energy difference between X_0 and X_{min} in Fig. 6.2. In this work we conduct theoretical calculations for the \tilde{X} and \tilde{A} states of C_7H_7 with the express purpose of acquiring a good initial estimate of the PES characteristics of the \tilde{X} and \tilde{A} states. We use the experimental information to refine the PESs. We apply the methodology followed in Refs. 100 and 104, with some approximations, to the vibronic structure of the C_7H_7 radical in its \tilde{X} and \tilde{A} states.

Information from theoretical calculations is required at the points of X_0 and X_{min} of Fig. 6.2 of the \tilde{X} and \tilde{A} states of C_7H_7 . The equation-of-motion electron affinity coupled cluster with singles and doubles (EOMEA-CCSD) formalism in ACES II⁸⁵ was employed for the calculation of the Jahn-Teller distortion vector \vec{d} (see Section 6.2.2) using the 6-31G* basis set, abbreviated EOMEA-CCSD/6-31G*. For the calculation of the normal modes and vibrational frequencies of C_7H_7 at X_0 the following approach was taken. Geometry optimization at the B3LYP/6-31G** level of theory in GAUSSIAN 98⁸⁴ was undergone for the ground-state structure $\tilde{X}^1A'_1$ of the tropyl cation $C_7H_7^+$. The hypothesis is that the geometries at the degeneracy points of the \tilde{X} and \tilde{A} states in the neutral species should be similar to the one calculated above for the ion. The D_{7h} geometry of C_7H_7 at the conical intersection of the \tilde{X} - and \tilde{A} -state PESs was approximated by the ground-state cationic geometry. Ideally the normal coordinates and harmonic vibrational frequencies at X_0 in the electronically degenerate \tilde{X} and \tilde{A} states of tropyl would result from calculations for the *average* of the

respective two Jahn-Teller split potential energy surfaces in each case, but this is not presently possible with the EOMEA-CCSD approach of ACES II. The ground-state frequencies of $C_7H_7^+$ are reported in this work unscaled. Several different basis sets were used for the B3LYP calculation to test the stability of the normal coordinates and vibrational frequencies. All reported vibrational frequencies used a 6-31G** basis set.

Section 6.2.2 details the approach that we follow to calculate the linear Jahn-Teller stabilization energies, ε_i , along each linearly Jahn-Teller active normal mode in the $\tilde{X}^2E''_2$ and $\tilde{A}^2E''_3$ states of C_7H_7 . The sum of these energies is defined as ε_T and is schematically depicted in Fig. 6.2. Symmetry dictates that the conical intersection be at the D_{7h} geometry of C_7H_7 in its $\tilde{X}^2E''_2$ and $\tilde{A}^2E''_3$ states. The direction of the Jahn-Teller distortion vector \vec{d} is determined from the difference between the D_{7h} and the global minimum geometry. This approach defines the length and direction of the Jahn-Teller distortion vector. With the distortion vector components known from EOMEA-CCSD calculations of ACES II, we use the model potential of the \tilde{X} and \tilde{A} states to calculate the Jahn-Teller stabilization energies ε_i for the corresponding linearly Jahn-Teller active normal modes in each state.

6.2.2 The Spectroscopic Model of the Jahn-Teller PES

It is convenient to work in the 3N-6 normal coordinate system, Q_i , of the undistorted symmetric configuration of C_7H_7 when we describe its motion in the $\tilde{X}^2E''_2$ and $\tilde{A}^2E''_3$ states. While the linear Jahn-Teller effect is realized along the two orthogonal vectors, Q_a and Q_b , which span a different symmetry space of molecular distortion

between the \tilde{X} and \tilde{A} states, these may be expressed as linear combinations of the normal coordinates Q_i as they constitute a subspace of the normal coordinate space.

The general Hamiltonian for our system is

$$\hat{\mathcal{H}} = \hat{\mathcal{H}}_T + \hat{\mathcal{H}}_e + \hat{\mathcal{H}}_{SO} \quad (6.2)$$

where $\hat{\mathcal{H}}_T$ is the nuclear kinetic energy operator, $\hat{\mathcal{H}}_e$ is the electronic Hamiltonian, and $\hat{\mathcal{H}}_{SO}$ is the spin-orbit coupling Hamiltonian. If experience with past work on cyclopentadienyl^{100,103} and the benzene cation¹⁰⁴ becomes a guide, then the spin-orbit coupling is expected to be effectively quenched in the \tilde{X} and \tilde{A} states of C₇H₇, therefore $\hat{\mathcal{H}}_{SO}$ may be omitted here.

In Refs. 100, 103 we showed, as have others, that the potential energy surfaces, V_{\pm} , of a Jahn-Teller active molecule may be expressed in terms of matrix elements of the electronic Hamiltonian $\hat{\mathcal{H}}_e$, i.e.,

$$V_{\pm} = \left\langle \Lambda_{+} \left| \hat{\mathcal{H}}_e \right| \Lambda_{+} \right\rangle \pm \left(\left\langle \Lambda_{+} \left| \hat{\mathcal{H}}_e \right| \Lambda_{-} \right\rangle \left\langle \Lambda_{-} \left| \hat{\mathcal{H}}_e \right| \Lambda_{+} \right\rangle \right)^{1/2}, \quad (6.3)$$

where $\left\langle \Lambda_{+} \left| \hat{\mathcal{H}}_e \right| \Lambda_{+} \right\rangle = \left\langle \Lambda_{-} \left| \hat{\mathcal{H}}_e \right| \Lambda_{-} \right\rangle$ and Λ_{\pm} are complex wave functions related to the real electronic wave functions, Λ_a and Λ_b by $\Lambda_{\pm} = 1/\sqrt{2}(\Lambda_a \pm i\Lambda_b)$. The diagonal and off-diagonal terms of Eq. 6.3 considering only terms up to second order in the normal coordinates Q_i of the symmetric C₇H₇ obtain similar expressions to the corresponding ones for Ag₃ given in Chapter 4 (equations 4.9 and 4.10). What is different now is that C₇H₇ involves a greater number of vibrational degrees of freedom than Ag₃.

The definitions of the parameters involved in the spectroscopic potential of C₇H₇ are summarized in Table 6.1. These parameters are the harmonic force constants

Symbol	Description	Definition
k_i	linear Jahn-Teller coupling coefficient	$\frac{\partial}{\partial Q_{i,\pm}} \left(\langle \Lambda_{\pm} \hat{H}_e \Lambda_{\mp} \rangle \right)_0$
λ_i	harmonic force constant of the Jahn-Teller active i mode	$\frac{\partial^2}{\partial Q_{i,+} \partial Q_{i,-}} \left(\langle \Lambda_{\pm} \hat{H}_e \Lambda_{\pm} \rangle \right)_0$
λ_i'	harmonic force constant of the Jahn-Teller inactive i mode	$\frac{\partial^2}{\partial Q_i^2} \left(\langle \Lambda_{\pm} \hat{H}_e \Lambda_{\pm} \rangle \right)_0$
g_{ii}	quadratic Jahn-Teller coupling coefficient	$\frac{\partial^2}{\partial Q_{i,\pm}^2} \left(\langle \Lambda_{\pm} \hat{H}_e \Lambda_{\mp} \rangle \right)_0$
g_{ij}	cross-quadratic Jahn-Teller coupling coefficient	$\frac{\partial^2}{\partial Q_{i,\pm} \partial Q_{j,\pm}} \left(\langle \Lambda_{\pm} \hat{H}_e \Lambda_{\mp} \rangle \right)_0$
b_{ij}	bilinear Jahn-Teller coupling coefficient	$\frac{\partial^2}{\partial Q_i \partial Q_{j,\pm}} \left(\langle \Lambda_{\pm} \hat{H}_e \Lambda_{\mp} \rangle \right)_0$

Table 6.1: The Jahn-Teller coupling coefficients that parameterize the effective spectroscopic Hamiltonian and their relationships to the terms of the Taylor series expansion of the potential.

of the linear Jahn-Teller active modes and of all other vibrational modes represented, respectively, by λ_i and $\lambda_{i'}$, the linear Jahn-Teller coupling coefficients, k_i , the quadratic Jahn-Teller coupling coefficients between the same degenerate coordinate g_{ii} , the quadratic Jahn-Teller coupling coefficients between different degenerate coordinates, called the cross-quadratic coupling coefficients g_{ij} , and the quadratic coupling coefficients between a degenerate coordinate and a non-degenerate coordinate, called the bilinear coupling coefficients, b_{ij} . Note that p and s are the numbers of linear and quadratic Jahn-Teller active vibrational modes, respectively, and l designates the number of doubly degenerate vibrational modes that couple with non-degenerate modes. (As will be shown later on p , s and l do not correspond to the same numbers for the $\tilde{X}^2\text{E}_2''$ and $\tilde{A}^2\text{E}_3''$ electronic states of tropyl.)

Certain terms in the mathematical expression of $\langle \Lambda_{\pm} | \hat{\mathcal{H}}_e | \Lambda_{\mp} \rangle$ are zero for certain symmetries of the doubly degenerate Jahn-Teller active normal coordinates of the $\tilde{X}^2\text{E}_2''$ and $\tilde{A}^2\text{E}_3''$ states of tropyl in the D_{7h} point group. We consider their transformation properties under \hat{C}_n rotation with $n = 7$ following the approach that was taken in Ref. 16. We use Eq. 26 of this reference and generalize it to make it applicable for the case of modes with different symmetry

$$\left[2s_e + (-1)^{s_k} k \sum_i s_{v,i} \right] \mod n = 0 \quad (6.4)$$

where s_e and s_v are determined by the electronic symmetry, E_{s_e} , and vibrational symmetry, e_{s_v} . The order of Jahn-Teller coupling is represented by k , i.e., for linear Jahn-Teller coupling $k = 1$, for quadratic Jahn-Teller coupling $k = 2$, etc. For a given vibrational mode e_{s_v} and a given electronic state of symmetry E_{s_e} , a value for s_k of

either 0 or 1 may be chosen to satisfy Eq. 6.4. By doing this exercise we can identify the terms in the mathematical expression of $\langle \Lambda_{\pm} | \hat{\mathcal{H}}_e | \Lambda_{\mp} \rangle$ that may be non-zero. These symmetry considerations are summarized in Table 6.2, which is an extension of Table 2 of Ref. 16 that includes the rarely seen case of $n = 7$, where n is the order of the \hat{C}_n rotation. By applying Eq. 6.4 to $\tilde{X}^2E''_2$ and $\tilde{A}^2E''_3$ tropyl with $n = 7$, $s_e = 2$ and $s_e = 3$, respectively, we can determine which terms are non-zero in the mathematical expression of $\langle \Lambda_{\pm} | \hat{\mathcal{H}}_e | \Lambda_{\mp} \rangle$ for our six doubly degenerate symmetry species, e'_1 , e''_1 , e'_2 , e''_2 , e'_3 , and e''_3 .

n	k	s_e	s_v	s_k
3	1	1	1	0
	2	1	1	1
4	1	1	2	0 or 1
	2	1	1	0 or 1
5	1	1	2	1
	2	1	0	
6	1	1	1	
	2	2	1	
7	1	1	2	1
	2	2	0	
	2	1	1	
	1	2	0	
	2	1	0	
	2	2	1	
	2	3	0	
	3	1	0	
	2	1	1	
	2	2	1	
	3	3	1	

Table 6.2: Allowed values of s_e , s_v and s_k for $n \leq 7$ and $k = 1$ or 2

Starting with the $\tilde{X}^2\text{E}_2''$ state of tropyl, and according to Eq. 6.4 and Table 6.2, the linear Jahn-Teller coupling coefficients, k_i , are non-zero for only the e'_3 and e''_3 normal coordinates. The e''_3 terms are zero,¹³⁸ since the k_i coupling terms must overall be symmetric with respect to reflection through a mirror plane. Hence four modes of e'_3 symmetry are linear Jahn-Teller active in the $\tilde{X}^2\text{E}_2''$ state. The quadratic Jahn-Teller coupling coefficients, g_{ii} , are non-zero only for the e'_2 (four in number) and e''_2 (two) normal coordinates. The cross-quadratic Jahn-Teller coupling coefficients, g_{ij} , are non-zero for the terms between doubly degenerate normal coordinates with $s_v=1$ and $s_v=2$, and, $s_v=1$ and $s_v=3$, which have the same property with respect to reflection through a mirror plane, i.e., for the pairs (e'_1, e'_2) , (e''_1, e''_2) , (e'_1, e'_3) , and (e''_1, e''_3) . The bilinear coupling coefficients are non-zero only for the following combinations of normal coordinates: (a'_1, e'_3) , (a'_2, e'_3) , and (a''_2, e''_3) .

Similarly for the $\tilde{A}^2\text{E}_3''$ state of tropyl, the linear terms, represented by k_i , are non-zero for only the e'_1 (three) normal coordinates. The quadratic terms g_{ii} are non-zero only for the e'_3 (four) and e''_3 (two) normal coordinates. The cross-quadratic terms g_{ij} are non-zero for the following pairs of doubly degenerate normal coordinates: (e'_1, e'_2) , (e''_1, e''_2) , (e'_2, e'_3) , and (e''_2, e''_3) . The bilinear coupling coefficients are non-zero only for the following combinations of normal coordinates: (a'_1, e'_1) , (a'_2, e'_1) , and (a''_2, e''_1) .

Note that the quadratic Jahn-Teller terms are zero for the linearly Jahn-Teller active e'_3 modes of the $\tilde{X}^2\text{E}_2''$ state, and for the e'_1 modes of the $\tilde{A}^2\text{E}_3''$ state in D_{7h} symmetry. Hence the moat, for both the \tilde{X} and \tilde{A} states, in Fig. 6.1 will, as expected,^{100,139,140} have the same energy in all directions.

In the expansion of the potential, only the linear Jahn-Teller terms, k_i , will be considered for the \tilde{X}^2E_2'' and \tilde{A}^2E_3'' states of tropyl, i.e., those due to the e'_3 and e'_1 modes, respectively. The quadratic Jahn-Teller terms, g_{ii} , are expected to be non-negligible in the potentials of the \tilde{X} and \tilde{A} states of tropyl. Their only effect, however, is to flatten the lower sheet and compress the upper sheet of the PES seen along the normal coordinates e'_2 and e''_2 of the \tilde{X} state, and along the coordinates e'_3 and e''_3 of the \tilde{A} state. The quadratic Jahn-Teller term does not resolve the degeneracy of the symmetric PES point, but the linear Jahn-Teller term does. The latter term moves the lowest-energy point from the symmetric-configuration PES point (D_{7h} symmetry) to a lower-energy one. (C_{2v} symmetry.) Hence, it is the linear Jahn-Teller terms of the potentials of the \tilde{X}^2E_2'' and \tilde{A}^2E_3'' states of tropyl that are expected to have the largest impact on the spectroscopy, so these terms should play a central role in the analysis. The remaining non-zero terms, the cross-quadratic terms, g_{ij} , and the bilinear terms, b_{ij} , will be neglected. They have been shown by Köppel *et al.*¹⁰² to have little effect on the vibronic spectrum of CH₃O. We have had success analyzing the spectrum of C₅(H/D)₅^{100,103} using this approach. Additionally the experimental results for the closely related molecules C₆F₆⁺,^{141,142} C₆(H/D)₆⁺¹⁰⁴ and C₆H₃F₃⁺^{141,142} have been successfully analyzed without invoking these terms.

The topography of the potential energy surface is quite dependent on the symmetry of the normal coordinate along which one views the surface. The entire potential energy surface is approximated by the equation

$$V_{\pm} = \sum_{i=1}^{2p} V_{\pm,i}^l + \sum_{j=1}^{3N-6-2p} V_{\pm,j}^h, \quad (6.5)$$

where p is the number of linear Jahn-Teller active modes of the \tilde{X} or \tilde{A} states of tropyl and

$$V_{\pm,i}^l = \frac{1}{2} \lambda_i \rho_i^2 \pm k_i \rho_i, \quad (6.6)$$

$$V_{\pm,j}^h = \frac{1}{2} \lambda_j Q_j^2. \quad (6.7)$$

Eqs. 6.6 and 6.7 have been written based on the polar coordinate representation of the doubly degenerate normal coordinates, $Q_{\pm,i} = \rho_i e^{\pm i\phi_i}$. $V_{\pm,i}^l$ expresses the contribution from the linear Jahn-Teller term and the harmonic oscillator potential term to describe the PES seen along the e'_3 normal coordinates of the $\tilde{X}^2E''_2$ state (or the e'_1 normal coordinates of the $\tilde{A}^2E''_3$ state). $V_{\pm,j}^h$ refers to the harmonic oscillator potential of the \tilde{X} - or \tilde{A} -state PES seen along any of the non-linear-Jahn-Teller active normal coordinates. With k_i positive, the minus sign in Eqs. 6.6 and 6.7 designates the lower sheet of the PES, while the plus sign corresponds to the upper sheet of the PES.

We introduce the harmonic vibrational frequency of the i^{th} mode evaluated at the conical intersection of the \tilde{X} - or \tilde{A} -state PES, $\omega_{e,i}$, and the linear Jahn-Teller coupling constant of the i^{th} mode, D_i , and define them as previously^{100, 103, 104}

$$\omega_{e,i} = \frac{1}{2\pi c} \left(\frac{\lambda_i}{M_i} \right)^{1/2} \quad (6.8)$$

and

$$D_i = \frac{k_i^2}{2\hbar} \left(\frac{M_i}{\lambda_i^3} \right)^{1/2} \quad (6.9)$$

where M_i corresponds to the reduced mass of the i^{th} vibrational mode of tropyl. By taking the derivative of Eq. 6.6 with respect to ρ_i (which is independent of the angle ϕ_i) and setting it to zero we derive the following equations

$$\rho_i^{min} = \frac{k_i}{\lambda_i} = \left(\frac{\hbar D_i}{\pi c M_i \omega_{e,i}} \right)^{1/2} \quad (6.10)$$

$$\varepsilon_i^{min} = -\frac{k_i^2}{2\lambda_i} = -2\hbar\pi c D_i \omega_{e,i}, \quad (6.11)$$

where ρ_i^{min} corresponds to the distance from the D_{7h} point to the distorted potential energy minimum along the linear Jahn-Teller active normal coordinates $Q_{i,\pm}$, and ε_i^{min} refers to the magnitude of the linear Jahn-Teller stabilization energy due to Jahn-Teller distortion along $Q_{i,\pm}$, measured with reference to X_0 which is taken as zero. The total linear Jahn-Teller stabilization energy is given, within our approximation, by

$$\varepsilon_T = \sum_i^p \varepsilon_i^{min}. \quad (6.12)$$

Relationship of the Spectroscopic Model and Theoretical Results

The relationship between the molecular parameters of the experimental analysis and theoretical results has been given in the past. In this section we review the previous general methodology^{100,104} and apply it specifically on the tropyl radical.

We refer the reader to Fig. 6.2 which illustrates the cross-section through the conical intersection (with geometry X_0) and the global minimum (with geometry X_{min})

of the Jahn-Teller distorted PES of the \tilde{X}^2E_2'' or \tilde{A}^2E_3'' states of tropyl. We define the distortion vector, labeled by \vec{d} , as the vector that describes the atomic displacements necessary to occur for the molecule to reach the global minimum starting from the conical-intersection geometry.

The vector, \vec{Q}_i , defined along one of the normal coordinates, i , may be expressed

$$\vec{Q}_i = Q_i \vec{u}_{Q_i} = \sum_{\alpha} q_{i\alpha} l_{\alpha i}^{-1} \vec{u}_{\alpha} \quad (6.13)$$

with

$$q_{i\alpha} = m_{\alpha}^{1/2} x_{\alpha} = \sum_i l_{\alpha i} Q_i. \quad (6.14)$$

While the direction of \vec{Q}_i (its length determined by Q_i) is given by the unit vector \vec{u}_{Q_i} , the directions of the atomic Cartesian displacements ($x_1, y_1, z_1, x_2, y_2, z_2 \dots x_{3N}, y_{3N}, z_{3N}$) are given by the unit vectors \vec{u}_{α} . Note that in the above equations \mathbf{l} , with elements $l_{\alpha i}$, represents a $3N \times 3N$ orthogonal transformation matrix. It diagonalizes the mass-weighted force constant matrix expressed in the atomic Cartesian coordinate system. In our approach the force constant matrix is computed by B3LYP/6-31G** calculations at the minimum energy of $\tilde{X}^1A'_1$ of $C_7H_7^+$. Such calculations provide a good approximation to the unperturbed harmonic frequencies, $\omega_{e,i}$, and the corresponding normal coordinates of C_7H_7 in its \tilde{X}^2E_2'' and \tilde{A}^2E_3'' states. Based on Eqs. 6.13 and 6.14, the unit vector \vec{u}_{Q_i} may be expressed as

$$\vec{u}_{Q_i} = \sum_{\alpha} l_{\alpha i}^{-1} \vec{u}_{q_{\alpha}}. \quad (6.15)$$

Note that the unit vector \vec{u}_{Q_i} is normalized hence it holds that $\vec{u}_{Q_i} \cdot \vec{u}_{Q_i} = 1$.

The distortion vector \vec{d} is obtained as the vector difference between the vectors pointing from the origin at the center-of-mass to the conical intersection geometry (X_0) and the global-energy-minimum geometry (X_{min}) as determined by the EOMEA-CCSD calculations, i.e.,

$$\vec{d} = \vec{X}_0 - \vec{X}_{min} = \sum_{\alpha} d_{\alpha} \vec{u}_{q_{\alpha}}, \quad (6.16)$$

where \vec{X}_0 and \vec{X}_{min} are vectors expressed in the atomic Cartesian coordinate system. We choose to work in a mass-weighted coordinate system; we define the mass-weighted distortion vector, \vec{d}_m by

$$\vec{d}_m = \sum_{\alpha} d_{\alpha} m_{\alpha}^{1/2} \vec{u}_{q_{\alpha}}, \quad (6.17)$$

and the d_{α} 's are determined by Eq. 6.16. Since \vec{d}_m lies in the space spanned by the p doubly degenerate linear Jahn-Teller active normal coordinates of the \tilde{X} or \tilde{A} states of tropyl, we can write

$$\vec{d}_m = \sum_{i=1}^p \sum_{j=a,b} d_{i,j}^q \vec{u}_{Q_{i,j}}, \quad (6.18)$$

where

$$d_{i,a}^q = \vec{d}_m \cdot \vec{u}_{Q_{i,a}} = \rho_i^{min} \cos \phi_i, \quad (6.19)$$

$$d_{i,b}^q = \vec{d}_m \cdot \vec{u}_{Q_{i,b}} = \rho_i^{min} \sin \phi_i, \quad (6.20)$$

and $\vec{u}_{Q_{i,a/b}}$ are the unit vectors given by Eq. 6.15 for the a and b degenerate components of mode i .

By summing the squares of Eqs. 6.19 and 6.20 we obtain

$$(\rho_i^{min})^2 = (d_{i,a}^q)^2 + (d_{i,b}^q)^2 \quad (6.21)$$

$$= (\vec{d}_m \cdot \vec{u}_{Q_{i,a}})^2 + (\vec{d}_m \cdot \vec{u}_{Q_{i,b}})^2. \quad (6.22)$$

We calculate the dot products of Eq. 6.22 expressed in the atomic Cartesian coordinate system, based on our theoretically computed parameters of $\vec{u}_{Q_{i,a/b}}$ and \vec{d} , and estimate ρ_i^{min} .

If we rearrange Eq. 6.10 for ρ_i^{min} , and solve for D_i we have

$$D_i = (\rho_i^{min})^2 \omega_{e,i} \pi c \hbar^{-1} \quad (6.23)$$

$$= \left[\left(\vec{d}_m \cdot \vec{u}_{Q_{i,a}} \right)^2 + \left(\vec{d}_m \cdot \vec{u}_{Q_{i,b}} \right)^2 \right] \omega_{e,i} \pi c \hbar^{-1} \quad (6.24)$$

$$= \left[\left(\sum_{\alpha} l_{\alpha i_a}^{-1} d_{\alpha} m_{\alpha}^{\frac{1}{2}} \right)^2 + \left(\sum_{\alpha} l_{\alpha i_b}^{-1} d_{\alpha} m_{\alpha}^{\frac{1}{2}} \right)^2 \right] \omega_{e,i} \pi c \hbar^{-1} \quad (6.25)$$

where everything on the right side of Eq. 6.25 is known from the theoretical calculations. We can compute the total, and individual mode, linear Jahn-Teller stabilization energy by using Eqs. 6.11 and 6.12 given the values of D_i and $\omega_{e,i}$. Tables 6.3 and 6.4 summarize the results of our theoretical findings.

6.3 Theoretical

6.3.1 Vibronic Eigenvalues and Eigenfunctions

In section 6.2 we applied the general theory for Jahn-Teller distortions specifically to the case of C₇H₇. We found that we could write the vibronic Hamiltonian $\hat{\mathcal{H}}$ as

$$\hat{\mathcal{H}} = \hat{\mathcal{H}}_T + \hat{V} = \hat{\mathcal{H}}_T + \hat{\mathcal{H}}_h + \hat{\mathcal{H}}_l, \quad (6.26)$$

Mode ^a	Symmetry ^a	C ₇ H ₇ ⁺		C ₇ H ₇	
		$\tilde{X}^1A'_1$ Calc ^b	$\tilde{X}^2E''_2$ Exp ^c	$\tilde{A}^2E''_3$ Exp ^c	
1	a'_1	3210	
2	a'_1	881	840	858	
3	a'_2	1441	
4	a''_2	664	632	677	
5	e'_1	3205	
6	e'_1	1519	1482	...	
7	e'_1	1014	1060	...	
8	e''_1	891	788	849	
9	e'_2	3196	
10	e'_2	1637	1643	1699	
11	e'_2	1255	1265	1191	
12	e'_2	438	487	...	
13	e''_2	1079	1050	1104	
14	e''_2	1061	1144	1032	
15	e'_3	3187	
16	e'_3	1568	...	1545	
17	e'_3	1313	...	1253	
18	e'_3	898	...	857	
19	e''_3	564	564	...	
20	e''_3	224	...	294	

Table 6.3: The vibrational frequencies (cm^{-1}) of the geometrically optimized C₇H₇⁺ in its $\tilde{X}^1A'_1$ state calculated at the B3LYP/6-31G** level of theory compared to experimental values of the $\tilde{X}^2E''_2$ and $\tilde{A}^2E''_3$ states of C₇H₇.

^a The Herzberg numbering scheme is used to label the vibrations. The symmetry of the vibrational modes is given in the D_{7h} group. ^b The calculated harmonic frequencies are not scaled. ^c Experimental values taken from Section 6.5.

where $\hat{\mathcal{H}}_T$ is the nuclear kinetic energy operator and the non-zero electronic matrix elements of the terms of the effective potential, \hat{V} , are given¹⁶ by

$$\begin{aligned}\left\langle \Lambda_{\pm} \left| \hat{\mathcal{H}}_h \right| \Lambda_{\pm} \right\rangle &= \frac{1}{2} \sum_{i=1}^p \sum_{r=+,-} \lambda_i |Q_{i,r}|^2 + \frac{1}{2} \sum_{i=1}^{3N-6-2p} \lambda'_i |Q_i|^2 \\ &= \sum_{i=1}^p \sum_{r=+,-} \left(\sqrt{2} \pi c M_i^{1/2} \omega_{e,i} \right)^2 |Q_{i,r}|^2 \\ &+ \sum_{i=1}^{3N-6-2p} \left(\sqrt{2} \pi c M_i^{1/2} \omega'_{e,i} \right)^2 |Q_i|^2\end{aligned}\quad (6.27)$$

and

$$\left\langle \Lambda_{\pm} \left| \hat{\mathcal{H}}_l \right| \Lambda_{\mp} \right\rangle = \sum_{i=1}^p k_i Q_{i,\pm} = \sum_{i=1}^p \left(8\pi^2 c^3 h M_i^2 \omega_{e,i}^3 D_i \right)^{1/2} Q_{i,\pm}. \quad (6.28)$$

In this formulation, $\omega_{e,i}$ and $\omega'_{e,i}$ refer to the vibrational frequencies of the i^{th} normal mode, $Q_{i,\pm}$ and Q_i , respectively, defined at the D_{7h} conical intersection, X_0 , of the \tilde{X} - and \tilde{A} -state potential energy surfaces (PES) of tropyl, and D_i is the linear Jahn-Teller coupling parameter. The sum over i is for the $p = 4$ e'_3 modes of the \tilde{X} $^2E''_2$ state of C₇H₇ or the $p = 3$ e'_1 modes of its \tilde{A} $^2E''_3$ state. As was noted in section 6.2, the normal coordinates, $Q_{i,\pm}$, have been introduced by the relationship,

$$Q_{i,\pm} = \rho_i e^{\pm i\phi}. \quad (6.29)$$

A summary of our calculated PES parameters of section 6.2 is given in Table 6.4.

While in general the potential, \hat{V} , may be dependent on ϕ , this does not hold for a molecule of nominal D_{7h} symmetry. (See section 6.2.) In section 6.2 we showed, as have others, that the potential, $\hat{V} = \hat{\mathcal{H}}_h + \hat{\mathcal{H}}_l$, has a global minimum for the values

$\tilde{X}^2\text{E}_2''$ State ^a of C ₇ H ₇						$\tilde{A}^2\text{E}_3''$ State ^a of C ₇ H ₇							
Mode	Calc			Exp			Mode	Calc			Exp		
	ω_i	D _i	ε_i	ω_i	D _i	ε_i		ω_i	D _i	ε_i	ω_i	D _i	ε_i
15	3187	<0.01	<1	5	3205	<0.01	<1
16	1568	0.56	878	1600	0.50	800	6	1519	0.14	213	1519	0.10	152
17	1313	0.22	289	1350	0.12	162	7	1014	0.72	730	950 (10 ^b)	0.70	665
18	898	0.11	99	900	0.09	81		1043		943			
ε_T			1266								817		

Table 6.4: Jahn-Teller Parameters of the $\tilde{X}^2\text{E}_2''$ and $\tilde{A}^2\text{E}_3''$ electronic states of C₇H₇.

^a All constants have units of cm⁻¹, except D_i which is unitless. ^b Anharmonicity constant $\omega_e \chi_e$ in cm⁻¹.

of ρ_i^{min} given by

$$\rho_i^{min} = \left(\frac{\hbar D_i}{\pi c M_i \omega_{e,i}} \right)^{1/2}, \quad (6.30)$$

with a Jahn-Teller stabilization energy $-\varepsilon_T$ (measured with respect to zero at X_0)

$$\varepsilon_T = \sum_{i=1}^p \varepsilon_i = \sum_{i=1}^p 2\hbar\pi c D_i \omega_{e,i}. \quad (6.31)$$

A high-data throughput computer program called SPEC-SOCJT¹³¹ was specifically designed for eigenvalues and functions of $\hat{\mathcal{H}}_e$ for the \tilde{A} - and \tilde{X} -state C₇H₇ spectral analysis. It was implemented in Fortran and C++ and enabled fast computational methods for the construction of the Hamiltonian matrix and the solution of the Schrödinger equation. The data input and output interfaces were developed using Microsoft Visual C++ tools and allow for a quick exchange of information between the calculational core and the user. The graphic user interface part of the program was developed to display and compare in one step all pairs of \tilde{X} - and \tilde{A} -state experimental and simulated spectra of the tropyl radical. To facilitate ease of use the data input can be made in dialog boxes, and the user can also perform a one-dimensional parameter scan with the simple touch of the mouse wheel.

SPEC-SOCJT can be used to numerically solve for the $\tilde{X} \ ^2E''_2$ - and $\tilde{A} \ ^2E''_3$ -state vibronic energy levels based on the Hamiltonian matrix defined in Eqs. 6.27 and 6.28. Using the known¹⁶ matrix elements of $\hat{\mathcal{H}}$, in terms of the experimental parameters, $\omega_{e,i}$, $\omega'_{e,i}$, and D_i , SPEC-SOCJT can construct this matrix in a suitable basis set and find its eigenpairs. The basis set used in SPEC-SOCJT is a product of electronic and

vibrational wave functions represented by

$$|\Lambda\rangle \prod_{i=1}^p |v_i l_i\rangle, \quad (6.32)$$

with quantum numbers $\Lambda = \pm 1$, $v_i = 0, 1, 2, \dots$, $l_i = v_i, v_i - 2, \dots, -v_i + 2, -v_i$. $\Lambda = \pm 1$ refer to the two electronic components of the doubly degenerate (\tilde{X} or \tilde{A}) electronic state of tropyl, v_i are the principal vibrational quantum numbers of the linear Jahn-Teller active modes, and l_i are their vibrational angular momentum quantum numbers. Since the linear Jahn-Teller term in the Hamiltonian is off-diagonal in the Λ , v_i , and l_i quantum numbers it is useful to define a quantum number, j , that is conserved, and is given by¹⁶

$$j = l_t + \frac{1}{2}\Lambda, \quad (6.33)$$

with

$$l_t = \sum_i l_i. \quad (6.34)$$

From Eq. 6.33 it is obvious that there will be multiple energy levels with identical values of j , hence we define a second quantum number, n_j , which takes on the values $1, 2, 3, \dots, \infty$ and serves only to provide unique labels to the eigenvalues of the same j , ordered by increasing energy. Thus we denote eigenkets as $|j, n_j\rangle$.

The basis set defined above is infinite in size. Obviously one must truncate the basis set to some reasonable size before diagonalizing the Hamiltonian matrix. In practice the calculated eigenvalues were tested for convergence by systematically increasing the number of basis functions until the change in the eigenvalues was less than 0.1 cm^{-1} . For C₇H₇, the final matrices used were of order 5×10^4 .

6.3.2 Selection Rules

The selection rule for the j quantum number, derived from the selection rules for l_i and Λ , dictate that¹⁶ excitation from the vibrationless level of the \tilde{X} state of tropyl can only terminate on levels in the \tilde{A} state with $j = \frac{1}{2}$, i.e., $\Delta j = 0$. Hereafter we consider transitions allowed by the electric dipole moment component $\mu_{x,y} = E'_1$. Speaking in terms of D_{7h} point-group symmetry labels, the excitation from the vibrationless level of the $\tilde{X}^{\ 2E''_2}$ state of tropyl with e''_2 vibronic symmetry will terminate on levels in the $\tilde{A}^{\ 2E''_3}$ state with e''_3 vibronic symmetry and vice versa. The vibrational modes with e'_3 symmetry are Jahn-Teller inactive in the $\tilde{A}^{\ 2E''_3}$ state and the $\tilde{X} \rightarrow \tilde{A}$ transition to these levels may be vibronically allowed. The e'_1 vibrational modes are Jahn-Teller inactive in the $\tilde{X}^{\ 2E''_2}$ state and the $\tilde{A} \rightarrow \tilde{X}$ transition to such levels may be allowed vibronically. All quanta of excitation to the \tilde{A} state or emission to the \tilde{X} state are vibronically allowed for the Jahn-Teller inactive modes with symmetries a'_2 and e'_2 . Only the transitions in double quanta are fully electronically allowed for the Jahn-Teller inactive vibrational modes with symmetries $a''_2^{(\prime\prime)}$, e''_1 , $e''_2^{(\prime\prime)}$, and e''_3 . Similarly, the $\tilde{X} \rightarrow \tilde{A}$ transitions to the e'_3 levels and the $\tilde{A} \rightarrow \tilde{X}$ transitions to the e'_1 levels are fully electronically allowed only in double quanta of excitation or emission, correspondingly. Progressions built upon the a'_1 vibrational modes are electric-dipole allowed. Only the electronically or vibronically allowed transitions to combination levels of the \tilde{X} or \tilde{A} state are considered.

6.4 Experimental Details

The experimental setup used to obtain both the LIF spectrum of the \tilde{A}^2E_3'' state and the LEDF spectra of the \tilde{X}^2E_2'' state is depicted graphically in Fig. 6.3. A few torr of the cycloheptatriene vapor were entrained into the jet flow by passing a carrier gas at a suitable backing pressure over the liquid contained in a stainless steel reservoir maintained at a suitable temperature depending upon the vapor pressure. The seeded flow was then expanded through a 300- μm standard pulsed nozzle (General Valve) into the jet chamber which was evacuated by a mechanical booster pump backed by a rotary oil pump. The tropyl radicals were generated *in situ* in the gas pulse of the hydrocarbon precursor mixed with the carrier gas by striking a pulsed electrical discharge. The tropyl radicals were produced by the abstraction of a hydrogen atom from cycloheptatriene. A summary of the experimental conditions for the LIF and LEDF experiments is given in Table 6.5. (Note that bands A-C are shown in Fig. 6.4.)

The resulting free-jet expansion was crossed approximately 10-15 mm downstream of the pulsed discharge nozzle by the frequency doubled output (Inrad Autotracker II) of a tunable dye laser (SpectraPhysics PDL-3) pumped by the second harmonic of a Nd:YAG (Quanta Ray DCR) laser at 532 nm. This work required the use of four laser dyes, namely, LDS 698, 750, 751 and 765. The delay time between the striking of the discharge and the firing of the dye laser, along with the time delay and the opening time of the nozzle, were controlled by a pulse generator (Stanford Research DG535).

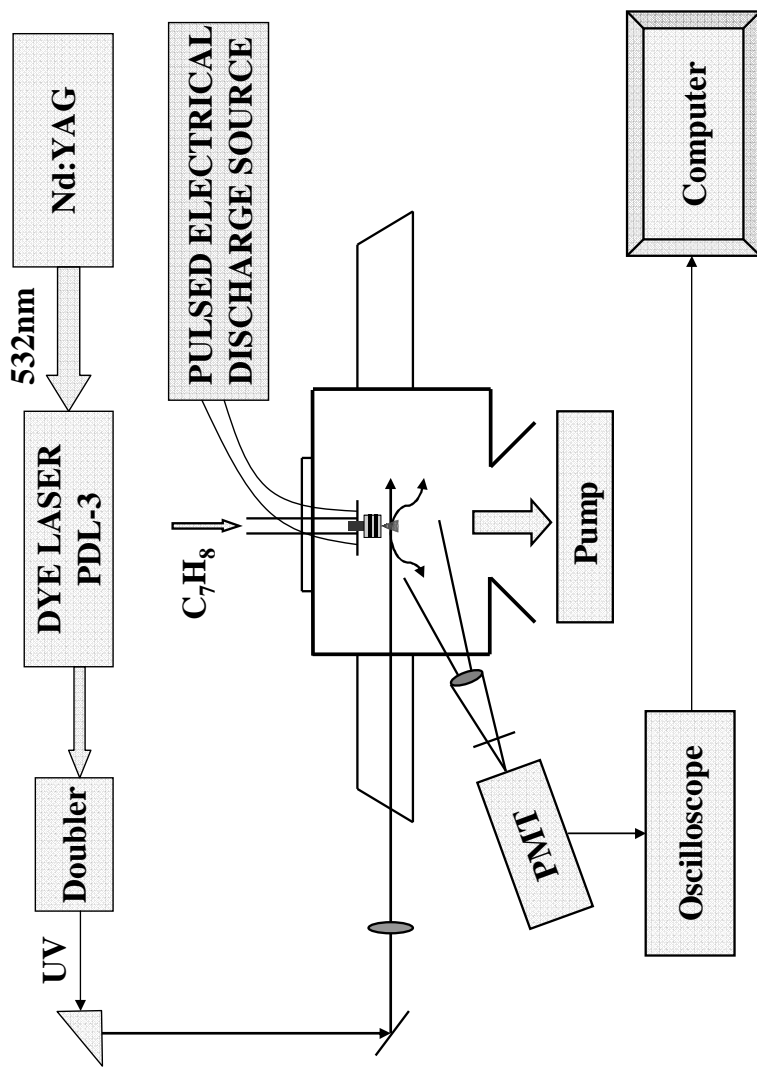


Figure 6.3: Schematic diagram of the experimental apparatus for obtaining the LIF spectrum. The apparatus for the LEDF experiments was similar except the fluorescence was dispersed.

Experiment	LIF	LEDF
carrier gas	He	Ar
temperature of the sample bomb (°C)	-10	5
backing pressure (psi)	30-60	30
opening time of the jet (μ sec)	600	300
discharge voltage (V)	1000	400-500
discharge pulse duration (μ sec)	850	80-200
resolution (cm^{-1})	4	20
accumulation time (min)	-	90, ^a 60, ^b 30 ^c
slit width (μm)	-	125
grating (grooves/mm)	-	1800

Table 6.5: Summary of the conditions used for the LIF and LEDF experiments with the tropyl radical.

^a The accumulation time for the LEDF collection via band A was extended two hours for the first 2000 cm^{-1} redshifted from the pumping frequency, and 90 min for $> 2000 \text{ cm}^{-1}$ above the origin. ^b The accumulation time for the LEDF collection via band B was extended to three hours for the first 2000 cm^{-1} redshifted from the pumping frequency, and 60 min for $> 2000 \text{ cm}^{-1}$ above the origin. ^c The accumulation time for the LEDF collection via band C was extended to 60 min for the first 2000 cm^{-1} redshifted from the pumping frequency, and 30 min for $> 2000 \text{ cm}^{-1}$ above the origin.

The probe beam passed through the vacuum chamber. The fluorescence signal was collected perpendicularly to the laser beam. On one side of the chamber, the fluorescence emission was collimated by a 1 in. diameter lens ($f/1$) and a second lens focused the radiation onto the photocathode of the photomultiplier tube (EMI 9659Q) connected to an amplifier. The amplified LIF signal was integrated by a boxcar averager, digitized by an A/D converter and fed into a personal computer for further data processing. On the other side of the chamber, the fluorescence emission was dispersed by a Spectra Pro 300i monochromator using a 1800 grooves/mm grating and then imaged onto an intensified charge-coupled device (ICCD). The detection of the dispersed photons was done with the Princeton Instruments PI-MAX512HB camera. The entrance slit width of the monochromator was set at $125\mu\text{m}$. The emission frequencies reported for the LEDF spectra and the excitation frequencies for the LIF spectrum of the tropyl radical were obtained by calibrating them against a Fe-Ne optogalvanic lamp and known Ar atomic lines.

6.5 Results

6.5.1 Assignment of the $\tilde{A}^2\text{E}_3''$ State

Although the REMPI¹ spectrum of “cold” C₇H₇ has been known for some time, there are still open questions as to the complete assignment of the spectrum. In this work, we have recorded the LIF spectrum of the $\tilde{A}^2\text{E}_3''$ state of C₇H₇. The LIF and REMPI spectra of C₇H₇ are shown in Fig. 6.4. The stars in the LIF spectrum designate the bands of the \tilde{A} state that we have dispersed the emission from. The second and third

columns of Table 6.6 give the experimental frequencies of the $\tilde{A} \leftarrow \tilde{X}$ spectrum of the tropyl radical observed in the REMPI¹ experiment, and the fifth and sixth columns the experimental frequencies recorded in the LIF experiment. There is agreement between our LIF work and the results from the REMPI experiment, as one can see from Fig. 6.4 and Table 6.6. In the first column of Table 6.6 under assignment we give the spectroscopic designation of the terminating energy levels of the transitions originating in $|\frac{1}{2}, 1\rangle$ of the \tilde{X} state of C₇H₇. Their vibrational symmetry labels are given in the sixth column of the Table. Note that for the Jahn-Teller energy levels and their combinations, the symmetry space spanned by the harmonic-oscillator wave functions is given instead. The Jahn-Teller energy levels reported in this Table span only a vibronic subspace of it with e_3'' symmetry.

We first consider spectral assignments of the observed levels in the LIF spectrum. (See Fig. 6.4.) The assignments are guided by our \tilde{A}^2E_3'' -state theoretical calculations from section 6.2.

We assigned the electronic origin of the $\tilde{A}^2E_3'' - \tilde{X}^2E_2''$ excitation spectrum at $26572 \pm 4 \text{ cm}^{-1}$, hereafter referred to as band A, based on experimental indication. Although we didn't perform detailed fluorescence lifetime measurements on C₇H₇, we observed that the lowest frequency band in this energy region that showed a temporal total fluorescence profile consistent with the one "expected" for tropyl was band A. Specifically, we noticed that the temporal profile for bands A-C had a full width at half maximum (fwhm) of approximately $2 \mu\text{s}$, and that it decreased to $1.1 \mu\text{s}$ for the three bands in the higher energy region that we recorded emission from. (See Fig.

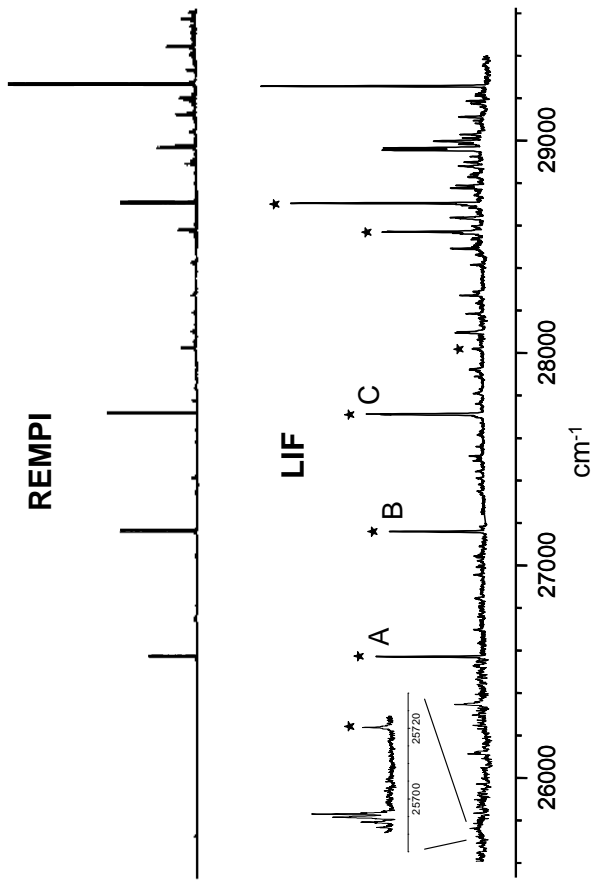


Figure 6.4: REMPI (top) and LIF (bottom) spectra of C_7H_7 . The REMPI spectrum was taken from Ref. 1 and the LIF spectrum comes from the present work. The stars in the excitation spectrum designate the bands of the $\tilde{\text{A}}$ state that we have dispersed emission from. Of central importance for the analysis of the vibronic structure of the $\tilde{\text{X}}^2\text{E}_2''$ state is the LEDF emission collected by pumping bands A-C of the $\tilde{\text{A}}^2\text{E}_3''$ state. The x axis indicates the excitation frequency. The intensities observed in the LIF spectrum were not corrected for the dye-laser power deviations. The experimental resolution was 4 cm^{-1} .

Assignment ^a	Frequency (cm ⁻¹)					
	Ref. 1	Absolute	Relative to 0 ₀ ⁰	Absolute	Relative to 0 ₀ ⁰	Symmetry
25719 ^b	25719 ^b	...	25719 ^b	26117 ^c
...	26345 ^c
₂ , 1 > (A)	26573 ^b	0	26572 ^b	0	d' ₁	...
_{20₀²} (B)	27159	586	27160	588	a' ₁ ⊕ e' ₁	...
₂ , 2 > (C)	27711	1138	27713	1141	e' ₁	...
_{20₀²} (α)	28018	1445	28018	1446	a' ₁ ⊕ e' ₁	...
₂ , 3 >	28096	1524	a' ₁ ⊕ e' ₂	...
(8 ₀ ² /10 ₀ ¹) ^e	28269	1696	28271 ^d	1699	(a' ₁ ⊕ e' ₂ /e' ₂) ^e	...
₁ , 4 >	28493	1921	e' ₁ ⊕ e' ₃	...
18 ₀ ¹ ₂ , 2 > (β)	28571	1998	28570	1998	e' ₂ ⊕ e' ₃	...
14 ₀ ²	28636 ^d	2064	a' ₁ ⊕ e' ₃	...
16 ₀ ¹ 20 ₀ ² (γ)	28704	2131	28705	2133	e' ₂ ⊕ 2e' ₃	...
13 ₀ ²	28780 ^d	2208	a' ₁ ⊕ e' ₃	...
2 ₀ ² 20 ₀ ² (δ)	28877	2304	28876	2304	a' ₁ ⊕ e' ₁	...
11 ₀ ²	28954	2381	28955	2383	a' ₁ ⊕ e' ₃	...
17 ₀ ¹ ₂ , 2 > (ε)	28965	2392	28966	2394	e' ₂ ⊕ e' ₃	...
₂ , 5 >	29110	2537	29111	2539	a' ₁ ⊕ e' ₂ ⊕ e' ₃	...
4 ₀ ² 17 ₀ ¹ (ζ)	29184	2611	29180	2608	e' ₃	...
16 ₀ ¹ ₂ , 2 > (η)	29254	2681	29256	2684	e' ₂ ⊕ e' ₃	...

Table 6.6: Frequencies and $\tilde{A}^2\text{E}_3'' \leftarrow \tilde{X}^2\text{E}_2''$ transition assignments of C₇H₇.

^a We denote with letters (A-C) those bands of the \tilde{A} state that we report emission spectra from. ^b We have reassigned^{1,143} the electronic origin to the feature at 26573 cm⁻¹ (band A).^c Possibly due to artifacts of the discharge. ^d Tentative assignment. ^e Dual assignment.

6.4.) In the energy region lower than 26572 cm^{-1} , the three bands at 25719, 26117, and 26345 cm^{-1} showed a temporal profile with fwhm approximately 500 ns. (See Table 6.6.)

The next intense feature to the blue in the excitation spectrum of the $\tilde{A}\text{ }^2\text{E}_3''$ state appears at 27160 cm^{-1} , 588 cm^{-1} above the origin, and will be hereafter referred to as band B. As we will see later on in the analysis, this band may not be assigned as a transition to a Jahn-Teller level of the \tilde{A} state based on our $\tilde{A}\text{ }^2\text{E}_3''$ -state theoretically calculated Jahn-Teller parameters. Band B may be attributed to a transition to the fundamental of $\omega_4(a_2'')$, $\omega_{12}(e_2')$, $\omega_{19}(e_3'')$, or the first overtone of $\omega_{20}(e_3'')$ which, based on our theoretically calculated frequencies from section 6.2 and neglecting anharmonicity, are predicted at 664, 438, 564, and 448 cm^{-1} , respectively. We assign this band to the transition to the \tilde{A} state level 20^2 as this transition is the only one fully electronically allowed via $\mu_{x,y} = E'_1$. (The transition to the fundamentals of $\omega_4(a_2'')$ and $\omega_{19}(e_3'')$ is neither electronically nor vibronically allowed, while the transition to the fundamental of $\omega_{12}(e_2')$ is only vibronically allowed.) This assignment places the fundamental of ω_{20} in the \tilde{A} state at 294 cm^{-1} neglecting anharmonicity. There may be large contributions from anharmonicity terms, especially given the low frequency of this vibration. The first overtone of ω_{20} may gain intensity in the \tilde{A} state due to quadratic Jahn-Teller interactions in the excited state. We examined the emission spectra from bands A and B shown at the bottom and middle traces of Fig. 6.5, respectively. Based on the above assignment for band B, we expect that its emission to the \tilde{X} state will be allowed only in double quanta, i.e., $\Delta\omega = 0, \pm 2, \pm 4, \dots$ By

subtracting the emission frequencies observed in the LEDF spectrum of Fig. 6.5B by 415 cm^{-1} , we are led to the spectrum of Fig. 6.6B which seems to be almost identical with the emission from band A, shown in Fig. 6.6A. The correspondence between the spectra of Figs. 6.6A and 6.6B is depicted by dotted lines. We conclude that the predominant mechanism of emission from band B is for $\Delta\omega = 0$, which corresponds to the transition to the level 20_2 of the \tilde{X} state, with the fundamental of ω_{20} in the \tilde{X} state at 208 cm^{-1} , neglecting anharmonicity. By comparing the spectra of Figs. 6.5A and 6.5B, we found a common set of experimental frequencies. For the emission through band B, these correspond to transitions to the \tilde{X} state for $\Delta\omega = -2$ and are identified by a star on the spectrum of Fig. 6.6B.

The next intense feature to the blue peaks at 27713 cm^{-1} , 1141 cm^{-1} above the origin, hereafter referred to as band C. The only fully electronically allowed transition expected in this region is 19_0^2 , predicted at 1128 cm^{-1} by neglecting anharmonicity, and the one allowed by the Jahn-Teller interactions in the \tilde{A} state. Although there is no obvious reason to exclude 19_0^2 , we favor the assignment of this band to a transition to a Jahn-Teller level of the \tilde{A} state as the $\tilde{A}^2\text{E}_3''$ -state theoretically calculated Jahn-Teller parameters lead to a simulation with an intense feature lying in the energy region of band C. (See later on in the analysis for further information.)

We assign the weak peak at 28018 cm^{-1} , 1446 cm^{-1} above the origin, to the electronically allowed transition $2_0^1 20_0^2$. As the emission through this band, notwithstanding its broadness, resembles the emission through band B, assigned as 20_0^2 , we reject the only other alternative assignment of this feature to 3_0^1 , which is expected

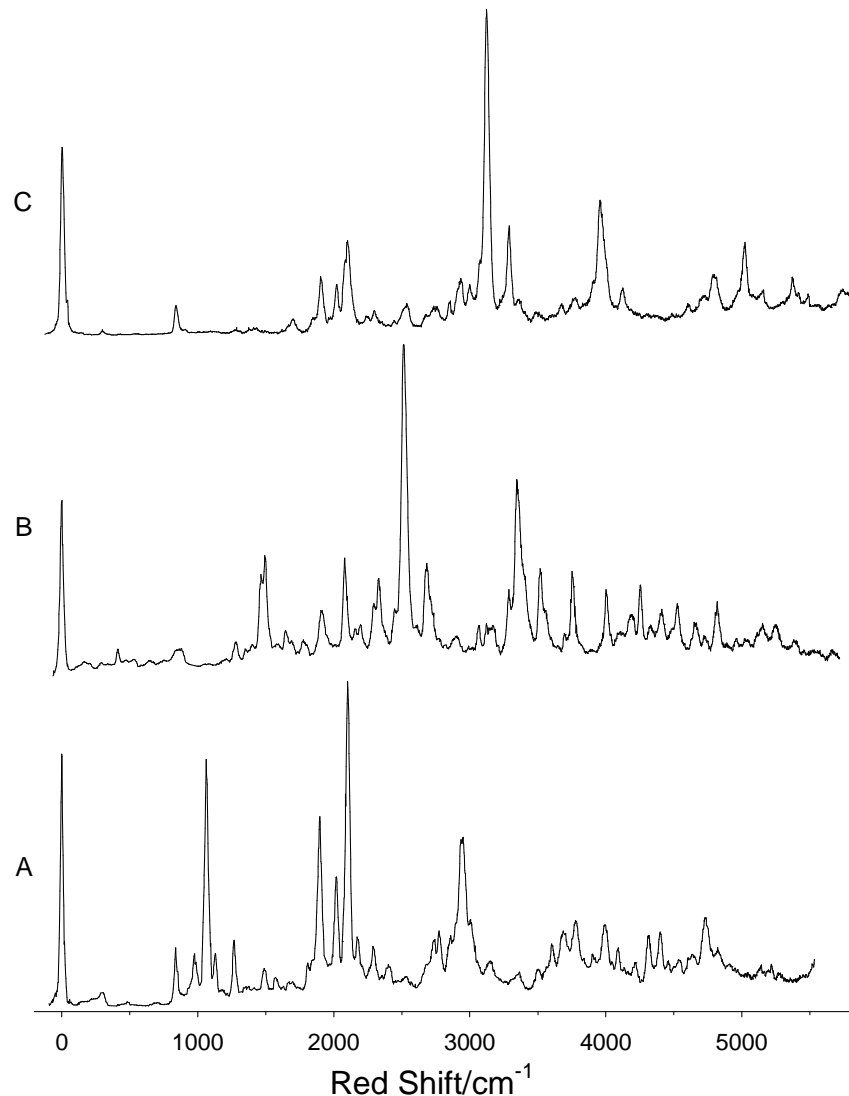


Figure 6.5: Dispersed fluorescence spectra of the C_7H_7 radical collected by pumping bands A (bottom), B (middle), and C (top) of the $\bar{A}^2\text{E}_g''$ state. The entrance slit width before the monochromator was $125 \mu\text{m}$. The x axis indicates (red) shift from the pump frequency. The intensities were not corrected for the grating efficiency and the camera sensitivity curves. The experimental resolution was 20 cm^{-1} . Note also that the structure observed approximately $< 700 \text{ cm}^{-1}$ in the emission from bands A and B are due to artifacts of the discharge source.

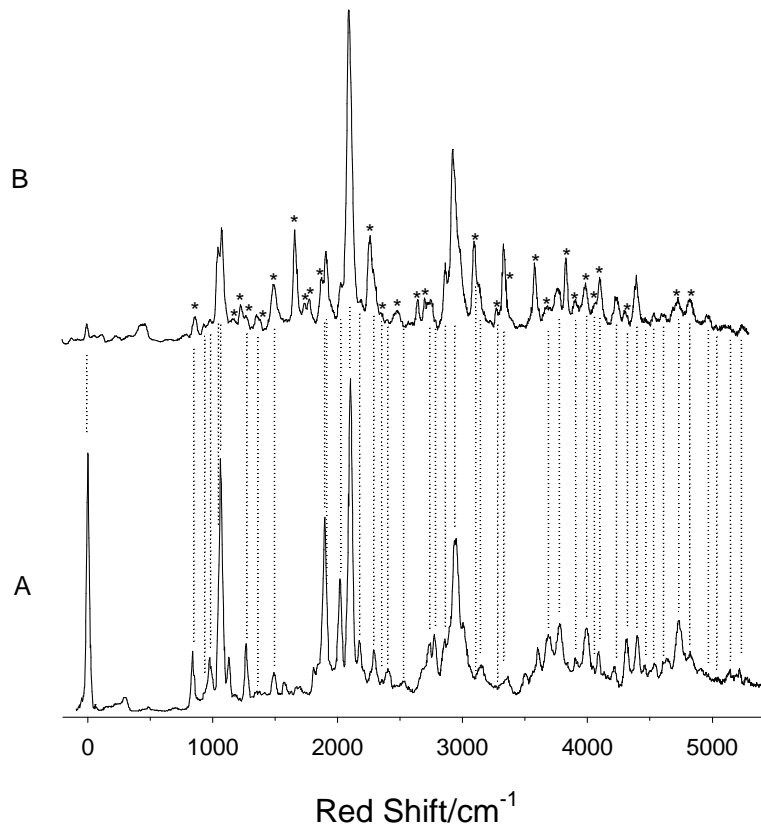


Figure 6.6: Dispersed fluorescence spectra of the C_7H_7 radical collected by pumping bands A (bottom) and B (top) of the $\tilde{A}^2\text{E}_g''$ state. The entrance slit width before the monochromator was $125 \mu\text{m}$. For the emission through band A, the x axis indicates (red) shift from the pump frequency. The emission through band B in this figure corresponds to the subtraction of the emission frequencies of Fig. 6.5B by 415 cm^{-1} . The intensities were not corrected for the grating efficiency and the camera sensitivity curves. The experimental resolution was 20 cm^{-1} .

from the calculations at 1441 cm^{-1} and is only vibronically allowed. The experimental frequency of the fundamental of ω_2 is placed at 858 cm^{-1} and compares well with the theoretical value of 881 cm^{-1} . We probably do not observe the transition to the level 2^1 of the \tilde{A} state due to a weak Franck-Condon factor. Note that this vibration was previously observed in electronic transitions to Rydberg states²³ of C_7H_7 with frequency at $862 \pm 6\text{ cm}^{-1}$, as well as in the $\tilde{X}^1A'_1$ state¹⁴⁴ of C_7H_7^+ with frequency at 868 cm^{-1} .

The first prominent feature in the higher energy region appears at 28570 cm^{-1} , 1998 cm^{-1} above the origin. Based on the theoretically calculated frequencies, possible transitions for assignment to this experimental feature are 13_0^2 , 14_0^2 , and 18_0^2 , predicted, neglecting anharmonicity, at 2158 , 2122 , and 1796 cm^{-1} , respectively. The transition to the combination between band C and the fundamental of $\omega_{18}(e'_3)$, assuming that the experimental frequency for the latter is 857 cm^{-1} , is the last possibility. The theoretical value of the fundamental of ω_{18} is 898 cm^{-1} . The strongest candidates for assignment are either 18_0^2 or the transition to the combination with ω_{18} as this mode is linearly Jahn-Teller active in the $\tilde{X}^2\text{E}_2''$ state. We don't observe a transition to the fundamental of ω_{18} of the \tilde{A} state, though expected, possibly due to poor Franck-Condon factors. As we will see later on in the analysis the transitions to the fundamentals of $\omega_{16}(e'_3)$ and $\omega_{17}(e'_3)$ of the \tilde{A} state are also not observed experimentally, nor are the transitions to their first overtones, possibly for the same reason. Only transitions to their combination levels may be assigned. Hence we favor the assignment of the feature at 28570 cm^{-1} to the transition to the combination between

band C and the fundamental of ω_{18} . The emission spectrum collected through this band, notwithstanding its broadness, is consistent with this assignment. (We spectroscopically identified band C, simulated the emission collected through the band at 28570 cm^{-1} of the \tilde{A} state based on the best-fit Jahn-Teller parameters of the $\tilde{X}\text{ }^2\text{E}_2''$ state, and found sufficient agreement with the above assignment.)

The next intense feature appears at 28705 cm^{-1} , 2133 cm^{-1} above the origin, and is assigned as a transition to a combination between band B and the fundamental of $\omega_{16}(e'_3)$, assuming that the experimental frequency for the latter is 1545 cm^{-1} . The theoretical value for 16^1 is 1568 cm^{-1} . This transition is vibronically allowed, as expected from the selection rules for ω_{16} . Alternative assignments to 14_0^2 and 13_0^2 , calculated neglecting anharmonicity at 2122 and 2158 cm^{-1} , are rejected for the following reasons. We have the emission spectrum through this band; notwithstanding its broadness, it is still consistent with this assignment. Based on the intensity profile of this feature in the \tilde{A} state, as well as that of the feature peaking at 29256 cm^{-1} which as we will see is also assigned as a transition to a combination level of the fundamental of ω_{16} , it seems that the Franck-Condon factors are favoring the transitions to the combinations with the fundamental of ω_{16} of the \tilde{A} state. This is not surprising as the linear Jahn-Teller constant of ω_{16} has been theoretically predicted to be the largest in the $\tilde{X}\text{ }^2\text{E}_2''$ state. (See Table 6.4.)

The weak feature at 28876 cm^{-1} , 2304 cm^{-1} above the origin, may be assigned to the transition $2_0^2 20_0^2$. There is no reasonable other candidate based on the theoretically calculated frequencies. This assignment presupposes no anharmonicity in the

\tilde{A} -state potential of the ring-breathing mode ω_2 . The intense feature at 28955 cm^{-1} , 2383 cm^{-1} above the origin may be assigned to the transition 11_0^2 which is predicted at 2510 cm^{-1} , neglecting anharmonicity and based on the theoretically calculated frequency of $\omega_{11}(e'_2)$. This transition is fully electronically allowed, and is probably gaining intensity in the \tilde{A} state as this mode is quadratically Jahn-Teller active in the \tilde{X} state. Hence it is likely that large off-diagonal Franck-Condon factors may be introduced along its normal coordinate. We assign the intense feature at 28966 cm^{-1} (2394 cm^{-1} above the origin) as the transition to the combination between band C and the fundamental of $\omega_{17}(e'_3)$. This assignment is based on the good agreement between the theoretically calculated frequency of ω_{17} at 1313 cm^{-1} and the experimentally determined value at 1253 cm^{-1} . No other plausible candidate could be found. The weak feature at 29180 cm^{-1} , 2608 cm^{-1} above the origin, may be assigned to the transition $4_0^2 17_0^1$, following the same methodology of assignment. The experimental frequency, neglecting anharmonicity, of the fundamental of ω_4 is 677 cm^{-1} , and it is in good agreement with the theoretically calculated frequency of 664 cm^{-1} . Finally, the strongest feature in the high energy region that centers at 29256 cm^{-1} , 2684 cm^{-1} above the origin, is assigned to the transition to the combination band between band C and the fundamental of $\omega_{16}(e'_3)$. This is the only possible assignment considering that the alternative transitions 3_0^2 and 17_0^2 are not options; the first one because there is absolutely no justifiable reason for the first overtone of $\omega_3(a'_2)$ to exhibit such a

strong intensity profile in the $\tilde{A} \ ^2E_3''$ state, and the second because we already have assigned the fundamental of ω_{17} , and based on this assignment its first overtone is not easily placed at 2684 cm^{-1} above the origin.

Several other tentative assignments to weak experimental features were made, namely, to the bands peaking at 28271, 28636, and 28780 cm^{-1} . These bands were assigned based on the theoretical expectations from the calculated frequencies and by a process of elimination to 8_0^2 (an alternative assignment is 10_0^1), 14_0^2 , and 13_0^2 , respectively. Note that $\omega_{10}(e'_2)$, $\omega_{13}(e''_2)$ and $\omega_{14}(e''_2)$ are vibrations with quadratic Jahn-Teller interactions in the $\tilde{X} \ ^2E_2''$ state of tropyl. Of all these transitions, only the one to the level 10^1 of the \tilde{A} state is vibronically allowed. A number of weak bands have appeared in our LIF spectrum and not in the REMPI spectrum. These features are likely due to artifacts of our discharge source. As it has previously been discussed,¹⁴⁵ molecules may fragment, isomerize or energize under such conditions.

Our assignments for the \tilde{A} -state levels $\leq 2700 \text{ cm}^{-1}$ are in disagreement with past work,¹ as the origin of the $\tilde{A} \ ^2E_3''-\tilde{X} \ ^2E_2''$ excitation spectrum was tentatively¹⁴³ assigned to the weak feature at 26573 cm^{-1} whereas we assigned it to the band at 26572 cm^{-1} . Additionally, Pino *et al*¹ did not attempt a multimode Jahn-Teller analysis as we did in the present work, owing to the fact that they identified a small number of lines in the $\tilde{A} \ ^2E_3''$ state and hence could not provide reliable experimental Jahn-Teller parameters for the excited state. Their theoretical calculations did not involve computation of the \tilde{A} -state linear Jahn-Teller parameters.

We simulated the vibronic structure of the \tilde{A}^2E_3'' - \tilde{X}^2E_2'' excitation spectrum, using the above assignments. Our assumption was that only the lowest vibronic wave function of the \tilde{X} state, i.e. $|\frac{1}{2}, 1\rangle$, is populated in the jet expansion. We expect transitions to the \tilde{A} state that satisfy $\Delta j = 0$.

The experimental LIF spectrum of the \tilde{A}^2E_3'' state of tropyl is shown in Fig. 6.7A. The assignment of the transitions to the $j = 1/2$ Jahn-Teller vibronic levels started with a simulation of the spectrum using the theoretically calculated Jahn-Teller parameters of the \tilde{A}^2E_3'' state, listed in the ninth and tenth columns of Table 6.4. (Fig. 6.7B.) Note that only the modes ω_6 and ω_7 were introduced in the Jahn-Teller simulation of the \tilde{A} state. The excitation intensities are calculated by SPEC-SOCJT assuming all oscillator strength results from the Jahn-Teller mixing for the e'_1 modes of the \tilde{A} state. The most intense feature to the blue of the origin of the simulation in Fig. 6.7B must reasonably correlate with band C of the experimental spectrum. Assignment to band C of the experimental trace produced an \tilde{X} -state simulation consistent with the experimental observation for the ground electronic state, as we will see in Section 6.5.2. Thus the feature is assigned to the second experimental band and the Jahn-Teller parameters adjusted accordingly. (See Fig. 6.7C.) We only slightly refined the theoretically calculated Jahn-Teller coupling parameters of the \tilde{A} state, as we place great confidence on them. (The twelfth and thirteen columns of Table 6.4 summarize the experimental Jahn-Teller parameters of the \tilde{A}^2E_3'' state.)

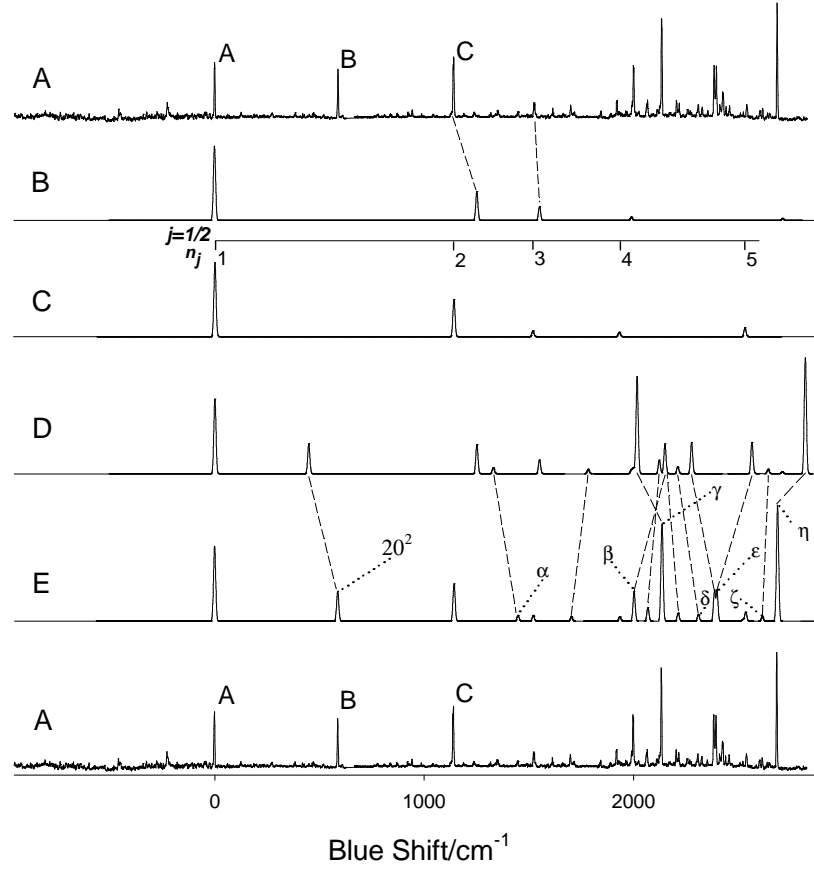


Figure 6.7: Excitation spectrum of C_7H_7 , laser excited from the vibrationless level of the $\tilde{X}^2\text{E}_g''$ state.

(A) Experimental trace. Bands A-C are denoted in the figure (top and bottom traces); (B) Positions of the transitions to the e' Jahn-Teller active levels with $j = 1/2$ symmetry, computed using the theoretically calculated Jahn-Teller parameters of the $\tilde{A}^2\text{E}_g''$ state; (C) Same as (B) but using the best-fit Jahn-Teller parameters of the $\tilde{A}^2\text{E}_g''$ state; (D) Same as (B) plus the positions of the transitions to the first overtone of ω_{20} , ω_8 , ω_{14} , ω_{13} , and ω_{11} as well as a number of combination levels (labelled in E as α , β , γ , δ , ϵ , ζ , and η). The intensity of the transition to the levels $\omega_{20}^2 - \omega_{11}^2$ and $\alpha - \eta$ was adjusted to the experimentally observed; (E) Same as (D) but using the experimentally determined spectral parameters of the $\tilde{A}^2\text{E}_g''$ state.

The “comb” in Fig. 6.7C mark the progression in $j = \frac{1}{2}$ levels. Only the first five members are shown. Table 6.7 summarizes the calculated and experimentally observed Jahn-Teller transitions. Notice the good agreement between the theoretically

$ 1/2, n_j\rangle$		
n_j	Calc.	Exp.
1	0	0
2	1141	1141
3	1518	1524
4	1929	1921
5	2529	2539

Table 6.7: Calculated and experimentally observed Jahn-Teller transitions to the $\tilde{A}^2E''_3$ state of C_7H_7 .^a

^a In the first column we give the spectroscopic designation of the vibronic terminating levels of the transitions to the $\tilde{A}^2E''_3$ state originating in $|\frac{1}{2}, 1\rangle$ of the $\tilde{X}^2E''_2$ state of C_7H_7 . We follow the $|j, n_j\rangle$ formalism. The calculated excitation frequencies were based on the best-fit Jahn-Teller parameters of the $\tilde{A}^2E''_3$ state, and are given in the second column, while their experimental counterparts are listed in the third column.

calculated frequencies and the experimentally recorded. The spectroscopic assignment of band C is given by the transition to the level $|\frac{1}{2}, 2\rangle$ of the \tilde{A} state. There are three additional assignments to weak experimental bands of the \tilde{A} state that we can make; the band at 28096 cm^{-1} may be attributed to the transition to $|\frac{1}{2}, 3\rangle$, the band at 28493 cm^{-1} to the transition to $|\frac{1}{2}, 4\rangle$ and the transition to the level $|\frac{1}{2}, 5\rangle$ may be assigned to the feature at 29111 cm^{-1} .

Fig. 6.7D presents the transitions to the $j = 1/2$ levels of the \tilde{A} state plus all other transitions that we previously assigned to the experiment, i.e., those terminating in

the levels 20^2 , 8^2 (10^1), 14^2 , 13^2 , 11^1 , as well as those to the combinations 2^120^2 (α), $18^1 \mid \frac{1}{2}, 2 >$ (β), 16^120^2 (γ), 2^220^2 (δ), $17^1 \mid \frac{1}{2}, 2 >$ (ε), 4^217^1 (ζ), and $16^1 \mid \frac{1}{2}, 2 >$ (η). The calculations were based on the theoretical spectral parameters of the $\tilde{A} \ ^2E_3''$ state. Their intensities were matched to those of the experimental spectrum. With further adjustment of their position to the experiment we are led to Fig. 6.7E which is the same as 6.7D but calculated based on the experimental spectral parameters of the $\tilde{A} \ ^2E_3''$ state.

6.5.2 Assignment of the $\tilde{X} \ ^2E_2''$ State

LEDF spectra were collected from each of the three labelled bands shown in the C_7H_7 excitation spectrum in Fig. 6.4. The $\tilde{A} \ ^2E_3''$ -state assignments are critical to the interpretation of the LEDF spectra. Our initial assignments for the emission frequencies particularly with respect to intensities were largely based on our *ab initio* spectral parameters for the ground state, as we believe they are very reliable. A summary of all emission frequencies lower than ca. 2500 cm^{-1} originating in bands A-C of the \tilde{A} state is given in Table 6.8. The emission frequencies listed in the second and fifth columns arise from the emission from bands A and C, respectively. The emission frequencies in the third column were produced by subtracting the ones observed in the emission from band B by 415 cm^{-1} , in accordance with $\Delta\omega=0$. The latter are listed in the fourth column of the Table ($\Delta\omega=-2$). The average value of the observed emission frequencies from bands A-C of the \tilde{A} state is given in the sixth column. All emission frequencies reported in Table 6.8 are given in cm^{-1} . In the first column under assignment we give the spectroscopic designation of the terminating

energy levels of the transitions originating in bands A-C of the \tilde{A} state. The symmetry of the energy levels are given in the seventh column. Note that for the Jahn-Teller energy levels and their combinations, the symmetry space spanned by the harmonic-oscillator wave functions is given instead. The Jahn-Teller energy levels reported in this table span only a vibronic subspace of it with e_2'' symmetry. As the emission from band B is similar to the emission from band A, we analyze the latter spectrum and describe any additional features observed in the emission from band B.

6.5.3 Emission from Bands A and B of the \tilde{A} State of C₇H₇

The experimental LEDF spectrum from band A of the \tilde{A}^2E_3'' state is shown in Fig. 6.8A. Transitions involving the Jahn-Teller active levels $|1/2, n_j\rangle$ are shown in Figs. 6.8B-6.8G. The emission intensities are calculated by SPEC-SOCJT assuming that all oscillator strength results from the Jahn-Teller mixing for the e_3' modes. We first make assignments to transitions to the e_3' Jahn-Teller spectrum and then consider the transitions to a number of other vibrational levels as well as their combinations with the e_3' Jahn-Teller levels.

The assignment of the transitions to the e_3' Jahn-Teller vibronic energy levels started with a simulation of the spectrum using the *ab initio* calculated parameters of the \tilde{X}^2E_2'' state of C₇H₇, listed in the second and third columns of Table 6.4. (Fig. 6.8B.) Note that the modes ω_{16} , ω_{17} and ω_{18} were only introduced in the Jahn-Teller simulation of the \tilde{X} state. The vibronic structure of the emission spectra from bands A-C of the \tilde{A} state was considered simultaneously during the process of assignment. The most intense feature to the red of the origin of the simulation

Assignment ($ j, n_j\rangle$)	Emitting State ^a					
	Band A		Band B		Band C	
	$\Delta\omega=0$	$\Delta\omega=-2$			Average	Symmetry
$ 1/2, 1\rangle$	0	0 ^b	0	0	0	a'_1
2_1	838	842 ^c	u	840	840	a'_1
$ 1/2, 2\rangle$	927 ^c	926	...	924	926	e'_3
12_2	974	976	975	$a'_1 \oplus e'_3$
13_1^d	u	1050 ^c	1050	e''_2
7_1	1059	1061	1060	e'_1
19_2	1128	1128	$a'_1 \oplus e'_1$
4_2	1261	1263	1267	1267	1264	a'_1
$ 1/2, 3\rangle$	1374	u	u	1379	1376	$a'_1 \oplus e'_1$
6_1	1482	1482	u	...	1482	e'_1
8_2^e	1577	...	1578	...	1577	$a'_1 \oplus e'_2$
$ 1/2, 4\rangle$	1617	u	u	...	1617	$e'_2 \oplus e'_3$
2_2	1678	u	1680	1682	1680	a'_1
2_1+12_2	1807	u	1806	u	1806	$a'_1 \oplus e'_3$
$ 1/2, 5\rangle$	1893	u	u	1895	1894	$a'_1 \oplus e'_1 \oplus e'_2$
2_1+7_1	u	1900	1900	u	1900	e'_1
$ 1/2, 6\rangle$	2013	2013 ^c	...	2014	2013	$e'_1 \oplus e'_2 \oplus e'_3$
13_2	u	u	2081	2081 ^c	2081	$a'_1 \oplus e'_3$

Table 6.8: Experimentally observed spectral transitions to the $\tilde{X}^2\text{E}_2''$ state originating in bands A-C of the $\tilde{A}^2\text{E}_3''$ state of C_7H_7 .

^a u denotes unresolved transitions. The estimated experimental error is $\approx 10 \text{ cm}^{-1}$. ^b The direct product of $a'_1 \oplus e'_1$ with the symmetries listed in the seventh column should be considered for the symmetry characterization of the energy levels given in the third column. ^c Possible shoulder. ^d Tentative assignment. ^e Dual assignment; 10_1 . The symmetry of this level is e'_2 .

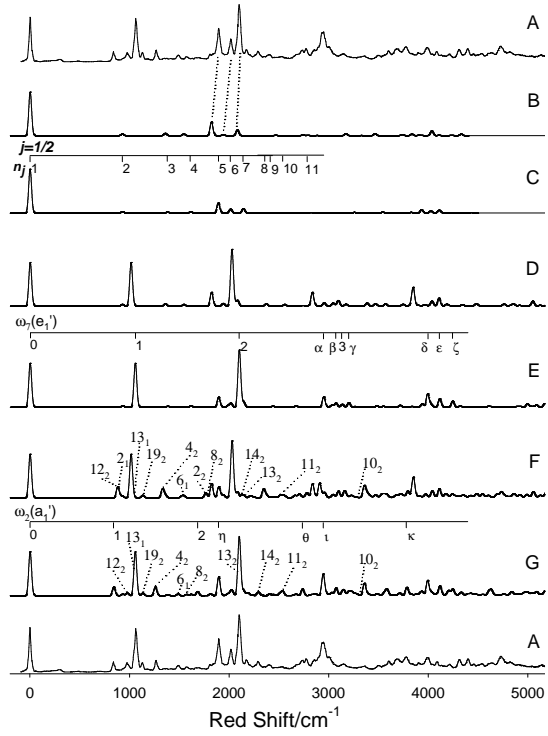


Figure 6.8: Emission spectrum of C_7H_7 , laser excited to the vibrationless level of the $\tilde{A}^2\text{E}_3''$ state, band A.

(A) Experimental trace (top and bottom traces); (B) Positions of the transitions to the e'_3 Jahn-Teller active levels with $j = 1/2$ symmetry, computed using the *ab initio* calculated Jahn-Teller parameters of the $\tilde{X}^2\text{E}_2''$ state; (C) Same as (B) but using the best-fit Jahn-Teller parameters of the $\tilde{X}^2\text{E}_2''$ state; (D) Same as (B) plus the positions of the transitions to the fundamental of ω_7 and its first and second overtones (labelled in E as 1-3), as well as their combinations (labelled in E as $\alpha, \beta, \gamma, \delta, \varepsilon, \zeta$) with the Jahn-Teller active levels. The intensity of the transitions to the fundamental, first and second overtones of ω_7 was adjusted to experiment; (E) Same as (D) but using the experimentally determined parameters of the $\tilde{X}^2\text{E}_2''$ state; (F) Same as (D) plus the positions of the transitions to levels built upon $\omega_2, \omega_4, \omega_6, \omega_8, \omega_{10}, \omega_{11}, \omega_{12}, \omega_{13}, \omega_{14}$ and ω_{19} (labelled in F and G), their combinations with the Jahn-Teller active levels, as well as their combinations among themselves and with the ω_7 energy levels. (The combinations built upon ω_7 and ω_2 are labelled in G as $\eta, \theta, \iota, \kappa$.) The intensity of the transitions to the fundamental and first overtone of ω_2 , the fundamental of ω_6 and ω_{13} , as well as the first overtones of $\omega_4, \omega_8, \omega_{10}, \omega_{11}, \omega_{12}, \omega_{13}, \omega_{14}$ and ω_{19} was adjusted to the experimental observation; (G) Simulated emission spectrum obtained by using the experimentally determined parameters of the $\tilde{X}^2\text{E}_2''$ state in (F).

in Fig. 6.8B must reasonably correlate with the second most intense feature of the experimental spectrum at 1893 cm^{-1} . The assignment to this experimental band of this feature is consistent with the experimental observation in the emission from band C of the \tilde{A} state. Note that the predicted intensity of this feature matches more closely the intensity of its experimental counterpart in the emission from band C. (See later on in the analysis for an explanation to why this happens.) The only other possible candidates for assignment are the electronically allowed transitions to the levels 2_2 and 8_2 of the \tilde{X} state, which we do not favor as their theoretically predicted frequencies, 1762 and 1782 cm^{-1} , respectively, and neglecting anharmonicity, do not match with experiment. The transitions to the levels 2_2 and 8_2 of the \tilde{A} state were previously assigned to experimental features of the \tilde{A} state based on a good match with the theoretical prediction. Thus this feature is assigned to the experimental band at 1893 cm^{-1} . The next feature to the red of the Jahn-Teller simulation must correspond to the next feature to the red of the experimental trace at 2013 cm^{-1} . Such an assignment is consistent with the experimental observation in the emissions from bands B and C. The alternative assignments to the fully electronically allowed transitions to the levels 7_2 (theoretically predicted frequency neglecting anharmonicity at 2028 cm^{-1}), 13_2 (2158 cm^{-1}) and 14_2 (2122 cm^{-1}) of the \tilde{X} state are not favored. We have identified the first four members of the \tilde{X} -state vibronic progression built upon the vibrational mode ω_7 from the analysis of the emission spectra from bands A-C. (See later on for further details.) The latter transitions are strong candidates for assignment to other experimental features. (See later on in the analysis.) Hence

the feature at 2013 cm^{-1} is assigned as a transition to the e'_3 Jahn-Teller spectrum of the \tilde{X} state. The predicted small intensity of the next Jahn-Teller feature of the simulation makes it impossible for assignment to the intense experimental feature centered at 2100 cm^{-1} . The alternative assignment to the weak band at 2180 cm^{-1} is rejected as there is a stronger candidate for it which also explains why it is observed in the emission from bands A and B and not in the emission from band C. (See later on in the analysis.) We conclude that this feature is experimentally unresolved due to the band peaking at 2100 cm^{-1} . Based on the above assignments to the e'_3 Jahn-Teller vibronic energy levels and a number of others which came about by a process of elimination and are described in the analysis that follows (their experimentally observed emission frequencies are summarized in the third column of Table 6.9), the Jahn-Teller parameters were adjusted accordingly. (See Fig. 6.8C.) We only slightly refined the theoretically calculated Jahn-Teller coupling parameters of the \tilde{X} state, as we place great confidence on them. The fifth and sixth columns of Table 6.4 summarize the experimental Jahn-Teller parameters of the $\tilde{X}\ ^2\text{E}_2''$ state, while the second column of Table 6.9 lists the calculated energies of the e'_3 Jahn-Teller levels based on the best-fit Jahn-Teller parameters of the $\tilde{X}\ ^2\text{E}_2''$ state.

The “combs” in Fig. 6.8C mark the progression in the $j = 1/2$ e'_3 Jahn-Teller levels. Only the first eleven members are shown. Aside from the trivial assignment of the origin, there are nine assignments to experimental transitions; the features at $926, 1376, 1617, 1894$ and 2013 cm^{-1} may be attributed to transitions to $|\frac{1}{2}, n_j\rangle$ levels of the $\tilde{X}\ ^2\text{E}_2''$ state with $n_j=2-6$, respectively. The transition to the level $|\frac{1}{2}, 7\rangle$ is

$ 1/2, n_j\rangle$	n _j	Calc.	Exp.
	1	0	0
	2	926	926
	3	1379	1376
	4	1612	1617
	5	1892	1894
	6	2013	2013
	7	2142	2146
	8	2340	2340
	9	2425	...
	10	2534	2530
	11	2790	2786

Table 6.9: Calculated and experimentally observed Jahn-Teller transitions to the \tilde{X}^2E_2'' state of C₇H₇.^a

^a In the first column we give the spectroscopic designation of the vibronic terminating levels of the transitions to the \tilde{X}^2E_2'' state originating in the bands A-C of the \tilde{A}^2E_3'' state of C₇H₇. We follow the $|j, n_j\rangle$ formalism. The calculated emission frequencies were based on the best-fit Jahn-Teller parameters of the \tilde{X}^2E_2'' state, and are given in the second column, while their experimental counterparts are listed in the third column. All levels with $n_j \leq 11$ except the one with $n_j=9$ were used in the fit which included the six parameters D₁₆, ω_{16} , D₁₇, ω_{17} , D₁₈, and ω_{18} . The fit had a root-mean-square (rms) error of ca. 4 cm⁻¹.

experimentally unresolved in the emission from bands A and C, but resolved in the emission from band B at 2146 cm^{-1} . The experimental features at 2340 and 2787 cm^{-1} may be attributed to transitions to the levels $|\frac{1}{2}, 8\rangle$ and $|\frac{1}{2}, 11\rangle$ of the \tilde{X} state, though they are both predicted with negligible intensity. No other alternative assignments could be made to explain these features. The transition to the level $|\frac{1}{2}, 10\rangle$ may explain the band at 2530 cm^{-1} which however may also be attributed to a transition to the level 11_2 of the $\tilde{X}\ ^2\text{E}_2''$ state. No plausible experimental assignment could be made to the transition to the level $|\frac{1}{2}, 9\rangle$ of the \tilde{X} state, which was also predicted to have negligible intensity.

Fig. 6.8D presents the transitions to the $j = 1/2$ levels plus those terminating in the $\omega_7(e'_1)$ levels and their combinations with the e'_3 Jahn-Teller levels. The calculations were based on the *ab initio* spectral parameters of the $\tilde{X}\ ^2\text{E}_2''$ state. The only logical experimental candidate for assignment to a transition to the fundamental of $\omega_7(e'_1)$ (theoretically predicted harmonic frequency at 1014 cm^{-1}) is the first most intense feature to the red from the origin at 1059 cm^{-1} . The alternative assignments to transitions to the \tilde{X} -state levels 13_1 (theoretically predicted harmonic frequency at 1079 cm^{-1}), 14_1 (1061 cm^{-1}), and 19_2 (theoretically predicted frequency neglecting anharmonicity at 1128 cm^{-1}) are possible but less likely. The vibrational mode ω_7 exhibits the strongest linear Jahn-Teller activity in the $\tilde{A}\ ^2\text{E}_3''$ state, while ω_{13} , ω_{14} (in the \tilde{X} state), and ω_{19} (in the \tilde{A} state) are quadratically Jahn-Teller active vibrational modes. By making this assignment, further adjustment of its position to the experiment, and assuming for ω_7 an anharmonicity constant of 6 cm^{-1} , a good

match in position is achieved between the transitions to the next three members of its progression in the \tilde{X} state and the experimentally observed features, i.e, the ones at 2100 cm^{-1} (assigned to 7_2^0 , and observed in the emission from bands A-C), at 3122 cm^{-1} (7_3^0 , observed in the emissions from bands A-C, resolved in the emissions from bands B and C), and at 4125 cm^{-1} (7_4^0 , observed in the emission from band C). The intensities of these bands are adjusted to experiment in Fig. 6.8D. Note their intensity variations across the emission spectra from bands A-C. Our simulations reproduce the variations in intensity. We first spectroscopically identified bands A and C of the $\tilde{A}\ ^2\text{E}_3''$ state, then we used the best-fit parameters of the \tilde{A} state, and in the \tilde{X} -state simulation of their emissions found the following. The transition to the first member of the ω_7 progression of the $\tilde{X}\ ^2\text{E}_2''$ state was predicted, in the emission from band A, with a strong relative intensity, while in the emission from band C, with depleted intensity. The exact opposite was observed for the transition to the third member of the ω_7 progression in the simulations of the emission spectra from bands A and C. While the average of the calculated intensities of the transition to the second member of the progression in the emissions from A and C approximates the corresponding experimental one, the relative intensity is predicted opposite to experiment. (Likely due to the neglect of the off-diagonal Franck-Condon factors in the theoretical model.) The transition to the fourth member of the progression is predicted with depleted relative intensity in the simulation of the emission from band A, while the corresponding one in the emission from band C is predicted with small

but not negligible intensity. Consequently the experimentally observed relative intensity pattern of the transitions to the members of the ω_7 progression of the $\tilde{X}^2E''_2$ state is mainly due to the e'_1 Jahn-Teller mixing in the $\tilde{A}^2E''_3$ state.

Fig. 6.8E shows these results. It is constructed from $j = 1/2$ levels, $\omega_7(e'_1)$ levels and their combinations with the e'_3 Jahn-Teller levels and is calculated based on the experimental spectral parameters of the $\tilde{X}^2E''_2$ state. We keep the intensities of the transitions to the $\omega_7(e'_1)$ levels fixed to experiment.

The $\tilde{A} \rightarrow \tilde{X}$ transitions to the energy levels of the first three quanta of excitation of $\omega_7(e'_1)$ are marked with 1-3 in Fig. 6.8E. The transitions to the combinations between the first two members of the $\omega_7(e'_1)$ progression and the Jahn-Teller levels $| \frac{1}{2}, n_j \rangle$ with $n_j=5-7$ are depicted in the figure with the Greek letters ($\alpha-\zeta$); the transition to the \tilde{X} -state level $7_1+|1/2, 5\rangle$ (α) is resolvable in the emission through band A at 2953 cm^{-1} (symmetry space: $a'_1 \oplus a'_2 \oplus 2e'_1 \oplus e'_2 \oplus e'_3$), to $7_1+|1/2, 6\rangle$ (β) is resolvable in the emission through band B ($\Delta\omega=-2$) at 3070 cm^{-1} ($a'_1 \oplus a'_2 \oplus e'_1 \oplus 2e'_2 \oplus 2e'_3$), to $7_1+|1/2, 7\rangle$ (γ) is unresolved in the emission through bands A and B ($\Delta\omega=0,-2$) ($a'_1 \oplus a'_2 \oplus 2e'_1 \oplus 2e'_2 \oplus 2e'_3$), to $7_2+|1/2, 5\rangle$ (δ) is resolvable in the emission from bands A and B ($\Delta\omega=0,-2$) at the average frequency of 3994 cm^{-1} ($2a'_1 \oplus a'_2 \oplus 2e'_1 \oplus 2e'_2 \oplus 2e'_3$), to the level $7_2+|1/2, 6\rangle$ (ε) is resolvable in the emission from bands A and B ($\Delta\omega=0,-2$) at the average frequency of 4097 cm^{-1} ($a'_1 \oplus a'_2 \oplus 3e'_1 \oplus 2e'_2 \oplus 3e'_3$), and finally the transition to the level $7_2+|1/2, 7\rangle$ (ζ) of the \tilde{X} state is resolvable in the emission from band A at 4233 cm^{-1} ($2a'_1 \oplus a'_2 \oplus 3e'_1 \oplus 3e'_2 \oplus 3e'_3$).

However the structure in Fig. 6.8E only accounts for part of the experimental spectrum. The band at 838 cm^{-1} in the emission from band A is assigned as an $\tilde{A} \rightarrow \tilde{X}$ transition to the fundamental of the ring-breathing mode ω_2 , based on the theoretical prediction of 881 cm^{-1} for its harmonic frequency. This feature is observed at the average frequency of 840 cm^{-1} in the emissions from bands A-C. The alternative assignments to transitions to the levels 12_2 (theoretically predicted frequency at 876 cm^{-1}) and 8_1 (891 cm^{-1}) of the $\tilde{X}^2\text{E}_2''$ state are less favorable. The latter one is only vibronically allowed via the z component of the electric dipole moment in D_{7h} ($\mu_z = A_2''$). However the former transition is fully electronically allowed. The \tilde{A} -state fundamental frequency of ω_2 has previously been determined at 858 cm^{-1} . The value of 838 cm^{-1} for the frequency of its fundamental in the $\tilde{X}^2\text{E}_2''$ state is reasonable. If we assume that the potential of the vibrational mode ω_2 is harmonic in the \tilde{X} state, its first overtone would be placed at 1680 cm^{-1} . Indeed we observe a transition at this frequency in the emissions from bands A-C. As a final piece of evidence, we observe the transitions to the combinations between the ω_2 vibrational levels and the ω_7 vibrational levels of the \tilde{X} state in the emission from bands A-C. As there is a progression in the ring-breathing mode in the $\tilde{X}^2\text{E}_2''$ state, we expect that the D_{7h} ring will have a different size between the $\tilde{A}^2\text{E}_3''$ and $\tilde{X}^2\text{E}_2''$ states of $C_7\text{H}_7$.

The feature at 974 cm^{-1} observed in the emission trace from band A (also observed in the emission from band B) is assigned as a transition to the level 12_2 of the $\tilde{X}^2\text{E}_2''$ state. This transition is the only candidate for assignment that is electronically allowed, and may be gaining intensity in the \tilde{X} state as the $\omega_{12}(e'_2)$ vibrational mode

is subject to quadratic Jahn-Teller interactions in the $\tilde{X} \ ^2\text{E}_2''$ state. Assignment to this feature produces an experimental frequency for the \tilde{X} -state fundamental of ω_{12} of 487 cm^{-1} . Note that the transition to the combination between its first overtone with the fundamental of ω_2 is also observed in the emission spectra from bands A-C at 1806 cm^{-1} .

The feature at 1128 cm^{-1} is observed only in the emission from band A. It is assigned as a transition to the level 19_2 of the \tilde{X} state based on the good agreement with the theoretically predicted frequency at 1128 cm^{-1} . The experimental frequency of the \tilde{X} -state fundamental of ω_{19} is 564 cm^{-1} . This vibrational mode exhibits quadratic Jahn-Teller activity in the $\tilde{A} \ ^2\text{E}_3''$ state; its potential in the \tilde{A} state would nominally change due to this, and hence the electronically allowed transition to its overtone of the $\tilde{X} \ ^2\text{E}_2''$ state would exhibit intensity due to off-diagonal Franck-Condon factors. The transition to the combination between its first overtone and the fundamental of ω_7 is also observed in the emission spectra from bands A and B at the average frequency of 2184 cm^{-1} .

The feature at 1261 cm^{-1} in the emission from band A is attributed to the $\tilde{A} \rightarrow \tilde{X}$ transition 4_2^0 (theoretical frequency at 1328 cm^{-1}). The only other candidate for assignment is the transition to the fundamental of $\omega_{11}(e'_2)$ in the \tilde{X} state which is only vibronically allowed (theoretical harmonic frequency at 1255 cm^{-1}). The experimental frequency of its fundamental in the $\tilde{X} \ ^2\text{E}_2''$ state, neglecting anharmonicity, is 630 cm^{-1} , while the corresponding one in the $\tilde{A} \ ^2\text{E}_3''$ state is 677 cm^{-1} . The \tilde{A}

$\rightarrow \tilde{X}$ transition to the combination levels $4_2 + 12_2$ (in the emission spectra from bands A-C) and $4_2 + 7_1$ (in the emission spectra from bands A and B) is observed at 2242 cm^{-1} , and is unresolved, respectively.

The band at 1482 cm^{-1} in the emission from Band A is assigned as a transition to the fundamental of $\omega_6(e'_1)$ in the $\tilde{X}\ ^2\text{E}_2''$ state (theoretically predicted harmonic frequency at 1519 cm^{-1}). This feature is also observed in the emission from band B. No other candidate for assignment is possible based on the theoretical prediction. This vibrational mode is linearly Jahn-Teller active in the $\tilde{A}\ ^2\text{E}''$ state. (See Table 6.4.) Its experimental fundamental frequency in the $\tilde{X}\ ^2\text{E}_2''$ state is 1482 cm^{-1} and the transition to its first overtone is expected at 2964 cm^{-1} , neglecting anharmonicity, which is placed in a congested energy region and is unresolved. The $\tilde{A} \rightarrow \tilde{X}$ transition to $6_1 + |\frac{1}{2}, 2\rangle$ is observed in the emission from bands A and B at the average frequency of 2408 cm^{-1} .

The feature at 1577 cm^{-1} is observed in the emission from bands A and B and is attributed to the transition to the level 8_2 of the $\tilde{X}\ ^2\text{E}_2''$ state (theoretically predicted frequency, neglecting anharmonicity, at 1782 cm^{-1}). The only other possibility is assignment of this feature to a transition to the level 10_1 of the \tilde{X} state (theoretically predicted harmonic frequency at 1637 cm^{-1}). While the former transition is fully electronically allowed, the latter one is only vibronically allowed. However the vibrational mode $\omega_{10}(e'_2)$ is quadratically Jahn-Teller active in the $\tilde{X}\ ^2\text{E}_2''$ state. This band may have dual assignments.

The peak at the average frequency of 2081 cm^{-1} (resolved in the emissions from bands B and C) is assigned to the transition 13_2^0 (theoretically predicted frequency at 2158 cm^{-1}). The only other alternative assignment is 14_2^0 (theoretically predicted frequency at 2122 cm^{-1}) which is rejected. The information that we have from the $\tilde{A}\text{ }^2\text{E}''$ -state analysis is that the transitions 14_0^2 and 13_0^2 are placed at 2064 and 2208 cm^{-1} , respectively. Assuming no anharmonicity in their potentials, we expect their fundamental frequencies in the \tilde{A} state to be 1032 and 1104 cm^{-1} , respectively. Assignment to 13_2^0 of the feature at 2081 cm^{-1} suggests that its fundamental frequency in the \tilde{X} state is 1040 cm^{-1} , neglecting anharmonicity, which further indicates non-negligible off-diagonal Franck-Condon factors. The shoulder at 1050 cm^{-1} of the peak centered at 1061 cm^{-1} in the emission from band B was tentatively assigned to the $\tilde{A} \rightarrow \tilde{X}$ vibronically-only-allowed transition 13_1^0 . Assuming the correctness of this assignment, we conclude that $\omega_{13}(e_2'')$ must be subject to large quadratic Jahn-Teller interactions in the $\tilde{X}\text{ }^2\text{E}_2''$ state. The band at 2288 cm^{-1} (observed in the emission from bands A-C) is attributed to the transition 14_2^0 . The experimental frequency for the fundamental level of $\omega_{14}(e_2'')$ in the $\tilde{X}\text{ }^2\text{E}_2''$ state is 1144 cm^{-1} .

Finally, the feature at 2530 cm^{-1} (observed in the emission from bands A-C) is attributed to the transition to the level 11_2 of the $\tilde{X}\text{ }^2\text{E}_2''$ state (theoretically predicted frequency at 2510 cm^{-1}). No other candidate is possible. Its experimental fundamental frequency in the \tilde{X} state, assuming no anharmonicity, is 1265 cm^{-1} , while the corresponding one in the \tilde{A} state is 1191 cm^{-1} . Note that the vibrational mode $\omega_{11}(e_2')$ is quadratically Jahn-Teller active in the $\tilde{X}\text{ }^2\text{E}_2''$ state.

The information contained in Fig. 6.8D plus the positions of the discussed transitions to levels built upon ω_2 , ω_4 , ω_6 , ω_8 , ω_{10} , ω_{11} , ω_{12} , ω_{13} , ω_{14} and ω_{19} (labelled in F and G), their combinations with the Jahn-Teller active levels, as well as their combinations among themselves and with the ω_7 energy levels are included in Fig. 6.8F. This simulation is calculated based on the theoretical spectral parameters of the $\tilde{X}^2E''_2$ state. The intensity of the transitions to the fundamental and first overtone of ω_2 , the fundamental of ω_6 and ω_{13} , as well as the first overtones of ω_4 , ω_8 , ω_{10} , ω_{11} , ω_{12} , ω_{13} , ω_{14} and ω_{19} was adjusted to the experiment.

Our final simulated emission spectrum (Fig. 6.8G) contains the same information as Fig. 6.8F but is constructed based on the experimental spectral parameters of the $\tilde{X}^2E''_2$ state. The combinations built upon ω_7 and ω_2 are labelled in 6.8G as $\eta, \theta, \iota, \kappa$; the transition to the \tilde{X} -state level 2_1+7_1 (η) is resolvable in the emission through band B ($\Delta\omega=0,-2$) at the average frequency of 1900 cm^{-1} (symmetry: e'_1), to 2_2+7_1 (θ) is resolvable in the emission through bands A, B ($\Delta\omega=0$) and C at the average frequency of 2739 cm^{-1} (e'_1), to the level 2_1+7_2 (ι) is resolvable in the emission through bands A, B ($\Delta\omega=0$) and C at the average frequency of 2940 cm^{-1} ($a'_1 \oplus e'_2$), and finally the transition to the level 2_2+7_2 (κ) of the \tilde{X} state is resolvable in the emission through bands A, B ($\Delta\omega=0$) and C at the average frequency of 3778 cm^{-1} ($a'_1 \oplus e'_2$). Notice the particular contribution that the $\omega_7(e'_1)$ vibrational structure has to the overall simulation presented in Fig. 6.8G. There seems to be a one-to-one correspondence between the experimentally observed features and the simulated ones in Fig. 6.8G.

6.5.4 Emission from Band C of the \tilde{A} State of C_7H_7

We briefly review the emission from band C which is the e'_1 Jahn-Teller level $| \frac{1}{2}, 2 \rangle$ of the $\tilde{A}^2E''_3$ state. The majority of the observed spectral features are common with the emission through the origin of the excitation spectrum, namely, band A.

The experimental spectrum is given in Fig. 6.9A. Our Jahn-Teller simulation is presented in Fig. 6.9B. Jahn-Teller levels of $j = 1/2$ symmetry are computed based on the theoretically calculated Jahn-Teller parameters of the $\tilde{X}^2E''_2$ state. (See Table 6.4.) Fig. 6.9C includes the same information as Fig. 6.9B but is constructed using the best-fit Jahn-Teller parameters of the $\tilde{X}^2E''_2$ state. The first eleven members of the $j = 1/2$ progression are shown.

Fig. 6.9D included the same information as Fig. 6.9B plus the positions of the transitions to the fundamental of ω_7 and its first, second and third overtones (labelled in E as 1-4), as well as their combinations (labelled in E as α) with the Jahn-Teller active levels. The transition to the \tilde{X} -state level $7_3 + |1/2, 5\rangle$ (α) is resolvable in the emission through band C at 5016 cm^{-1} ($a'_1 \oplus a'_2 \oplus 3e'_1 \oplus 3e'_2 \oplus 3e'_3$). The intensities of the transitions to the fundamental, first, second and third overtones of ω_7 was adjusted to experiment. Fig. 6.9E contains the same transitions as Fig. 6.9D, but is based on the experimentally determined parameters of the $\tilde{X}^2E''_2$ state.

Fig. 6.9F contains the same information as Fig. 6.9D plus the positions of the transitions to levels built upon ω_2 , ω_4 , ω_{10} , ω_{11} , ω_{12} , ω_{13} and ω_{14} (labelled in F and

G), their combinations with the Jahn-Teller active levels, as well as their combinations among themselves and with the ω_7 energy levels. The intensities of the transitions to the fundamental and first overtone of ω_2 , as well as the first overtones of ω_4 , ω_{10} , ω_{11} , ω_{12} , ω_{13} and ω_{14} were adjusted to the experiment.

Finally, Fig. 6.9G shows the simulated emission spectrum obtained by using the experimentally determined parameters of the $\tilde{X}^2\text{E}_2''$ state in Fig. 6.9F. The combinations built upon ω_7 and ω_2 are labelled in Fig. 6.9G as $\beta, \gamma, \delta, \varepsilon, \zeta$; the transition to the \tilde{X} -state level 2_1+7_1 is depicted by β in Fig. 6.9G, the one to 2_2+7_1 by γ , the transition to 2_1+7_2 by δ , the transition to the level 2_2+7_2 by ε , and finally the one to 2_1+7_3 by ζ .

6.6 Discussion

Our primary goal was to understand the vibronic structures of the $\tilde{X}^2\text{E}_2''$ and $\tilde{A}^2\text{E}_3''$ states of C₇H₇. We used our *ab initio* calculated Jahn-Teller parameters as starting points for the Jahn-Teller simulations. These parameters were refined by adjusting them until the Jahn-Teller vibronic state energies and intensities matched the experimental line positions and intensities based on reasonable assignments in the \tilde{A} and \tilde{X} states. In the following, the *ab initio* calculated Jahn-Teller molecular parameters of the $\tilde{A}^2\text{E}_3''$ and $\tilde{X}^2\text{E}_2''$ states of C₇H₇ are compared with the experimental ones, and their ramifications on the Jahn-Teller distorted potential energy surface in each case are discussed.

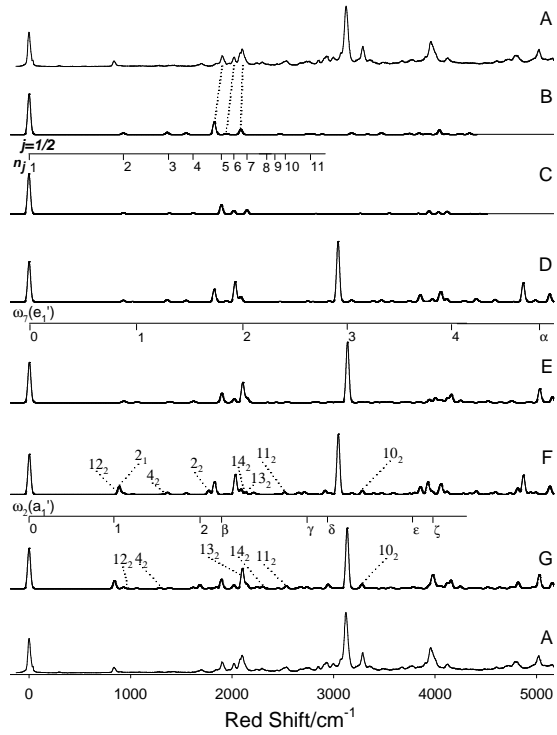


Figure 6.9: Emission spectrum of C_7H_7 , laser excited to the $|1/2, 2 >$ Jahn-Teller level of the $\tilde{A}^2\text{E}_2''$ state, band C.

(A) Experimental trace (top and bottom traces); (B) Positions of the transitions to the e'_3 Jahn-Teller active levels with $j = 1/2$ symmetry, computed using the *ab initio* calculated Jahn-Teller parameters of the $\tilde{X}^2\text{E}_2''$ state; (C) Same as (B) but using the best-fit Jahn-Teller parameters of the $\tilde{X}^2\text{E}_2''$ state; (D) Same as (B) plus the positions of the transitions to the fundamental of ω_7 and its first, second and third overtones (labelled in E as 1-4), as well as their combinations (labelled in E as α) with the Jahn-Teller active levels. The intensities of the transitions to the fundamental, first, second and third overtones of ω_7 were adjusted to experiment; (E) Same as (D) but using the experimentally determined parameters of the $\tilde{X}^2\text{E}_2''$ state; (F) Same as (D) plus the positions of the transitions to levels built upon ω_2 , ω_4 , ω_{10} , ω_{11} , ω_{12} , ω_{13} and ω_{14} (labelled in F and G), their combinations with the Jahn-Teller active levels, as well as their combinations among themselves and with the ω_7 energy levels. (The combinations built upon ω_7 and ω_2 are labelled in G as $\beta, \gamma, \delta, \varepsilon, \zeta$.) The intensities of the transitions to the fundamental and first overtone of ω_2 , as well as the first overtones of ω_4 , ω_{10} , ω_{11} , ω_{12} , ω_{13} and ω_{14} were adjusted to the experimental observation; (G) Simulated emission spectrum obtained by using the experimentally determined parameters of the $\tilde{X}^2\text{E}_2''$ state in (F).

Our *ab initio* calculated and experimental spectral parameters for the $\tilde{X} \ ^2\text{E}_2''$ state are in good agreement. The experimentally determined frequencies $\omega_{e,16}-\omega_{e,18}$ for the $\tilde{X} \ ^2\text{E}_2''$ state were found to deviate by no more than approximately 5% from their corresponding calculated values. Our calculated linear Jahn-Teller coupling constants D_i are in excellent agreement with our experimental values as is clearly shown in Table 6.4.

Our *ab initio* calculated and experimental spectral parameters for the $\tilde{A} \ ^2\text{E}_3''$ state are also in good agreement. There is a satisfactory frequency match between the experimental and *ab initio* calculated frequencies $\omega_{e,6}$ and $\omega_{e,7}$. Our *ab initio* calculated linear Jahn-Teller coupling parameters D_i are in close agreements with their experimental counterparts.

The Jahn-Teller molecular parameters contain valuable information about the topographic characteristics of the Jahn-Teller distorted potential energy surfaces. In Table 6.4 the *ab initio* calculated and experimentally determined Jahn-Teller stabilization energies for the i^{th} vibrational mode, ε_i , as well as the total stabilization energies, ε_T of the \tilde{X} - and \tilde{A} -state PESs of C_7H_7 are given. These were computed based on Eq. 6.31. The calculated stabilization energies and experimental ones for the \tilde{X} and \tilde{A} states are in fair agreement. For the $\tilde{X} \ ^2\text{E}_2''$ state, the global minima lie 1043 cm^{-1} below the D_{7h} conical intersection, while for the $\tilde{A} \ ^2\text{E}_3''$ state the corresponding value is 817 cm^{-1} .

6.7 Conclusions

The jet-cooled laser excited, dispersed fluorescence emission spectra and the laser induced fluorescence excitation spectrum of the tropyl radical have been successfully analyzed utilizing the *ab initio* molecular parameters. There is good agreement between the experimental and theoretical Jahn-Teller parameters for the $\tilde{A} \ ^2E_3''$ and $\tilde{X} \ ^2E_2''$ states. The vibronic structures of the $\tilde{A} \ ^2E_3''$ and $\tilde{X} \ ^2E_2''$ states reveal the Jahn-Teller distortion of their potential energy surfaces. The contribution from the e'_3 vibrational modes is important in the excitation spectrum, and that from the e'_1 vibrational modes (particulary the one that is the most Jahn-Teller active in the \tilde{A} state) in the emission spectra.

CHAPTER 7

Conclusions

The investigation of the electronic-structure and vibrational properties of molecules is oftentimes a challenging task which however can be accomplished once suitable theoretical and experimental methodologies are incorporated. This dissertation describes a number of accomplishments in this area.

The calculation of accurate binding energies requests the use of an accurate correlation treatment and adequate basis sets. In calculating the ground-state interaction energy of the iodide ion and the (isoelectronic) Xe atom with decaborane several theoretical methods were used: MP2, CCSD(T), CCSD, spin-orbit CISD, and DFT using the B3LYP, B3PW91, PW91PW91, and PBE0 methods. If one takes the high-level wave-function-based estimates as a reliable reference, we can conclude that selected DFT methods can be efficient alternatives when dealing with very large systems. The present study has found that the PW91PW91 and PBE0 functionals do describe dispersion interactions and are the better choices for studying weak-interaction systems. However, the counterpoise corrections are necessary to obtain reliable results. A detailed description of the electronic-structure characteristics of $B_{10}H_{14}I^-$ and $B_{10}H_{14}Xe$ is given for the first time. Relativistic effective core potentials were used for the I, Xe,

and B atoms. Basis sets for use with these potentials are discussed as is the question of basis set balance in molecules. We find $\text{B}_{10}\text{H}_{14}\text{I}^-$ to be bound by 19.8 kcal/mol and $\text{B}_{10}\text{H}_{14}\text{Xe}$ by 1.1 kcal/mol, indicating that the charge and polarizability of I^- play the major role in the interaction energy.

The alkoxy radicals have been the subject of extensive experimental and theoretical studies, as they are intermediates in the degradation of volatile organic compounds injected in our atmosphere. Their reactions affect the yield of ozone, air toxics, and organic aerosols in the atmosphere. Also the existence of multiple reaction pathways for alkoxy radicals complicates efforts for the understanding of the potential oxidation scheme of hydrocarbons. Hence elucidation of their chemistry is paramount in modeling the chemistry of the atmosphere. Information about the ground \tilde{X} and low-lying \tilde{A} state vibrational structure and dynamics of the alkoxy radicals has been relatively sparse.

In the work described in this dissertation a detailed analysis of the LEDF spectra of 1-propoxy, 1-butoxy, 2-propoxy, and 2-butoxy radicals is given for the first time. These were recorded under supersonic jet-cooling conditions by pumping different vibronic bands of the $\tilde{B}-\tilde{X}$ LIF excitation spectrum. The LEDF spectra were observed for both conformers of 1-propoxy, three conformers of the possible five of 1-butoxy, the one possible conformer of 2-propoxy, and two conformers of the possible three of 2-butoxy. A detailed analysis of the spectra yields the energy separations of the vibrationless levels of the ground \tilde{X} and low-lying \tilde{A} electronic state as well as their vibrational frequencies. In all cases, the vibrational structure of the LEDF spectra

is dominated by a CO stretch progression yielding the ν_{CO} stretching frequency for the \tilde{X} state and in most cases for the \tilde{A} state. In addition to the experimental work, quantum chemical calculations were carried out to aid the assignment of the vibrational levels of the \tilde{X} state and for some conformers the \tilde{A} state as well. Geometry optimizations of the different conformers of the isomers were performed and their energy differences in the ground states were determined. The results of the calculation of the energy separations of the close-lying \tilde{X} and \tilde{A} states of the different conformations are provided for comparison with the experimental observations.

These experimental results are quite valuable, since the energy of the excited \tilde{A} state is quite important with respect to its participation in thermal reaction chemistry. Moreover, the most advanced quantum chemistry calculations today can only give a qualitative idea at best as to its value. While the ability of calculations to predict vibrational frequencies is much better today, experiment clearly provides the “gold standard” for the frequencies. As we have shown the LEDF experiments measure a fairly large number of \tilde{X} (and \tilde{A}) state vibrational frequencies for the alkoxies. Since modes involving the CO stretch character are the strongest we have the most information for them.

In this document extensive work on the analysis of the electronic and vibrational properties of Jahn-Teller active molecules is detailed. Suitable theoretical models were constructed with the express purpose of characterizing the Jahn-Teller distorted PES. High-level *ab initio* calculations were utilized in order to obtain initial spectral

parameters for the analysis. As a second step the spectral parameters were refined by using the experimental data. In doing so, reliable information about the topographical characteristics of the Jahn-Teller distorted PES is obtained.

To analyze the experimentally observed $\tilde{A}^2E'' - \tilde{X}^2E'$ electronic spectrum of Ag_3 , *ab initio* calculations were performed for the \tilde{X}^2E' and \tilde{A}^2E'' states. These calculation utilized a newly constructed basis set for Ag, which can be used in studies of molecules containing Ag. The molecular parameters describing the Jahn-Teller effect were calculated for the \tilde{X} and \tilde{A} states and the magnitude of the spin-orbit effects for this relativistic system was also calculated for the \tilde{X}^2E' and \tilde{A}^2E'' states. Using all this information, the $\tilde{X} - \tilde{A}$ electronic spectrum is predicted for Ag_3 . Additionally, the geometries and symmetries of the global minima and saddle points as well as the barrier to pseudorotation around the moat of the PES are determined for both states.

The laser excited, jet-cooled $\tilde{A}^2E'' - \tilde{X}^2E'$ electronic spectrum of the silver trimer yields detailed information about its \tilde{A} - and \tilde{X} -state vibronic structure. Following extensive parameter fitting, the absorption and emission spectra are simulated and the bands are assigned. Analysis of the \tilde{A} and \tilde{X} vibronic structures are performed to reveal the Jahn-Teller distortion of their PESs. The Jahn-Teller analysis includes both linear and quadratic coupling terms, considered simultaneously with spin-orbit coupling. The spin-orbit splitting is shown to be largely quenched in both the \tilde{A} and \tilde{X} electronic states.

A similar methodological approach was followed for the tropyl radical. As this molecule is subject to a multi-mode Jahn-Teller effect, the spectroscopic model was properly developed to address this. To guide the analysis of the experimentally observed $\tilde{A}^2E_3'' - \tilde{X}^2E_2''$ electronic spectrum, theoretical calculations are performed for the \tilde{X}^2E_2'' and \tilde{A}^2E_3'' states of C₇H₇. Consequently, the spectroscopically obtainable parameters describing the Jahn-Teller effect are calculated for the \tilde{X} and \tilde{A} states, and based on them the $\tilde{X} - \tilde{A}$ electronic spectrum is predicted for C₇H₇.

LIF and LEDF spectra of the tropyl radical have been observed under supersonic jet-cooling conditions. The LEDF emission was collected by pumping different vibronic bands of the $\tilde{A}^2E_3'' \leftarrow \tilde{X}^2E_2''$ electronic spectrum. A straightforward assignment of the \tilde{A} vibronic structure is presented. Analysis of the LEDF spectra yields valuable information about the vibrational levels of the \tilde{X}^2E_2'' state. The \tilde{X} - and \tilde{A} -state vibronic structures reveal a comprehensive picture of the Jahn-Teller distortion of their PESs. A thorough analysis reveals Jahn-Teller activity in four e'_3 modes for \tilde{X}^2E_2'' and three e'_1 modes for \tilde{A}^2E_3'' and provides values for their deperturbed vibrational frequencies as well as linear Jahn-Teller constants. The molecular parameters characterizing the Jahn-Teller interaction in the \tilde{X} and \tilde{A} states of C₇H₇ are compared to theoretical results and are found to be in good agreement.

The studies on the silver trimer and the tropyl radical described in this dissertation have shown a number of things. While the understanding of conical intersections has always been a difficult goal to achieve, Jahn-Teller active molecules can serve as excellent tests of this. By using analytical expressions of the PESs it is possible to

reproduce the experimental spectra of Jahn-Teller active molecules. For the studies of Ag_3 and C_7H_7 , analytical PESs were developed for their ground and excited electronic states as these both are subject to Jahn-Teller distortion. Notwithstanding the difficulty of such analyses, it was shown by these studies that the Jahn-Teller-distorted PESs can still be accurately described once suitable parameterized spectroscopic models are developed. Finally, modern computational chemistry codes can be utilized to provide excellent initial estimates for Jahn-Teller parameters.

In conclusion, this dissertation gives a detailed account of the electronic and vibrational properties of a number of interesting molecules. In this document, suitable theoretical and experimental methodologies have been described for their analyses which can be used as alternatives for the investigation of similar molecules.

BIBLIOGRAPHY

- [1] T. Pino, F. Güthe, H. Ding, and J. P. Maier, *J. Phys. Chem. A* **106**, 10022 (2002), and references therein.
- [2] M. E. Jenkin and G. D. Hayman, *Atmos. Environ.* **33**, 1275 (1999).
- [3] R. Atkinson, *Int. J. Chem. Kinet.* **29**, 99 (1997).
- [4] C. C. Carter, J. R. Atwell, S. Gopalakrishnan, and T. A. Miller, *J. Phys. Chem. A* **104**, 9165 (2000).
- [5] C. C. Carter, S. Gopalakrishnan, J. R. Atwell, and T. A. Miller, *J. Phys. Chem. A* **105**, 2925 (2001).
- [6] S. Gopalakrishnan, C. C. Carter, L. Zu, V. Stakhursky, G. Tarczay, and T. A. Miller, *J. Chem. Phys.* **118**, 4954 (2003).
- [7] S. Gopalakrishnan, L. Zu, and T. A. Miller, *J. Phys. Chem. A* **107**, 5189 (2003).
- [8] X. Liu, V. Stakhursky, E. D. Olmon, V. A. Lozovsky, T. A. Miller, and C. B. Moore, *58th OSU International Symposium on Molecular Spectroscopy* (The Ohio State University, Columbus Ohio, 2003).
- [9] X. Zhu, M. M. Kamal, and P. Misra, *Pure Appl. Opt.* **5**, 1021 (1996).
- [10] J. Yoon, K. S. Kim, and K. K. Baeck, *J. Chem. Phys.* **112**, 9335 (2000), and references therein.
- [11] K. Balasubramanian and M. Z. Liao, *Chem. Phys.* **127**, 313 (1988).
- [12] K. Balasubramanian and P. Feng, *Chem. Phys. Lett.* **159**, 452 (1989).
- [13] K. Balasubramanian and P. Feng, *J. Phys. Chem.* **94**, 1536 (1990).
- [14] A. M. Ellis, E. S. J. Robles, and T. A. Miller, *Chem. Phys. Lett.* **201**, 132 (1993).

- [15] S. P. Walch, C. W. Bauschlicher, and S. R. Langhoff, *J. Chem. Phys.* **85**, 5900 (1986).
- [16] T. A. Barckholtz and T. A. Miller, *Int. Rev. Phys. Chem.* **17**, 435 (1998).
- [17] E. E. Wedum, E. R. Grant, P. Y. Cheng, K. F. Willey, and M. A. Duncan, *J. Chem. Phys.* **100**, 6312 (1994), and references therein.
- [18] F. Wallimann, H.-M. Frey, S. Leutwyler, and M. Riley, *Z. Phys. D* **40**, 30 (1997).
- [19] P. Y. Cheng and M. A. Duncan, *Chem. Phys. Lett.* **152**, 341 (1988).
- [20] K. LaiHing, P. Y. Cheng, and M. A. Duncan, *Z. Phys. D* **13**, 161 (1989).
- [21] R. G. Satink, G. Meijer, and G. von Helden, *J. Am. Chem. Soc.* **125**, 15714 (2003), and references therein.
- [22] E. P. F. Lee and T. G. Wright, *J. Phys. Chem. A* **102**, 4007 (1998), and references therein.
- [23] R. D. Johnson, *J. Chem. Phys.* **95**, 7108 (1991), and references therein.
- [24] S. K. Shin, *Chem. Phys. Lett.* **280**, 260 (1997).
- [25] B. J. Smith and N. E. Hall, *Chem. Phys. Lett.* **279**, 165 (1997).
- [26] H. J. Silverstone, D. E. Wood, and H. M. McConnell, *J. Chem. Phys.* **41**, 2311 (1964).
- [27] R. F. Gunion, W. Karney, P. G. Wenthold, W. T. Borden, and W. C. Lineberger, *J. Am. Chem. Soc.* **118**, 5074 (1996).
- [28] B. A. Thrush and J. J. Zwolenik, *Faraday Discuss. Chem. Soc.* **35**, 196 (1963).
- [29] J. R. Wermer, O. Hollander, J. C. Huffman, J. A. K. Bauer, D. Dou, L.-Y. Hsu, D. L. Leussing, and S. G. Shore, *Inorg. Chem.* **34**, 3065 (1995), and references therein.
- [30] B. Liu and A. D. McLean, *J. Chem. Phys.* **59**, 4557 (1973).
- [31] F. B. van Duijneveldt, J. G. C. M. van Duijneveldt-van de Rijdt, and J. H. van Lenthe, *Chem. Rev.* **94**, 1873 (1994).
- [32] S. F. Boys and F. Bernardi, *Mol. Phys.* **19**, 553 (1970).

- [33] T. van Mourik, A. K. Wilson, K. A. Peterson, D. E. Woon, and T. H. Dunning, in *Adv. Quantum Chem.* (Löwdin, P.-O., Ed.; Academic Press: New York, 1999), Chap. Quantum Systems in Chemistry and Physics, Part I.
- [34] S. S. Xantheas, *J. Chem. Phys.* **104**, 8821 (1996).
- [35] See www.clarkson.edu/~pac/reps.html for complete references and a library of potentials.
- [36] L. F. Pacios and P. A. Christiansen, *J. Chem. Phys.* **82**, 2664 (1985).
- [37] M. M. Hurley, L. F. Pacios, P. A. Christiansen, R. B. Ross, and W. C. Ermler, *J. Chem. Phys.* **84**, 6840 (1986).
- [38] L. A. LaJohn, P. A. Christiansen, R. B. Ross, T. Atashroo, and W. C. Ermler, *J. Chem. Phys.* **87**, 2812 (1987).
- [39] R. B. Ross, J. M. Powers, T. Atashroo, W. C. Ermler, L. A. LaJohn, and P. A. Christiansen, *J. Chem. Phys.* **93**, 6654 (1990).
- [40] W. C. Ermler, R. B. Ross, and P. A. Christiansen, *Int. J. Quantum Chem.* **40**, 829 (1991).
- [41] Y. S. Lee, W. C. Ermler, and K. S. Pitzer, *J. Chem. Phys.* **67**, 5861 (1977).
- [42] P. A. Christiansen, Y. S. Lee, and K. S. Pitzer, *J. Chem. Phys.* **71**, 4445 (1979).
- [43] R. B. Ross, W. C. Ermler, and P. A. Christiansen, *J. Chem. Phys.* **84**, 3297 (1986).
- [44] T. H. Dunning, *J. Chem. Phys.* **90**, 1007 (1989).
- [45] P. A. Christiansen, *J. Chem. Phys.* **112**, 10070 (2000).
- [46] J. P. Blaudeau, S. R. Brozell, S. Matsika, Z. Zhang, and R. M. Pitzer, *Int. J. Quantum Chem.* **77**, 516 (2000).
- [47] N. M. Wallace, J. P. Blaudeau, and R. M. Pitzer, *Int. J. Quantum Chem.* **40**, 78 (1991).
- [48] J. M. L. Martin and A. Sundermann, *J. Chem. Phys.* **114**, 3408 (2001).
- [49] The basis sets where we took the f exponents are located in <http://theochem.weizmann.ac.il/web/papers/SDB-cc.html>.

- [50] K. A. Peterson, D. Figgen, E. Goll, H. Stoll, and M. Dolg, *J. Chem. Phys.* **119**, 11113 (2003).
- [51] See <http://www.emsl.pnl.gov:2080/forms/basisform.html>.
- [52] COLUMBUS programs are described at <http://www.itc.univie.ac.at/~hans/Columbus/Columbus.html>.
- [53] R. J. Harrison, J. A. Nichols, T. P. Straatsma, M. Dupuis, E. J. Bylaska, G. I. Fann, T. L. Windus, E. Apra, W. de Jong, S. Hirata, M. T. Hackler, J. Anchell, D. Bernholdt, P. Borowski, T. Clark, D. Clerc, H. Dachsel, M. Deegan, K. Dyall, D. Elwood, H. Fruchtl, E. Glendening, M. Gutowski, K. Hirao, A. Hess, J. Jaffe, B. Johnson, J. Ju, R. Kendall, R. Kobayashi, R. Kutteh, Z. Lin, R. Littlefield, X. Long, B. Meng, T. Nakajima, J. Nieplocha, S. Niu, M. Rosing, G. Sandrone, M. Stave, H. Taylor, G. Thomas, J. van Lenthe, K. Wolinski, A. Wong, and Z. Zhang, *NWChem, A Computational Chemistry Package for Parallel Computers, Version 4.1* (Pacific Northwest National Laboratory, Richland, Washington 99352-0999, USA., 2002).
- [54] J. Noga and R. J. Bartlett, *J. Chem. Phys.* **86**, 7041 (1987).
- [55] J. Noga and R. J. Bartlett, *J. Chem. Phys.* **89**, 3401 (1988).
- [56] S. A. Kucharski and R. J. Bartlett, *J. Chem. Phys.* **97**, 4282 (1992).
- [57] K. Raghavachari, G. W. Trucks, J. A. Pople, and M. Head-Gordon, *Chem. Phys. Lett.* **157**, 479 (1989).
- [58] K. Raghavachari, J. A. Pople, E. S. Replogle, and M. Head-Gordon, *J. Phys. Chem.* **94**, 5579 (1990).
- [59] P. Hohenberg and W. Kohn, *Phys. Rev.* **136**, B 864 (1964).
- [60] W. Kohn and L. J. Sham, *Phys. Rev.* **140**, A 1131 (1965).
- [61] A. D. Becke, *J. Chem. Phys.* **98**, 5648 (1993).
- [62] C. Lee, W. Yang, and R. G. Parr, *Phys. Rev. B* **37**, 785 (1988).
- [63] J. P. Perdew, J. A. Chevary, S. H. Vosko, K. A. Jackson, M. R. Pederson, D. J. Singh, and C. Fiolhais, *Phys. Rev. B* **46**, 6671 (1992).
- [64] C. Adamo and V. Barone, *J. Chem. Phys.* **110**, 6158 (1998).

- [65] J. V. der Maas Redy and W. N. Lipscomb, *J. Am. Chem. Soc.* **81**, 754 (1959).
- [66] D. Sands and A. Zalkin, *Acta Crystallogr.* **15**, 410 (1962).
- [67] T. H. Dunning, *J. Phys. Chem. A* **104**, 9062 (2000).
- [68] S. Yabushita, Z. Zhang, and R. M. Pitzer, *J. Phys. Chem. A* **103**, 5791 (1999).
- [69] M. P. Briggs, J. N. Murrell, and J. G. Stamper, *Mol. Phys.* **17**, 381 (1969).
- [70] B. M. Riemenschneider and N. R. Kestner, *Chem. Phys.* **3**, 193 (1974).
- [71] F. Maeder and W. Kutzelnigg, *Chem. Phys. Lett.* **37**, 285 (1976).
- [72] W. Kutzelnigg, *Faraday Discuss. Chem. Soc.* **62**, 185 (1977).
- [73] W. Meyer, P. C. Hariharan, and W. Kutzelnigg, *J. Chem. Phys.* **73**, 1880 (1980).
- [74] S. Kristyan and P. Pulay, *Chem. Phys. Lett.* **229**, 175 (1994).
- [75] R. J. Meier, *Faraday Discuss.* **124**, 405 (2003).
- [76] A. Görling, *J. Chem. Phys.* **123**, 62203 (2005).
- [77] P. Hobza, J. Šponer, and T. Reschel, *J. Comput. Chem.* **16**, 1315 (1995).
- [78] A. K. Rappe and E. R. Bernstein, *J. Phys. Chem. A* **104**, 6117 (2000).
- [79] X. Xu, Q. Zhang, R. P. Muller, and I. W. A. Goddard, *J. Chem. Phys.* **122**, 14105 (2005).
- [80] T. A. Wesolowski, O. Parisel, Y. Ellinger, and J. Weber, *J. Phys. Chem. A* **101**, 7818 (1997).
- [81] T. A. Wesolowski, Y. Ellinger, and J. Weber, *J. Chem. Phys.* **108**, 6078 (1998).
- [82] J. P. Perdew and Y. Wang, *Phys. Rev. B* **45**, 13244 (1992).
- [83] A. H. Blatt, in *Organic Synthesis, Collective Volume*; (Wiley, New York, 1943).
- [84] M. J. Frisch, G. W. Trucks, H. B. Schlegel, G. E. Scuseria, M. A. Robb, J. R. Cheeseman, V. G. Zakrzewski, J. A. Montgomery, R. E. Stratmann, J. C. Burant, S. Dapprich, J. M. Millam, A. D. Daniels, K. N. Kudin, M. C. Strain, O. Farkas, J. Tomasi, V. Barone, M. Cossi, R. Cammi, B. Mennucci, C. Pomelli, C. Adamo, S. Clifford, J. Ochterski, G. A. Petersson, P. Y. Ayala, Q. Cui, K.

Morokuma, D. K. Malick, A. D. Rabuck, K. Raghavachari, J. B. Foresman, J. Cioslowski, J. V. Ortiz, A. G. Baboul, B. B. Stefanov, G. Liu, A. Liashenko, P. Piskorz, I. Komaromi, R. Gomperts, R. L. Martin, D. J. Fox, T. Keith, M. A. Al-Laham, C. Y. Peng, A. Nanayakkara, C. Gonzalez, M. Challacombe, P. M. W. Gill, B. Johnson, W. Chen, M. W. Wong, J. L. Andres, C. Gonzalez, M. Head-Gordon, E. S. Replogle, and J. A. Pople, *Gaussian 98, Revision A.7* (Gaussian, Inc., Pittsburgh PA, 1998).

- [85] J. F. Stanton, J. Gauss, W. J. Lauderdale, J. D. Watts, and R. J. Bartlett. The package also contains modified versions of the MOLECULE Gaussian integral program of J. Almlöf and P. R. Taylor, the ABACUS integral derivative program written by T. U. Helgaker, H. J. As. Jensen, P. Jørgensen, and P. R. Taylor, and the PROPS property evaluation integral code of P. R. Taylor.
- [86] G. Tarczay, S. Gopalakrishnan, and T. A. Miller, *J. Mol. Spectrosc.* **220**, 276 (2003).
- [87] R. S. Mulliken, *J. Chem. Phys.* **23**, 1997 (1953).
- [88] T. M. Ramond, G. E. Davico, R. L. Schwartz, and W. C. Lineberger, *J. Chem. Phys.* **112**, 1158 (2000).
- [89] A. G. Császár, W. D. Allen, Y. Yamaguchi, and H. F. Schaefer, in *Computational Molecular Spectroscopy* (Wiley, New York, 2000), Chap. Ab Initio Determination of Accurate Potential Energy Hypersurfaces for the Ground Electronic States of Molecules.
- [90] E. R. Davidson and W. T. Borden, *J. Phys. Chem.* **87**, 4783 (1983).
- [91] J. F. Stanton, *Chem. Phys. Lett.* **237**, 20 (1995).
- [92] J. F. Stanton, *J. Chem. Phys.* **115**, 10382 (2001).
- [93] Y.-Y. Lee, G.-H. Wann, and Y.-P. Lee, *J. Chem. Phys.* **99**, 9465 (1993).
- [94] S. C. Foster, P. Misra, T.-Y. D. Lin, C. P. Damo, C. C. Carter, and T. A. Miller, *J. Chem. Phys.* **92**, 5914 (1988).
- [95] Y. Shen and J. J. BelBruno, *J. Chem. Phys.* **118**, 9241 (2003), and references therein.
- [96] T. L. Haslett, K. A. Bosnick, S. Fedrigo, and M. Moskovits, *J. Chem. Phys.* **111**, 6456 (1999).

- [97] P. Y. Cheng and M. A. Duncan, Chem. Phys. Lett. **156**, 420 (1989).
- [98] R. L. Martin and E. R. Davidson, Mol. Phys. **35**, 1713 (1977).
- [99] P. García-Fernández, I. B. Bersuker, J. A. Aramburu, M. T. Barriuso, and M. Moreno, Phys. Rev. B **71**, 184117 (2005).
- [100] B. E. Applegate, T. A. Miller, and T. A. Barckholtz, J. Chem. Phys. **114**, 4855 (2001).
- [101] R. Meiswinkel and H. Köppel, Chem. Phys. **129**, 463 (1989).
- [102] U. Höper, P. Botschwina, and H. Köppel, J. Chem. Phys. **112**, 4132 (2000).
- [103] B. E. Applegate, A. J. Bezant, and T. A. Miller, J. Chem. Phys. **114**, 4869 (2001).
- [104] B. E. Applegate and T. A. Miller, J. Chem. Phys. **117**, 10654 (2002).
- [105] P. Pulay, Mol. Phys. **17**, 197 (1969).
- [106] M. C. Payne, M. P. Teter, D. C. Allan, T. A. Arias, and J. D. Joannopoulos, Rev. Mod. Phys. **64**, 1045 (1992).
- [107] B. O. Roos and P. E. M. Siegbahn, in *Methods of Electronic Structure Theory* (H. F. Schaefer III, Plenum, New York, 1977), p. 277.
- [108] R. F. Hausmann and C. F. Bender, in *Methods of Electronic Structure Theory* (H. F. Schaefer III, Plenum, New York, 1977), p. 319.
- [109] E. R. Davidson, J. Comput. Phys. **17**, 87 (1975).
- [110] S. R. Langhoff and E. R. Davidson, Int. J. Quantum Chem. **8**, 61 (1974).
- [111] E. R. Davidson and D. W. Silver, Chem. Phys. Lett. **52**, 403 (1977).
- [112] P. E. M. Sieghabn, Chem. Phys. Lett. **55**, 386 (1978).
- [113] P. J. Bruna, S. D. Peyerimhoff, and R. J. Buenker, Chem. Phys. Lett. **72**, 278 (1981).
- [114] P. G. Burton, R. J. Buenker, P. J. Bruna, and S. D. Peyerimhoff, Chem. Phys. Lett. **95**, 379 (1983).

- [115] See www.clarkson.edu/~pac/reps.html for complete references and a library of potentials.
- [116] ATMSCF program, original version, Roothaan, C. C. J.; Bagus, P.S. Meth Comp Phys 1963, 2, 47-94; present version, Pitzer, R. M. QCPE 1990, 10, 587. Also see R. Pitzer, Comput. Phys. Comm. 170, 239 (2005).
- [117] V. Beutel, H.-G. Krämer, G. L. Bhale, M. Kuhn, K. Weyers, and W. Demtröder, J. Chem. Phys. **98**, 2699 (1993).
- [118] C. E. Moore, Atomic energy levels (Natl. Bur. Stds., Washington, 1971).
- [119] S. P. Walch and B. C. Laskowski, J. Chem. Phys. **84**, 2734 (1986).
- [120] M. N. Huda and A. K. Ray, Eur. Phys. J. D **22**, 217 (2003).
- [121] V. Bonačić-Koutecký, L. Češpiva, P. Fantucci, and J. Koutecký, J. Chem. Phys. **98**, 7981 (1993).
- [122] C. W. Bauschlicher, S. R. Langhoff, and H. Partridge, J. Chem. Phys. **91**, 2412 (1989).
- [123] H. Partridge, C. W. Bauschlicher, and S. R. Langhoff, Chem. Phys. Lett. **175**, 531 (1990).
- [124] W. Andreoni and J. L. Martins, Surf. Sci. **156**, 635 (1985).
- [125] K. Balasubramanian and M. Z. Liao, J. Chem. Phys. **86**, 5587 (1987).
- [126] K. Balasubramanian and K. K. Das, Chem. Phys. Lett. **186**, 577 (1991).
- [127] J. R. Lombardi and B. Davis, Chem. Rev. **102**, 2431 (2002), and references therein.
- [128] G. A. Ozin and D. F. McIntosh, J. Phys. Chem. **90**, 5756 (1986).
- [129] C. M. Brown and M. L. Ginter, J. Mol. Spectrosc. **69**, 25 (1978).
- [130] G. Herzberg, in *Infrared and Raman Spectra* (D. Van Nostrand Co., Princeton, 1966).

- [131] V. L. Stakhursky, V. A. Lozovsky, C. B. Moore, and T. A. Miller, *Simulations of Vibronic Levels in Degenerate Electronic States in the Presence of Jahn-Teller Coupling-Expansion of PES Through Third Order* (60th International Symposium on Molecular Spectroscopy, The Ohio State University, Columbus Ohio USA, 2005).
- [132] <http://www.chemistry.ohio-state.edu/~vstakhur/FC.php>.
- [133] S. P. Walch, *J. Chem. Phys.* **87**, 6776 (1987).
- [134] H. Handschuh, C.-Y. Cha, P. S. Bechthold, G. Ganteför, and W. Eberhardt, *J. Chem. Phys.* **102**, 6406 (1995).
- [135] J. W. Zwanziger, R. L. Whetten, and E. R. Grant, *J. Phys. Chem.* **90**, 3298 (1986).
- [136] A. M. Ellis, E. S. J. Robles, and T. A. Miller, Unpublished work (1991).
- [137] G. A. Bishea and M. D. Morse, *J. Chem. Phys.* **95**, 8779 (1991).
- [138] G. Herzberg, in *Molecular Spectra and Molecular Structure III. Electronic Spectra and Electronic Structure of Polyatomic Molecules* (D. Van Nostrand, Princeton, NJ, 1966).
- [139] P. C. Engelking and W. C. Lineberger, *J. Chem. Phys.* **67**, 1412 (1977).
- [140] M. S. Child, *Mol. Phys.* **3**, 601 (1960).
- [141] T. J. Sears, T. A. Miller, and V. E. Bondybey, *J. Chem. Phys.* **72**, 6070 (1980).
- [142] T. J. Sears, T. A. Miller, and V. E. Bondybey, *J. Chem. Phys.* **74**, 3240 (1981).
- [143] J. P. Maier, private communication (2006). The assignment of the feature at 26573 cm^{-1} to the origin of the REMPI excitation spectrum is uncertain as it was found either absent or present but with a weak intensity in the repeated spectra. It is likely that this feature corresponds to a hot band.
- [144] W. G. Fateley, B. Curnette, and E. R. Lippincott, *J. Chem. Phys.* **26**, 1471 (1957).
- [145] F. Gütthe, H. Ding, T. Pino, and J. P. Maier, *Chem. Phys.* **269**, 347 (2001).